Thermal and superfluid properties of the two-dimensional Bose gas

Rémi Desbuquois

Département de physique
École Normale Supérieure

Laboratoire Kastler Brossel

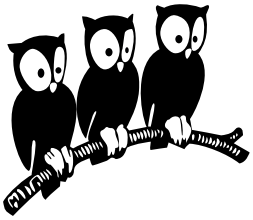

THÈSE de DOCTORAT de l'UNIVERSITÉ PARIS 6

Spécialité : Physique Quantique

présentée par

Rémi Desbuquois

pour obtenir le grade de DOCTEUR de l'UNIVERSITÉ PARIS 6

Thermal and superfluid properties of the two–dimensional Bose gas

---

Soutenue le 3 Juin 2013

devant le jury composé de :

M.	**Tilman Esslinger**	Rapporteur
M.	**Pascal Szriftgiser**	Rapporteur
M.	**David Guéry-Odelin**	Examinateur
M.	**Markus Holzmann**	Examinateur
M.	**Jean Dalibard**	Directeur de thèse

And then the man he steps right up to the microphone
And says at last just as the time bell rings
"Thank you goodnight now it's time to go home"
And he makes it fast with one more thing
"We are the Sultans of Swing"

Dire Straits, *Sultans of Swing*, 1979

Contents

Résumé

Introduction

En 1995, l'observation de Bose–Einstein (CBE) dans des vapeurs atomiques diluées a ouvert la voie à un vaste domaine de la physique atomique. Aux très basses températures, la longueur d'onde thermique des particules individuelles et la distance entre particules sont comparables. La statistique quantique joue alors un rôle essentiel dans leur comportement. À cet égard, la condensation de Bose – Einstein constitue la manifestation macroscopique la plus spectaculaire de la nature quantique de particules individuelles : pour un système de bosons suffisamment froids, la statistique quantique des particules les conduit à s'accumuler dans un seul état quantique, formant une "onde de matière géante". La prédiction théorique d'un tel comportement a été faite dès 1925 par Einstein, fondée sur un travail antérieur de Bose. Pendant longtemps, la seule manifestation expérimentale de la CBE était l'hélium superfluide. Cependant, l'hélium superfluide est un système en interaction forte, ce qui complique la fois les mesures et la comparaison avec la théorie. En effet, lors de la mesure de sa fraction condensée en 1979, il a été constaté que seulement 10% des atomes occupent le même état quantique. À cet égard, bien que les propriétés de l'hélium superfluide découlent directement de sa nature bosonique, il ne se forme pas de fonction d'onde macroscopique prévue lors de la condensation de Bose–Einstein d'un gaz parfait.

En revanche, les systèmes dilués sont naturellement en interaction faible, et se prêtent à une description de champ moyen plus simple. Dans ce cas, le gaz est décrit avec précision par une fonction d'onde unique, dont le comportement est régi par une équation de Schrödinger non linéaire : l'équation de Gross–Pitaevskii. Pendant les années qui ont suivi la réalisation expérimentale de la CBE, la recherche a été principalement orientée vers l'exploration des phénomènes bien décrits dans ce cadre. La nature ondulatoire de la CBE a été démontrée par l'interférence de deux CBE. La cohérence à longue distance de ce système a été alors observée et a conduit à la réalisation expérimentale d'un laser à atomes. Le caractère superfluide d'un CBE a été démontré par l'observation des tourbillons quantifiés, et de leur disposition dans des réseaux Abriko-

sov. Notons que les réalisations expérimentales n'étaient pas limitées aux gaz de Bose : dans les années qui ont suivi l'observation d'un CBE, le gaz de Fermi a été amené à la dégénérescence quantique par des techniques expérimentales similaires.

L'intérêt continu apporté aux atomes froids est en grande partie dû au degré élevé de contrôle que l'on peut exercer sur ces systèmes. Ce contrôle repose sur deux outils puissants : la variabilité des interactions, grâce à l'utilisation des résonances de Feshbach, et la possibilité d'ajuster la géométrie du système, en choisissant des potentiels de piégeage optique et magnétique adaptés.

La résonance de Feshbach est d'un intérêt particulier, car non seulement la force des interactions peut être ajustée, mais aussi leur signe. Dans un gaz de Fermi, de fortes interactions attractives conduisent à la formation de molécules faiblement liés fermioniques, tandis que des interactions attractives faibles conduisent à la formation de paires de Cooper. À une température suffisamment basse, les molécules peuvent alors former un CBE, tandis que les paires de Cooper peut former un superfluide, qui est bien décrit par la théorie BCS. En outre, l'accordabilité des interactions a permis une étude d'un phénomène associé : le passage d'un BCE à un superfluide décrit par la théorie BCS. En utilisant les résonances de Feshbach, le régime fortement interaction peut être atteint, tant pour les gaz de Bose que pour les gaz de Fermi. Plus récemment, les mesures de l'équation d'état de ces systèmes ont révélé des contributions au-delà de la théorie de champ moyen.

Le contrôle de la géométrie permet en outre la réalisation de gaz ultrafroids en dimension réduite. En confinant un gaz de Bose ultrafroid en une géométrie unidimensionnelle, il a été possible d'observer un gaz de Tonks–Girardeau, ce qui constitue le premier exemple d'un liquide de Luttinger bosonique. La réalisation d'un gaz de Bose à deux dimensions conduit à l'observation de la transition de phase entre un état normal et un état superfluide : c'est la transition Berezinskii – Kosterlitz – Thouless (BKT).

De nouvelles phases de la matière peuvent également être créés grâce à l'utilisation de réseaux optiques. Dans ce cas, l'utilisation des potentiels de piégeage spatialement modulés force les atomes à se disposer périodiquement, de manière similaire aux électrons dans un solide. Ces systèmes constituent une réalisation très pure d'un modèle fondamental de la physique de l'état solide : le hamiltonien de Hubbard. En général, l'utilisation des réseaux optiques permet d'entrer dans le régime des interactions fortes, et d'observer des phénomènes au-delà du champ moyen. En particulier, cette technique a conduit à l'observation de la transition de phase quantique entre une phase superfluide et une phase isolante de Mott, tant des systèmes bosoniques que fermioniques.

Cette correspondance particulière entre les atomes ultrafroids dans des réseaux optiques et les électrons dans le réseau cristallin d'un solide illustre la notion de *simulation quantique* proposée par Feynman en 1982. Au lieu d'étudier un système donné, on peut en reproduire les caractéristiques importantes, et mesurer directement les propriétés de la copie. De cette manière, les atomes dans un réseau optique permettent de simuler des électrons dans un solide, dépouillés de tous défauts ou de champs perturbateurs, permettant ainsi une meilleure compréhension de la physique sous-jacente. Avec cette correspondance à l'esprit, on peut espérer gagner un nouvel éclairage sur de nombreux problèmes de la physique à N corps, tels que la supraconductivité à haute température ou l'effet Hall quantique fractionnaire (EHQF). Pour cette raison, des efforts considérables ont été réalisés pour concevoir des hamiltoniens spécifiques dans des expériences d'atomes froids, pour atteindre ces états fortement corrélés.

L'EHQF apparait lorsqu'un gaz bidimensionnel d'électrons en interactions est soumis à un champ magnétique, à des températures suffisamment basses. Puisque les atomes utilisés dans nos expériences sont neutres, nous avons besoin de générer un champ magnétique efficace pour étudier ces phases de la matière. Cela peut se faire par exemple en exploitant l'équivalence de la force de Lorentz et la force de Coriolis : la rotation du système agit comme un champ magnétique artificiel. De manière alternative, nous pouvons profiter de la similitude entre la phase d'Aharonov – Bohm et la phase de Berry, qui apparait en présence d'un état interne dépendant de l'espace. Une phase non-triviale de Berry peut par exemple résulter de la création d'états habillés. Une technique similaire peut être mise en œuvre dans les réseaux optiques, qui peuvent être conçus de telle sorte qu'un atome acquière une phase en passant d'un site de réseau à l'autre par effet tunnel, et simuler ainsi un champ magnétique.

Le travail effectué pendant ma thèse a porté sur l'étude du gaz de Bose à deux dimensions. Ce système est particulièrement intéressant pour plusieurs raisons. Comme l'a fait remarquer Peirls en 1934, la dimensionnalité d'un système affecte fortement ses phases d'équilibre. En effet, les fluctuations thermiques sont suffisantes pour empêcher la formation d'un CBE à la limite thermodynamique en deux dimensions, sauf à température nulle. Ceci constitue un cas particulier du théorème de Mermin – Wagner – Hohenberg, qui interdit toute sorte d'ordre à longue distance à la limite thermodynamique, dans les systèmes uni- et bidimensionnels, avec des interactions à courte portée et une symétrie continue du hamitonien. Toutefois, la limite thermodynamique n'est atteinte que pour les systèmes exponentiellement grands : en pratique, " l'échantillon devrait être plus grand que l'État du Texas pour que le théorème de Mermin – Wagner théorème soit pertinent". En ce sens, la géométrie bidimensionnelle peut être

considéré comme marginale : les effets de taille finie jouent toujours un rôle important dans tout système réaliste. En outre, même dans la limite thermodynamique, la présence d'interactions est suffisante pour donner lieu à une transition vers un état superfluide. La théorie associée à cette transition a été développé par Berezinskii, Kosterlitz et Thouless, conduisant à la désignation usuelle de la transition BKT.

Puisque le théorème de Mermin – Wagner – Hohenberg empêche la brisure des symétries continues, il n'y a pas de discontinuité de l'équation d'état au point de transition, la seule exception étant la densité superfluide. Pour cette raison, la transition BKT est souvent dite d' *ordre infini*. Bien qu'il n'y ait pas d'ordre à longue portée dans la phase superfluide, la transition est néanmoins marquée par un changement important dans la fonction de corrélation à un corps. Dans la phase superfluide, la fonction de corrélation à un corps décroit algébriquement avec la distance, au lieu de suivre une décroissance exponentielle ou gaussienne dans la phase normale. La transition est également accompagnée d'une réduction significative des fluctuations de densité, ce qui peut s'expliquer par une simple analyse de Bogolioubov.

La transition BKT a d'abord été observée dans des films d'hélium superfluide, et a fait l'objet d'intenses recherches récentes dans le domaine des atomes ultrafroids. En particulier, une expérience d'interférence entre plusieurs gaz de Bose 2D a révélé la présence de tourbillons, qui sont cruciaux pour le mécanisme microscopique associé à la transition BKT. D'autres études ont également révélé les propriétés de cohérence du gaz de Bose à 2D, ainsi que son invariance d'échelle approximative en présence d'interactions faibles. Le travail présenté dans cette thèse explore plusieurs propriétés associées à cette transition de phase, et est décrit dans ce qui suit.

Corps de la thèse

Élements de théorie

Nous commençons par présenter quelques résultats théoriques essentiels à la compréhension du gaz de Bose bidimensionnel. La première partie se concentre sur le gaz de Bose idéal à deux dimensions. Un critère suffisant pour montrer l'existence de la CBE repose sur la saturation des niveaux excités à une particule. En effet, à trois dimensions, le nombre d'atomes pouvant occuper les niveaux excités à température non-nulle est fini, et les atomes excédentaires doivent s'accumuler dans le niveau fondamental. En revanche, il n'existe pas une telle saturation des niveaux excités à la limite thermodynamique, excepté à

température nulle. Ce résultat est en bon accord avec le théorème de Mermin–Wagner–Hohenberg, qui interdit l'émergence d'un ordre à longue portée à température non-nulle à deux dimensions. Ce résultat doit cependant être nuancé. En effet, nos expériences ont lieu dans un système piégé de taille finie. Bien qu'il n'existe pas d'ordre à longue portée, la longueur de corrélation croit néanmoins exponentiellement avec la densité dans l'espace des phases. Conséquemment, il existe une température non-nulle telle que cette longueur de corrélation soit de la taille du système. Ainsi, un CBE sera toujours présent à température non-nulle dans un système bi-dimensionnel de taille finie. En particulier, nous pouvons calculer le nombre d'atome nécessaire pour obtenir un CBE dans un piège harmonique.

Dans la deuxième partie, nous considérons le gaz de Bose à deux dimensions en interaction. Afin de présenter un traitement correct des interactions, il importe de prendre en compte correctement l'existence d'une troisième dimension dans toute réalisation expérimentale. Le fort confinement selon un axe de l'espace permet de réaliser un gaz 2D, et définit également une épaisseur caractéristique. Lorsque cette longueur est nettement plus grande que la portée effective du potentiel d'interaction entre particules, les collisions sont dites *quasi-2D*, et peuvent être décrites par un potentiel de contact. De plus, si cette épaisseur caractéristique est également grande devant la longueur de diffusion tri-dimensionnelle, l'amplitude de diffusion est constante, de manière analogue au cas 3D. Ces propriétés collisionnelles ont pour importante conséquence l'invariance d'échelle approchée de l'équation d'état du gaz de Bose 2D. Cette propriété peut être mise en évidence dans les deux régimes où l'équation d'état est connue : le gaz thermique est décrit par la théorie Hartree–Fock de champ moyen, et le gaz fortement dégénéré est décrit par l'équation de Thomas–Fermi. Bien que la condensation de Bose–Einstein ne puisse pas avoir lieu dans un système infini, il existe néanmoins une transition vers un état superfluide, appelée transition BKT. Au voisinage du point critique, l'équation d'état n'est pas connue analytiquement. En revanche, il existe une prédiction numérique, fondée sur une simulation Monte–Carlo de champ classique. Lors de nos études du gaz en interaction, l'invariance d'échelle est une propriété que nous utilisons dans toutes nos études du gaz de Bose 2D, tandis que la transition BKT constitue l'objectif principal de nos investigations.

Dispositif expérimental

Le chapitre suivant sert de complément au premier chapitre : il présente le dispositif expérimental nécessaire pour la réalisation de gaz de Bose bidimen-

sionnels ultrafroids. Puisque l'expérience a déjà été décrite par les doctorants, nous allons principalement détailler les modifications les plus récentes. La séquence expérimentale se déroule de la manière suivante. Un nuage atomique est capturé par un piège magnéto-optique depuis la vapeur de rubidium ambiante, puis transféré dans un piège quadrupolaire. Il est ensuite transporté magnétiquement vers une partie de l'enceinte où règne un vide plus poussé. Là, la température du nuage est abaissée par refroidissement évaporatif par radio-fréquences. Une fois le nuage suffisamment froid, il est transféré dans un piège hybride : le confinement est réalisé à deux dimensions par un faisceau laser désaccordé vers le rouge de la transition atomique, et le piège magnétique réalise le confinement selon la troisième dimension. Ce piège hybride permet de conserver des taux de collisions élevés. De plus, un choix géométrique judicieux permet d'éviter les pertes Majorana. Enfin, ce piège s'affranchit des contraintes associées à un piège croisé (donc avec deux faisceaux), et facilite l'alignement. Ainsi, il est possible de produire un CBE tri-dimensionnel en 36s depuis le chargement du PMO. Le confinement bi-dimensionnel est ensuite assuré par un second piège dipolaire. Par une technique holographique, il est possible de produire deux feuille de lumière, très proches l'une de l'autre. Pour un faisceau laser choisi désaccordé vers le bleu de la transition, les atomes sont repoussés par la lumière, et occupent les régions de faible intensité. En particulier, les atomes situés entre les deux plans lumineux constituent notre système bi-dimensionnel. Les atomes résiduels situés de part et d'autre du plan central sont éliminés en les éclairant sélectivement avec un faisceau laser résonant, qui les dépompe vers un autre état hyperfin. Une fois le système 2D préparé, sa température peut être contrôlée par une étape supplémentaire de refroidissement évaporatif par radio-fréquences.

La deuxième partie de ce chapitre est consacrée à notre procédure d'acquisition de données. La méthode usuelle pour sonder les nuages ultrafroids consiste à en réaliser l'image par absorption. Cependant, pour obtenir une détermination correcte de la densité atomique, il est nécessaire d'avoir une bonne connaissance de la relation entre densité atomique et intensité lumineuse. Dans nos échantillons, la distance moyenne inter-particules peut être plus petite que la longueur d'onde d'imagerie, d'où une section transversale dépendant de la densité d'absorption lors de l'imagerie faiblement saturante traditionnelle. Ce problème est résolu par l'utilisation de l'imagerie de haute intensité, qui vise plutôt à saturer la transition, afin de fournir une image fidèle de l'échantillon. Dans ce cas, on peut considérer que chaque atome occupe son état fondamental la moitié du temps, et son état excité l'autre moitié. Dans ce cas là, la densité atomique est directement proportionnelle au nombre de photons manquant lors de

la détection. Notons que cette méthode présente un niveau de bruit intrinsèquement plus élevé que l'imagerie par absorption usuelle, à cause de bruit de grenaille photonique. Pour cette raison, nous utiliserons les deux méthodes. L'imagerie traditionnelle permet d'obtenir un bon rapport signal-sur-bruit dans les régions de faible densité, tandis que l'imagerie à haute intensité permet d'obtenir une image fidèle de la distribution atomique. Expérimentalement, nous utilisons deux axes d'imageries complémentaires, qui nous permettent non seulement de diagnostiquer et d'ajuster notre expérience, mais aussi d'avoir un accès direct à la densité atomique de nos échantillons 2D. Enfin, les images obtenues de cette manière peuvent subir un traitement statistique, visant à améliorer le rapport signal-sur-bruit. A cette fin, nous avons mis en place un algorithme de traitement d'image, l'analyse en composantes principales. En exploitant la similarité entre différentes images expérimentales, il est possible d'augmenter encore le rapport sigal-sur-bruit.

Équations d'état

Le chapitre suivant présente une mesure de l'équation d'état du gaz de Bose à deux dimensions, avec deux méthodes différentes. La première de ces méthodes a fait l'objet d'une publication dans une revue à comité de lecture, et est résumée brièvement ici. Nous sommes en mesure de préparer des CBE bidimensionnels en suivant la procédure expérimentale décrite plus haut. Une configuration donnée (nombre d'atomes et température) est préparée deux fois, de façon à pouvoir prendre une image de la distribution atomique à basse et haute intensité. Les images prises à basses intensité sont caractérisées par un rapport signal-sur-bruit élevé dans les régions de basse densité. Nous les utilisons donc pour effectuer un ajustement de la théorie Hartree–Fock de champ moyen, et mesurer ainsi la température et le potentiel chimique au centre du piège. Par ailleurs, les images prises à haute intensité donnent une image fidèle de la densité atomique, et permettent de mesurer le nombre d'atomes total contenu dans le système. Enfin, en combinant nombre d'atomes et températures, il est possible de déterminer la pression au centre du piège. En préparant des échantillons atomiques de nombre d'atomes et des températures différents, nous sommes en mesure d'explorer un large éventail de paramètres et de reconstruire l'équation d'état du gaz de Bose 2D. Cela constitue la première détermination d'une équation d'état du gaz de Bose à deux dimensions. De manière similaire, nous pouvons mesurer la densité atomique au centre du piège, et en déduire la densité dans l'espace des phases au centre du piège en la combinant avec la température, ce qui constitue une deuxième équation d'état. Finalement,

la combinaison de la pression et de la densité dans l'espace des phases nous permet de déterminer l'entropie par particule au centre du piège. Tous ces résultats sont en très bon accord avec la prédiction numérique évoquée précédemment.

La seconde méthode conduit à des résultats similaires, mais suit une approche plus globale, inspirée par les expériences réalisées au MIT dans le groupe de M. Zwierlein. Ainsi, la première méthode présentée repose sur un ajustement de la théorie Hartree–Fock de champ moyen sur chaque image, et est ainsi sensible aux erreurs systématiques, en particulier sur la calibration de l'imagerie. En combinant la dérivée et l'intégrale de la densité par rapport au potentiel local, nous sommes en mesure de former deux quantités sans dimensions, qui sont donc une forme de l'équation d'état. Cette procédure peut être répétée pour toutes les images, afin d'accroitre le rapport signal-sur-bruit des quantités ainsi formées. Afin de revenir à une variable thermodynamique plus usuelle, telle que la densité dans l'espace des phases, nous pouvons effectuer l'intégration d'une combinaison judicieuse de ces quantités. Enfin, la détectivité de notre système d'imagerie est calibrée en effectuant un unique ajustement de l'équation d'état ainsi formée avec la théorie Hartree–Fock de champ moyen. Cette méthode peut ensuite être affinée pour tenir compte de la population des états excités dans la direction fortement confinée. Les deux méthodes présentées sont en excellent accord entre elles, ainsi qu'avec la prédiction numérique.

Superfluidité du gaz de Bose à deux dimensions

Bien que les mesure d'équations d'état présentées ici soient en bon accord avec les prédictions numériques, elles ne constituent cependant pas une preuve directe de la présence ni de la transition BKT, ni d'un superfluide. La principale caractéristique d'un superfluide est l'absence de dissipation lors de la perturbation par un défaut en mouvement, lorsque la vitesse du défaut est en deçà d'une certaine vitesse critique. La détermination de cette vitesse critique à partir des premiers principes est en général un problème compliqué. En effet, le mécanisme de dissipation mis en œuvre dépend de la taille du défaut. Un défaut de taille comparable à la longueur de cicatrisation conduit à une dissipation portée par des phonons, tandis qu'un défaut significativement plus gros génère des anneaux de vorticité à trois dimensions, ou des paires de tourbillons à deux dimensions. Ainsi, la vitesse critique dépend de la taille du défaut.

Afin de mesurer le caractère superfluide du gaz de Bose à deux dimensions, nous créons une perturbation locale de la densité, en focalisant un faisceau laser désaccordé vers le bleu de la transition atomique sur le CBE bi-dimensionnel. La haute qualité de notre système optique nous permet de générer des défauts

de taille micrométrique. Avec un miroir monté sur cales piézo-électriques, nous pouvons ensuite déplacer ce défaut à travers le CBE, selon une trajectoire et une vitesse contrôlée. Nous mesurons ensuite l'accroissement de température du nuage selon la vitesse de déplacement du défaut, pour différentes trajectoires suivies. Nous pouvons ainsi mettre en évidence deux réponses du système. Dans la partie normale du nuage, la température augmente continument avec la vitesse, alors que dans la partie superfluide, il existe une vitesse critique en deçà de laquelle la température ne change pas. De plus, la réponse du nuage suit la dépendance attendue par rapport à la densité dans l'espace des phases : seules les parties fortement dégénérées présentent une réponse superfluide. Enfin, le taux d'accroissement de la température dans la partie normale est en bon accord avec une description qualitative de la dissipation, et rend correctement compte de la diminution de la densité normale au-delà de la transition BKT. Ce travail a également été publié dans une revue à comité de lecture.

Fluctuations du gaz de Bose bi-dimensionnel

Ce chapitre présente une étude poussée des fluctuations liées à la transition BKT. En relâchant le gaz de Bose à deux dimensions le long de la direction fortement confinée, les fluctuations de phases présentes dans la distribution d'équilibre sont converties en fluctuations de densité, qui peuvent ensuite être révélées par l'imagerie par absorption. Dans un premier temps, nous nous intéressons aux minima locaux de la densité. En effet, le mécanisme microscopique associé à la transition BKT fait intervenir des tourbillons, soit des défauts locaux de densité. Il est donc naturel d'en chercher une trace. L'étude des minima montre que ceux-ci sont plus nombreux et plus prononcés après une évolution libre que dans la distribution d'équilibre. Ceci est en bon accord avec le comportement attendu : pour un gaz de Bose bi-dimensionnel dégénéré, seules les fluctuations de phases jouent un rôle, alors que les fluctuations de densité sont gelées. Ainsi, l'augmentation du nombre de minima après une évolution libre est en bon accord avec cette propriété. Néanmoins, ces observations ne sont pas suffisantes pour conclure à la présence de tourbillon. En effet, dans une image simple, un unique tourbillon dans un nuage de densité uniforme conduit à une déplétion locale de la densité, et brise donc explicitement la symétrie entre minima et maxima. Or, une analyse des maxima ne révèle aucune différence avec les minima : il est donc peu probable que les tourbillons soient responsables des fluctuations de densité observées.

Dans un second temps, nous nous intéressons à la fonction de corrélation à deux corps : ses propriétés après évolution libre sont directement reliées à

celles de la fonction de corrélation à un corps de la distribution d'équilibre. Cette quantité révèle également une augmentation de l'amplitude des fluctuations après une évolution libre, et confirme le rôle prépondérant joué par les fluctuations de phase. De plus, la transformée de Fourier de cette fonction de corrélation présente des pics marqués, qui peuvent être interprétés simplement en terme d'effet Talbot. Pour les parties fortement dégénérées du nuage, seul un pic apparait, qui est attribué aux fluctuations de phase. En revanche, dans la région critique et dans la partie normales, deux pics secondaires apparaissent, qui sont directement liés aux fluctuations de densité. Ces résultats sont en accord quantitatif avec une étude théorique précédente, au moins dans la partie dégénérée du nuage.

Gas de Bose 2D dans un piège uniforme

Dans ce chapitre, nous proposons d'étudier l'interaction entre les transitions CBE et BKT. En effet, le mécanisme physique sous-jacent diffère entre les deux. Dans le cas de la CBE, la statistique bosonique conduit à l'établissement d'une onde de matière macroscopique. En revanche, la transition BKT est directement induite par les interactions, et conduit à la formation d'un superfluide. Le piège harmonique que nous avons utilisé dans nos expériences antérieures n'est pas bien adapté à cette tâche : la présence d'interactions modifie fortement la distribution atomique par rapport au gaz idéal. Les deux transitions peuvent être plus facilement comparées par l'étude d'un système dans un potentiel en forme de boîte. Considérons un tel système à une température fixe. Alors que le nombre de particules est augmenté, une des deux transitions se produit en premier : soit la densité de l'espace de phase atteint la valeur critique pour la transition BKT, ou alors les états excités deviennent saturés, conduisant à la formation d'un CBE. L'ordre dans lequel ces transitions ont lieu dépend de la taille de la boîte et de la température : dans un système infini, la transition BKT aura lieu en premier (puisque la CBE ne se produit qu'à une température nulle), alors que dans un système suffisamment petit, les niveaux excités vont saturer premier. Ainsi, pour une taille de boîte convenable, nous pouvons espérer observer séparément l'effet des deux transitions, en fonction de la température du système.

Un tel potentiel en forme de boite peut être réalisé de deux façons. Par holographie, il est possible de créer un faisceau de mode Laguerre–Gauss d'ordre élevé. Cependant, cette méthode est assez sensible aux défauts présents dans la lame de phase, et ne permet pas de générer une distribution d'intensité satisfaisante. Une seconde méthode passe par la formation directe de l'image d'un

masque sur les atomes. Ici, la qualité du piège ainsi créé est conditionnée par la qualité du système d'imagerie utilisé, et en particulier par son ouverture numérique. Une telle méthode conduit à des résultats plus satisfaisants, qui devraient permettre d'observer un gaz 2D prochainement. Lors de l'écriture de ce manuscrit, ce travail est encore cours et devrait bientôt porter ses fruits.

Imagerie à atomes uniques

Enfin, le dernier chapitre présente un travail en cours : la réalisation d'un système de détection d'atomes uniques. À cette fin, nous mettons en place un système similaire à celui mis au point à Harvard et au MPQ à Munich. Dans cette configuration, les atomes sont figés dans un réseau tridimensionnel de grande profondeur, et refroidis simultanément par une mélasse optique. Les photons diffusés à partir du faisceau de la mélasse sont ensuite détectées et utilisées pour reconstruire le profil de densité de l'échantillon. Pour réaliser le réseau optique de grande profondeur nécessaire à ce dispositif, nous avons choisi de nous désaccorder faiblement de la transition atomique, afin de ne pas avoir besoin de trop de puissance laser. Dans ce cas, il importe de choisir soigneusement le désaccord du réseau, afin de ne pas perturber le fonctionnement de la mélasse. Deux effets sont particulièrement néfastes. D'une part, la structure hyperfine de la transition atomique considérée donne lieu à une contribution vectorielle à l'opérateur déplacement lumineux, qui lève la dégénérescence entre les états Zeeman. Ainsi, si l'écart entre les états Zeeman est trop important, les mécanismes de refroidissement sub-Doppler dans la mélasse ne seront pas suffisamment efficaces pour figer la distribution atomique. D'autre part, le dépompage d'un atome dans l'autre niveau hyperfin fondamental peut lui communiquer une énergie cinétique significative, qui peut être trop importante pour être dissipée dans la mélasse. Afin d'éviter ces deux effets, le désaccord du réseau doit être suffisamment grand. Enfin, un effet de type " mélasse grise " peut se produire pour des faisceaux désaccordés vers le rouge de la transition, qui peuvent conduire à un chauffage supplémentaire. Bien que nous n'ayons pas pu estimer l'amplitude de cet effet, nous avons néanmoins choisi de nous placer sur le bleu de la transition, afin de prévenir cet éventuel problème.

Une caractérisation préliminaire du système a montré que chaque élément fonctionne correctement indépendamment. La profondeur du réseau a été caractérisée par diffraction de Raman–Nath, et le bon fonctionnement de la mélasse a été mis en évidence par une mesure du coefficient de diffusion atomique. En revanche, nous n'avons pas été en mesure de geler et d'imager un échantillon atomique. Nous sommes convaincus que la limitation principale est

d'ordre technique : la puissance laser utilisée pour réaliser le réseau ne permet pas d'atteindre les profondeurs requises. Une modification du système laser devrait pallier le problème. Par conséquent, nous espérons réaliser ce système de détection dans les prochains mois.

Conclusion et perspectives

A partir du travail qui a été présenté ici, nous pouvons définir deux grandes directions de recherche. Nous pouvons continuer à étudier le gaz de Bose à deux dimensions, en réalisant un gaz de Bose uniforme. D'autre part, une fois que notre système de détection d'atome unique sera opérationnel, nous pouvons profiter de cela pour sonder les états fortement corrélés à peu de particules. Dans ce qui suit, nous allons détailler ces deux points de vue. Une première extension de notre travail serait bien sûr de compléter l'étude en cours de l'interaction entre la CBE et la transition BKT. Une fois qu'un potentiel en forme de boîte approprié sera réalisé et caractérisé, nous proposons la mesure suivante.

Pour un nombre d'atome donné, nous mesurons la distribution d'impulsion, que ce soit par des expériences de temps de vol, ou en effectuant une tomographie de l'état du système. Lorsque la température de l'échantillon est abaissée, l'apparition d'un pic dans la distribution d'impulsion caractérise l'émergence de la condensation de Bose-Einstein. En effectuant cette mesure pour différents nombres d'atomes, on peut obtenir une détermination de la température critique en fonction du nombre d'atomes. Cette expérience peut être réalisé à la fois dans un piège harmonique et dans une boîte. L'effet de la différente densité d'état serait alors révélé par la comparaison des deux mesures.

En outre, la réalisation d'un uniforme 2D gaz de Bose permettrait une étude plus poussée de ses fluctuations, semblable à celle présentée précédemment. Dans ce cas, nous ne serions pas limités par le manque d'homogénéité du potentiel de piégeage, et nous pourrions sonder les propriétés de corrélation du gaz à plus grande échelle. En outre, un rapport signal-bruit plus important dans la détermination de la fonction de corrélation à deux corps après le temps de vol devrait nous permettre de démontrer la décroissance algébrique de la fonction de corrélation à un corps, et à mesurer son exposant.

On peut également profiter de la densité uniforme pour réaliser des expériences similaires à celles ayant permis de mettre en évidence les propriétés superfluides du système. Dans ce cas, nous pourrions observer le sillage laissé par ce faisceau, qui devrait dépendre du caractère superfluide du fluide et de la vitesse du défaut. En particulier, au-dessus de la vitesse critique, on devrait

observer un sillon similaire à celui apparaissant dans l'effet Cherenkov. Une telle expérience a été réalisée avec des polaritons dans un semi-conducteur en microcavité, mais dans un système hors équilibre.

Comme nous l'avons indiqué dans l'introduction, les atomes ultrafroids sont particulièrement bien adaptés à la simulation des phénomènes de la matière condensée. Dans ce contexte, nous voulons réaliser de grands champs magnétiques effectifs pour atteindre les états fortement caractéristiques de l'effet Hall quantique fractionnaire (EHQF), comme l'état Laughlin pour les bosons. Plusieurs possibilités pour créer un tel champ magnétique effectif ont été, telles que la rotation du, ou l'utilisation de champs de jauge artificiels. Les deux méthodes ont été réalisées avec succès, mais le champ magnétique généré de cette manière était trop petit pour entrer dans le régime fortement corrélés. Le champ magnétique maximal est limité par l'anisotropie statique résiduelle du piège dans le cas de la rotation, tandis que l'émission spontanée des faisceaux de couplage limite le champ dans le cas de champs de jauge artificiels.

Pour atteindre le régime fortement corrélés, nous considérons donc deux options. Tout d'abord, au lieu d'essayer d'augmenter le champ magnétique, on peut plutôt réduire le nombre d'atomes. Nous visons donc à préparer de très petits échantillons, contenant entre 3 et 10 atomes. Le champ magnétique artificiel sera réalisé par injection de moment angulaire dans le système, en habillant les états internes par couplage Raman, plutôt que directement par la rotation du piège. Une fois l'état fortement corrélé atteint, la fonction d'onde peut être ensuite magnifiée en laissant le nuage s'étendre à deux dimensions. La distribution de densité sera alors par imagée par la détection à atomes uniques décrite précédemment.

Une deuxième façon de produire un état fortement corrélé réside dans la réalisation de réseaux de flux optique. Dans un tel réseau optique, la bande d'énergie la plus basse est topologiquement équivalente au niveau de Landau le plus bas, ce qui est essentiel à la formation d'états à N corps. Notons qu'un tel régime n'est pas conceptuellement limité à un petit nombre d'atomes. En effet, les réseaux de flux optique génèrent un grand flux magnétique par cellule unitaire du réseau, ce qui permet de réaliser une telle expérience avec un grand nombre d'atomes.

Introduction

In 1995, the observation of Bose–Einstein condensation (BEC) in dilute atomic vapors [1–3] opened the way to a wide domain in atomic physics. At very low temperatures, the thermal wavelength of individual particles and the interparticle spacing are comparable, and quantum statistics play an essential role in their behavior. In this respect, Bose–Einstein condensation constitutes the most spectacular macroscopic manifestation of the quantum nature of individual particles: for a sufficiently cold bosonic system, the quantum statistics of the particles leads them to accumulate in a single quantum state, forming a "giant matter wave". The initial prediction for this behavior was made as early as 1925 by Einstein [4], based on a previous work by Bose [5]. For a long time, the only experimental manifestation of BEC was in superfluid ^{4}He [6]. However, superfluid ^{4}He is a strongly interacting system, thus complicating both the measurements and the comparison with theory. Indeed, when its condensed fraction was measured in 1979 [7], it was found that only 10 % of the atoms occupy the same quantum state. In this respect, though the properties of superfluid ^{4}He stem directly from its bosonic nature, it does not constitute the macroscopic wave function expected in the Bose Einstein condensation of an ideal gas.

By contrast, dilute systems are naturally weakly interacting, and lend themselves to a simpler mean field description. In this picture, the gas is accurately described by a single wave function, whose behaviour is governed by a nonlinear Schrödinger equation: the Gross–Pitaevskii equation [8, 9]. During the years following the experimental realization of BEC, the research was mainly directed towards the exploration of phenomena well described within this framework. The ondulatory nature of the BEC was demonstrated by the interference of two BECs [10]. The long range coherence of this system was then observed [11], and led to the experimental realization of an *atom laser* [12–14]. The superfluid character of the BEC was demonstrated through the observation of quantized vortices [15, 16], and of their arrangement in Abrikosov lattices [17]. Note that experimental realizations were not limited to Bose gases: in the years following the observation of a BEC, the Fermi gas was brought to degeneracy with similar experimental techniques [18–20].

The sustained interest in cold atoms is largely due to the high degree of con-

trol that one can exert over these system (see [21] for a review). Such control rests on two powerful tools: the tunability of interactions, through the use of Feshbach resonances [22, 23], and the possibility to adjust the geometry of the system, by choosing adapted optical and magnetic trapping potentials.

The Feshbach resonance is of special interest, since not only can the strength of the interactions be tuned, but also their sign. In a Fermi gas, strong attractive interactions lead to the formation of weakly bound fermionic molecules [24], while weak attractive interactions lead to the formation of Cooper pairs. At sufficiently low temperature, the molecules can then undergo Bose–Einstein condensation [25–27], whereas the Cooper pairs can form a superfluid, which is well described by the BCS theory. Furthermore, the tunability of the interactions allowed a study of the associated BEC–BCS crossover [28–31]. By using Feshbach resonances, the strongly interacting regime can be reached, both for Bose gases [32] and Fermi gases [33, 34]. More recently, measurements of the equation of state of these systems revealed contributions beyond the mean–field theory [35, 36].

The control over the geometry allows for example the realization of ultracold gases of reduced dimensionality. By confining an ultracold Bose gas to a unidimensional geometry, it was possible to observe a Tonks–Girardeau gas [37, 38], which constituted the first example of a Bosonic Luttinger liquid. The realization of a bidimensional Bose gas led to the observation of the phase transition between a normal and a superfluid state: the Berezinskii–Kosterlitz–Thouless (BKT) transition [39].

Novel phases of matter can also be created through the use of optical lattices [40]. In this case, the use of spatially modulated trapping potentials forces the atoms to arrange themselves periodically, much like the electrons in a solid. These systems constitute a very pure realization of a fundamental model of solid state physics: the Hubbard hamiltonian. In general, the use of optical lattices allows one to enter the regime of strong interactions, and to observe beyond mean-field phenomena. In particular, this technique led to the observation of the quantum phase transition between a superfluid phase and a Mott insulating phase, both in bosonic [41–44] and fermionic [45] systems.

This particular correspondence between ultracold atoms in optical lattices and electrons in the crystalline lattice of a solid illustrates the notion of *quantum simulation* put forward by Feynman in 1982 [46]. Instead of studying a given system, one can reproduce its important features, and directly measure the properties of the copy. In this manner, atoms in an optical lattice simulate electrons in a solid, stripped of any defects or perturbing fields, thus allowing for a better understanding of the underlying physics. With this correspondence

in mind, one can hope to gain new insight on many–body problems, such as the high temperature superconductivity and the fractional quantum Hall effect (FQHE). For this reason, there have been considerable efforts to design specific hamiltonians in cold atoms experiments to reach these strongly correlated states.

The FQHE arises when a bidimensional gas of interacting electrons is subjected to a large magnetic field, at low enough temperatures. Since the atoms used in our experiments are neutral, one needs to generate an effective magnetic field to study these phases of matter. This can be done for example by exploiting the equivalence of the Lorentz force and the Coriolis force: the rotation of the system acts as an artificial magnetic field [47]. This technique was successfully used in [48, 49]. Alternately, one can take advantage of the similarity between the Aharonov–Bohm phase and the Berry's phase [50], which arises in the presence of a space-dependent internal state. A non-trivial Berry's phase can for example result from the creation of optically dressed states, as proposed in [51, 52], and later successfully implemented in the group of I. Spielman [53]. A similar technique can be implemented in optical lattices, which can be engineered such that an atom acquires a phase when tunneling from one lattice site to the next, and simulate as well a magnetic field [54, 55].

The work carried out during my thesis focused on the study of the two-dimensional Bose gas. This system is of particular interest, for several reasons. As was noticed by Peirls in 1934, the dimensionality of a system strongly affects its equilibrium phases [56]. Indeed, thermal fluctuations are sufficient to prevent the formation of a BEC at the thermodynamic limit in two dimensions, except at zero temperature. This constitutes a particular case of the Mermin–Wagner–Hohenberg theorem [57, 58], which forbids any sort of long range order at the thermodynamic limit in one- and two-dimensional systems with short range interactions and a continuous hamitonian symmetry. However, the thermodynamic limit is only reached for exponentially large systems: in practice, "the sample would need to be bigger than the state of Texas for the Mermin–Wagner theorem to be relevant".[1] In this sense, the bidimensional geometry can be considered as marginal: the finite size effects always play an important role in any realistic system. Furthermore, even in the thermodynamic limit, the presence of interactions is sufficient to drive a transition to a superfluid state. The theory associated with this transition was developed by Berezinskii [60] and Kosterlitz and Thouless [61], leading to the usual name of BKT transition.

1. This statement was published in [59] in the context of 2D magnetism, but nevertheless conveys the correct idea for the two-dimensional Bose gas.

Since the Mermin–Wagner–Hohenberg theorem precludes the breaking of continuous symmetries, there is no discontinuity of the equation of state at the transition point, with the only exception being the superfluid density. For this reason, the BKT transition is often said to be of *infinite order*. Though there is no long–range order in the superfluid phase, the transition is nevertheless marked by a significant change in the one-body correlation function. In the superfluid phase, the one-body correlation function only decays algebraically with distance, instead of following an exponential or a gaussian decay in the normal phase. The transition is also accompanied by a significant reduction of density fluctuations, which can be explained by a simple Bogoliubov analysis.

The BKT transition was initially observed in superfluid helium films [62], and has been the subject of intense recent research in the field of ultracold atoms. In particular, an interference experiment between several 2D Bose gases revealed the presence of vortices [39], which are crucial to the microscopic mechanism associated with the BKT transition. Subsequent measurements revealed the coherent behaviour of the 2D Bose gas [63, 64], as well as its approximate scale-invariance in the weakly interacting regime [65]. The work presented in this thesis explores several properties associated with this phase transition, and is outlined in the following.

Outline

- In chapter 1, we present a few theoretical results essential to the understanding of the two dimensional Bose gas. The first part focuses on the ideal two-dimensional Bose gas. Though it does not Bose-condense in the thermodynamic limit except at zero temperature, the finite-size effects, which are always present in a real experiment, are sufficient to drive the transition at a non-zero temperature. In the second part, we consider the interacting two-dimensional Bose gas. After briefly introducing the interactions between atoms in two dimensions, we present the two key features underlying the rest of the work presented in this manuscript. First, the weakly interacting two-dimensional Bose gas is approximately *scale invariant*. Second, the interactions drive a phase transition from a normal phase to a superfluid, known as the BKT transition. Of these two features, the former is a property we use in all our studies of the 2D Bose gas, while the latter is the main focus of our investigations.
- Chapter 2 serves as a complement to chapter 1: it presents the experimental apparatus necessary for the realization of ultracold bidimensional Bose

gases. Since the experiment has already been described by previous PhD students (see [66–68]), we will mainly detail the most recent modifications. In particular, we describe in further detail the hybrid trap, which led to a vast improvement in the duty cycle of our experiment by reducing the evaporation time from 60s to 25s. We also detail the steps specific to the creation of a 2D Bose gas. The second half of this chapter is devoted to our data acquisition procedure. In our samples, the mean inter-particle distance can be smaller than the imaging wavelength, leading to a density-dependent cross-section when performing traditional weakly saturating absorption. This issue is resolved through the use of high intensity imaging, which aims instead to saturate the transition, in order to provide a faithful image of the sample. By combining both techniques, we are able to probe high density regions of the cloud, while maintaining a satisfactory signal-to-noise ratio in the low density regions. We also present an image processing algorithm, the Principal Component Analysis, which enhances further this signal-to-noise ratio.

– In chapter 3, we present a measurement of the equation of state of the two-dimensional Bose gas with different methods. For a single atomic sample, we can determine its temperature and chemical potential by fitting the wings of the cloud by a mean–field equation of state. We can also measure its pressure, phase-space density and entropy per particle. By preparing atomic samples at different atom numbers and temperatures, we are able to explore a wide range of parameters, and to reconstruct the equation of state of the 2D Bose gas. In particular, we were able to experimentally confirm its scale invariance, as was also done in the group of C. Chin [65]. This work was published in a refeered journal [69], and is reproduced without modifications. We also develop an alternative method, inspired by experiments performed at MIT in the group of M. Zwierlein [36]. By combining the derivative and the integral of the density with respect to the local potential, we are able to measure the equation of state, with a single adjustable parameter: the detectivity of our imaging system. This method can then be further refined to account for the population of excited states along the tightly confined direction.
– In chapter 4, we start by giving a brief overview of the dissipation mechanisms in a superfluid, both in a two- and three-dimensional fluid. We then present a direct measurement of the superfluid character of the 2D Bose gas, by locally probing the system with a moving defect. In particular, we show evidence for both a normal and a superfluid behavior, depending on the degree of degeneracy of the cloud. Furthermore, these results are in qual-

itative agreement with the existence of a normal to superfluid transition. This work was also published in a refereed journal [70], and is reproduced without modifications.

- Chapter 5 focuses on the fluctuations associated with the BKT transition. By releasing the two-dimensional Bose gas along the tightly confined direction, we are able to reveal the phase fluctuations of the steady state distribution. An analysis of the extrema of the density after time of flight and a study of the two-body correlation function are in good agreement with a dynamics dominated by phonons in the degenerate part of our samples. This behavior is further confirmed by a study the two-body correlation function. In particular, we reach a quantitative agreement with the theoretical analysis presented in [71].
- In chapter 6, we propose to study the interplay between the BEC and the BKT transition. Indeed, the underlying physical mechanism differs between the two. The harmonic trap we used in our previous experiments is not well suited to this task: the presence of interactions strongly modify the atomic distribution with respect to the ideal gas. By contrast, a box-like potential should allow us to better disentangle the BEC and the BKT transition. We then present two possible experimental techniques to realize this type of potentials. At the time of writing, this constitutes a work in progress, which will hopefully soon bear fruits.
- Finally, chapter 7 presents an ongoing work: the realization of a single-atom detection scheme. To this end, we implement a similar scheme to the one pioneered at Harvard [72] and at MPQ in Munich [73]. In this configuration, atoms are frozen in a deep tri-dimensional lattice, and simultaneously cooled down by an optical molasses. The photons scattered from the molasses beam are subsequently detected, and used to reconstruct the density profile of the sample. In particular, we discuss the different constraints associated with the choice of the lattice detuning. Though we were not able to freeze and image an atomic sample, we are confident that this is mainly a technical limitation. Consequently, we hope to realize this detection scheme in the coming months.

1. Phase transitions with ultracold two-dimensional Bose gases

The aim of this first chapter is to introduce the theoretical basis upon which our experiments are built. The intention is to give an overview of the features of the two-dimensional Bose gas, without aiming for exhaustivity. A more complete picture can be found in recent reviews, such as [21, 74].
Already in 1934, Peierls noticed that the properties of system are strongly affected by its dimensionality [56]. In particular, Bose–Einstein condensation (BEC) occurs in the infinite ideal tri-dimensional Bose gas, but only takes place at zero temperature in the bi-dimensional case. Indeed, this is a particular example of a more general theorem: as noted by Mermin and Wagner [57] and Hohenberg [58], spontaneous symmetry breaking and long-range order are impossible at non-zero temperature in 1D and 2D systems with short-range interactions and a continuous Hamiltonian symmetry. However, there exists a different phase transition from a normal state to a superfluid state for an infinite interacting 2D Bose gas: the Berezinskii–Kosterlitz–Thouless (BKT) transition [60, 61].
In any experimental realization of the 2D Bose gas, the two transitions are relevant: the finite size of the system restores the BEC transition at a non-zero temperature. In the first section, we will review the properties of the ideal Bose gas, both in an infinite system, and in a trapped geometry. We will then provide a description of the interactions in two dimensions [75–77], and provide a mean field description of the system. Finally, we will introduce the BKT transition, and present numerical results directly relevant for our experiments [78, 79].

1.1. The ideal gas

In this section, we describe the way non-interacting bosons can arrange themselves among the available energy levels in a two-dimensional geometry. This means that energy levels can only be accessed in a single plane: the particles are considered to be confined to a single quantum state along the remaining direction, which we choose to be z. This is achieved as long as the energy necessary

to reach the first excited state along z is large compared to the temperature T.

1.1.1. The infinite uniform two-dimensional Bose gas

The usual argument for the presence of a Bose–Einstein condensate (BEC) in a non-interacting system is the saturation of the excited single-particle states at non-zero temperature, following Einstein's standard argument [4, 5]. For a given temperature, if such a maximal occupation of the excited states $N_{\mathrm{exc}}(T)$ exists, all particles beyond this critical number must accumulate in the single-particle ground state, leading to a macroscopically populated quantum state. It is important to note that this is a sufficient condition for the presence of a BEC, but not a necessary one.
A generalization of this phenomenon was proposed by Penrose and Onsager [80], which associates Bose–Einstein condensation with the existence of a macroscopic eigenvalue in the one-body correlation function $g_1(r)$. Finite size effects, or the presence of interactions can lead to a BEC even in the absence of saturated excited states (see for example [59]).
We place ourselves in the grand canonical ensemble, with chemical potential μ and temperature T. In a non-interacting case, the number of particles in the excited states is given by:

$$N_{\mathrm{exc}} = \sum_{i=1}^{\infty} \frac{1}{e^{\beta\,(E_i-\mu)} - 1} \tag{1.1}$$

$$N_{\mathrm{exc}} = \int_0^{\infty} \frac{D(\epsilon)}{e^{\beta(\epsilon-\mu)} - 1} \mathrm{d}\epsilon. \tag{1.2}$$

Eq. 1.1 describes a system with discrete energy levels E_i and becomes Eq. 1.2 in the case of an infinite system. In this equation, $D(\epsilon)$ is the density of states and $\beta = 1/k_{\mathrm{B}}\,T$. For the the non-interacting Bose gas, μ is necessarily inferior to the ground state energy, and the excited levels are maximally populated when μ reaches the ground state energy. For the homogeneous 2D Bose gas, the density of states is uniform: $D(\epsilon) = m\mathcal{S}/(2\pi\hbar^2)$ where $\mathcal{S}$ is the surface of the system, and m is the mass of the particles. In this case, the occupation of the excited states simplifies to:

$$N_{\mathrm{exc}} = -\frac{m\mathcal{S}k_{\mathrm{B}}T}{2\pi\hbar^2} \ln\left(1 - e^{\mu/k_{\mathrm{B}}T}\right). \tag{1.3}$$

Taking the thermodynamic limit $N \to \infty$, $\mathcal{S} \to \infty$ with $N/\mathcal{S} = n$, we obtain the

result in terms of phase-space density:

$$\mathcal{D} \equiv n\,\lambda_{\mathrm{T}}^2 = -\ln\left(1 - e^{\mu/k_{\mathrm{B}}T}\right), \tag{1.4}$$

where $\lambda_{\mathrm{T}} = \sqrt{2\pi\hbar^2/(mk_{\mathrm{B}}\,T)}$ is the thermal wavelength. Contrarily to the three dimensional case, the phase-space density can become arbitrarily large: this indicates that there is no saturation of the excited levels in two dimensions, and no BEC for the infinite 2D ideal Bose gas. Eq. 1.4 does not include the ground state, but since the system never undergoes condensation, the population of the ground state is always negligible. Therefore, it describes properly the whole system, and it is the first equation of state that we can write: it connects directly the phase space density to chemical potential and temperature. This result is in accordance with the Mermin-Wagner theorem: since long-range order is forbidden in our system at non-zero temperature, no eigenstate can be macroscopically populated.

The absence of long-range order can be seen more directly by looking at the one-body correlation function:

$$\begin{aligned} g^{(1)}(\boldsymbol{r}) &\equiv \langle \Psi^*(\boldsymbol{r})\Psi(0)\rangle \\ &= \frac{1}{(2\pi)^2}\int_0^\infty \frac{e^{i\,\boldsymbol{k}\,\boldsymbol{r}}}{e^{\beta(\epsilon_{\boldsymbol{k}}-\mu)}-1}\mathrm{d}^2k, \end{aligned} \tag{1.5}$$

where $\boldsymbol{k}$ is the characteristic wave-vector of the plane wave of energy $\epsilon_{\boldsymbol{k}} = \hbar^2k^2/(2m)$. This quantity always vanishes at $r \to \infty$, again in accordance with the Mermin-Wagner theorem. For a non-degenerate gas ($\mathcal{D} \ll 1$), the one-body correlations decays as a gaussian, and the correlation length is the thermal wavelength. Even though there is no phase transition, in the degenerate regime ($\mathcal{D} \gg 1$), the correlation function decays exponentially for large distances:

$$g^{(1)}(r) \approx e^{-r/l_{\mathrm{C}}}, \tag{1.6}$$

with the one body correlation length $l_C = \frac{\lambda_{\mathrm{T}}}{\sqrt{4\pi}}e^{\mathcal{D}/2}$ (see [74] for a full derivation).

1.1.2. Bose-Einstein condensation in a finite system

Even though no condensation occurs in an infinite system, it is known that the finite size of a system can significantly affect its properties. In particular,

we saw that the one-body correlation length l_C grows exponentially with the phase-space density in the degenerate regime (Eq. 1.6). For a homogeneous system in a finite box of characteristic size L, there exists a non-zero temperature T such that the correlations span the entire system. In this case, there is a significant phase correlation between any two points, and the system undergoes Bose-Einstein condensation. This occurs when $l_C \approx L$, or equivalently when the phase space density reaches the critical value:

$$\mathcal{D}_c \approx \ln\left(4\pi \frac{L^2}{\lambda_T^2}\right). \tag{1.7}$$

However, this criterion is not a quantitative definition for the critical atom number. This can be derived more accurately for a given geometry by calculating the maximal population of the excited states following Eq. 1.1. This shall be done in the following in three different geometries.

Square box In a square box, the eigenfunctions are of the form:

$$\psi(x,y)_{i,j} = \frac{2}{L}\sin\left(\frac{i\,\pi\,x}{L}\right)\sin\left(\frac{j\,\pi\,y}{L}\right) \tag{1.8}$$

with i and j strictly positive integers. The eigenenergies are $E_{i,j} = \pi^2\,\hbar^2/(2\,m\,L^2)$ (i^2+j^2-2), taking the energy of the ground state to be 0. In this case, the maximal population of the excited levels is given by:

$$N_c = \sum_{i>1,j>1} \frac{1}{e^{\beta\,E_{i,j}}-1} \equiv f_{sq}\left(\frac{L^2}{\lambda_T^2}\right). \tag{1.9}$$

Circular box In a circular box of radius L, the eigenfunctions are of the form:

$$\psi(r,\theta)_{s,n} = \frac{1}{\sqrt{\pi}\,L\,J_{|n|+1}(j_{s,|n|})} J_{|n|}(j_{s,|n|}\,r/L)\,e^{i\,n\,\theta} \tag{1.10}$$

where n is an integer, J_n is the Bessel function of order n of the first kind, and $j_{s,n}$ is its s-th zero. The eigenenergies are therefore $E_{s,n} = \hbar^2/(2\,m\,L^2)(j_{s,n}^2 - j_{0,0}^2)$, taking the energy of the ground state to be 0. In this case, the maximal population of the excited levels is given by:

$$N_c = \sum_{s,n} \frac{1}{e^{\beta\,E_{s,n}}-1} \equiv f_{circ}\left(\frac{\pi\,L^2}{\lambda_T^2}\right). \tag{1.11}$$

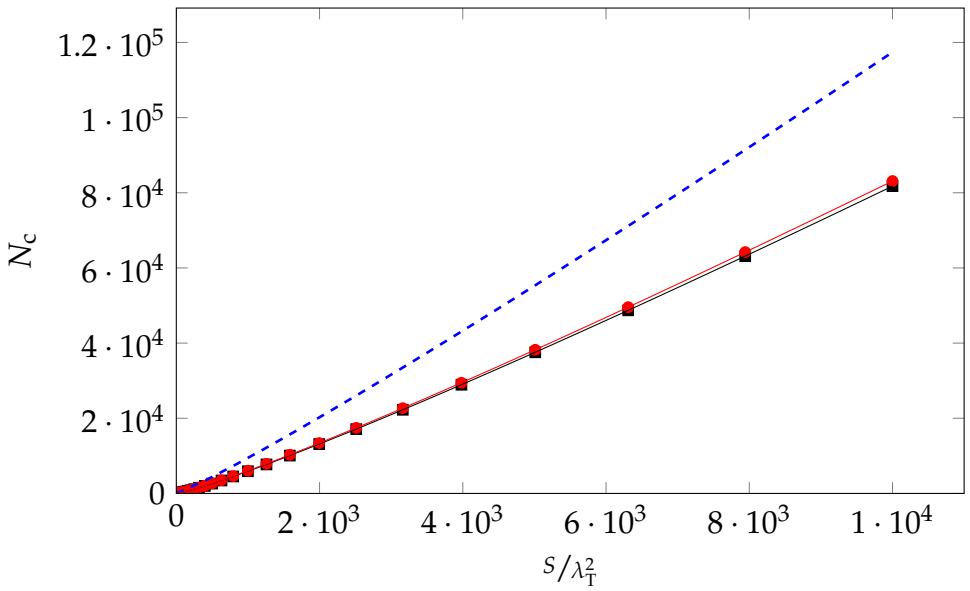

Figure 1.1.: Critical atom number against S/λ_T^2 for a square box (black squares) and a circular box (red circles). The qualitative prediction from Eq. 1.7 is indicated by the blue dashed line. The black (red) line represents a fit of the critical atom number for a square (circular) box by the model from Eq. 1.12. Fit parameters are $\xi = 0.9878(5)$, $\eta = 0.0313(1)$ for the square box and $\xi = 0.9892(4)$, $\eta = 0.0355(1)$ for the circular box.

The functions f_{sq} and f_{circ} can be evaluated numerically, and compared to the functional form introduced in Eq. 1.7. We choose the following fitting function:

$$N_{\mathrm{c,fit}} = \xi \frac{\mathcal{S}}{\lambda_T^2} \ln\left(\eta 4\pi \frac{\mathcal{S}}{\lambda_T^2}\right) \tag{1.12}$$

where $\mathcal{S}$ is the surface of the box, and ξ and η are the fitting parameters. The results are shown in Fig. 1.1, along with the prediction from Eq. 1.7. The numerical results are well described by the prediction from Eq. 1.12, with the shape of the box influencing mainly the coefficient η.

Harmonic trap Experimentally, the most relevant geometry for the Bose gas is the harmonically trapped system. In this case, owing to the different density of states, the gas always undergoes a phase transition at a non-zero temperature, even in the thermodynamic limit.[1] We can assume without loss of generality

1. We will see later how this apparent contradiction with the Mermin–Wagner–Hohenberg theorem is resolved.

that the trap is isotropic, with a trapping frequency ω. The density of states for a two-dimensional harmonic trap is $D(\epsilon) = \epsilon/(\hbar\omega)^2$, and Eq. 1.2 yields the following for the maximal population of the excited states:

$$N_{\mathrm{c,harm}} = \frac{\pi^2}{6}\left(\frac{k_{\mathrm{B}}\,T}{\hbar\,\omega}\right)^2. \tag{1.13}$$

It is also possible to derive the equation of state for the trapped 2D Bose gas, by using the local density approximation (LDA). If the trapping potential is varying smoothly enough, it can be considered as constant over a region in which the particles are at the thermodynamic equilibrium. In this case, particles in this region will be described by the equation of state for a homogeneous system, with a local potential $\mu(r) = \mu_0 - V(r)$, where μ_0 is the chemical potential at the center of the trap, and $V(r)$ the trapping potential. In the case of a harmonic trap, this substitution in Eq. 1.4 gives the density distribution for the excited states:

$$n(r)\lambda_{\mathrm{T}}^2 = -\ln\left(1 - e^{\mu_0/k_{\mathrm{B}}T - \frac{m\omega^2}{2k_{\mathrm{B}}T}r^2}\right). \tag{1.14}$$

The number of atoms occupying excited states in a harmonic trap can be obtained by integrating the previous equation:

$$N(\mu_0, T) = \mathrm{Li}_2\left(e^{\mu_0/k_{\mathrm{B}}T}\right)\left(\frac{k_{\mathrm{B}}\,T}{\hbar\,\omega}\right)^2 \tag{1.15}$$

where Li_2 is the dilogarithm function. In particular, when $\mu_0 \to 0$, we recover the critical atom number from Eq. 1.13. Note that Eq. 1.14 indicates that the density in the center of the trap diverges when $\mu_0 \to 0$, which is in fact due to the integration: performing the calculation with Eq. 1.1 gives a finite value. This divergence in the semi-classical limit resolves an apparent paradox: in Eq. 1.13 when taking the thermodynamic limit $N \to \infty$, $\omega \to 0$ with $n = N\,m\,\omega^2/(2\pi\,k_{\mathrm{B}}T)$ kept constant, the critical temperature remains apparently finite. However, in this case, the semi-classical limit applies, and the density n has to diverge, indicating the critical temperature must be zero.
Contrarily to the uniform case, Eq. 1.15 does not always give the equation of state for the whole system: when $\mu_0 \to 0$, the atoms in excess of $N_{\mathrm{exc,harm}}$ will occupy the ground state, and are not accounted for in Eq. 1.14.

1.2. The interacting two-dimensional Bose gas

Up to this point, we did not take into account the existence of a third dimension, and assumed the problem was strictly two-dimensional. However, the experimental realization of such a system relies on imposing a confining potential, which will freeze the excitations along one dimension. Let us suppose that the confining potential is harmonic: $U(z) = m\omega_z^2 z^2/2$. When the temperature is low enough (typically $\hbar\omega_z \gg k_B T$), the system occupies a single quantum state along z and its wave function can be factorized:

$$\Psi(r,\theta,z) = \frac{1}{(\pi l_z^2)^{1/4}}\psi_{(2D)}(r,\theta)e^{-\frac{z^2}{2l_z^2}}. \tag{1.16}$$

In this case, the dynamics of the system is contained in $\psi_{(2D)}(r,\theta)$, which constitutes a realization of the 2D Bose gas. The third direction does not have a direct effect on the dynamics of the 2D Bose gas, though it introduces a characteristic thickness of the system: the spread of the ground state of the harmonic oscillator $l_z = \sqrt{\hbar/m\omega_z}$. As we will see, the third dimension still has an influence on the collisional properties of the particles.

1.2.1. Interactions in two dimensions: the quasi 2D regime

Since experimental realizations of the 2D Bose gas with cold atoms are carried out at low enough densities, we can restrain the interactions to binary collisions, which are well characterized by a contact potential in three dimensions [81]:

$$V(\boldsymbol{r}_i - \boldsymbol{r}_j) = g_{3D}\delta^{(3D)}(\boldsymbol{r}_i - \boldsymbol{r}_j) = \frac{4\pi\hbar^2}{m}a_s\delta^{(3D)}(\boldsymbol{r}_i - \boldsymbol{r}_j) \tag{1.17}$$

where a_s is the scattering length (for ^{87}Rb , $a_s = 5.1$ nm). This describes a three dimensional collision process, and cannot be directly transposed to the 2D case [75]. In order to determine the collisional properties, we need to distinguish two different regimes, depending on the thickness of the system l_z:

- the true 2D regime, where the motion of the atoms is strictly confined to the xy plane. This regime is reached when $l_z \ll R_e$, where R_e is the effective range of the interaction potential. In this case, the scattering amplitude is energy-dependent, and cannot be characterized by a constant scattering amplitude.
- the quasi 2D regime, where the microscopic motion of the atoms remains three-dimensional, which corresponds to $l_z \gg R_e$. This condition is typically realized in our experiment, where $l_z \approx 180$ nm and $R_e \sim a_s = 5.1$ nm

(see for example [82] for a derivation of R_e). In this regime, the interactions can be expressed by a contact potential as in Eq. 1.17, and a general expression for the two-dimensional coupling constant was given by Petrov *et al.* [76, 77]

$$g = \frac{\sqrt{8\pi}\hbar^2}{m} \frac{1}{l_z/a_s - \ln(\pi q^2 l_z^2)/\sqrt{2\pi}} \quad \text{where} \quad q^2 = 2m\mu/\hbar^2. \tag{1.18}$$

For our experimental parameters, the logarithmic contribution is negligible, and the 2D scattering amplitude remains constant, as in three dimensions. In the case of a harmonic confinement along the z direction, it is given by:

$$g = \frac{\hbar^2}{m}\tilde{g} \quad \text{where} \quad \tilde{g} = \sqrt{8\pi}\frac{a_s}{l_z} \tag{1.19}$$

In this limit, the interaction energy of the 2D Bose gas is:

$$E_{\text{int}} = \frac{g}{2}\int \langle n^2(\boldsymbol{r})\rangle \mathrm{d}^2 r = \frac{\hbar^2\tilde{g}}{2m}\int \langle n^2(\boldsymbol{r})\rangle \mathrm{d}^2 r \tag{1.20}$$

Note that the same result can be obtained by a naive integration of the three-dimensional interaction energy, assuming the gas is described by Eq. 1.16. However, the condition $l_z \gg a_s$ remains hidden in this procedure.
One can also estimate the strength of the interactions by comparing the interaction energy to the kinetic energy in a uniform gas of N particles. The interaction energy can be estimated by neglecting the density fluctuations ($\langle n^2\rangle = \langle n\rangle^2$):

$$E_{\text{int}} \approx \frac{\hbar^2}{2m}\tilde{g}\frac{N^2}{\mathcal{S}} \tag{1.21}$$

Using the density of states in 2D $D(\epsilon) = m\mathcal{S}/(2\pi\hbar^2)$, the kinetic energy can be estimated :

$$E_{\text{kin}} = \int_0^{E_N} \epsilon D(\epsilon)\mathrm{d}\epsilon = \frac{\pi\hbar^2}{m}\frac{N^2}{\mathcal{S}} \quad \text{where} \quad N = \int_0^{E_N} D(\epsilon)\mathrm{d}\epsilon \tag{1.22}$$

The strongly interacting regime is defined as $E_{\text{int}} = E_{\text{kin}}$, which corresponds to $\tilde{g} = 2\pi$. This result does not depend on the density, as opposed to the 3D case, where the strength of interactions depends explicitly on the

density through the parameter $n_{3D}a_s^3$. According to Eq. 1.19, the strongly interacting limit also corresponds to $a_s \approx l_z$. Consequently, the quasi 2D regime is only an appropriate description for the weakly interacting 2D Bose gas. Experimentally, values of $\tilde{g}$ for cold atoms range from 0.01 to 3 [64, 65, 83–85], and can reach 1 in the more strongly interacting helium films [86].

1.2.2. Scale invariance in 2D

One important consequence of Eq. 1.19 is the scale invariance of the equation of state of the 2D Bose gas. To properly characterize the 2D Bose gas, we aim to establish an equation of state (EoS), for example for the density. The general form of such an EoS is:

$$F(n, \mu, T, \tilde{g}) = 0 \tag{1.23}$$

where F is the function to be determined. Using dimensional analysis, Eq. 1.23 must take the form:

$$G(\mathcal{D}, \mu/k_B T, \tilde{g}) = 0 \quad \text{or equivalently} \quad \mathcal{D} = f(\mu/k_B T, \tilde{g}). \tag{1.24}$$

Not only is $\tilde{g}$ dimensionless, it is also independent of the density in the weakly interacting regime. Therefore, contrarily to the three dimensional case, the interactions do not introduce a characteristic energy scale. In this respect, the EoS for the 2D Bose gas is said to be scale invariant: multiplying chemical potential and temperature by the same amount will not change the phase space density of the system. Note that this is only an approximate result, which breaks down if the logarithm in Eq. 1.18 is large enough.

In particular, the EoS for the ideal gas (Eq. 1.4) has the correct functional form: the phase-space density only depends on $\mu/k_B T$. More generally, all dimensionless thermodynamic quantities characterizing the homogeneous gas can only depend on $\tilde{g}$ and $\mu/k_B T$.

1.2.3. The mean-field Hartree–Fock approximation

In the presence of interactions, the EoS is established by the mean-field Hartree–Fock method. In this approach, the interactions are taken into account by replacing μ by $\mu - 2gn$ in the equation of state of the ideal gas [87, 88]:

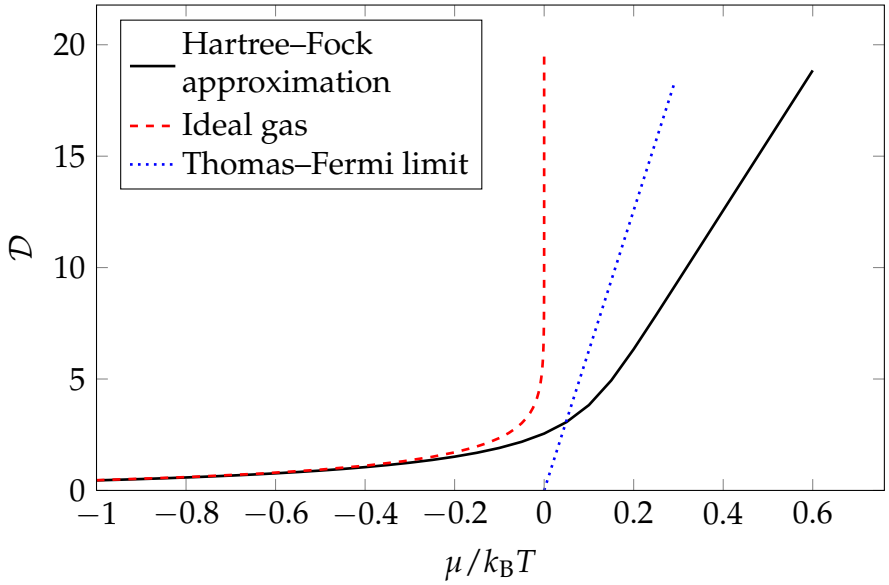

Figure 1.2.: Equations of state for the ideal gas (dashed red line), for the interacting gas ($\tilde{g}$ =0.1) in the Hartree–Fock mean field approximation (full black line) and for the interacting gas in the Thomas–Fermi limit (blue dotted line)

$$\begin{aligned}\mathcal{D} &= -\ln\left(1-e^{\beta\mu-2\beta g n}\right)\\ &= -\ln\left(1-e^{\mu/k_{\mathrm{B}}T-\tilde{g}\mathcal{D}/\pi}\right)\end{aligned} \tag{1.25}$$

This self-consistent equation for the phase space density can be solved numerically for D. Remarkably, in the presence of interactions, the chemical potential is unconstrained, and can take any value. In particular, the singularity at $\mu = 0$ for the ideal gas vanishes. In the case of the harmonically trapped Bose gas, using the LDA gives us:

$$\mathcal{D}(r) = -\ln\left(1-e^{\frac{\mu}{k_{\mathrm{B}}T}-\frac{m\omega^2}{2k_{\mathrm{B}}T}r^2-\tilde{g}\mathcal{D}(r)/\pi}\right) \tag{1.26}$$

Since μ is not constrained to negative values anymore, the number of atoms derived from this equation can be made arbitrarily large. The condensation phenomenon which occurred for the ideal gas disappears in the presence of interactions in a harmonic trap.

However, the underlying assumption is that the density fluctuations are important, so that $\langle n^2\rangle = 2\langle n\rangle^2$. A Bogoliubov analysis shows that when the

phase-space density reaches $\mathcal{D} \gg 2\pi/\tilde{g}$, density fluctuations decrease, until the regime where $\langle n^2 \rangle = \langle n \rangle^2$ is reached [74]. In the zero temperature limit, the gas is described by the Thomas-Fermi approximation : $\mu = g\, n$. From this observation, the Hartree–Fock approximation is only a good description for small $\mathcal{D}$.

1.2.4. The Berezinskii-Kosterlitz-Thouless (BKT) transition

Though it appears Bose–Einstein condensation does not occur in the presence of interactions, there exists a phase transition at low temperatures to a superfluid state. This transition is unusual, since it cannot break any continuous symmetry, in accordance with the Mermin–Wagner–Hohenberg theorem. For this reason, there is no long range order in the superfluid state. It is often classified as a transition of *infinite order*, since most thermodynamics quantities vary smoothly at the transition point: the only exception is the superfluid density, which jumps from 0 in the normal phase to $4/\lambda_T^2$ in the superfluid phase at the transition point.
The microscopic theory of the transition was developed by Berezinskii [60] and Kosterlitz and Thouless [61]. It is associated with the existence of vortices in the gas. These are points around which the phase winds by a multiple of 2π. At the center of vortices, the density drops to zero, over a typical length scale given by the healing length: $\xi = 1/\sqrt{\tilde{g}n}$. We can restrict our description to the single-charged vortices with phase winding of $\pm 2\pi$, which are energetically stable. Above the critical temperature, the vortices form a disordered gas, and each vortex modifies the phase of the gas significantly, preventing the appearance of a superfluid state. However, below the transition temperature, formation of pairs of vortices of opposite circulation is energetically favorable. The total circulation of the phase around such pairs is 0, which indicates that the pair only perturbs locally the gas, thus allowing the existence of a superfluid state.
Even though the value of the superfluid density at the transition point is universal, the BKT theory does not tell us when this transition occurs. In general, computing the transition parameters as a function of the total density n and the interaction strength is a difficult problem. However, in the weakly interacting limit, classical field Monte-Carlo calculations performed by Prokof'ev, Ruebenacker and Svistunov [78] give a value for the phase space density and the chemical potential at the transition point:

$$\mathcal{D}_c = n\frac{2\pi\hbar^2}{m\,k_\mathrm{B}\,T_\mathrm{BKT}} = \ln\left(\frac{\xi_D}{\tilde{g}}\right) \tag{1.27}$$

$$\mu_c = k_\mathrm{B}T\frac{\tilde{g}}{\pi}\ln\left(\frac{\xi_\mu}{\tilde{g}}\right) \tag{1.28}$$

with $\xi_D = 380(3)$ and $\xi_\mu = 13.2(4)$. In our experiments, $\tilde{g} \approx 0.1$, so we expect $\mathcal{D}_C \approx 8$.

In a following article, Prokof'ev and Svistunov [79] numerically calculated the equation of state around the critical point for an infinite system. This allows us to interpolate between the two known limits:

– for $\mathcal{D} \ll \mathcal{D}_C$, the Hartree–Fock analysis remains valid
– for $\mathcal{D} \gg \mathcal{D}_C$, the gas is well described by the Thomas–Fermi approximation

The resulting contributions to the equation of state for the phase space density are shown in Fig. 1.3. From these three predictions, we can create a composite equation of state, which we will later use to model our data.

Since this equation of state is calculated for a homogeneous system, one needs to use the LDA to describe a weakly interacting trapped Bose gas. The validity of this procedure was addressed by quantum Monte–Carlo calculations performed by Holzmann and Krauth [89] and Holzmann, Chevallier and Krauth [90], for harmonically trapped systems and for atom numbers similar to our experimental observations.

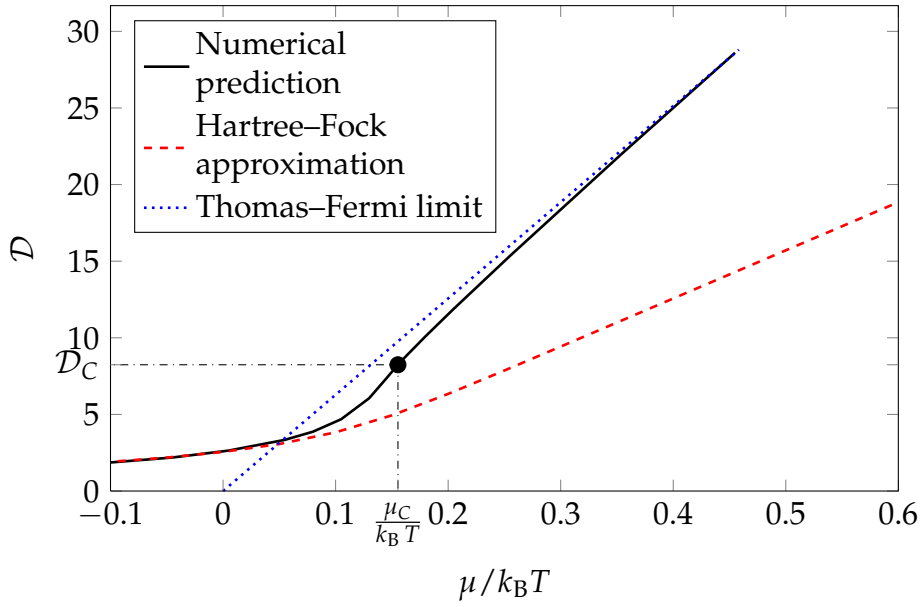

Figure 1.3.: Interpolation by the numerical prediction (full black line) between the Hartree–Fock approximation (dashed red line) and the Thomas–Fermi limit (dotted blue line). The black circle indicates the BKT transition for $\tilde{g} = 0.1$.

2. Producing and imaging two–dimensional Bose gases

Since this experimental apparatus was built for a large part by previous PhD students, a detailed description of it can be found in [66–68]. Therefore, in the first half of this chapter, we provide a simple description of the experimental sequence. We will detail further both the most recent modifications, and the experimental steps specific to the preparation of a two-dimensional Bose gas. In the second half, we will describe in detail our image acquisition process, both in its theoretical and experimental aspects.

2.1. Experimental setup

2.1.1. Experimental sequence

Our experimental setup consists of a vacuum system composed of two chambers: a steel "MOT chamber" and a glass "science cell", linked by a differential pumping stage. A scheme of the vacuum chamber with the magnetic coils is presented in Fig. 2.1. Preparation and measurement of a BEC requires a complex sequence of different computer-controlled events, with a precise timing. To this end, we installed a program created at MIT by Aviv Keshet: the Cicero Word generator [91]. Using this software, a series of different phases are defined, and described below.

1. **MOT phase (6 s)**
   We load a magneto-optical trap from the background ^{87}Rb gas: the loading rate is typically $5 \cdot 10^9$ atoms/s. Eventually, the cloud contains $\approx 7 \cdot 10^9$ atoms. The cloud is then compressed during a cMOT phase [92], the atoms are optically pumped into the internal state $\mid F = 2,\ m_F = 2 \rangle$ and transferred to a quadrupole trap with magnetic gradient $b'_z = 140$ G/cm. At the end of this sequence, the quadrupole trap contains $\approx 5 \cdot 10^9$ atoms, at 320 μK.
2. **Magnetic transport (6 s)**
   We transport the atoms from the MOT chamber to the science cell, using a

series of 9 pairs of coils, and load a quadrupole trap with $b'_z = 90$ G/cm. The transport is nearly adiabatic: heating mainly comes from the collisions with the background gas in the first stages of the transport. In the most recent version of the experiment, we cannot readily estimate the number of atoms in the science cell: *in situ* imaging fails because the magnetic field is not homogeneous over the cloud, and time-of-flight imaging is strongly perturbed by eddy currents. Measurements on a previous version of the experiment indicated a transport efficiency of ≈ 50 %. Alternatively, the two-way transport can provide a lower bound for the one-way transport efficiency.

3. **Radio-frequency evaporation in the quadrupole trap (16 s)**
   The quadrupole trap gradient is increased to $b'_z = 140$ G/cm in order to increase the collision rate. We apply a radio-frequency evaporation ramp (on the transition between different Zeeman substates) from 30 MHz to 2 MHz, bringing the atom number down to $2.5 \cdot 10^7$ and the temperature down to 25 μK.

4. **Optical evaporation in the hybrid trap (9 s)**
   The hybrid trap (see 2.1.2) is loaded in 1 s. We then lower the dipole trap power from 4.5 W to ≈ 85 mW in 8 s to obtain a BEC: the end point of the ramp can be adjusted to choose the final temperature of the atomic cloud.

5. **Transfer into the Hermite–Gauss trap and final evaporation (4 s)**
   The Hermite-Gauss beam (see 2.1.3) is ramped up in 1 s, splitting the cloud in three parts as shown in Fig. 2.5a. The atoms outside of the Hermite–Gauss beam are removed, leaving us with a single two-dimensional plane (see Fig. 2.5b). We then perform another stage of evaporative cooling to achieve degeneracy in our samples.

2.1.2. A new setup: the hybrid trap

The first stage of evaporative cooling takes place in a quadrupole trap, which is the easiest magnetic trap to build. It is also well suited for radio-frequency evaporation: indeed, as opposed to the optical evaporation, lowering the trap depth does not weaken the confinement. However, a quadrupole trap has a major drawback: since the magnetic field cancels at its center, atoms crossing this region can be lost through Majorana spin-flips. The loss rate is inversely proportional to the temperature: hot clouds can be efficiently trapped and evaporated, but Majorana losses put an upper bound on the phase space density obtained in

this trap [93]. For realistic experimental parameters, it is not possible to create a condensate in these conditions.

On the first version of our experimental setup, this problem was avoided by applying a time-orbiting bias field, to realize a TOP trap [1]. In this setup, the effective magnetic field seen by the atoms does not cancel at the center of the trap, thus suppressing the spin-flip induced losses. However, this approach led to weak confinement frequencies: $2\pi \times (32, 32, 92)$ Hz in our experiment. Consequently, the collision rate could not be made very large, thus evaporative cooling in this trap was quite slow: our optimal condensation sequence took 80 s to complete. In order to shorten this duration, we chose instead to circumvent Majorana losses by adding an attractive optical trap to the quadrupole, as demonstrated in [94] and [95].

The idea is superpose an attractive dipole trap of depth $\mathcal{U}_{\mathrm{H}}$ with the quadrupole trap. When the cloud is sufficiently cold ($k_{\mathrm{B}}\, T \leq \mathcal{U}_{\mathrm{H}}$) but before Majorana losses start to be significant, the gradient of magnetic field is adiabatically lowered, which simultaneously cools down the atoms, and transfers them inside the dipole trap. To prevent Majorana losses both during and after the transfer,

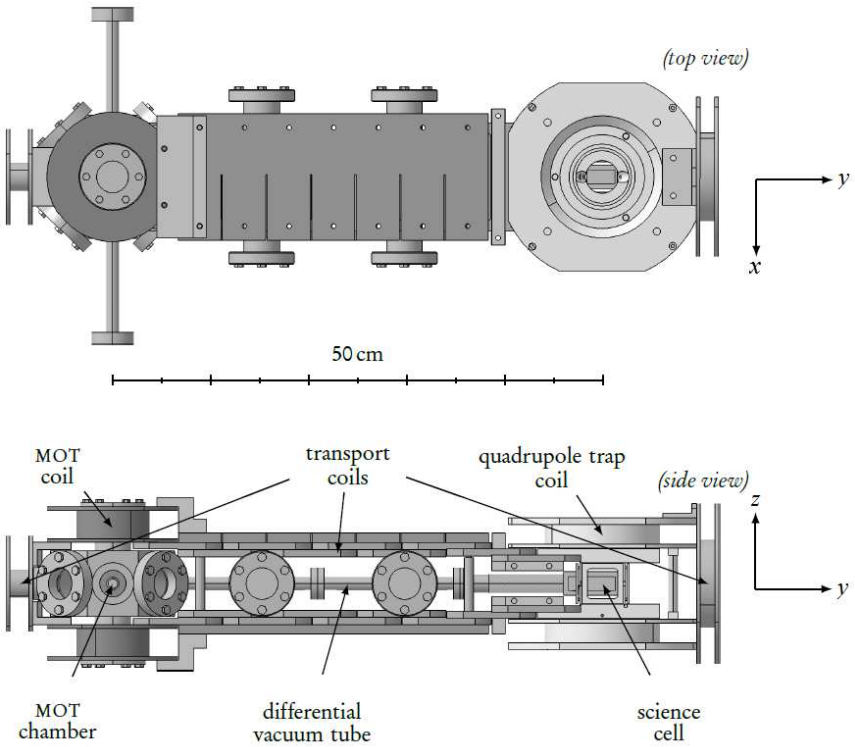

Figure 2.1.: Top and side view of the vacuum system, with the magnetic coils

the center of the dipole trap is offset from the center of the quadrupole. The remaining magnetic field gradient provides a harmonic confinement along the direction of propagation of the dipole trap. The total potential is then given by:

$$\mathcal{V}(\mathbf{r}) = \mu_B b'_z \sqrt{\frac{x^2}{4} + \frac{y^2}{4} + z^2} - \mathcal{U}_H \exp\left(-2\frac{(y-y_0)^2 + (z-z_0)^2}{w^2}\right) + m\,g\,z \tag{2.1}$$

Experimentally, we choose the following parameters:

– The dipole trap is generated with a 1560 nm laser beam, propagating along the x axis (see Fig. 2.2). It is focused on the atoms with a waist of $w = 50\,\mu$m, and the available laser power is 4.5 W. From these parameters, we can expect a trap depth $\mathcal{U}_H = 52\ \mu$K. Its position (y_0, z_0) relative to the center of the quadrupole trap ($y = 0$, $z = 0$) is adjusted by a mirror mount with micrometric screws, and is chosen to maximize the number of atoms transferred in the dipole trap. The optimum is found for $z_0 = -90\ \mu$m, with a transfer efficiency of 20 %. While the precise value of y_0 does not influence strongly the loading of the dipole trap, it significantly affects the properties of the trap for low depths, and we thus chose $y_0 = 0$. Along the propagation direction, the Rayleigh range of the dipole trap is too large

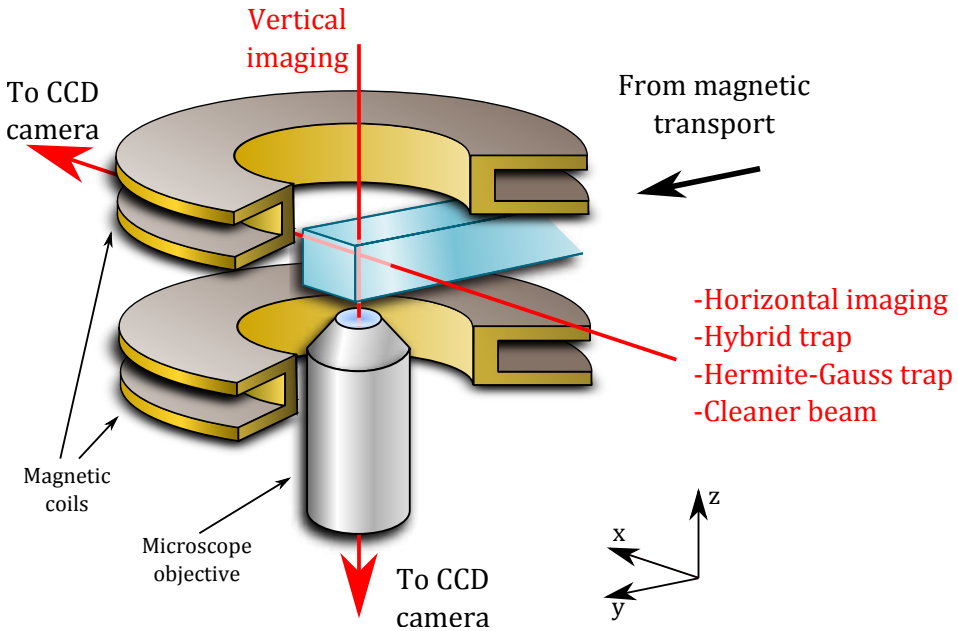

Figure 2.2.: Directions of propagation of the different laser beams used during the sequence.

($Z_R = 5$ mm) for it to affect significantly the position of the cloud: it is therefore imposed by the magnetic field.

– The magnetic gradient is initially $b'_z = 140$ G/cm and is lowered in 1 s to $b'_z = 12.5$ G/cm, which corresponds to a gradient slightly lower than gravity for atoms in the $|\, F = 2, m_F = 2 \rangle$ state. For the optimal value of z_0 presented above, this creates a field of 110 mG at the location of the atoms: this is not sufficient to fully prevent Majorana losses. After the decompression of the quadrupole, the zero of magnetic field is therefore moved to $z_1 = -150$ μm to increase the field at the location of the atoms, and thus increase the lifetime in the trap.
– In the final configuration, a linearization of the potential in Eq. 2.1 around its minimum yields the following trap frequencies:

$$\omega_y = \omega_z = \sqrt{\frac{4\mathcal{U}_{\mathrm{H}}}{m\, w^2}} = 2\pi \times 421 \text{ Hz} \tag{2.2}$$

$$\omega_x = \sqrt{\frac{\mu_{\mathrm{B}}\, b'_z}{4\, m\, z_1}} = 2\pi \times 18 \text{ Hz} \tag{2.3}$$

and the bias field at the location of the atoms is

$$B = |b'_z\, z_1| = 188\,\mathrm{mG}. \tag{2.4}$$

2.1.3. Preparing two-dimensional Bose gases and reaching degeneracy

The Hermite–Gauss beam As we saw in Sec. 1.1, the experimental realization of a two-dimensional Bose gas requires a strong confinement along one direction of space, which is chosen to be the vertical z direction. The temperature of the cloud is typically 100 nK: this requires a confining harmonic potential of characteristic angular frequency $\omega_z > k_{\mathrm{B}}/\hbar\, 100\,\mathrm{nK} = 2\pi \times 2$ kHz. This harmonic trapping is realized by a 532 nm laser beam (blue detuned with respect to the atomic resonance). To achieve a suitable geometry for the optical trap, we shine a collimated laser beam on a phase plate. This phase plate imprints a phase of π on the upper half of the beam ($z > 0$) with respect to the other half ($z < 0$). The beam then propagates, and is focused on the atoms by a converging lens (see Fig. 2.2 for the geometrical arrangement).

At the focus of the lens, the electric field is the Fourier transform of the electric field after the phase plate in the paraxial approximation. The expected intensity profile can then be calculated: the two halves of the beam interfere destructively, and the intensity distribution presents a minimum in the center (Fig.

2.3). In the nodal plane, the intensity distribution around the minimum can be approximated by:

$$I(y, z \ll w_z) \approx I_0 \frac{4}{\pi} \frac{z^2}{w_z^2} e^{-2\frac{y^2}{w_y^2}} \tag{2.5}$$

where w_z is the waist of the beam in the z direction. Therefore, the smaller w_z, the tighter the confinement. However, we want the trap to have a significant extension in the xy plane, in order to have a uniform confinement over the whole cloud. Along the propagation direction, the extension of the trap is given by the Rayleigh range of the laser ($Z_R = 140\,\mu$m for $w_z = 5\,\mu$m). Along the remaining direction, the extension of the trap is given by the waist w_y, so the aspect ratio of the beam must be properly chosen. These constraints can be summed up as follows:

- w_z must be as small as possible to achieve a tight confinement
- w_z is limited by the numerical aperture of the focusing lens. In our setup, this means $w_z \geq 5\,\mu$m
- w_y must be larger than the size of the cloud. For a typical sample, this means $w_y \gg 20\,\mu$m
- on the other hand, for a fixed laser power, increasing w_y decreases the intensity, and thus the confinement, so w_y cannot be too large.

To satisfy all these conditions, we choose $w_y = 150\,\mu$m and $w_z = 5\,\mu$m. The trapping potential is given by $U = \alpha\, I = m\omega_z^2 z^2/2$, with $\alpha = 6.5 \cdot 10^{-8}$ μK m^2/W. For a laser power of 1W, we expect a confinement of $\omega_z = 2\pi \times 4.2$ kHz. This corresponds to a harmonic oscillator length scale $l_z = 165$ nm, and a coupling constant $\tilde{g} = 0.15$.

It must be noted that the previous result assumes a perfect optical setup, and is only true at the focus of the Hermite–Gauss beam. In practice, the harmonic oscillator frequency is closer to $\omega_z = 2\pi \times 2$ kHz. Indeed, when loading the Hermite–Gauss trap, a balance must be found between achieving a strong confinement and loading a large number of atoms. As we saw, the confinement increases with decreasing w_z. However, the number of atoms loaded into the Hermite–Gauss beam is given by the overlap between the trap and the atomic distribution. In particular, it is directly proportional to the distance between the two barriers, which is in turn proportional to w_z. Consequently, the number of loaded atoms increases with w_z. Of course, if w_z is too large, the height of the barriers will not be sufficient to keep the atoms in the nodal plane of the beam. For this reason, since we cannot dynamically control w_z, a compromise must then be found between a high atom number and a high harmonic oscillator fre-

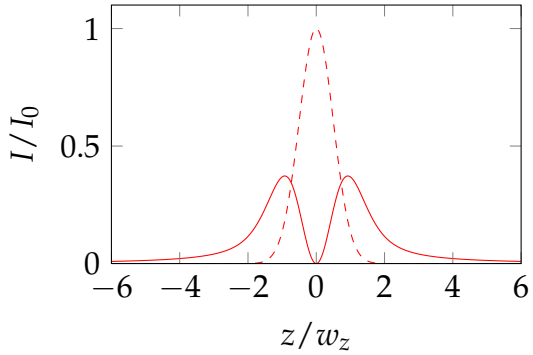

Figure 2.3.: Normalized intensity profile in the focal plane of the lens (red full line). For comparison, the intensity profile without a phase plate is presented in red dashed line

quency. Experimentally, the optimum was found when the atoms are trapped between one and two Rayleigh ranges away from the focus, with the precise value depending on the quality of the optical alignment.

Loading the two-dimensional trap Once the three-dimensional atomic sample is sufficiently cold, the power of the Hermite–Gauss beam is linearly increased in 3 s. During this step, the Hermite–Gauss beam is superposed with the weak optical and magnetic confinement. In particular, along the z direction, the potential has the form shown in Fig. 2.4. Atoms will therefore be trapped in three different regions of space, and the cloud has the shape shown in Fig. 2.5a: the central part of this cloud is inside the Hermite–Gauss beam, and is two-dimensional, while the outer lobes are not necessary for the rest of the experiment. However, since we want to image the two-dimensional plane perpendicularly to it, these outer lobes block our imaging and must be removed.

To this end, the top and bottom part of this cloud are selectively illuminated with a linearly polarized laser beam resonant with the transition $|F = 2\rangle \rightarrow |F' = 2\rangle$ during 40μs (see Fig. 2.2 for the geometrical arrangement). The atoms in these regions will then be depumped to the $|\, F = 1\,\rangle$ hyperfine state, which is undetected by our imaging system. The spatial selection is done by projecting the shadow of a thin wire over the cloud: the central plane of interest to us will be shielded from the resonant photons, while atoms in the remaining side wells will eventually be depumped (Fig. 2.4). At the end of this process, we are left with a single plane, as shown in Fig. 2.5b.

The wire has a diameter of $100\,\mu$m, and its image is created with a $1/5^{\text{th}}$ magnification, so the dark region is $\approx 20\,\mu$m across. As one can expect, the contrast

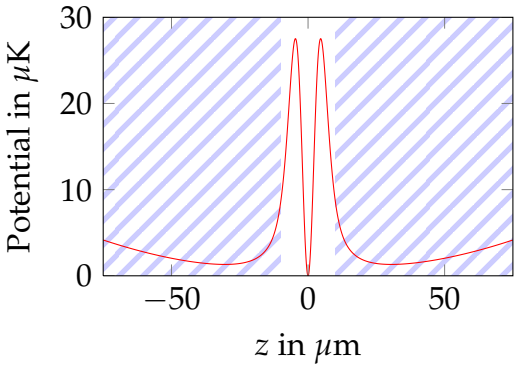

Figure 2.4.: Total trapping potential along the z direction. The central minimum is due to the Hermite–Gauss beam, while the minima on the sides result from the weak optical confinement. The blue hashed zone indicates the parts of the trap exposed to resonant light during the cleaning phase

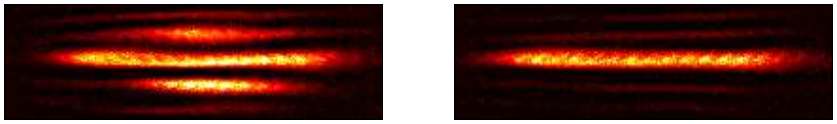

(a) Before removal **(b)** After removal

Figure 2.5.: Horizontal absorption images of the atomic distribution, before and after removing atoms in the side wells.

between the dark shadow and the rest of the beam is not perfect, so atoms in the central plane can still be depumped, or heated by the scattering of photons. Experimentally, we found that a contrast of 40 is needed to achieve a good preparation of a single two-dimensional plane: all atoms in the side wells are efficiently depumped, while atoms in the central plane are nearly not affected.

2.2. Imaging two-dimensional Bose gases and processing the data

Once the preparation of the atomic cloud is complete, it must be probed and analyzed to extract relevant physical parameters. For cold atoms experiments, the most straightforward method is absorption imaging. The accurate determination of the atomic density thus relies both on a precise measurement of the intensity distribution of the laser beam used to image the cloud, and on the correct knowledge of the relation between the atomic density and the light

intensity. The data obtained in this manner can then be further processed to improve the signal-to-noise ratio, and to finally determine quantities other than the density by a fitting process, such as the chemical potential and the temperature.

2.2.1. Using absorption images to determine the density

Standard absorption imaging and its limitations Once the intensity distribution is measured, both with and without atoms, it must be linked to the atomic density. For most experiments, performing absorption imaging yields the optical density (OD), which is sufficient to determine the density with the Beer–Lambert law:

$$\mathrm{OD} \equiv -\ln\left(\frac{I_\mathrm{f}(\mathbf{r})}{I_\mathrm{i}(\mathbf{r})}\right) = n(\mathbf{r})\,\sigma \tag{2.6}$$

where n is the density integrated along the line of sight (simply the density for two-dimensional samples), σ is the absorption cross-section, I_i is the intensity of the probe beam without atoms, and I_f is the intensity with atoms. The cross-section σ characterizes the interaction between the atom and the probe beam. It can be determined from the properties of the electronic transition. The Beer–Lambert law is only valid if σ does not depend on the intensity and the density is sufficiently low. The first condition is fulfilled when $I_\mathrm{i} \ll I_\mathrm{sat}$ where I_sat is the saturation intensity. In this regime, the cross-section is given by:

$$\sigma = \frac{\sigma_0}{1 + 4\Delta^2/\Gamma^2} \qquad \text{where} \qquad \sigma_0 \equiv \frac{3\lambda_0^2}{2\pi} \tag{2.7}$$

and where λ_0 is the transition wavelength, Γ is its natural width and Δ is the detuning of the probe beam from the transition.
However, this relation breaks down when the inter-atomic distance becomes on the order of the wavelength (see for example [96] for an overview). In a two dimensional sample, an optical density $\mathrm{OD} = 1$ at resonance corresponds to a mean inter-atomic distance $0.7\,\lambda_0$. In such a dense medium, an emitted photon can be re-absorbed by a neighbouring atom, giving rise to dipole-dipole interactions between atoms. These interactions will in turn shift the energy levels proportionally to $\hbar\Gamma/(k_0 r)^3$ where $k_0 = 2\pi/\lambda_0$ is the wavevector associated with the transition and r is the distance between two atoms. From this picture, it appears that for inter-atomic distances r smaller than the wavelength, the energy levels can be shifted by more than the natural linewidth of the transition, leading to a density dependent absorption cross–section. Consequently,

the absorption cross–section is reduced at resonance when probing high atomic densities.

This phenomenon was observed in our group when imaging dense bidimensional ^{87}Rb gases [69, 84]. In actual systems, there are many more than two atoms, and multiple scattering events can take place. A qualitative interpretation can then only be provided by modeling the interaction between one photon and N atoms. Such an analysis was carried out in our group by Lauriane Chomaz and coworkers, and is presented in details in [97]. In this work, the main features of our observations were qualitatively reproduced: the optical density is significantly lower than predicted by the Beer–Lambert law (see Fig. 2.6). However, a full quantitative agreement could not be reached: modeling the imaging transition in ^{87}Rb ($|\, F = 2\,\rangle \rightarrow |\, F' = 3\,\rangle$) is computationally difficult: therefore, the calculations were performed on a simpler $|\, J = 0\,\rangle \rightarrow |\, J' = 1\,\rangle$ transition.

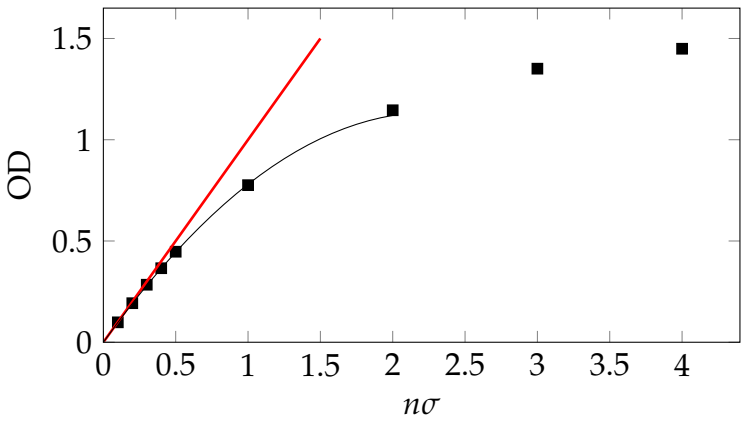

Figure 2.6.: Variation of the optical density as a function of the Beer–Lambert prediction, for resonant probe light. The simulated sample has zero thickness in the propagation direction of the beam. The red line is the straight line of slope 1, and the black line is an empirical fit of the data: OD $= n\sigma(1 - \mu\, n\sigma)$ with $\mu = 0.22$.

High intensity absorption imaging Since the collective phenomenon render the absorption cross-section dependent on the density, we instead choose to work with high intensity imaging pulses, as was done in [98]. Instead of probing the atomic density with a weakly saturating laser pulse, we aim to fully saturate the imaging transition. In this regime, each atom will scatter $\Gamma/2$ photons per second, independently of their environment, thus allowing us to deduce the

density from the number of missing photons. Here, multiple scattering events do not play a role in the number of scattered photons, but will merely change the saturation intensity. Consequently, the effective saturation intensity for a dense medium will be higher than for a single atom, but the transition will always be saturated for a high enough intensity. In the following, we detail the calibration of this imaging scheme.

The following section was initially published as part of the supplemental material of [69], and is reproduced without modifications

The calibration of absorption imaging consists in relating the number of missing photons on a pixel to the number of atoms on this pixel. The interaction between a probe beam and a single atom is characterized by the absorption cross section σ defined by the relation $\gamma = \sigma I/(\hbar\omega_L)$, where γ is the photon scattering rate, I the intensity of the beam on the atoms and $\omega_L/2\pi$ its frequency. In the case of a monochromatic resonant beam probing a two-level atom:

$$\gamma = \frac{\Gamma}{2}\frac{I}{I + I_{sat}}. \tag{2.8}$$

In the limit where $I \ll I_{sat}$ the absorption cross section is $\sigma_0 \equiv \Gamma\hbar\omega_L/2I_{sat}$.

In practice one must take into account stray magnetic fields, non-zero linewidth of the probe laser, optical pumping effects, etc. To model this complex situation, we heuristically replace I_{sat} by an effective saturation intensity αI_{sat} and Γ by an effective linewidth $\beta\Gamma$. We then write the number of photons N_p scattered during an imaging pulse of given duration τ

$$N_p \equiv \gamma\tau = \frac{\beta\Gamma}{2}\frac{I}{I + \alpha I_{sat}}\tau, \tag{2.9}$$

or equivalently

$$\sigma = \sigma_0\frac{\beta}{\alpha + I/I_{sat}}. \tag{2.10}$$

At low intensity N_p is proportional to I as in the two-level case, but with a multiplicative coefficient β/α due (for example) to the broadening of the resonance line. At large intensity the number of scattered photons saturates at $\beta\Gamma\tau/2$ instead of $\Gamma\tau/2$, which models a reduction that can be caused by optical pumping effects, for instance.

We now turn to the description of absorption imaging of a 2D atomic cloud. The imaging process consists in shining a resonant laser beam on an atomic sample, and in imaging the transmission of the sample on a camera. In order to relate the missing photon number to the atomic density $n(x, y)$, we calculate

the probability for a photon of the probe beam to reach a pixel of the camera. We introduce the area $\mathcal{A}$ associated to this pixel in the atomic plane. In the limit where $\sigma \ll \mathcal{A}$ a photon has a probability $\sigma/\mathcal{A}$ to be absorbed by a given atom, hence a probability $P_t = (1-\sigma/\mathcal{A})^N$ to be transmitted, where N is the number of atoms in the area $\mathcal{A}$. Thus we find:

$$P_t \approx e^{-\sigma n}, \tag{2.11}$$

where we have used $n = N/\mathcal{A}$, assuming that the atomic density varies smoothly over the pixel size. The intensity of the beam at the output of the cloud is $I_f = P_t I_i$ and we obtain:

$$-\ln\left(\frac{I_f(x,y)}{I_i}\right) = \sigma\, n(x,y), \tag{2.12}$$

where σ depends on the effective intensity I on the atoms [Eq. (2.10)]. If the optical thickness of the cloud is large, *i.e.* if the intensity I_f just after the plane of atoms is significantly lower than the intensity I_i just before this plane, the effective intensity I must be determined in a self-consistent manner by imposing:

$$I_f = I_i - n\,\sigma(I)\,I. \tag{2.13}$$

The elimination of the effective intensity I from Eqs. (2.10)-(2.13) yields:

$$n\sigma_0\,\beta = -\alpha \ln\left(\frac{I_f}{I_i}\right) + \frac{I_i - I_f}{I_{sat}}. \tag{2.14}$$

It is interesting to note that even though the derivation in a 2D system differs from the 3D case, the result is similar to the one given in [98]. The first member of the right-hand side of Eq. (2.14) is dominant in the weak intensity limit, and corresponds to the 2D analog of the 3D Beer–Lambert law. In the high intensity limit, the second member of the right-hand side dominates. We calibrated $\alpha = 2.6\,(3)$ using the same method as in [98]: we performed absorption imaging of clouds obtained in similar experimental conditions with various intensities I_i ranging from $0.1\,I_{sat}$ to $6\,I_{sat}$, and imposed that these measurements provide the same result for the left-hand side of Eq. (2.14). Here we restricted ourselves to low atomic density regions, to ensure that collective effects in the optical response of the gas were negligible. The calibration of $\beta = 0.40\,(2)$ was performed as in [84], using the HFMF prediction as a fit to the low-density parts of our atomic distributions, and using μ, T and β as optimization parameters. In [84] where only low intensity imaging was used, this calibration provided

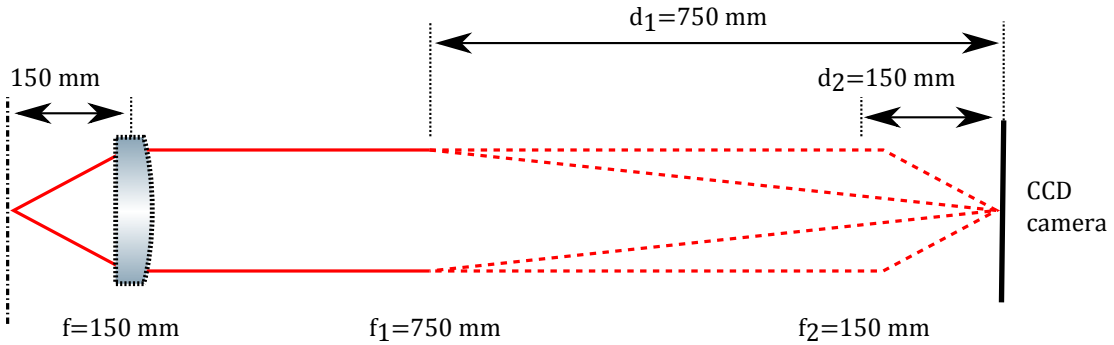

Figure 2.7.: Optical scheme for the horizontal imaging. The second lens can be chosen to adjust the magnification: either $\mathcal{M} = 5$ with $f_1 = d_1 = 750$ mm or $\mathcal{M} = 1$ with $f_2 = d_2 = 150$ mm.

the detectivity factor ξ, which is related to the present parameters α and β by $\xi = (15/7)\beta/\alpha$.

2.2.2. Imaging setup

Our experiment relies on the complementary use of two orthogonal imaging directions: horizontal (along the x axis) and vertical (along the z axis) imaging. Both directions are shown in Fig. 2.2.

Horizontal imaging The horizontal imaging beam is colinear with both the dipole trap used in the hybrid trap and with the Hermite–Gauss beam. The intensity distribution in the plane of the atoms is imaged onto a CCD camera by two optical doublets forming a telescope, as shown in Fig. 2.7. The magnification of this imaging system can be either $\mathcal{M} = 1$ or $\mathcal{M} = 5$, depending on the second doublet used in the setup. This axis is primarily a diagnostic tool: since it is colinear with two dipole traps, it is used to align them. For this reason, we do not necessarily need a faithful picture of the density over the whole cloud: imaging along this axis is performed in the weakly saturating regime, for an exposure time $\tau_{\text{exp}} = 50\ \mu$s and an intensity $I \leq I_{\text{sat}}$.

Vertical imaging The vertical imaging beam is perpendicular to the two-dimensional atomic plane. This axis is used for precise measurements of the density. For this reason, it combines two high-performance elements.
The first of these is a custom made microscope objective (NA=0.45). Together with a triplet, it forms an intermediate image of the atoms with magnification

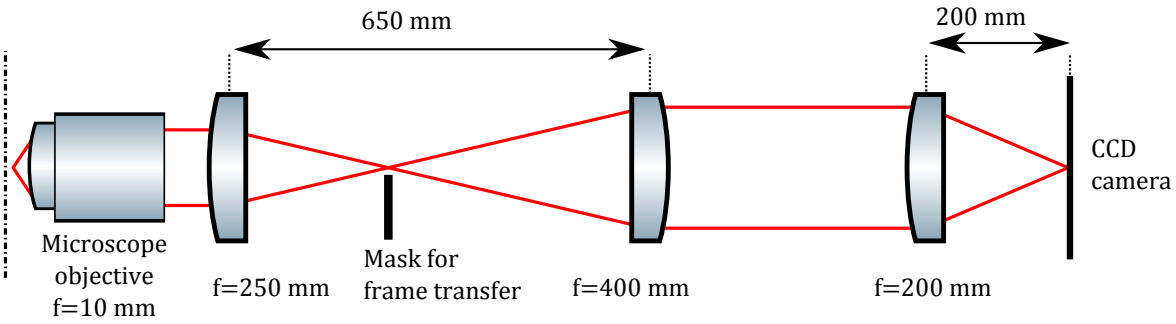

Figure 2.8.: Optical scheme for the vertical imaging. The mask for the frame transfer is placed at the intermediate focus. The total magnification is $\mathcal{M} = 12.5$

$\mathcal{M}_1 = 25$. This intermediate point also contains a razor blade, which is necessary for the *frame transfer* mode of the CCD camera described below. This intermediate image forms a source for a telescope of magnification $\mathcal{M}_2 = 0.5$, finally projecting the image on a CCD camera (*Pixis 1024*, Princeton Instruments) (Fig. 2.8). The total magnification of this system is $\mathcal{M} = 12.5$, and its resolution is mainly limited by the numerical aperture of the objective. The pixels of the camera have a real size of 13 μm, which corresponds to an effective pixel size of 1.01 μm with our magnification. Tests of the microscope objective [68] showed a resolution better than 1 μm on a test target. From an analysis of atomic images, we deduced that the total imaging system had a resolution lower than 2 μm. This corresponds to a depth of field on the order of 15 μm.

The CCD camera is the other critical element of our imaging setup: a high quantum efficiency for our wavelength (>95%) and a low-noise readout lead to shot-noise limited images. However, in order to fully exploit this feature, the readout time of the chip must be quite slow: around 1 s for 1024 lines of 1024 pixels. This is not compatible with absorption imaging, where the reference image must be taken as close as possible to the image with atoms, to reduce the noise stemming from the intensity fluctuations. It is possible to combine this constraint with a long readout time by using the *frame transfer* mode of the camera. In this method, the chip is split between an acquisition region, and a storage region. The storage region is defined both in the camera software, by specifying its size, and in the optical setup, by physically masking the storage region with the razor blade mentioned above, thus preventing photons from reaching the storage region. An imaging sequence proceeds as follows: the acquisition region is exposed, then its content is transferred to the storage region. After this step, the process can start again, and the chip is read only once the storage region is full. In our experiment, the transfer time is 650 μs for 203 lines

of 1024 pixels. This is sufficiently fast to filter most temporal variations of the light intensity. At the end of the imaging process, the CCD chip contains five stripes of 203 pixels. The first two are used to image the probe beam, both with and without atoms. The remaining frames are not exposed, and can be used to remove the contributions from background stray light.
As we saw earlier, full detectivity of a dense two-dimensional sample can only be reached in the limit of high intensity imaging. In this regime, the higher flux of photons can be sufficient to significantly accelerate the atoms during the imaging phase. The imaging time must therefore be short enough to image a static atomic distribution. Along the probe beam propagation direction, the displacement of the atoms is given by $\Delta z = (\Gamma/2)\,(\hbar k_0/m)\,(\tau_{\mathrm{exp}}^2/2)$. For $\tau_{\mathrm{exp}} = 2.5$ μs, the displacement is $\Delta z = 0.3\,\mu$m, which is sufficiently small compared to the depth of field of the imaging system. Furthermore, the minimal atomic signal which can be detected by this method is quite high. From Eq. 2.14 by neglecting the logarithmic contribution, we can deduce the variance of the atomic density, assuming Poissonian fluctuations for the photon number:

$$\delta n^2 = \frac{1}{\beta^2\sigma_0^2}\frac{\hbar\omega}{\mathcal{A}\,\tau_{\mathrm{exp}}}\frac{I_{\mathrm{f}}+I_{\mathrm{i}}}{I_{\mathrm{sat}}^2} \tag{2.15}$$

For $I \approx I_0 = 40\,I_{\mathrm{sat}}$ and $\mathcal{A} = 1\,\mu\mathrm{m}^2$, we find $\delta n = 5.75\,\mu\mathrm{m}^{-2}$, which gives an effective lower bound on the densities we can detect on a single pixel. Typically, the central density of our atomic samples is $> 50\,\mu\mathrm{m}^{-2}$, while the density in the thermal wings of the cloud can be lower than $1\,\mu\mathrm{m}^{-2}$.
We can perform the same analysis for low intensity imaging. Starting from eq. 2.14, and keeping only the logarithmic contribution, we find:

$$\delta n^2 = \frac{\alpha^2}{\beta^2\sigma_0^2}\frac{\hbar\omega}{\mathcal{A}\,\tau_{\mathrm{exp}}}\left(\frac{1}{I_{\mathrm{i}}}+\frac{1}{I_{\mathrm{f}}}\right) \tag{2.16}$$

For an exposure time $\tau_{\mathrm{exp}} = 50$ μs and $I \approx I_0 = 0.7\,I_{\mathrm{sat}}$, we find $\delta n = 0.45\,\mu\mathrm{m}^{-2}$. Consequently, we have two complementary imaging settings, which will be chosen depending on the requirements of the experiment:

- low intensity imaging ($\tau_{\mathrm{exp}} = 50$ μs, $I_0 = 0.7\,I_{\mathrm{sat}}$), which has a high signal-to-noise for low densities, but which fails for high densities due to collective effects
- high intensity imaging ($\tau_{\mathrm{exp}} = 2.5$ μs, $I_0 = 40\,I_{\mathrm{sat}}$), which can provide a faithful image of high density regions, but is on the order of the noise for densities smaller than $5.75\,\mu\mathrm{m}^{-2}$

For the data presented in [69], we chose to use a combination of the two settings.

Each atomic sample was prepared twice, and probed with each imaging regime.

2.2.3. An algorithm for image processing: the Principal Component Analysis (PCA)

The quality of our data processing is directly dependent on the signal-to-noise ratio of our image acquisition. Our imaging process is mainly limited by the photonic shot-noise, and we would like to resolve properly the thermal wings of our atomic samples, down to optical densities of 0.05, or to spatial densities of $0.2\,\mu\mathrm{m}^{-2}$. In the low-intensity configuration, the imaging beam illuminates the CCD with $N_{\mathrm{ph}} \approx 600$ photons, which means we hope to extract a signal from 30 missing photons. In comparison, the photonic shot-noise has a standard deviation $\sqrt{\delta N_{\mathrm{ph}}^2} = 25$ photons. Thus, small signals are comparable with the noise on a single-shot basis, but can easily be resolved by averaging, either by exploiting the LDA and the symmetry of the trap, or by combining several images of the same atomic sample. Another limitation is the presence of inhomogeneities in the intensity profile of the imaging beam: if these inhomogeneities shift between the atomic image and the reference image, the density profile will be affected. These defects will locally modify the density profiles, but not necessarily in the same way on different images.

The first noise reduction process stems from the rotational symmetry of the trap. For a harmonic trap of known frequencies ω_X and ω_Y, the density should be constant along contours defined by $\omega_X^2\,x^2 + \omega_Y^2\,y^2 = \mathcal{C}$. In the following, we will assume the trap to be isotropic without loss of generality. For a point located r pixels away from the center of the cloud, there are $2\pi \times r$ pixels sampling a region of identical trapping potential. For $r = 10$ pixels, an azimuthal average will then increase the signal-to noise ratio, by reducing the standard error introduced by the shot-noise to at most ≈ 5 photons. Thus, low densities can be efficiently probed as long as they are found far enough from the center of the cloud.

While azimuthal averaging is a good way to reduce uncorrelated noise, such as the photon shot-noise, it is less efficient in removing inhomogeneities in the beam profile. To this end, we implemented a noise reduction algorithm: the Principal Component Analysis (PCA), as was done in [99]. Let us briefly outline the principle of this method.

Consider a series of N images of S pixels each, represented by $\mathcal{I}_n(s)$ where $1 \leq s \leq S$ is the index of the pixel, and $1 \leq n \leq N$ is the index of the experimental realization. In a typical experiment, we change the parameters of the experiment for each image, and characterize the resulting density distribu-

tion. Typically, the measured density distributions all "look alike", for example a bell shaped distribution in our case. Even though the underlying physics differs from one image to the other, we can still use their similarity to remove unwanted contributions to the signal. We start by removing the mean value of each pixel:

$$\delta\mathcal{I}_n(s) \equiv \mathcal{I}_n(s) - \langle \mathcal{I}_n(s) \rangle_n \tag{2.17}$$

$\delta\mathcal{I}_n$ is the deviation of image n from the common mean value. This mean value does not have a physical meaning, since it stems from the average over different configuration: its role is purely mathematical. We then build the correlation matrix defined by

$$\mathcal{C}_{r,s} = \frac{1}{N} \sum_{n=1}^{N} \delta\mathcal{I}_n(r) \delta\mathcal{I}_n(s) \tag{2.18}$$

with $(r, s) \in \{1...S\}$. This matrix contains the variance associated with individual pixels on its diagonal, and the covariance associated with two different pixels elsewhere. For a shot-noise dominated image, all the pixels are uncorrelated, and the matrix $\mathcal{C}$ is diagonal. Contrarily, consider a series of images of an atomic distribution. In this case, the density on the i-th pixel is strongly correlated to the density of its neighbours. Therefore, the correlation matrix will have non-zero off-diagonal elements. It can then be diagonalized to yield its eigenvalues and eigenvectors

$$\mathcal{C}\, V_p = \sigma_p\, V_p. \tag{2.19}$$

Since $\mathcal{C}$ is a real symmetric matrix, its eigenvectors constitute a new basis for the images. In this basis, we have

$$\delta\mathcal{I}_n(s) = \sum_{p=1}^{S} a_{n,p} V_p(s). \tag{2.20}$$

Up to this point, there is no loss of information: we simply chose to represent each image on a basis of uncorrelated vectors rather than on the single-pixel basis. Furthermore, the eigenvalue σ_p is linked to the decomposition of the images on this new basis by

$$\sigma_p = \frac{1}{N} \sum_{n=1}^{N} a_{n,p}^2. \tag{2.21}$$

Consequently, the coefficients $a_{n,p}$ can only take a significant value for a large

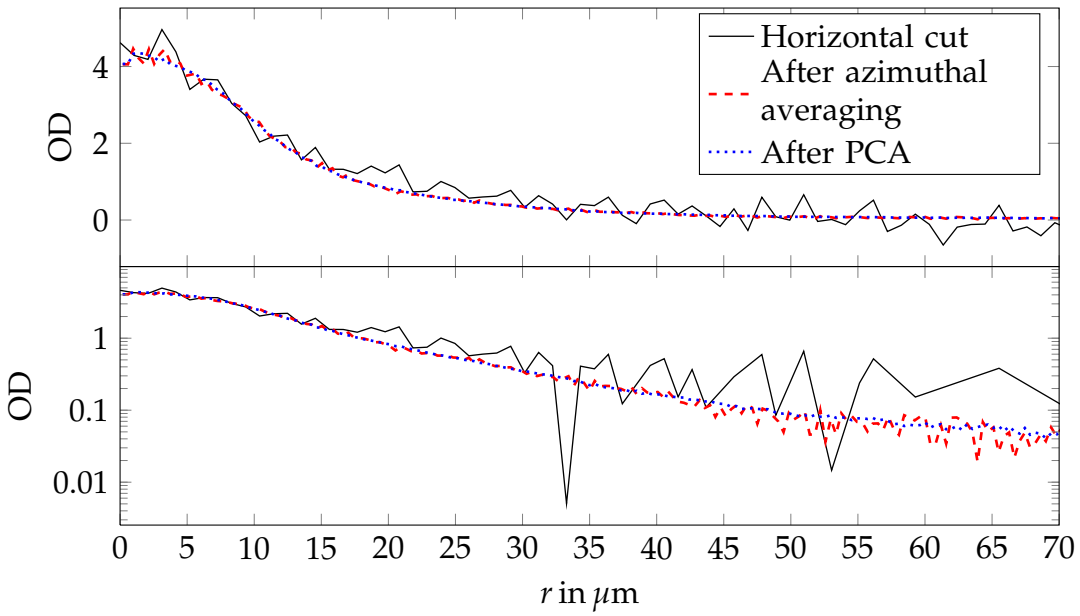

Figure 2.9.: Typical density profile from a cut in the two-dimensional image (black full line), after azimuthal average over the cloud (dashed red line) and after PCA on the series of profiles (dotted blue line)

eigenvalue σ_p. A small σ_p indicates that the corresponding eigenvector is irrelevant to describe the data. We can then limit the sum in Eq. 2.20 to the s_0 eigenvectors corresponding to the highest σ_p. This operation does not change the overall appearance of the image, but removes contributions which are uncorrelated from one image to the other. Provided $s_0 \ll S$, this represents a gain of $\sqrt{S/s_0}$ in signal-to-noise ratio. Here, the more similar are the images, the less eigenvectors are required to describe them. In practice, the choice of s_0 depends on the variety of the images. Therefore, the truncated sum must be compared to the initial image to ensure a minimal loss of information. Typically, we choose $s_0 = 10$, to compare with $\mathcal{S} = 22801$. In Fig. 2.9, we demonstrate the effectiveness of this method on a single image by comparing raw data, extracted from a cut in the cloud, with an azimuthally averaged density profile, and the same density profile processed by the method described above.

3. The equation of state of the two-dimensional Bose gas

During the presentation of the two–dimensional Bose gas in Ch. 1, we stressed out its property of scale invariance. An experimental test of this feature relies on the measurement of the equation of state (EoS) for a wide range of temperatures and atom numbers, in order to show evidence for this property.

A first measurement of the EoS of the 2D Bose gas performed in our group relies on the determination of the temperature T and chemical potential μ in the center of the trap [69], and is presented in the first half of this chapter. From these measurements and using the local density approximation (LDA), it is possible to reconstruct the phase-space density (PSD) at any point in the trap, or the pressure at the center of the trap. Furthermore, these quantities allow us to directly access the entropy per particle. We are also able disentangle the various contributions (kinetic, potential, interaction) to the energy of the trapped gas using a time-of-flight method, from which we infer the reduction of density fluctuations in a non fully coherent cloud. The EoS can be measured in a different manner, inspired by a recent work in the group of M. Zwierlein for the unitary Fermi gas [36]. This method can be easily transposed to the 2D Bose gas, and allows for another determination of the EoS. It is presented along with the resulting EoS in the second half of this chapter, and is shown to be in good agreement with the first measurement.

3.1. Exploring the thermodynamics of a two-dimensional Bose gas, Phys. Rev. Lett. 107, 130401 (2011)

The following section was initially published in [69], and is reproduced without modifications

Physical properties of homogeneous matter at thermal equilibrium are characterized by an equation of state (EoS), *i.e.* a relationship between some relevant state variables. For a fluid of particles, possible EoS's consist in expressions of pressure, density or entropy as functions of temperature T and chemical potential μ. In the ideal case the EoS is known in any dimension for a Bose or

Fermi gas. In the presence of interactions, one has to resort to approximations or numerical calculations, and a comparison with experiments is crucial to test their validity. Trapped atomic gases at thermal equilibrium provide a powerful tool for this purpose [100]. Within local density approximation (LDA), intensive state variables take at a point $\boldsymbol{r}$ in the trap the same value as in a homogenous system with the same temperature and the shifted chemical potential $\mu - V(\boldsymbol{r})$, where $V(\boldsymbol{r})$ is the confining potential.

The case of an interacting two-dimensional (2D) Bose fluid is particularly interesting in this context. Firstly, at non-zero temperature the Mermin–Wagner theorem precludes Bose–Einstein condensation [57, 58]. Therefore the EoS is expected to be continuous at any point, in spite of the existence of a superfluid, infinite-order phase transition, which is of the Berezinskii–Kosterlitz–Thouless (BKT) type [60, 61]. Secondly the EoS exhibits an approximate scale invariance [79] in the regime of relatively weak atomic interactions which is of interest here. It originates from the fact that the interaction strength is an energy-independent dimensionless coefficient $\tilde{g}$ ($\ll 1$), and thus provides no energy, nor length scale, in contrast with the 1D or 3D cases. This implies in particular that dimensionless thermodynamic variables such as the phase space density $\mathcal{D}$ or the entropy per particle $\mathcal{S}$ are functions of the ratio $\mu/k_{\mathrm{B}}T$ only, with $\tilde{g}$ as a parameter.

Recent experiments with trapped 2D Bose gases have demonstrated the existence of a BKT-type transition. One line of investigation exploited matter-wave interference to monitor the appearance of an extended coherence in the sample [39, 63], and another approach used a time-of-flight (ToF) technique to measure the momentum distribution of the gas [64]. The steady-state scale invariance was verified in [65]. In this paper we present a detailed experimental investigation of several thermodynamic properties of a 2D Bose gas. We describe measurements of the EoS for the pressure from a count of the total number of trapped atoms, for a wide range of thermodynamic parameters. From the same set of data we use the central spatial density to access the EoS for phase space density. Combining these two EoS with the scale invariance we obtain the EoS for the entropy per particle. We show that this quantity rapidly decreases around the superfluid transition and then approaches zero in the highly degenerate regime. We also present an original method to extract from a ToF the various contributions (kinetic, potential, interaction) to the total energy of the trapped gas. This method is applicable to any low-dimensional fluid. Here it shows that density fluctuations of our 2D Bose gas are essentially suppressed even when its thermal, non coherent fraction is significant.

3.1.1. Experimental preparation of 2D samples

Our 2D Bose gases are prepared along the lines detailed in [84]. We start with a 3D Bose–Einstein condensate of ^{87}Rb atoms confined in a magnetic trap in their $F = m_F = 2$ internal ground state with an adjustable temperature. We slice a horizontal sheet of atoms with an off-resonant, blue-detuned laser beam with an intensity node in the plane $z = 0$. It provides a strong confinement along the z axis with oscillation frequency $\omega_z/2\pi = 2.0\,(2)$ kHz. The interaction strength is $\tilde{g} = \sqrt{8\pi}a/\ell_z = 0.109\,(5)$, where a is the 3D scattering length and $\ell_z = \sqrt{\hbar/m\omega_z}$. The energy $\hbar\omega_z$ is similar to or larger than the thermal energy $k_B T$ and the interaction energy per particle. Our gas is thus in the so-called quasi-2D regime [76], where most of the atoms occupy the ground state of the vibrational motion along z, making it thermodynamically 2D, but where collisions still keep their 3D character since $a = 5.3\,\text{nm} \ll \ell_z = 240\,\text{nm}$. The magnetic trap provides a quasi-isotropic confinement in the xy plane with frequency $\omega\,/\,2\pi = 20.6\,(1)$ Hz [1].

After an equilibration time of 3 seconds in the combined magnetic+laser trap, we measure the *in situ* density distribution of the gas by performing absorption imaging with a probe beam propagating along z. The conventional procedure where one uses a weak probe beam with an intensity I well below the saturation intensity I_{sat} is problematic in this context [84]. Indeed for the relevant range of temperatures (40–150 nK), the atomic thermal wavelength $\lambda_T = (2\pi\hbar^2/mk_B T)^{1/2}$ is comparable to the optical wavelength used for probing, $\lambda_{\text{opt}} = 780$ nm. Consequently in the highly degenerate region of the gas ($\mathcal{D} \equiv n\lambda_T^2 \gg 1$), the average distance between neighboring atoms $n^{-1/2}$ is much smaller than λ_{opt} and the absorption of a weak probe is strongly perturbed by collective effects. To circumvent this problem we probe the gas with a short pulse (duration $\sim 2\,\mu$s) of an intense probe beam (typically $I/I_{\text{sat}} = 40$ to 100) [98]. The interaction of any given atom with light is then nearly independent of its neighbors.

High-intensity imaging, which was also used in [65], provides a faithful measurement of the atomic distribution in the central region of the trap, where the density is large. However the quality of the images suffers from a large photon shot noise, which spoils the detection of the low-density regions of the cloud (Fig. 3.1a). In order to probe reliably these regions on which we base our determination of T and μ, we complement the high-intensity imaging procedure

1. The residual anisotropy of the trap is $|\omega_x - \omega_y|/\omega < 6\%$ where $\omega = (\omega_x\omega_y)^{1/2}$; it plays no significant role in the subsequent analyses. Our procedure to handle slight deviations with respect to harmonicity is described 3.2.2.

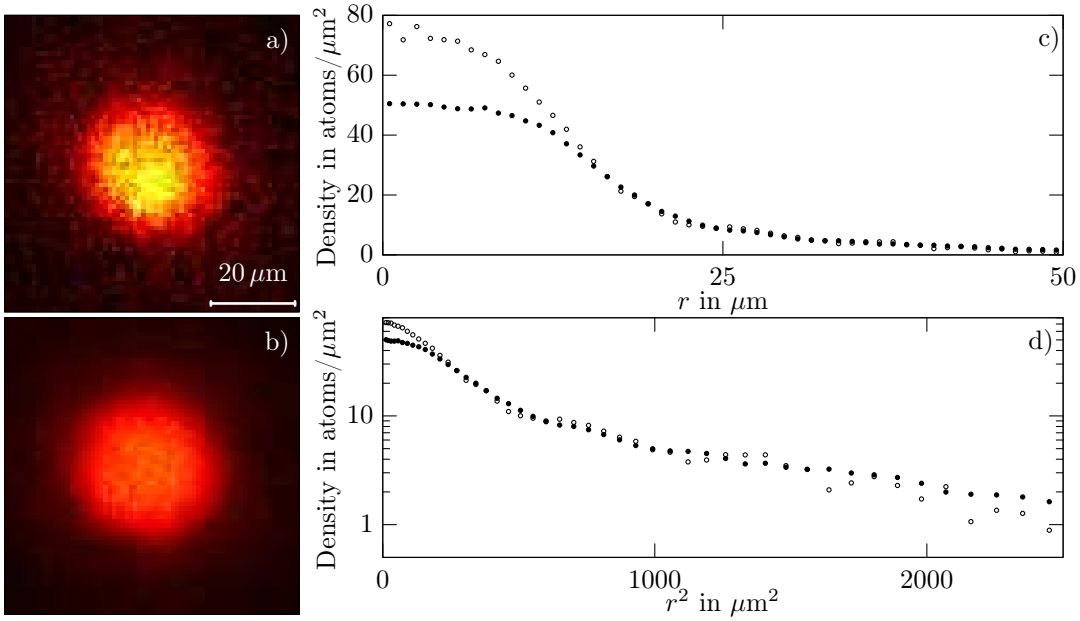

Figure 3.1.: Absorption imaging of quasi-2D clouds of ^{87}Rb atoms. (a) Image obtained with a short pulse ($\sim 2\mu$s) of an intense probe beam ($I/I_{\mathrm{sat}} = 40$) . (b) Image obtained with a longer pulse (50 μs) of a weak probe beam ($I/I_{\mathrm{sat}} = 0.5$). The processing of images (a) and (b) is detailed in the 2.2. (c) and (d) Radial density profiles for image (a) (hollow circles ○) and image (b) (filled circles ●) in linear (c) and logarithmic (d) scales. The solid line combines the predictions of the HFMF theory, of [79] in the intermediate regime and of the Thomas–Fermi approximation $\mu = \hbar^2 \tilde{g} n/m$ in the central region ($T = 133\,\mathrm{nK}$, $\mu/k_{\mathrm{B}} = 47\,\mathrm{nK}$).

by the conventional low-intensity one (Fig. 3.1b). In practice for each set of parameters, we perform one run of the experiment with high-intensity imaging, and one with low-intensity imaging immediately after. The reproductibility is checked by acquiring several pairs of images for a given set of experimental parameters.

The procedure for image processing is detailed in the Auxiliary Material. In short, for each pair of images it provides the temperature T, the chemical potential at center μ and the density $n(\boldsymbol{r})$ at any pixel of the image. We assume that the atoms in the excited states of the z motion are well described by the Hartree–Fock mean-field (HFMF) theory [64, 90, 101, 102]. We thus self-consistently calculate the populations of these states, and subtract them from $n(\boldsymbol{r})$ in order to obtain the density distribution $n_0(\boldsymbol{r})$ in the ground state. The validity of this procedure was checked by analyzing the results of a quantum Monte Carlo cal-

culation for parameters similar to ours [103].

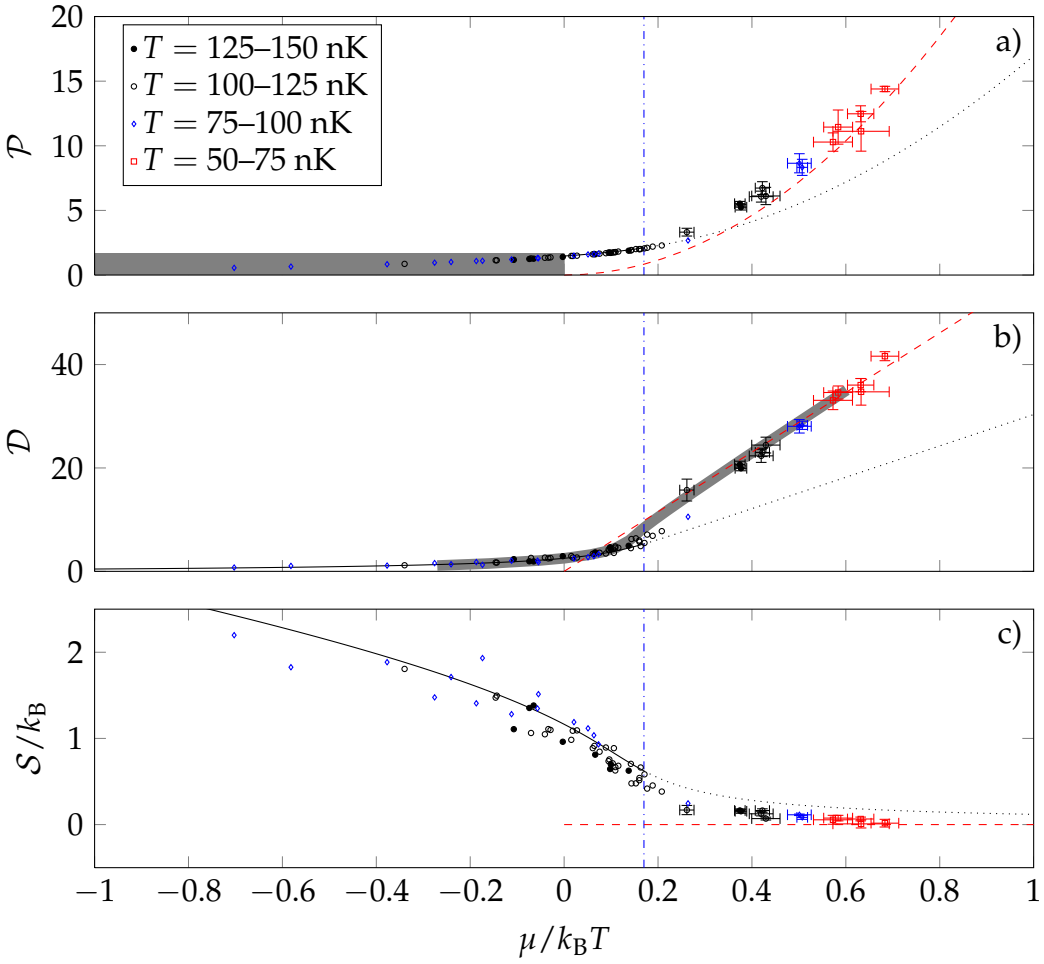

Figure 3.2.: Equations of state for (a) the reduced pressure $\mathcal{P}$, (b) the phase space density $\mathcal{D}$ and (c) the entropy per particle $\mathcal{S}$. The HFMF prediction is plotted in black full line and extended in dotted line beyond the expected superfluid transition. The dashed red line is the Thomas-Fermi prediction. In (a) the grey area indicates the region of parameter space accessible to an ideal gas. In (b) the thick grey line indicates the prediction from [79]. For $\mu/k_BT > 0.2$, data obtained for the same control parameters (trap loading time and evaporative cooling ramp) have been grouped and error bars indicate standard deviation of the measurement. For $\mu/k_BT < 0.2$, data are displayed for individual images, thus with no error bar. The vertical dash-dotted line (blue) indicates the prediction [78] for the superfluid transition.

3.1.2. Thermodynamic analysis

We start our thermodynamic analysis by inferring the pressure $P(\mu, T)$ of the homogeneous gas from our measurements. Here we adapt to the 2D case the technique presented in [100], which has been used successfully in 3D for Fermi gases [35]. We show that $P(\mu, T)$ is directly related to the atom number $N_0 = \int n_0(\boldsymbol{r})\, d^2r$ in our harmonic trap. Indeed, the LDA relates $n_0(\boldsymbol{r})$ to the density of the homogenous gas $n_{\mathrm{hom}}^{(2D)}[\mu - V(\boldsymbol{r}), T]$ [2]. For an isotropic harmonic potential $V(\boldsymbol{r}) = m\omega^2 r^2/2$ the total atom number is

$$N_0 = \frac{2\pi}{m\omega^2} \int_{-\infty}^{\mu} n_{\mathrm{hom}}^{(2D)}(\mu', T)\, d\mu', \tag{3.1}$$

and using the thermodynamic relation $n_{\mathrm{hom}}^{(2D)} = (\partial P/\partial \mu)_T$, we find $N_0 = (2\pi/m\omega^2)$ $P(\mu, T)$. Introducing the dimensionless quantity $\mathcal{P} = P\lambda_{\mathrm{T}}^2/k_{\mathrm{B}}T$, which we refer to as the reduced pressure, we then obtain

$$\mathcal{P}(\mu, T) = \left(\frac{\hbar\omega}{k_{\mathrm{B}}T}\right)^2 N_0, \tag{3.2}$$

where ω is to be replaced by the geometrical mean of ω_x and ω_y for an non-isotropic potential. Our results are summarized in Fig. 3.2a, where we plot $\mathcal{P}$ deduced from Eq. (3.2) as function of $\mu/k_{\mathrm{B}}T$. The temperatures of the data entering in this plot range from 40 nK to 150 nK. The fact that all data points collapse on the same line show that $\mathcal{P}$ is a function of the ratio $\mu/k_{\mathrm{B}}T$ only, as expected from the scale invariance of the system. The HFMF theory is represented by a continuous line in the normal region and by a dotted line in the superfluid region. The dashed line is the Thomas–Fermi prediction at zero temperature $\mathcal{P} = \pi(\mu/k_{\mathrm{B}}T)^2/\tilde{g}$. The grey area is the parameter subspace accessible to an ideal Bose gas. Interestingly, although the phase space density $\mathcal{D}$ can take arbitrarily large values, one can show in the ideal gas case that the reduced pressure $\mathcal{P} = \mathrm{Li}_2(z) \leq \pi^2/6$, where Li_2 is the dilogarithm function and $z = \exp(\mu/k_{\mathrm{B}}T)$ ($z \leq 1$ for an ideal Bose gas).

We show in Fig. 3.2b our measurements for the phase space density $\mathcal{D}$, obtained from the central density of each cloud. In wide gray line we plot the prediction of [79], which is in good agreement with our results. A further confirmation of this agreement is shown in Fig. 3.1c, where we plot in full line the

2. The LDA holds for short range interactions when the spatial density is nearly constant over the microscopic length scales set by λ_{T} and by the healing length $\xi = (\tilde{g}n)^{-1/2}$.

numerically generated profile using [79] for the fitted T and μ. A measurement of $\mathcal{D}(\mu/k_B T, \tilde{g})$ was also reported in [65] for a quasi-2D Cesium gas, for $\tilde{g}$ ranging from 0.05 to 0.26. Our results agree well with those measurements over the covered range ($\mathcal{D} < 20$ in [65] for $\tilde{g}$ similar to ours).

From our measurements of $\mathcal{P}$ and $\mathcal{D}$ we also obtain the equation of state for the entropy per particle $\mathcal{S}(\mu, T)$:

$$\frac{\mathcal{S}}{k_B} = 2\frac{\mathcal{P}}{\mathcal{D}} - \frac{\mu}{k_B T}\,, \tag{3.3}$$

which can be derived starting from the entropy per unit area $s = (\partial P/\partial T)\,|_\mu$, assuming the EoS for $\mathcal{P}$ to be scale invariant [3]. The corresponding result is shown in Fig. 3.2c. As expected, $\mathcal{S}$ is large in the non-degenerate regime and rapidly decreases around $\mu/k_B T \approx 0.17$, where the superfluid transition is expected for our value of $\tilde{g}$ [78]. Finally $\mathcal{S}$ tends to zero in the Thomas–Fermi regime. Our data points with the largest phase-space density ($\mu/k_B T > 0.5$) correspond to $\mathcal{S} = 0.06\,(1)\,k_B$ only. For comparison the entropy per particle reported in [73] for a 2D Mott insulator is $\sim 0.3\,k_B$. Note that since the BKT transition is of infinite order, one does not expect any discontinuous change for $\mathcal{P}$, $\mathcal{D}$ or $\mathcal{S}$ at the superfluid transition for an infinite homogeneous fluid, although the superfluid density jumps suddenly from 0 to $4/\lambda_T^2$ [104].

3.1.3. Measuring the interaction energy

We now turn to the last part of our study, where we illustrate how to measure the various contributions to the energy of our trapped 2D gases: potential energy E_p in the external trapping potential, kinetic energy of the particles E_k, and interaction energy between atoms E_i. We first point out the simple relation $E_p = E_k + E_i$, obtained from virial theorem assuming 2D contact interaction. We measure $E_p = \int n_0(\boldsymbol{r})\, V(\boldsymbol{r})\, d^2r$ from an *in situ* image, but we still need to disentangle the contributions of E_k and E_i to the total energy. This can be done by abruptly switching off interactions at time $t = 0$, either via a Feshbach resonance or effectively by using a "one dimensional" (1D) ToF described below. Each particle then undergoes a free harmonic motion $\boldsymbol{r}(t) = \cos(\omega t)\,\boldsymbol{r}(0) + \sin(\omega t)\,\boldsymbol{v}(0)/\omega$. The potential energy after a time t

3. A similar method has been used for a 3D Fermi gas at unitarity, Martin Zwierlein, private communication, February 2011.

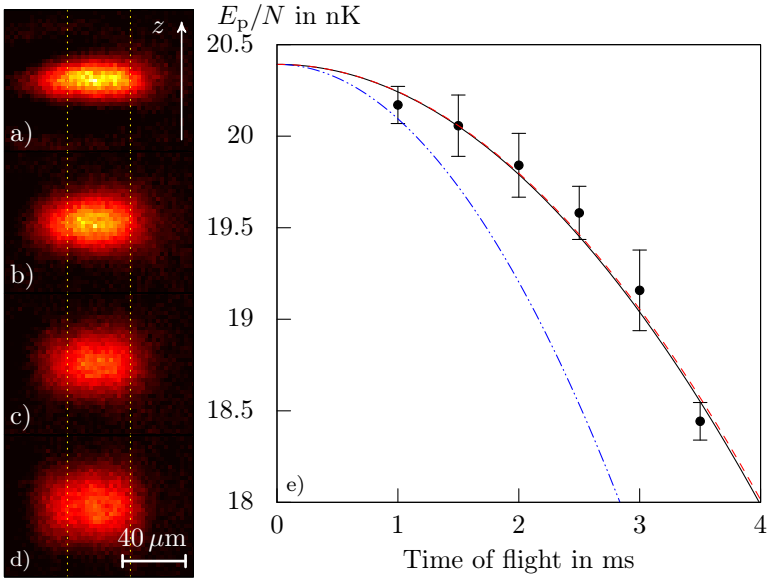

Figure 3.3.: (a) to (d) Side view of a cloud initially in the 2D regime and expanding along z once the laser providing the confinement in this direction has been switched off. (a) $t = 1\,\mathrm{ms}$; (b) $t = 2\,\mathrm{ms}$; (c) $t = 3\,\mathrm{ms}$; (d) $t = 4\,\mathrm{ms}$. (e) Time evolution of the potential energy E_p. The different lines represent a fit to the data of a parabola (solid black line), the time evolution assuming flattened density fluctuations (dashed red line) and the one expected for a dilute non-condensed gas (dash-dotted green line).

following the switching off of the interactions is

$$E_\mathrm{p}(t) = E_\mathrm{p}(0)\cos^2(\omega t) + E_\mathrm{k}(0)\sin^2(\omega t), \tag{3.4}$$

where we used the fact that the correlation $\langle \boldsymbol{r}(0)\cdot\boldsymbol{v}(0)\rangle$ is zero at thermal equilibrium. Thus we can extract $E_\mathrm{k}(0)$ from the time evolution of E_p, which we obtain from the density profiles at different times t.

In order to implement this procedure, we perform the 1D ToF mentioned above by switching off abruptly the laser providing the confinement along z while keeping the magnetic confinement in the xy plane. The gas then expands very fast along the initially strongly confined direction z, as shown in figures 3.3a to 3.3d, and interactions between particles drop to a negligible value after a time of a few ω_z^{-1}, where $\omega_z^{-1} \sim 100\,\mu\mathrm{s}$. The subsequent evolution in the xy plane occurs on a longer time scale given by $\omega^{-1} \sim 8\,\mathrm{ms}$. From Eq. (3.4) and $E_\mathrm{k}(0) < E_\mathrm{p}(0)$, we expect the size of the gas to decrease for $t \lesssim \omega^{-1}$, which can be understood in simple physical terms. The equilibrium state of the 2D gas

results from a balance between the trapping potential, which tends to compress the gas, and the kinetic and interaction energies, which tend to increase its area. When interaction energy drops to zero the equilibrium is broken and the gas implodes in the xy plane. A similar 1D ToF technique was used recently in Boulder with the value of t fixed at $\pi/2\omega$ [64]. For this particular choice the initial momentum distribution is converted into position distribution and can thus be measured accurately [105].

We show in figure 3.3e an example of measurement of $E_p(t)$ for a gas with $N_0 = 6.1\,10^4$, $T = 72\,\mathrm{nK}$, and $\mu/k_BT = 0.59$. From the contraction of the gas, we infer $E_k/E_p = 0.56\,(3)$, from which we deduce $E_i/E_p = 0.44\,(3)$ using virial theorem. This configuration is thus neither completely in the very dilute regime ($E_i \ll E_k \sim E_p$) nor in the Thomas–Fermi regime ($E_k \ll E_i \sim E_p$) and contains comparable thermal and quasi-coherent fractions.

The measurement of E_i is of particular interest in this case since it gives access to the density fluctuations in the gas. Indeed, by definition $E_i = (\hbar^2\tilde{g}/2m) \int \langle n_0^2(\boldsymbol{r})\rangle\, d^2r = (\hbar^2\tilde{g}/2m)\mathcal{F} \int \langle n_0(\boldsymbol{r})\rangle^2\, d^2r$ [106], where we have introduced the parameter $\mathcal{F}$ that characterizes the degree to which density fluctuation are reduced. In the limiting case of a dilute, non-condensed gas, one expects $\mathcal{F} = 2$, since $\langle n_0^2\rangle = 2\langle n_0\rangle^2$, while in the opposite limit of a 'flattened' density profile $\mathcal{F}$=1. Since our measurement provides us with E_i, we can infer the value of $\mathcal{F}$, from the comparison with the quantity $(\hbar^2\tilde{g}/2m) \int \langle n_0(\boldsymbol{r})\rangle^2\, d^2r$, calculated using the *in situ* density profile n_0. For the conditions of figure 3.3e, we find $\mathcal{F} = 1.1\,(1)$, very close to the value 1 for flattened density fluctuations. Note that this is obtained for a gas still far from the Thomas–Fermi limit since $E_k \sim E_i$. This "early" reduction of density fluctuations is an important ingredient for the proper operation of the BKT mechanism. This presuperfluid phase, whose existence was also inferred by different methods in [63–65], constitutes a medium that can support vortices, which pair at the superfluid threshold.

In conclusion we presented in this Letter various aspects of the thermodynamics of a 2D Bose gas, investigating first the EoS's for the pressure, the phase space density and the entropy. Our results confirm the scale invariance that was discussed theoretically in [79] and observed in [65] for $\mathcal{D}$. We point out that the entropy per particle drops notably below $0.1\,k_B$ beyond the transition point. With such a low entropy a 2D Bose gas can constitue excellent coolants for other quantum fluids such as a 2D Fermi gas [107]. We also presented a method that allows one to extract the various contributions to the total energy of the system. By applying it to a degenerate but not fully coherent 2D cloud, we find that density fluctuation are nearly frozen, marking the presuperfluid phase.

3.2. A fit-free equation of state: compressibility, density and pressure

The measure of the EoS presented above is probably the most straightforward one: using the LDA and the EoS for the non–degenerate gas, one can make a prediction for the spatial density in the wings of the cloud. This prediction can then be fitted to the data to retrieve the chemical potential μ and the temperature T. In the rest of this chapter, this method will be referred to as the *single image analysis*. However, any systematic error in the determination of the density, particularly in the calibration of the detectivity of the imaging system, will lead to inaccurate values of μ and T, and thus will affect the measurement of the EoS. This is further complicated by the mutual dependance of the fitting parameters μ, T and the detectivity β upon one another.

For this reason, we provide an alternate method, inspired by the measurements done in Martin Zwierlein's group. There, they present a study of the superfluid transition in a unitary balanced Fermi gas [36], which has a scale invariance, similarly to the 2D Bose gas. This method relies on a choice of suitable thermodynamics variables which remove the need to fit each image, and provide an easy determination of the detectivity.

In the following, we consider a 2D Bose gas in a known radial trapping potential V, and with interaction strength $\tilde{g}$. The density $n(V)$ is directly accessible by absorption imaging. We start by introducing the new dimensionless variables, then we describe how they can be used to reconstruct the usual EoS: phase–space density as a function of $\mu/k_{\mathrm{B}}T$. We then apply this method to our data, and present a low-noise determination of the EoS. Finally, we discuss the role of the excited states along the third dimension.

3.2.1. Choosing the correct dimensionless variables

To characterize the homogeneous two-dimensional Bose gas, one can use several different variables: the density n, the temperature T, the chemical potential μ, the compressibility $\kappa = 1/n^2 \partial n/\partial \mu|_T$, the pressure P defined by $n = \partial P/\partial \mu|_T$, etc ... These quantities are linked together by the equation of state. Owing to a dimensionality argument, any EoS must only link dimensionless quantities together. Therefore, it is necessary to combine these variables to form only dimensionless quantities. For example, the density n can be measured, and

be combined with the temperature T to form the phase space density

$$\mathcal{D} \equiv n\,\lambda_{\mathrm{T}}^2 = \frac{2\pi\hbar^2}{m\,k_{\mathrm{B}}\,T} n. \tag{3.5}$$

An accurate experimental determination of the phase space density relies both on a separate measurement of the temperature, and on a correct measurement of the density. This in turn depends on a precise calibration of the detectivity of the imaging process. All these measurements are done by fitting the Hartree–Fock mean field theory to the density profile of the cloud, for each experimental image. Such an approach was successfully pursued in [69], and presented above. However, it is possible to circumvent a large part of the problem and to use as few fits of the data as possible by choosing appropriate variables to describe the system.

To form dimensionless quantities, we need to introduce an energy scale other than the temperature T, since we do not wish to fit the data directly. Though there are no other *absolute* energy scales readily accessible, a *relative* energy scale is provided by the variation of the trapping potential $\mathrm{d}V$. With this new energy scale, we can create two dimensionless variables

$$\tilde{\kappa}_{\mathrm{m}} \equiv -\frac{\hbar^2}{m}\frac{\partial n_m}{\partial V}\bigg|_T \tag{3.6}$$

$$\tilde{p}_{\mathrm{m}} \equiv \frac{\int_V^\infty n_m(V')\mathrm{d}V'}{\frac{\hbar^2}{m}n_m^2} \tag{3.7}$$

where n_m is the measured density. We can also provide a physical interpretation for Eqs. 3.6 and 3.7. The measured density is linked by a global multiplicative factor β to the real density $n_m = \beta\, n$ (see 2.2), and following the LDA, the change in trapping potential is given by the negative change in local chemical potential, $\mathrm{d}\mu = -\mathrm{d}V$. We can therefore identify the compressibility κ and the pressure P in these equations:

$$\tilde{\kappa}_m = \beta\frac{\hbar^2}{m}\frac{\mathrm{d}n}{\mathrm{d}\mu}\bigg|_T = \beta\frac{\hbar^2}{m}n^2\kappa \tag{3.8}$$

$$\tilde{p}_m = \frac{1}{\beta}\frac{\int_{-\infty}^{\mu} n(\mu')\mathrm{d}\mu'}{\frac{\hbar^2}{m}n^2} = \frac{1}{\beta}\frac{m}{\hbar^2\,n^2}P. \tag{3.9}$$

Note that β is unknown at this stage: we can only access $\tilde{\kappa}_{\mathrm{m}}$ and $\tilde{p}_{\mathrm{m}}$. Finally, in

order to facilitate the following discussion, we introduce

$$\tilde{\kappa} \equiv \frac{\hbar^2}{m}\frac{\mathrm{d}n}{\mathrm{d}\mu}\bigg|_T = \frac{1}{\beta}\tilde{\kappa}_{\mathrm{m}} \tag{3.10}$$

$$\tilde{p}_m \equiv \frac{\int_{-\infty}^{\mu} n(\mu')\mathrm{d}\mu'}{\frac{\hbar^2}{m}n^2} = \beta\tilde{p}_{\mathrm{m}}. \tag{3.11}$$

From these definitions, we can derive analytical expressions in two simple limits: the ideal gas, and the zero temperature limit (Thomas–Fermi approximation).

– **Ideal gas**
For the ideal gas, $n\lambda_{\mathrm{T}}^2 = -\ln(1-e^{\mu/k_{\mathrm{B}}T})$, which leads to

$$\tilde{\kappa}_{\mathrm{id}} = -\frac{1}{2\pi}\frac{1}{1-e^{-\mu/k_{\mathrm{B}}T}} \qquad \text{and} \qquad \tilde{p}_{\mathrm{id}} = 2\pi\frac{\mathrm{Li}_2\left(e^{\mu/k_{\mathrm{B}}T}\right)}{\left(\ln(1-e^{\mu/k_{\mathrm{B}}T})\right)^2}. \tag{3.12}$$

– **Thomas–Fermi limit**
In the Thomas–Fermi limit, $\mu = \hbar^2/m\,\tilde{g}\,n$, and we have

$$\tilde{\kappa}_{\mathrm{TF}} = \frac{1}{\tilde{g}}, \qquad \text{and} \qquad \tilde{p}_{\mathrm{TF}} = \frac{\tilde{g}}{2}. \tag{3.13}$$

As we saw in 1.2.3, the EoS for the density for an interacting non-degenerate ($\mathcal{D} < 1$) 2D Bose gas is given by the Hartree–Fock mean field theory. This equation cannot be integrated analytically, but a numerical calculation of both $\tilde{\kappa}$ and $\tilde{p}$ can be carried out. Finally, an EoS for the degenerate 2D Bose gas was calculated in [79] by Prokofev *et al.* and presented in 1.2.4. This EoS can be combined with the Hartree–Fock prediction to yield $\tilde{\kappa}$ and $\tilde{p}$ for a degenerate gas. All these limits are presented in Fig. 3.4.

Once the normalized pressure and compressibility have been determined, it is possible to combine these variables to express the EoS in more familiar terms, for example by constructing the phase-space density $\mathcal{D}$ and the ratio $\alpha = \mu/k_{\mathrm{B}}T$. Indeed, since the weakly interacting two-dimensional Bose gas is scale invariant, for a fixed interaction strength $\tilde{g}$, two independent dimensionless quantities are sufficient to express the EoS in any other dimensionless variables.

Starting from the pressure P, we can define a function $\mathcal{P}$ (this function was

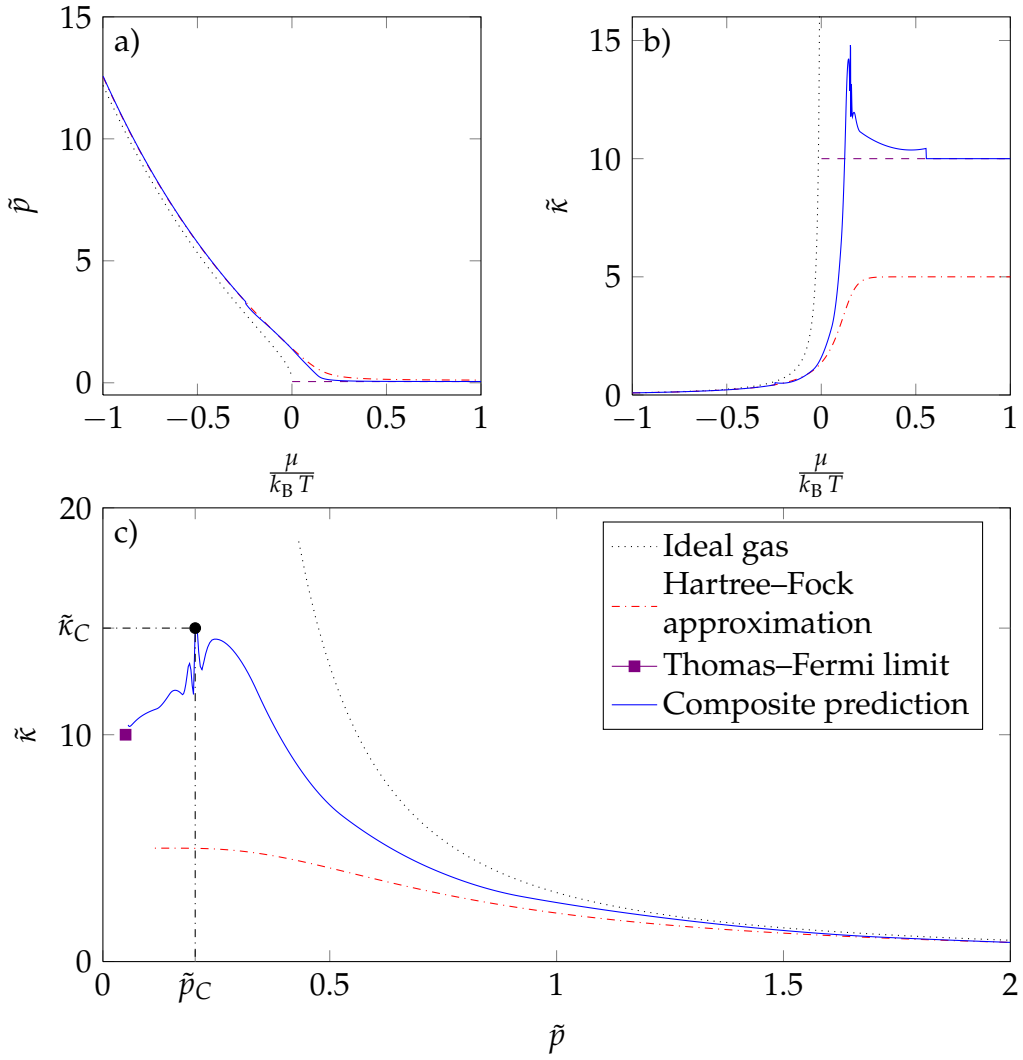

Figure 3.4.: Normalized pressure $\tilde{p}$ (a) and normalized compressibility $\tilde{\kappa}$ (b) as a function of $\mu/k_B T$, and as a function of each other (c). We show predictions for the ideal gas (dotted black line), for the interacting gas ($\tilde{g}$ =0.1) in the Hartree–Fock mean field approximation (dash dotted red line), for the interacting gas with the prediction from [79] (blue full line) and for the interacting gas in the Thomas–Fermi limit (purple square and purple dashed line). The black circle indicates the BKT transition. The irregularity in the composite prediction stems from the differentiation of numerical data. The degeneracy of the system increases with decreasing $\tilde{p}$.

called the reduced pressure in [69]) which is linked to the pressure by

$$\mathrm{P}(\mu, T) = \frac{k_\mathrm{B}\, T}{\lambda_\mathrm{T}^2} \mathcal{P}\left(\frac{\mu}{k_\mathrm{B}\, T}\right), \tag{3.14}$$

which allows us to derive expressions for the density and the compressibility

$$n(\mu, T) \equiv \left.\frac{\partial P}{\partial \mu}\right|_T = \frac{1}{\lambda_\mathrm{T}^2}\mathcal{P}' \qquad \text{and} \qquad \kappa\, n^2 \equiv \left.\frac{\partial n}{\partial \mu}\right|_T = \frac{1}{k_\mathrm{B} T\, \lambda_\mathrm{T}^2}\mathcal{P}''. \tag{3.15}$$

Note that the first derivative of the reduced pressure is directly the phase-space density $\mathcal{P}' = \mathcal{D}$. Eq. 3.15 allows us to link the normalized pressure and compressibility to the function $\mathcal{P}$ and its derivatives:

$$\tilde{p} = \frac{2\pi\, \mathcal{P}}{\mathcal{P}'^2} \tag{3.16}$$

$$\tilde{\kappa} = \frac{1}{2\pi}\mathcal{P}''. \tag{3.17}$$

Finally, we can write a differential equation to determine the phase-space density

$$\begin{aligned} \frac{\mathrm{d}\tilde{p}}{\mathrm{d}\mathcal{D}} &= \frac{\mathrm{d}\tilde{p}}{\mathrm{d}\alpha}\frac{\mathrm{d}\alpha}{\mathrm{d}\mathcal{P}'} \\ &= 2\pi \frac{1}{\mathcal{P}'}(1 - 2\tilde{p}\,\tilde{\kappa})\frac{1}{2\pi\,\tilde{\kappa}} \\ &= \frac{1}{\mathcal{D}}\left(\frac{1}{\tilde{\kappa}} - 2\tilde{p}\right) \end{aligned} \tag{3.18}$$

and the phase-space density is deduced by integration:

$$\mathcal{D}(\tilde{p}_f) = \mathcal{D}(\tilde{p}_i) \exp\left(\int_{\tilde{p}_i}^{\tilde{p}_f} \frac{\mathrm{d}\tilde{p}}{\frac{1}{\tilde{\kappa}} - 2\tilde{p}}\right). \tag{3.19}$$

Once the phase-space density is known, we can write a differential equation to determine $\mu/k_\mathrm{B}T$

$$\frac{\mathrm{d}\tilde{p}}{\mathrm{d}\alpha} = 2\pi \frac{1}{\mathcal{P}'}(1 - 2\tilde{p}\,\tilde{\kappa}) \tag{3.20}$$

which can be integrated to find

$$\alpha(\tilde{p}_f) = \alpha(\tilde{p}_i) + \int_{\tilde{p}_i}^{\tilde{p}_f} \frac{\mathcal{D}(\tilde{p})}{2\pi(1-2\tilde{\kappa}\tilde{p})}\mathrm{d}\tilde{p}. \tag{3.21}$$

To fully determine α and $\mathcal{D}$, we take $\tilde{p}_i$ to be lying in the thermal regime, where the value of $\mathcal{D}(\tilde{p}_i)$ and $\alpha(\tilde{p}_i)$ are known, where the Hartree–Fock mean field approximation is valid.

Note that this step constitutes the only reference to a theory, and must only be used for a single value of $\tilde{p}_i$. This must be contrasted with the *single image analysis*, where the Hartree–Fock mean field approximation was needed to fit each image over a wide range of pixels to determine the EoS.

A last difficulty stems from the incomplete knowledge of the imaging process. Indeed, our imaging does not allow for a quantitative measurement of the density and only provides an experimental determination of $\tilde{p}_\mathrm{m}$ and $\tilde{\kappa}_\mathrm{m}$. Therefore, we define two new functions:

$$\Pi(u) = \exp\left(\int_{u_0}^{u} \frac{\mathrm{d}\tilde{p}_\mathrm{m}}{\frac{1}{\tilde{\kappa}_\mathrm{m}} - 2\tilde{p}_\mathrm{m}}\right) \tag{3.22}$$

$$A(u) = \int_{u_0}^{u} \frac{\Pi(\tilde{p}_\mathrm{m})}{2\pi(1-2\tilde{\kappa}_\mathrm{m}\tilde{p}_\mathrm{m})}\mathrm{d}\tilde{p}_\mathrm{m}. \tag{3.23}$$

Since $\tilde{p}_\mathrm{m}$ and $\tilde{\kappa}_\mathrm{m}$ are linked to $\tilde{p}$ and $\tilde{\kappa}$ by the detectivity β (see Eqs. 3.6 and 3.7), equations 3.22 and 3.23 can be rewritten

$$\Pi(u) = \frac{\mathcal{D}(\beta u)}{\mathcal{D}(\beta u_0)} \tag{3.24}$$

$$A(u) = \frac{1}{\beta}\frac{\alpha(\beta u) - \alpha(\beta u_0)}{\mathcal{D}(\beta u_0)}. \tag{3.25}$$

Therefore, the values of α and of the phase-space density can be inferred by linear transformations from the quantities Π and A. Furthermore, the coefficients intervening in this transformation are strictly constrained by the value of the detectivity β and the link between $\alpha(\beta u_0)$ and $\mathcal{D}(\beta u_0)$. By choosing a value of u_0 such that the EoS around $\beta\, u_0$ is known, the value of β can then be determined by performing a least-square fit of this EoS to the portion of the EoS described by the Hartree–Fock mean field theory. Note that u plays the role of the variable describing a parametric plot: though it is proportional to the normalized pressure, its precise value is only relevant in u_0. In the following, we will refer

to this determination of the EoS as the *global method*.

3.2.2. Characterizing the trapping potential

Though the method presented above does not rely on a fitting process, a precise knowledge of the trapping potential is required to integrate and differentiate the data. We present in the following a determination of this trapping potential. *The following section was initially published as part of the supplemental material of [69], and is reproduced without modifications*

The confinement potential in the xy plane is essentially provided by our magnetic trap, but it may also be affected by some imperfections in the intensity profile of the beam that freezes the z degree of freedom. These imperfections are revealed by looking at the center of mass oscillations $x_{\mathrm{cm}}(t)$ and $y_{\mathrm{cm}}(t)$, shown in Fig. 3.5a,b. Whereas the oscillation along the direction of propagation of the "freezing laser" (x) shows no deviation with respect to harmonic motion, the oscillation along y is damped. This is likely caused by irregularities of the transverse intensity profile of the freezing laser. In order to cope with these defects we have abandoned the standard technique consisting in making angular aver-

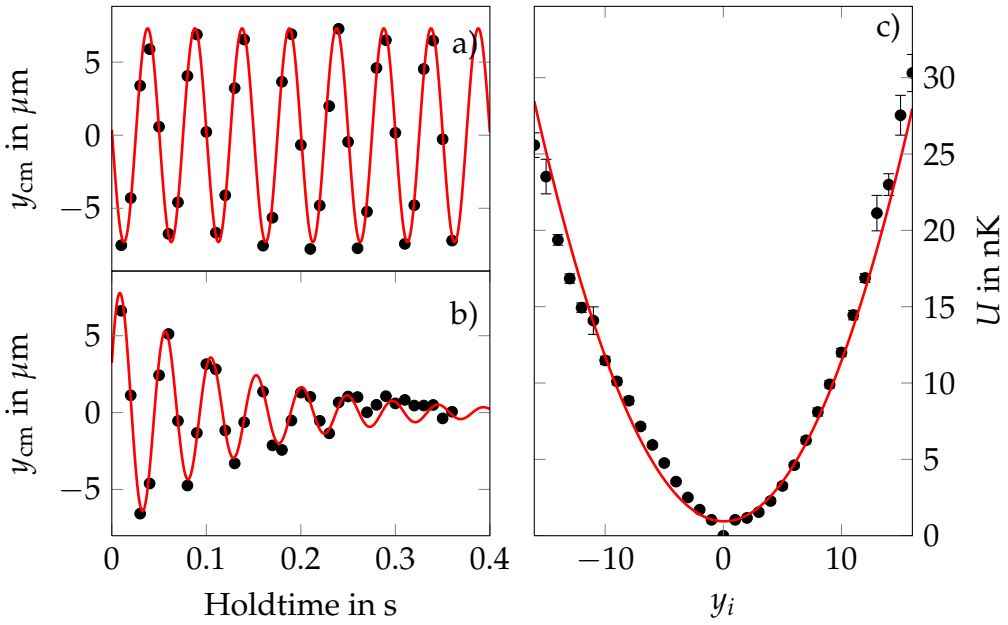

Figure 3.5.: (a) and (b) Center of mass oscillations (hollow circles ○) along x (a) and y (b). The red lines correspond to a fit with a sine (a) and a damped sine (b). (c) Reconstructed potential along the y axis (filled circles ●) and a harmonic fit (red line).

age of the images to produce radial density profiles. Instead we take advantage of the separability of the potential in the xy plane: $V(x,y) = m\omega_x^2 x^2/2 + U(y)$, where $U(y)$ accounts for the magnetic trapping potential and the irregularities of the freezing laser. We consider cuts of the measured density profile along the x direction, measured for various y_i's with $i = 1, \ldots, q$. In practice, we consider the $q = 31$ central lines of our images. We expect that two cuts corresponding to y_1 and y_2 coincide, provided we shift the second one by making the substitution $m\omega_x^2 x^2 \to m\omega_x^2 x^2 + U(y_2) - U(y_1)$. In practice we perform a least-square fit to optimize the superposition of the various cuts, taking the numbers $U(y_i)$ as parameters. We use a single set of $U(y_j)$ to fit a whole series of images taken at a given temperature. The robustness of the procedure is excellent, as shown in Fig. 3.5c, where we give the reconstructed potential $U(y)$, with bars corresponding to the statistical errors of the $U(y_j)$'s for various series of images acquired at different temperatures.

3.2.3. Measuring the equation of state with the global method

Once the trapping potential V is known, the data is processed in the following manner:

1. Each experimental image is converted into a relation between the measured density and the potential $n_m(V)$. In particular, the global detectivity factor β introduced in 2.2 is not taken into account. A proper calibration of this factor will only be done at the end of the analysis. The data can be acquired either at low or high intensity imaging. In practice, the low intensity images will not be used for the *global method* owing to the density dependent detectivity. Since the images must be differentiated afterward, we first increase the signal-to-noise ratio by performing the Principal Component Analysis (see 2.2.3) over a series of similar images (at least 50 images) (see Fig. 3.6a).The data is then smoothed by averaging over 70 consecutive values of the potential (see Fig. 3.6b). The binning window used in this case is typically ≈ 2 nK, which is on the order of 1 μm for our trapping potential.
2. $\tilde{\kappa}_{\mathrm{m}}$ and $\tilde{p}_{\mathrm{m}}$ are derived for each experimental image, for each value of the potential, as introduced in Eqs. 3.6 and 3.7. The resulting data may be further averaged, this time around fixed values of $\tilde{p}_{\mathrm{m}}$ to produce a uniform sampling of the EoS (see Fig. 3.6c). At this point, each experimental image yields a single realization of the EoS $\tilde{\kappa}$ versus $\tilde{p}$.
3. We can choose to use all the images to produce a low noise determination

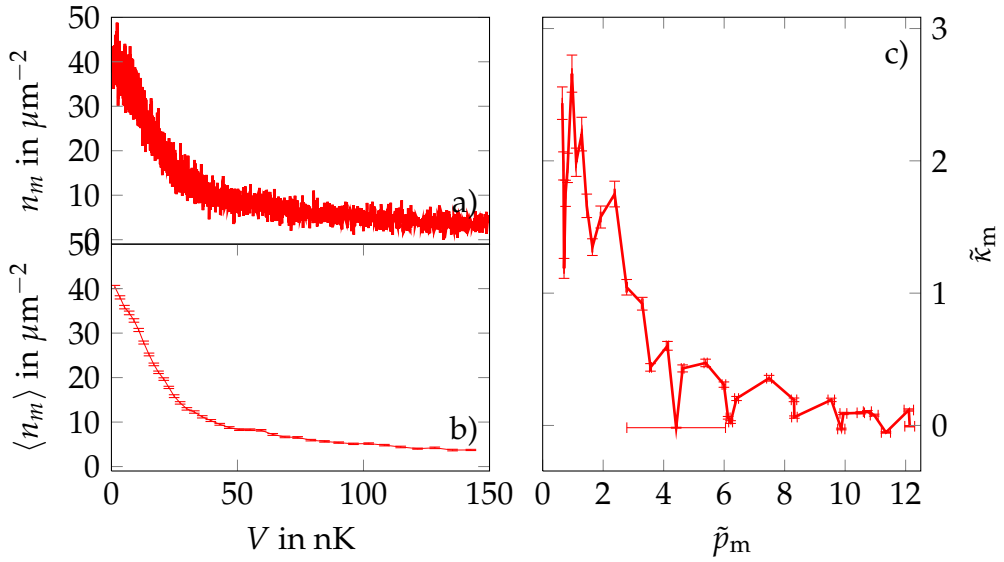

Figure 3.6.: (a) and (b) Experimental measurement of the optical density as a function of the trapping potential V. (a) shows the raw data, and (b) shows the same data, after averaging over 70 consecutive values of the potential. The error bars indicate the standard error resulting from this average. (c) shows the EoS $\tilde{\kappa}_\mathrm{m}$ as a function of $\tilde{p}_\mathrm{m}$, derived in the manner indicated in 3.8 and 3.9. The density n_m is determined as indicated in 2.2.

of $\tilde{p}_\mathrm{m}$ and $\tilde{\kappa}_\mathrm{m}$. The scale invariance of the 2D Bose gas allows us to average all the images together to produce the first EoS: $\tilde{\kappa}$ versus $\tilde{p}$.The result is presented in Fig. 3.7. We find that both known limits (Thomas–Fermi limit and non-degenerate Bose gas) are in reasonable agreement with the experimental results. However, there is a noticeable discrepancy between the numerical prediction and the data around the transition point $\tilde{p} \approx 0.25$. Note that since both the numerical prediction and the experimental data must be differentiated to allow for a direct comparison, this discrepancy may very well be the noise introduced by this procedure.

4. We can then turn back to the quantities Π and A introduced in Eqs. 3.22 and 3.23 to derive the EoS in terms of phase-space density. We aggregate all the images in single set of data. For both integrals, the noise on $\tilde{p}_\mathrm{m}$ and $\tilde{\kappa}_\mathrm{m}$ can cause the denominator of the argument to cancel. For this reason, we systematically remove data points responsible for these divergences [4]. Finally, when choosing the initial point of the integration, we

4. Typically, we remove points such that $\left|\frac{\mathrm{d}(1/(1-2\tilde{p}_\mathrm{m}\tilde{\kappa}_\mathrm{m}))}{\mathrm{d}V}\right| \geq 1$

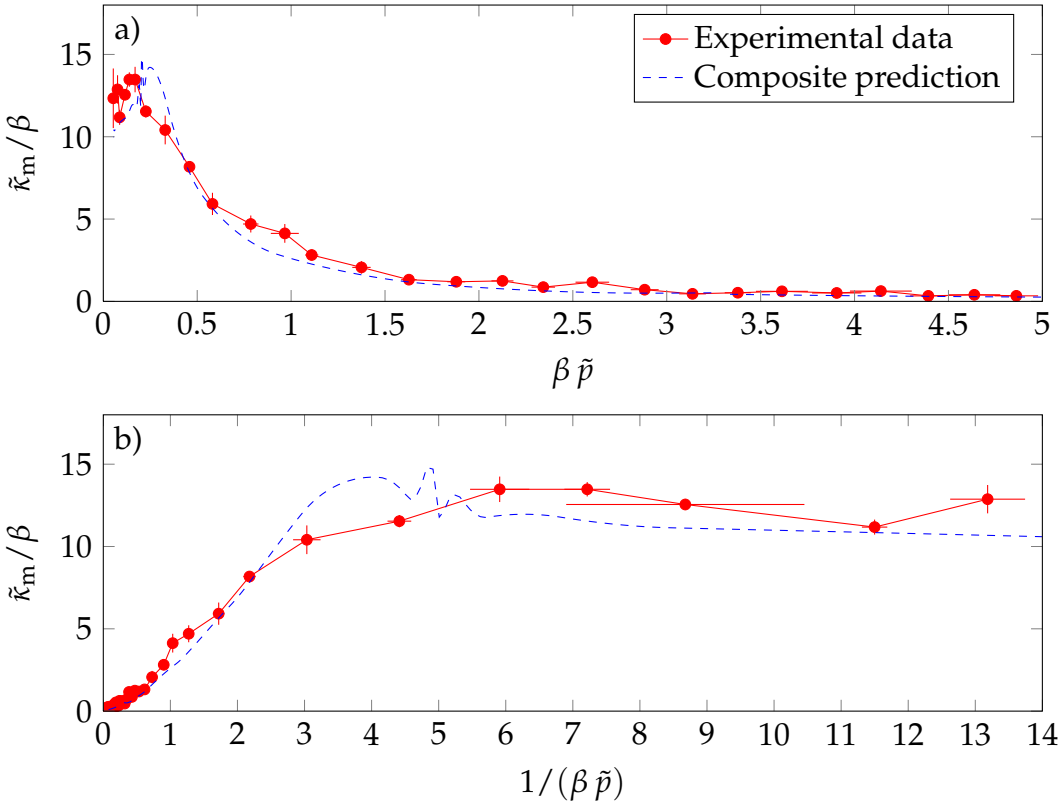

Figure 3.7.: EoS for $\tilde{\kappa}_m$ versus $\tilde{p}_m$. To allow for a comparison between the numerical prediction and the experimental results, we use the detectivity factor $\beta = 0.4$ which was determined in [69].

select $\beta\,u_0 = 3$: this corresponds to a phase-space density of 1.45, which is properly described by the Hartree–Fock mean-field theory. For lower values of $\beta\,u_0$, the Hartree–Fock mean field theory will not be valid, while higher experimental values of $\beta\,u_0$ have a significantly higher noise level. The resulting EoS is presented in Fig. 3.8. In particular, we find the optimal value for the detectivity $\beta = 0.46$, in good agreement with the determination which was presented in [69], where we found $\beta = 0.4$.

3.2.4. Thermometry on single images

Once the EoS of the two-dimensional Bose gas has been determined using the *global method* presented above and in Fig. 3.8, it can be used to determine the chemical potential μ and temperature T of individual images. Owing to the

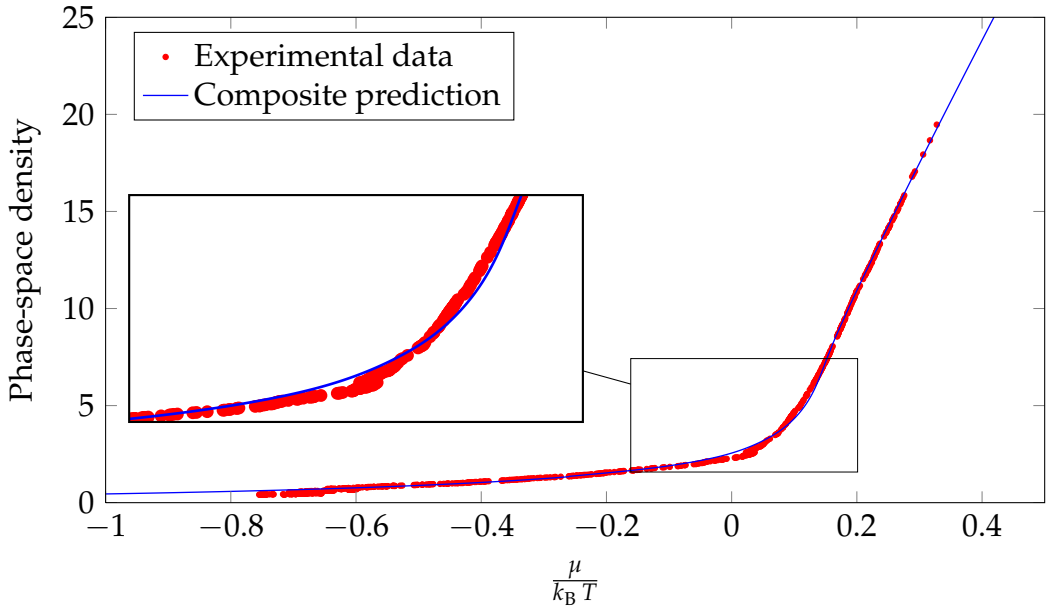

Figure 3.8.: $\mathcal{D}$ versus $\mu/k_B T$ (red points) and composite prediction from [79] (blue line). The detectivity is adjusted by a least-square fit of the data to the Hartree–Fock mean field theory, and is set at $\beta = 0.46$.

scale invariance, the atomic density must take the form

$$n(r) = \frac{m\, k_B\, T}{2\pi\, \hbar^2} \mathcal{D}\left(\frac{\mu - V(r)}{k_B\, T}\right). \tag{3.26}$$

For a given image, it is therefore possible to determine μ and T. This in turn allows for an experimental test of the scale invariance. When properly rescaled, all curves must collapse on top of each other. In Fig. 3.9a, we show a few resulting curves, for data covering a wide range of temperatures (40 nK $< T <$ 200 nK). Furthermore, this provides another way to establish the EoS, albeit linked to the *global method*, by averaging over several experimental images. Since this new determination combines the *global method* to establish an EoS and the analysis of individual images, we will refer to it in the following as the *hybrid method*. The resulting EoS is shown in Fig. 3.9b, along with the measurement with the *global method*. This new measurement is in very good agreement with the *global method*, except in the critical region.

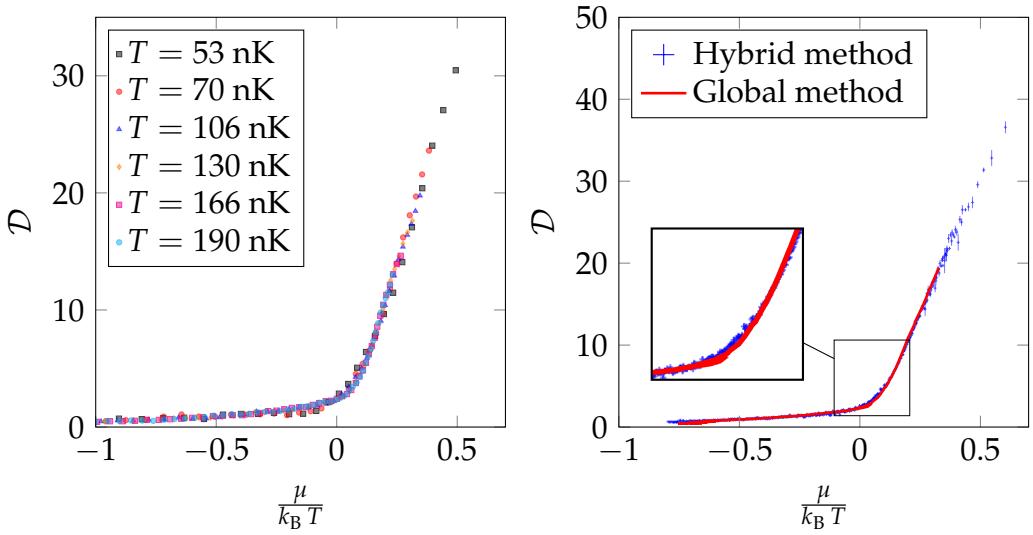

Figure 3.9.: (a) Typical density profiles, rescaled using Eq. 3.26, for a wide range of fitted temperatures. (b) The average over all the rescaled profiles is shown in blue crosses, where the size of the cross indicates the statistical error resulting from this average. The red line shows the EoS previously determined following the *global method* presented in 3.2.1.

3.2.5. Excited levels in the transverse direction

In the preceding analysis, we implicitly assumed that the quasi-2D regime was a correct description of our system. However, the harmonic oscillator level spacing along the tightly confining direction is $\hbar\omega_z = k_B \times 87$ nK. Consequently, for most of the data, a fraction of the atoms occupies the excited states. In particular, this introduces a new energy scale, which breaks the scale invariance introduced earlier. In particular, this can explain the slight discrepancy between the two determinations of the EoS presented in Fig. 3.9.

In order to study this temperature dependance, we process the data in the following manner:

1. We measure the temperature and the chemical potential of the atomic distribution of each individual image by fixing the detectivity β to the value determined above, and by fitting with the EoS measured by the *global method*. Since the EoS contains excited levels in its determination, we expect that the measured temperature will also be affected. Note that the population of the excited states is only 10 % of the total population: we therefore expect a similarly small shift of the temperature.
2. We use the method described in Appendix A to calculate the contribution

of the excited states to the total density, and subtract them to obtain an estimate of the population of the ground state.

3. Since we now have a better estimate of the population of the ground state for each image, we can generate a new EoS with the *global method*. We can also determine a new value of the detectivity by fitting the low phase–space density of the EoS to the mean–field theory.
4. In principle, we can iterate to obtain an even more accurate determination of the temperature for each image. However, this does not lead to an improved measurement.

Thus, we are able to self-consistently generate the EoS for the ground state, and compare it to the numerical prediction from [79]. For our set of data, we measure in this way the detectivity $\beta = 0.43$. On average, the fitted temperatures increase by $\approx 5\%$ between the start of the process and the final determination, while the ratio $\mu/k_B T$ decreases by $\approx 5\%$. Once the density of the ground state has been determined, we can provide a new measurement of the EoS. We show in Fig. 3.10 two different derivations of the EoS: either by the *global method* or by the *hybrid method*.

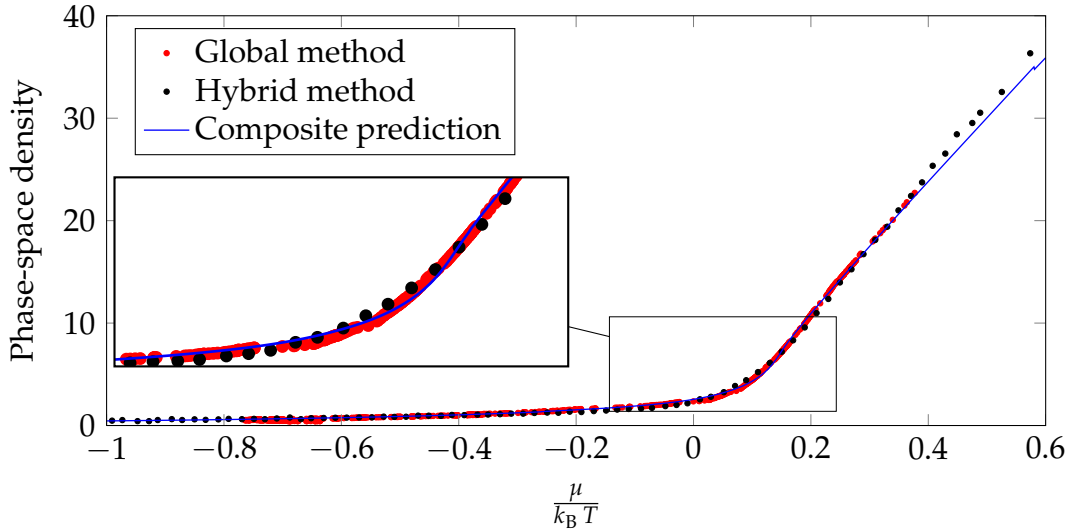

Figure 3.10.: $\mathcal{D}$ versus $\mu/k_B T$ for the ground state of the confining potential. The red points show the integration over several images following the method outlined in 3.2.1. The black points indicate the average over density profiles rescaled following Eq. 3.26. The blue line shows the composite prediction from [79] (blue line). The detectivity is fixed at $\beta = 0.43$.

4. Superfluidity in two dimensions

In the previous chapters, the measurements performed on the bidimensional Bose gas only revealed indirect evidence for the BKT transition. Both the equation of state (see chapter 3) and the fluctuations of the 2D Bose gas (see chapter 5) are consistent with the existence of the BKT transition, but do not constitute as such a direct measurement. To complement these measurements, we present in this chapter a direct characterization of the superfluid behaviour of the two-dimensional Bose gas. To this end, we study the response of an atomic sample to a moving perturbation, formed by a micron-sized laser beam. In the past, this method was successfully used in tri-dimensional Bose [108] and Fermi gases [109],

In this chapter, we start by giving a short overview of the possible dissipation mechanisms in a superfluid. In particular, we provide a simple physical argument linking the critical velocity to the superfluid density, both in two and three dimensions. We then present an experimental determination of the critical velocity in a two-dimensional Bose gas.

4.1. A brief theoretical overview

A superfluid is defined as a medium which can sustain a persistent flow of matter. If the velocity of such a flow is non-zero, then the system is not in its lowest energy configuration, and must be regarded as metastable. For a given velocity of the flow, the system has a finite probability per unit time to decay to a state of smaller superflow. It will therefore be considered a superfluid if this decay is too long to be observed. The lifetime of this metastable state depends on the height of the barrier separating it from the rest state, which in turn depends itself on the velocity of the superflow. As was shown first by Langer and Fisher [110], the primary mechanism responsible for the decay of the superflow is the formation of either vorticity rings in three dimensions, or of vortex dipoles in two dimensions.

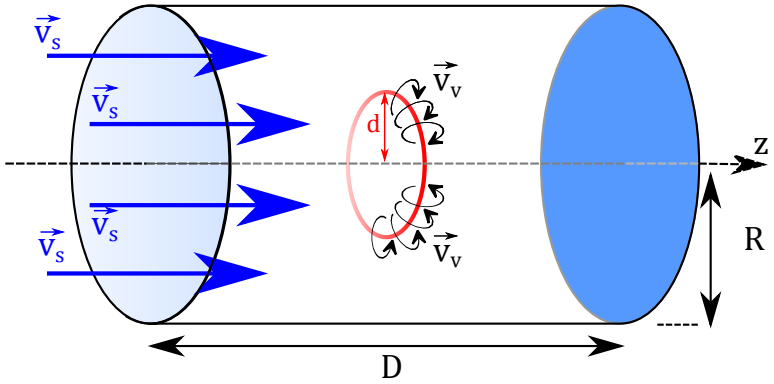

Figure 4.1.: Flow of a superfluid in a cylindrical geometry, with twisted boundary conditions: the density must be identical in $z = 0$ and $z = D$, while the phase must vary by multiples of 2π between these two points. The vorticity ring of radius d is indicated in red.

4.1.1. The three-dimensional case

In the following, we consider a three-dimensional superfluid in a cylindrical geometry, of radius R and length D, depicted in Fig. 4.1. The flow is directed along the revolution axis of the cylinder, which we take to be the z axis. The existence of a superflow is dictated by the twisted boundary conditions: the phase must jump by $n\,2\pi$ between $z = 0$ and $z = D$, with n an integer. Consequently, the wavefunction must take the form

$$\psi(\mathbf{r}) = e^{i\,\boldsymbol{k}\boldsymbol{r}} \qquad \text{where} \qquad \boldsymbol{k} = \frac{n\,2\pi}{D}\boldsymbol{e}_z. \tag{4.1}$$

In this case, the velocity of the superflow with respect to the walls of the container is given by $\boldsymbol{v}_s = \hbar\boldsymbol{k}/m$, which is quantized. In the following discussion, the walls of the cylinder are at rest, and constitute the frame of reference. We then consider a ring of vorticity centered on the z axis. Around this line, the phase winds by $\pm 2\pi$. Note that this object has the required topological properties to change the velocity: the particles crossing the inside of the ring have a difference of one quantum of velocity with respect to the other particles. Consequently, if such a vortex ring expands and reaches the edges of the cylinder, the total velocity of the fluid is changed by one quantum. In order to give an estimate of the barrier height separating two flow states, we can calculate the total energy of a system containing a single ring of vorticity. It is given by

$$E = \int \mathrm{d}^3 r\, \frac{\rho_{3D}}{2}\,(\boldsymbol{v}_v + \boldsymbol{v}_s)^2 \tag{4.2}$$

where ρ_{3D} is the superfluid density, $\boldsymbol{v}_s$ is the velocity of the superflow and $\boldsymbol{v}_v$ is the velocity field associated with the vortex ring. Eq. 4.2 can be further decomposed in three contributions:

$$E_0 = \int \mathrm{d}^3 r \, \frac{\rho_{3D}}{2} \, \boldsymbol{v}_s^2 \tag{4.3}$$

$$E_v = \int \mathrm{d}^3 r \, \frac{\rho_{3D}}{2} \, \boldsymbol{v}_v^2 \tag{4.4}$$

$$E_f = \int \mathrm{d}^3 r \, \frac{\rho_{3D}}{2} \, 2\boldsymbol{v}_v \boldsymbol{v}_s \tag{4.5}$$

Here, E_0 is the initial energy of the superflow, which will not play a role in estimating the height of the barrier. E_v is the cost in kinetic energy associated with the formation of a vortex ring, and E_f is the gain in kinetic energy stemming from the reduction of the flow going through the ring. An analytical calculation of these integrals is given in [110, 111] by

$$E_v = 2\pi^2 \frac{\rho_{3D} \hbar^2}{m} d \ln\left(\frac{d}{\xi}\right) \tag{4.6}$$

$$E_f = -2\pi^2 \, \rho_{3D} \, \hbar \, d^2 \, v_s \tag{4.7}$$

where $\xi = 1/\sqrt{a_s \rho_{3D}}$ is the healing length, with a_s the scattering length, and d is the radius of the vorticity ring (see Fig. 4.1). These two contributions to the energy lead to a maximum at

$$d_{\max} = \frac{\hbar}{m \, v_s} \tag{4.8}$$

within logarithmic accuracy, and the maximum is given by

$$E_{\max} = \frac{\pi^2}{2} \frac{\rho_{3D} \hbar^3}{m^2 \, v_s}. \tag{4.9}$$

Once we have determined the energy associated with the creation of the vortex ring (see Fig. 4.2), we can then imagine two possible decay mechanisms for the superflow.

- For sufficiently low barrier heights, the thermal fluctuations can be sufficient to cause vortex rings to grow, and dissipate on the walls on the container. In this case, the phase jump between $z = 0$ and $z = D$ decreases by 2π and the superflow decays. The stability of the flow can be written as

$\gamma k_B T \leq E_{max}$ where γ is a numerical factor, or alternatively as

$$v_s \leq v_c \equiv \frac{\rho_{3D}\hbar^3}{\gamma\, m^2\, k_B T}. \tag{4.10}$$

Experimentally, this situation is similar to the establishment of a persistent current, for example in a toroidal trap as was done in [112–114]. In this case, the flow can only persist on macroscopic time scales for velocities lower than v_c. In particular, note that the value of the critical velocity is directly proportional to the superfluid density.

– There also exists an extrinsic dissipation mechanism. Let us suppose that an external defect at rest of characteristic size d_{ext} is placed in the flow. Any vortex rings nucleated in the superfluid must then have a size d_{ext} as well. If a vorticity ring generated in this manner is larger than d_{max}, it will expand and subsequently reduce the flow (see Fig. 4.2). Equivalently, the flow will decay if its velocity is larger than

$$v_c = \hbar/(m\, d_{ext}). \tag{4.11}$$

This process is illustrated in Fig. 4.2. Note that in the limit of a point-like defect, the characteristic size d_{ext} must then be replaced by the healing length ξ. In that case, the result coincides with the well known Landau criterion: for a point-like defect, the critical velocity is also the sound velocity $c = \hbar/(m\xi)$. However, the dissipation in this case is usually associated to the generation of phonons, rather than vortex rings. Experimentally, this configuration can be realized by a creating a stationary defect in a flow, as was done in [115]. Furthermore, in the limit of large defects, the critical velocity does not depend on the superfluid density.

4.1.2. The two–dimensional case

In two dimensions, the vortex ring is replaced by a pair of vortices of opposite signs. The energy associated with such a pair is similar to the three-dimensional case presented in Eqs. 4.6 and 4.7. In two dimensions, we have

$$E_v = 2\pi \frac{\rho_{2D}\hbar^2}{m} \ln\left(\frac{d}{\xi}\right) \tag{4.12}$$

$$E_f = 2\pi\, \rho_{2D}\, \hbar\, d\, v_s \tag{4.13}$$

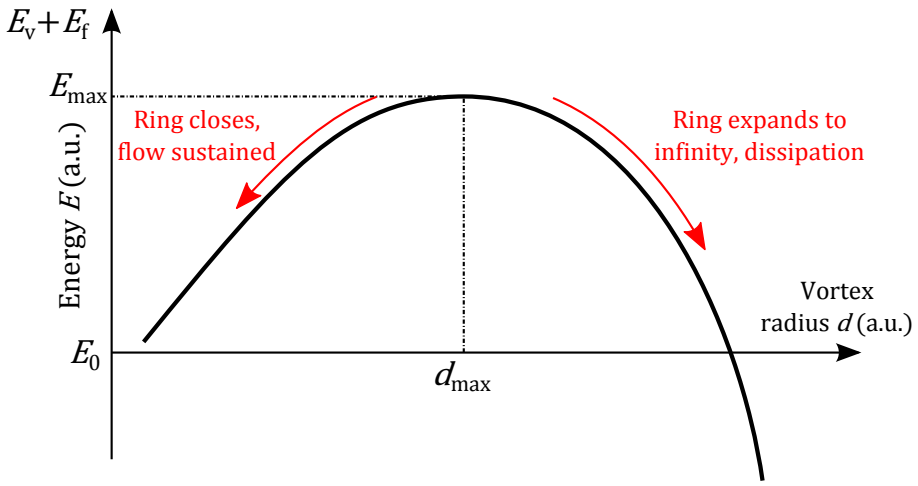

Figure 4.2.: Total energy of a vorticity ring. Rings smaller than d_{max} vanish, and the flow remains the same. However, rings larger than d_{max} expand, and vanish on the walls of the container, causing dissipation.

Again here, the total energy is maximal for

$$d_{max} = \frac{\hbar}{m\, v_s}. \tag{4.14}$$

However, the change in the dimension of space strongly modifies the height of the barrier, which is now given by

$$E_{max} = 2\pi \frac{\rho_{2D}\hbar^2}{m} \ln\left(\alpha \frac{\hbar}{m\, v_s\, \xi}\right) \tag{4.15}$$

with α a numerical constant. As was the case in three dimensions, there can be two different mechanisms causing a superflow to decay.

- An external defect can cause the vortex pairs to grow. The critical velocity associated with such an effect is the same as in the 3D case (see Eq. 4.11). This mechanism corresponds to the experiment presented in the next section.
- The situation changes when considering the thermal activation of a vortex pair. This phenomenon still occurs in two dimensions, but the critical velocity is now given by

$$v_c = \alpha c \, \exp\left(-\gamma \frac{m\, k_B T}{\hbar^2\, \rho_{2D}}\right). \tag{4.16}$$

In particular, contrarily to the 3D case, the critical velocity is not proportional to the superfluid density.

4.2. Superfluid character of a two-dimensional Bose gas, Nature Physics 8, 645-648 (2012)

The following section was initially published in [70], and is reproduced without modifications

'Flow without friction' is a hallmark of superfluidity [116]. It corresponds to a metastable state in which the fluid has a non-zero relative velocity v with respect to an external body such as the wall of the container or an impurity. This metastable state is separated from the equilibrium state of the system ($v = 0$) by a large energy barrier, so that the flow can persist for a macroscopic time. The height of the barrier decreases as v increases, and eventually passes below a threshold (proportional to the thermal energy) for a critical velocity v_c. The microscopic mechanism limiting the barrier height depends on the nature of the defect and is associated to the creation of phonons and/or vortices [116]. While the quantitative comparison between experiments and theory is complicated for liquid ^{4}He, cold atomic gases in the weakly interacting regime are well suited for precise tests of many-body physics. In particular, superfluidity was observed in 3D atomic gases by stirring a laser beam or an optical lattice through bosonic [108, 117–120] or fermionic [109] fluids and by observing the resulting heating or excitations. Here we transpose this search for dissipationless motion to a disc-shaped, non homogeneous 2D Bose gas. We use a small obstacle to locally perturb the system. The obstacle moves at constant velocity on a circle centered on the cloud, allowing us to probe the gas at a fixed density. We repeat the experiment for various atom numbers, temperatures and stirring radii and identify a critical point for superfluid behavior.

4.2.1. Experimental scheme

Our experiments are performed with 2D Bose gases of $N = 35000$ to 95000 ^{87}Rb atoms confined in a cylindrically symmetric harmonic potential $V(r) + W(z)$ (see [69]). The trap frequencies are $\omega_r/2\pi = 25.0(5)$ Hz in the horizontal plane and $\omega_z/2\pi = 1.4\,(1)$ kHz in the vertical direction. We use gases with temperature T and central chemical potential μ in the range 65-120 nK and $k_B \times$ (35-60) nK, respectively. The interaction energy per particle is given by $U_{\rm int} = (\hbar^2\tilde{g}/m)n$, where n is the 2D spatial density (typically 100 atoms/μm^2

in the center), m the atomic mass and $\tilde{g}$ the dimensionless interaction strength. Here $\tilde{g} = \sqrt{8\pi}a/l_z = 0.093$, where $a = 5.3\,\mathrm{nm}$ is the 3D scattering length and $l_z = \sqrt{\hbar/m\omega_z}$. The energy $\hbar\omega_z$ ($k_\mathrm{B} \times 70\,\mathrm{nK}$) is comparable to $k_\mathrm{B}T$ and U_int ($\sim k_\mathrm{B} \times 40\,\mathrm{nK}$ at the trap center). Thanks to Bose statistics, which limits to typically 10% the fractional atomic density in the axially excited states at the obstacle position, our gas is well described by the quasi-2D fluid model (see Supplemental Material of [69]).

We stir the cloud with a laser beam which creates a repulsive potential with height $V_\mathrm{stir} \approx k_\mathrm{B} \times 80\,\mathrm{nK}$. This is at least twice the local chemical potential $\mu_\mathrm{loc}(r) = \mu - V(r)$. The beam has a Gaussian profile with a waist of $w_0 = 2.0\,(5)\,\mu\mathrm{m}$, which is larger than the local healing length $\xi = 1/\sqrt{\tilde{g}n}$ ($\approx 0.3\,\mu\mathrm{m}$ at the trap center), but small compared to the size of the cloud (full width at half maximum $\approx 25\,\mu\mathrm{m}$) (see Fig. 4.3). We stir for typically $t_\mathrm{stir} = 0.2\,\mathrm{s}$ at constant velocity v in a circle of radius r centered on the cloud. The intensity of the stirring beam is ramped on and off in $\approx 5\,\mathrm{ms}$ without any significant additional heating. Once the stirring beam is switched off, we let the cloud relax for 0.1 s and measure the temperature T_f.

For each configuration (N, T, r), we repeat this experiment for various v from 0 to 2 mm/s and a fixed stirring time t_stir. We find two different regimes for the response and we show an example of each in Fig. 4.4. In Fig. 4.4**a**, there is a clear threshold behavior with no discernable dissipation below a critical velocity. In contrast, in Fig. 4.4**b**, the temperature increases without a threshold. We identify these behaviors as the superfluid and normal response, respectively. To model these data we choose for a given configuration the fit function

$$T_\mathrm{f}(v) = T_{\mathrm{f},0} + \kappa \cdot t_\mathrm{stir} \cdot \max[(v^2 - v_\mathrm{c}^2), 0], \tag{4.17}$$

which describes the heating of a 2D superfluid in the presence of a moving point-like defect [121]. In equation (4.17) the three fit parameters are the temperature at zero velocity $T_{\mathrm{f},0}$, the heating coefficient κ, and the critical velocity v_c. In the normal state, the fit finds $v_\mathrm{c} \sim 0$ and the according quadratic heating stems from the linear scaling of the drag force. In the absence of the stirring beam, there is no significant heating and we measure the temperature T_i. The presence of the stirring beam at zero velocity leads to a 'background heating' $T_{\mathrm{f},0} - T_\mathrm{i} \sim 10\,\mathrm{nK}$, which we attribute to photon scattering. In the following, we use the mean temperature $\bar{T} = (T_\mathrm{i} + T_{\mathrm{f},0})/2$ to characterize the cloud.

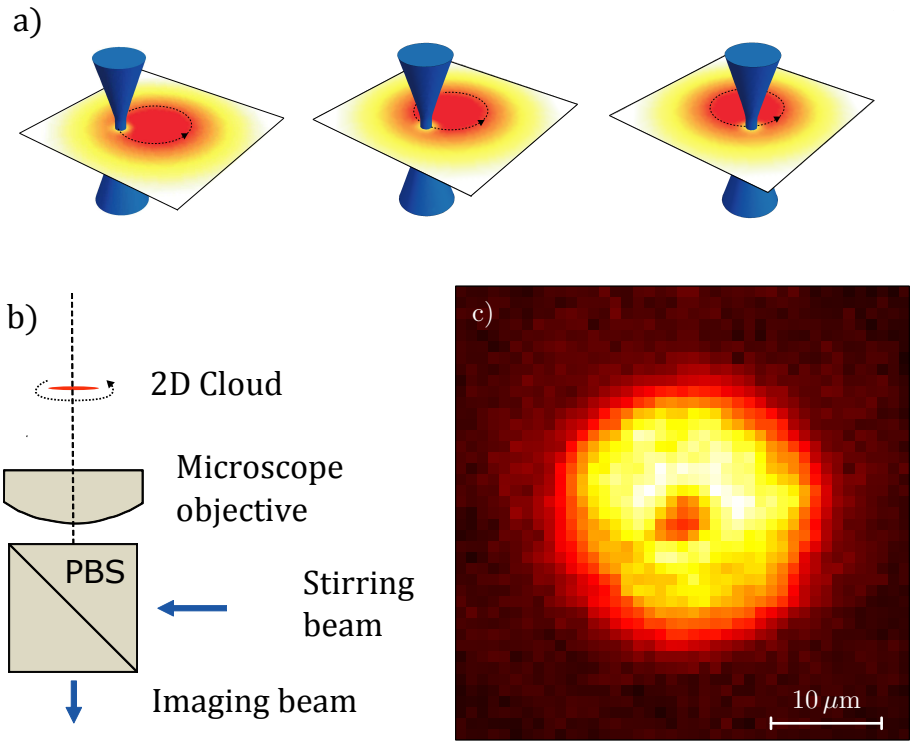

Figure 4.3.: Stirring a 2D Bose gas. **a**, A trapped 2D gas of ^{87}Rb atoms is perturbed by a focussed laser beam, which moves at constant velocity on a circle centred on the cloud. The stirring beam has a frequency larger than the ^{87}Rb resonance frequency ('blue detuning' of $\approx$ 2 nm) and thus creates a repulsive potential which causes a dip in the density profile. **b**, The stirring beam is focussed onto the 2D cloud via a microscope objective of numerical aperture 0.45, which is also used for imaging. We overlap the two beam paths with a polarizing beam splitter cube (PBS). The position of the stirring beam is controlled by a two-axis piezo-driven mirror. **c**, *in situ* false-color image of the 2D cloud in the presence of the laser beam (average over six images). From the dip in the density we deduce the waist of the laser beam as $w_0 = 2.0(5)\,\mu$m. In this image, the intensity of the beam is chosen three times higher than in the stirring experiment to make the hole well visible even in the center of the cloud. We use similar images, but with the stirring beam switched off, to determine the temperature T and the chemical potential μ from a fit of the Hartree-Fock prediction to the wings of the cloud [69].

4.2.2. Observation of a critical velocity

In Fig. 4.5, we summarize our data obtained for different configurations (N, $\bar{T}$, r). We show in Fig. 4.5**a** the fitted critical velocities versus the single parameter $\mu_{\mathrm{loc}}(r)\,/k_{\mathrm{B}}\bar{T}$. The relevance of this parameter results from (i) the local character of the excitation, so that the response of the fluid to the moving perturbation is expected to be similar to that of a uniform gas with the same temperature and the chemical potential μ_{loc}, (ii) the scale invariance of the weakly-interacting 2D Bose gas, whose thermodynamical properties do not depend separately on μ and T, but only on the ratio $\mu/k_{\mathrm{B}}T$ (see [65, 69, 79]). In particular, this ratio is univocally related to the phase space density, and thus characterizes the degree of degeneracy of the cloud.

Quite remarkably, the ensemble of our data for v_{c} when plotted as a function of $\mu_{\mathrm{loc}}/k_{\mathrm{B}}\bar{T}$ shows a threshold between values compatible with zero and clearly non-zero values. This threshold is located at $\mu_{\mathrm{loc}}/k_{\mathrm{B}}\bar{T} \approx 0.24$, somewhat above the prediction $(\mu/k_{\mathrm{B}}T)_{\mathrm{c}} = 0.15$ for the superfluid phase transition in a uniform system [79] with $\tilde{g} = 0.093$. If we assume that the stirrer must stand entirely in the superfluid core in order to yield a non-zero critical velocity, then the deviation can be attributed to the non-zero width of the stirring beam. The range of $\mu_{\mathrm{loc}}/k_{\mathrm{B}}\bar{T}$ corresponding to the extent of this beam is indicated by the horizontal error bars in Fig. 4.5**a**. Note that the finite size of our trapped atomic clouds might also shift the BKT transition, but the effect is expected to be small (a few percent) and in the opposite direction [79].

We limit the presented stirring radii to $r \geq 10\,\mu$m such that the stirring frequencies $\omega = v/r$ for the relevant velocities $v \sim v_{\mathrm{c}}$ are well below ω_r. Indeed, smaller radii correspond to a larger centripetal acceleration. This could lead to additional heating via the phonon analog of synchrotron radiation, as observed in the formally similar context of capillary waves generated by a rotating object [122].

4.2.3. Comparison with theory

For a homogeneous system, the value of the critical velocity is limited by two dissipation mechanisms, the excitation of phonons or vortices. For a point-like obstacle [121], phonon excitation dominates and v_{c} is equal to the speed of sound, given in the zero temperature limit by $c_{\mathrm{s}} = \hbar\sqrt{\tilde{g}n}/m$ ($\approx 1.6\,$mm/s for $n = 50\,\mathrm{atoms}/\mu\mathrm{m}^2$) (this situation is described by the celebrated Landau criterion [116]). When the obstacle size w_0 increases and becomes comparable to ξ, dissipation via the nucleation of vortex-antivortex pairs (vortex rings

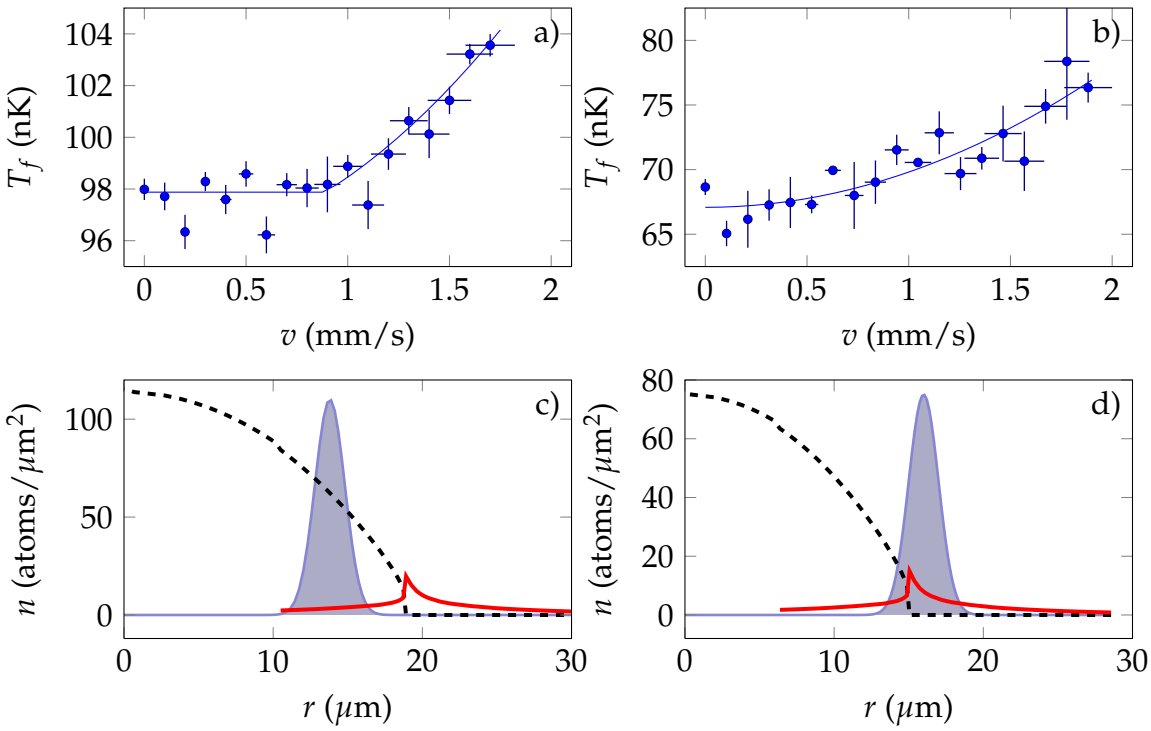

Figure 4.4.: Evidence for a critical velocity. Two typical curves of the temperature after stirring the laser beam at varying velocities. **a**, In the superfluid regime, we observe a critical velocity (here $v_c = 0.87(9)$ mm/s), below which there is no dissipation. **b**, In the normal regime, the heating is quadratic in the velocity. The fitted heating coefficients are $\kappa = 18(3)\,\mathrm{nK}\cdot\mathrm{s/mm^2}$ and $\kappa = 26(3)\,\mathrm{nK}\cdot\mathrm{s/mm^2}$ in **a** and **b**, respectively. The experimental parameters are (N, $\bar{T}$, μ, r)=(87000, 89 nK, $k_B \times 59$ nK, 14.4 ¯m) and (38000, 67 nK, $k_B \times 39$ nK, 16.6 ¯m) for **a** and **b**, respectively, yielding $\mu_{loc}/k_B\bar{T} = 0.36$ and $\mu_{loc}/k_B\bar{T} = 0.04$. The data points are the average of typically ten shots. The y error bars show the standard deviation. The x error bar denotes the spread of velocities along the size of the stirring beam ($1/\sqrt{e}$ radius). The solid line is a fit to the data according to equation (4.17). The stirring time is 0.2 s for all data points. Note that the three low-lying data points in **a** correspond to the completion of an odd number of half turns. For these data points, where we see a downshift of the temperature by approximately 1.5 nK, we also observe a displacement of the center of mass of the cloud by a few μm. **c** and **d**, Calculated radial density distribution for the clouds in **a** and **b**, respectively. The dashed blue curve shows the superfluid density, the solid red curve shows the normal density. The stirring beam potential is indicated by the grey shaded area (in arbitrary units). The densities are calculated via the local density approximation from the prediction for an infinite uniform system [79]. The jump of the superfluid density from zero to a universal value of $4/\lambda_{dB}^2$ (where λ_{dB} is the thermal de Broglie wavelength) is a prominent feature of the BKT transition. The normal density makes a corresponding jump to keep the total density continuous.

in 3D) becomes significant [110, 123, 124]. The corresponding v_c is then notably reduced with respect to c_s. In the limit of very large obstacles ($w_0 \gg \xi$), an analytical analysis of the superfluid flow stability yields $v_c \sim \hbar/mw_0 \ll c_s$ (see [125, 126]). With an obstacle size $w_0 \gtrsim \xi$, our experimental situation is intermediate between these two asymptotic regimes. For a non-homogeneous system like ours with the stirring obstacle close to the border of the expected superfluid regime, one can also excite surface modes [95, 127], which constitute an additional dissipation mechanism.

Our measured critical velocities are in the range 0.5–1.0 mm/s, *i.e.*, $v_c/c_s = 0.3 - 0.6$. By contrast, previous experiments in 3D clouds found lower fractions $v_c/c_s \sim 0.1$ (see [117]). The difference may be due to the larger size of the obstacles that were used, and to the average along the axis of the stirring beam of the density distribution in the 3D gas [128]. The dominant dissipation mechanism could be revealed by e.g. directly observing the created vortex pairs as in [120] or interferometrically detecting the Cerenkov-like wave pattern for $v > c_s$ as in experiments with a non-equilibrium 2D superfluid of exciton-polariton quasiparticles [115].

Fig. 4.5**b** shows the fitted heating coefficients κ for the normal (red circles) and superfluid data (blue circles). In the normal region, we expect the heating to scale linearly with the normal density n_{no} (see [118]). Using the prediction of [79] for $\bar{n}_{no}$ (averaged over the size of the stirring beam) we fit $\kappa = a_1 \cdot \bar{n}_{no}$ and obtain $a_1 \approx 3 \cdot 10^{-6}\,\mathrm{nK \cdot s}$. This value is in reasonable agreement with the prediction of a model [118] of a single particle with a thermal velocity distribution of mean $\bar{v} = \sqrt{\pi k_B T/2m}$ colliding with a moving hard wall of width $L = w_0$ yielding $a_1 = 16mL\bar{v}/\pi N k_B \sim 6 \cdot 10^{-6}\,\mathrm{nK \cdot s}$ (for $N = 65000$ and $T = 90\,\mathrm{nK}$). In particular our data nicely reproduce the maximum of $\bar{n}_{no}$ around the expected superfluid transition point. In the superfluid case and $v > v_c$, we empirically fit a quadratic scaling of the heating with density $\kappa = a_2 \cdot n_{SF}^2$ and find $a_2 = 8 \cdot 10^{-9}\,\mathrm{nK \cdot s \cdot ^{-}m^2}$. In principle, one could develop a more refined model to describe the superfluid region, by taking into account the coexistence of the normal and superfluid states via the sum of two heating terms. However, within the accuracy of our data, we did not find any evidence for the need of such a more refined description.

We have presented a direct proof of the superfluid character of a trapped 2D Bose gas. An interesting extension of our work would be the study of superfluidity from the complementary point of view of persistent currents, by adapting to 2D the pioneering experiments performed in 3D toroidal traps [112–114].

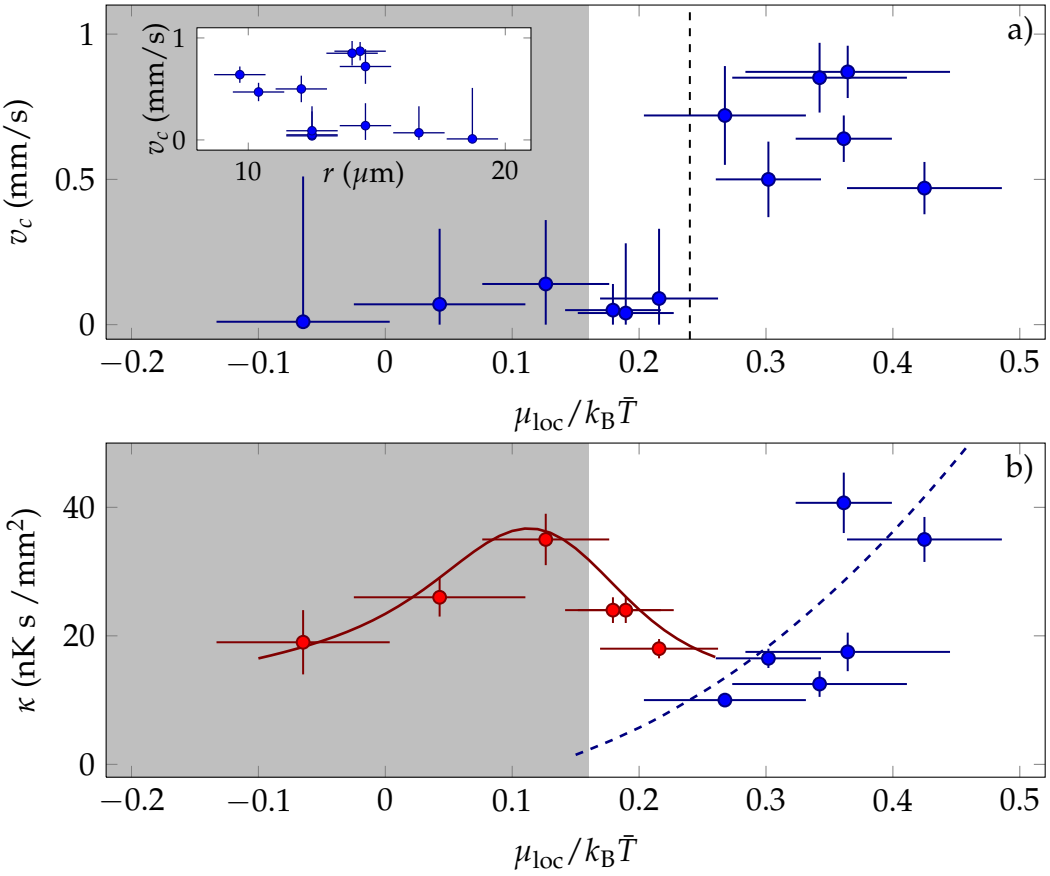

Figure 4.5.: Superfluid behaviour across the BKT transition. **a**, The critical velocities v_c obtained from the curves as in Fig.(4.4) plotted versus the single parameter $\mu_{\mathrm{loc}}/k_{\mathrm{B}}\bar{T}$, which is the relevant quantity due to the scale invariance of the weakly-interacting 2D Bose gas. Our data show a threshold between critical velocities compatible with zero and clearly non-zero critical velocities. It is located at $\mu_{\mathrm{loc}}/k_{\mathrm{B}}\bar{T} \approx 0.24$ (dashed line), somewhat above the prediction $(\mu_{\mathrm{loc}}/k_{\mathrm{B}}T)_c = 0.15$ for the BKT transition in an infinite uniform system [79] (the grey shaded area indicates the normal state by this prediction). The x error bars indicate the region of $\mu_{\mathrm{loc}}/k_{\mathrm{B}}\bar{T}$ that is traced by the stirring beam due to its size (using the $1/\sqrt{e}$ width of the beam) and due to the 'background heating'. The y error bar is the fitting error. The inset to **a** shows the critical velocity plotted versus the stirring radius r. Due to the different atom numbers and temperatures of the clouds, we can find superfluid or normal behaviour for the same radius. **b**, The heating coefficient κ as a function of $\mu_{\mathrm{loc}}/k_{\mathrm{B}}\bar{T}$ for the normal data (red circles) and the superfluid data (blue circles). The red solid line shows a fit of κ linear in the normal density, as expected from a single-particle model. The blue dashed line shows an empirical fit quadratic in the superfluid density. The calculation for the densities assumes $\bar{T} = 90\,\mathrm{nK}$ and the densities are averaged over the size of the stirring beam.

4.3. Closing remarks

In the previous section, we measured the typical response of a superfluid to an external perturbation, and found critical velocities between 0.5 and 1 mm/s. Let us briefly compare these numbers to the qualitative predictions presented in the first section.

Our samples have a typical density of 60 atoms $/\mu\text{m}^2$ at the location of the defect, and the speed of sound is then $c_s \approx 1.7$ mm/s. As we pointed out in the first section, the speed of sound is equal to the critical velocity only for point-like defects. Here, the healing length ξ is only 0.4 μm, while the defect size is ≈ 2 μm. Therefore, the speed of sound over estimates the critical velocity.

In order to provide a better prediction, we can use the critical velocity presented for a large obstacle in Eq. 4.11. In this case, for our defect size, the predicted critical velocity is $v_c = 0.35$ mm/s, below our experimental measurements.

The measured critical velocities therefore lie between the predictions made for two different dissipation mechanisms. It is likely that, for this intermediate size of defect ($w_0 = 5\xi$), the dissipation cannot be simply described by either vortex pairs or phonons, and is rather a mix of the two processes.

5. Fluctuations of the two-dimensional Bose gas

In Ch. 1, we introduced the BKT transition and presented the associated microscopic mechanism, which we briefly recall here. As the degeneracy of the system increases, the density fluctuations are gradually suppressed. The BKT transition leads to a superfluid phase, in which vortices can only exist in the form of bound pairs. Above the transition temperature, they proliferate and destroy the superfluid character of the system.

Although bound vortices are a key ingredient for the BKT transition, the pairing mechanism has not yet been observed directly in cold atoms experiments. The existence of single vortices was inferred from the dislocations of the interference pattern between two 2D gases in [39], and later in a similar experiment in [129]. Though these observations constituted clear evidence of the existence of vortices in 2D, they were not sufficient to extract information about their spatial distribution.

In this chapter, we present a detailed analysis of the density fluctuations of a two-dimensional Bose gas, both *in-situ* and after a short time of flight (ToF). Indeed, a short ToF allows for the study of *in-situ* phase fluctuations, by converting them into density fluctuations. We begin by introducing the experimental procedure used to reveal the phase fluctuations. We then present a quantitative analysis of the observed fluctuations, by studying two different features. First, we focus on the local extrema of the density. We then shift our attention to the *two-body* density correlations, and link their spatial dependance to the *in-situ* phase fluctuations.

5.1. Experimental procedure

We prepare a two-dimensional Bose gas along the lines presented in Ch. 2, and let it equilibrate for 3 s in the combined magnetic trap and light sheet. In the following, we will denote by ω the angular frequency of the harmonic confinement in the xy plane, and by ω_z the angular frequency of the two-dimensional confinement along z. In our experiment, $\omega = 2\pi \times 20$ Hz, and $\omega_z = 2\pi \times 2$ kHz.

At $t = 0$, we switch off the light sheet which realizes the tight confinement,

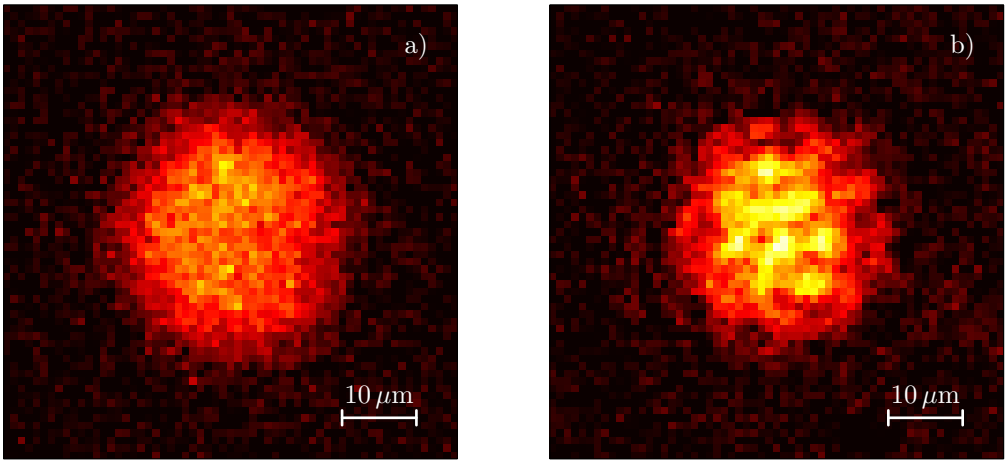

Figure 5.1.: Density distribution *in-situ* (a) and after a 3 ms ToF (b). Both images are acquired with high intensity imaging.

and monitor the subsequent ToF evolution. Owing the the zero-point energy $\hbar\omega_z/2$ of the motion, the cloud rapidly expands in the vertical direction (it doubles in ~ 0.1 ms). Thus, the interaction energy between atoms is divided by $\sim$2 in ω_z^{-1}, and can essentially be neglected. We let the cloud expand for $t_{\mathrm{ToF}} = 3$ ms, which is long compared to ω_z^{-1}, but much shorter than the characteristic time of motion in the xy plane. Thus the envelope of the density distribution only undergoes minor changes (see 3.1.3 for a detailed description) which will be neglected. After this evolution, we take an image of the atomic distribution, using high intensity imaging.

We show in Fig. 5.1a an image of the atomic distribution *in-situ*, and in Fig. 5.1b after $t_{\mathrm{ToF}} = 3$ ms. When comparing these two images, it is apparent that the density distribution is much less regular on short length scales after ToF than *in-situ*. Thus, the inhomogeneities in the density distribution shown in Fig. 5.1b can be attributed to *in-situ* phase fluctuations, which were converted to density fluctuations by the effective switching off of the interactions (see [130] for a similar experiment in a one-dimensional Bose gas). This in good agreement with a crucial aspect of the physics of the two-dimensional Bose gas: for degenerate samples, the density fluctuations are essentially frozen, and the dynamics is dominated by phase fluctuations (see 1.2.3). [1]

1. This is also in agreement with the measurement of the interaction energy presented in 3.1.3, which confirmed the strong suppression of the density fluctuations.

5.2. Local density fluctuations

From Fig. 5.1, a clear feature of the density distribution after ToF is the presence of pronounced density minima inside the cloud. As we presented in 1.2.4, the BKT mechanism rests on the existence of vortices, either in the form of bound pairs in the superfluid phase, or free in the normal phase. For the images presented in Fig. 5.1, a fit of the *in-situ* density distribution yields $T = 70$ nK and the phase-space density in the center of the trap is $\mathcal{D}(r = 0) = 37$. Using the Local Density Approximation (LDA), we find that the phase-space density reaches its critical value[2] $\mathcal{D}_c$ at $r_{\mathrm{BKT}} = 19$ μm. We show in Fig. 5.2 the variation of the local phase-space density with the radius, and define three regions. The strongly degenerate region starts for $\mathcal{D} \geq 2\mathcal{D}_c$, and the thermal regions ends at $\mathcal{D} \leq \mathcal{D}_c/2$. They are separated by the critical region, in which the BKT transition takes place.

Thus, a significant part of the cloud is either strongly degenerate, or in the critical region. It therefore seems natural to try and link the density holes appearing in our images to the vortices associated with the BKT transition. To this

2. We recall $\mathcal{D}_c = \ln(380/\tilde{g})$ (see Eq. 1.27)

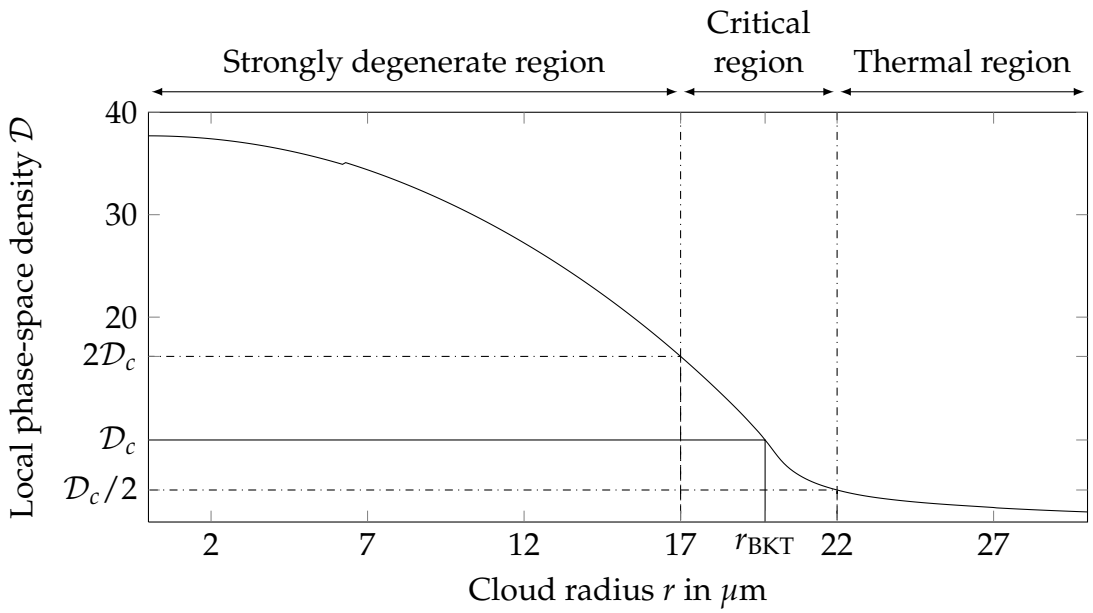

Figure 5.2.: Local phase-space density, determined with the LDA and the equation of state from 1.2.4. We indicate the six radii of interest in this chapter, as well as the location of the BKT transition.

end, we present a quantitative study of the density minima appearing in the cloud. This shall be done both for *in-situ* images, and for ToF images to allow for a direct comparison.

5.2.1. Characterizing the density minima

The atomic density is measured by high intensity absorption imaging (see 2.2). As we are interested in local density minima, it is natural to consider the number of atoms $N(i,j)$ detected on a single pixel of coordinates (i,j). It is given by

$$N(i,j) = \frac{\mathcal{A}}{\beta\sigma_0}\left(-\alpha \ln\left(\frac{I_{\mathrm{wi}}(i,j)}{I_{\mathrm{wo}}(i,j)}\right) + \frac{I_{\mathrm{wo}}(i,j) - I_{\mathrm{wi}}(i,j)}{I_{\mathrm{sat}}}\right) \tag{5.1}$$

where I_{wi} (resp. I_{wo}) is the intensity with atoms (resp. without atoms), I_{sat} is the saturation intensity of the atomic transition, σ_0 is the absorption cross-section, $\mathcal{A}$ is the area of the pixel and α and β are numerical factors. For high imaging intensities, the logarithmic contribution can be neglected, and the detected atom number can be written

$$N(i,j) = \frac{P_{\mathrm{wo}}(i,j) - P_{\mathrm{wi}}(i,j)}{\zeta} \tag{5.2}$$

where $P_{\mathrm{wi}}(i,j)$ (resp. $P_{\mathrm{wo}}(i,j)$) is the number of photo-electrons detected on the CCD camera at pixel (i,j) with (resp. without) atoms, and ζ is the mean number of photo-electrons resulting from absorption by a single atom during the imaging time. It is related to the parameters of Eq. 5.1 by

$$\zeta = \frac{\beta\sigma_0\, I_{\mathrm{sat}}\, \tau}{\hbar\omega_L} = \beta\frac{\Gamma}{2}\tau \tag{5.3}$$

where τ is the imaging time, ω_L is the angular frequency of the atomic transition, and Γ is its natural linewidth. For our parameters $\beta = 0.43$ and $\tau = 2.5\ \mu$s, $\zeta \approx 20$ photo-electrons/atom.

With this simple expression for $N(i,j)$, we now propose the following method to search for minima in the density. We first calculate the average $\langle P_{\mathrm{wo}}\rangle_m$ and $\langle P_{\mathrm{wi}}\rangle_m$ of a series of M images $P_{\mathrm{wo}}^{(m)}$ and $P_{\mathrm{wi}}^{(m)}$ (m varies between 1 and M, with typically $M \sim 10$). In principle, the minima of $N(i,j)^{(m)}$ are directly given by the maxima of $P_{\mathrm{wi}}^{(m)}/\langle P_{\mathrm{wi}}\rangle_m$. However, in order to reduce the effect of the fluctuations of the imaging beam profile between each image, we choose to work

instead with the relative fluctuations

$$f^{(m)} = \frac{P_{\mathrm{wo}}^{(m)}}{\langle P_{\mathrm{wo}} \rangle_m} - \frac{P_{\mathrm{wi}}^{(m)}}{\langle P_{\mathrm{wi}} \rangle_m}. \tag{5.4}$$

With this definition, the local minima of the density distribution are also the minima of f. A simple interpretation of f can be given in the limit of small atom numbers. For N atoms on a given pixel, we have

$$\begin{aligned} f^{(m)} &= \frac{P_{\mathrm{wo}}^{(m)}}{\langle P_{\mathrm{wo}} \rangle_m} - \frac{P_{\mathrm{wo}}^{(m)} - \zeta N^{(m)}}{\langle P_{\mathrm{wo}} \rangle_m - \zeta \langle N \rangle_m} \\ &\approx \zeta \frac{N^{(m)} - \langle N \rangle_m}{\langle P_{\mathrm{wo}} \rangle_m} \end{aligned} \tag{5.5}$$

if the fluctuations of the photon number can be neglected. Thus, f is directly proportional to the number of "missing atoms" on a pixel.

In the following, we define a minimum in the simplest possible manner: a pixel (i, j) is a minimum if $f^{(m)}(i, j)$ is inferior to its 8 nearest neighbors. Thus, we determine for each image the position of its local minima (i_p, j_p) and define their depth by

$$\delta = |f^{(m)}(i_p, j_p)|. \tag{5.6}$$

We then split each image in annuli centered on the cloud. The k-th annulus is delimited by its inner (resp. outer) radius R_{k-1} (resp. R_k), with $R_k = 2 + 5 \cdot k$ μm (these radii are shown in Fig. 5.2). For a given minimum, we record which annulus it belongs to.

Finally, we define the cumulative distribution of minima $F(\delta, k)$, which gives the fraction of pixels with depth inferior to δ, belonging to the k-th annulus. We show this function in Fig. 5.3, both for an *in-situ* image and for a 3 ms ToF.

Note that the photonic shot-noise can induce spurious local minima, which will also be detected by this method, and must be distinguished from the minima of interest. To discriminate between the two effects, we can repeat the search for minima on the quantity

$$f'^{(m)} = \frac{P_{\mathrm{wo}}^{(m)}}{\langle P_{\mathrm{wo}} \rangle_m} - \frac{P'^{(m)}_{\mathrm{wo}}}{\langle P'_{\mathrm{wo}} \rangle_m} \tag{5.7}$$

where the image $P'^{(m)}_{\mathrm{wo}}$ is recorded right after $P_{\mathrm{wo}}^{(m)}$, also in the absence of atoms. In that way, the minima of $f'^{(m)}$ characterize the photonic shot-noise. The cor-

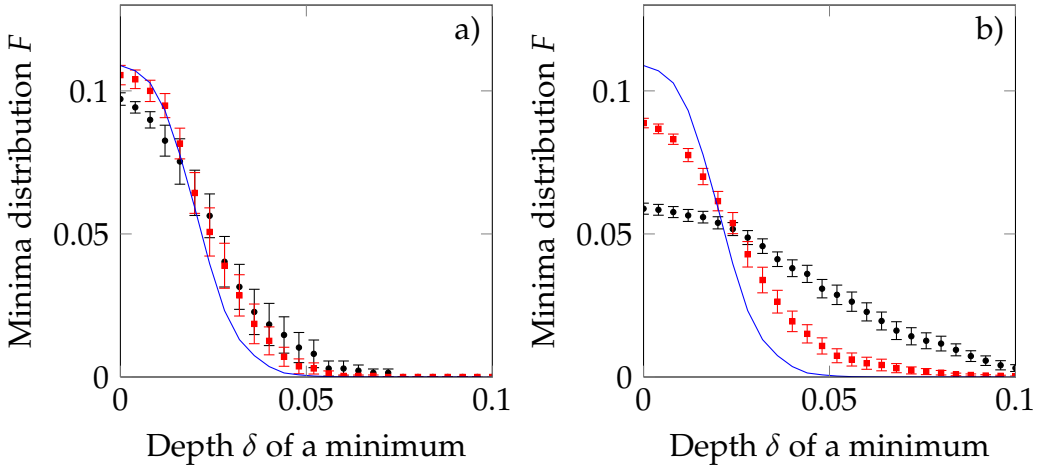

Figure 5.3.: Distribution function for the minima, for *in-situ* images (a) and after a 3 ms ToF (b). We show here two annuli: the minima for $0 \leq r \leq 10$ μm are shown in black circles, while the minima for 17 μm $\leq r \leq$ 22 μm are shown in red squares. The distribution F' for a shot-noise dominated distribution is shown in blue line. The error bars on F show the statistical error resulting from the averaging over different images. The statistical error in the determination of F' is negligible compared to the error in the determination of F, and is not shown here.

responding distributions F' are built in the same manner as above, and are also shown in Fig. 5.3.

5.2.2. Quantifying the distribution of minima

From Fig. 5.3, we note that $F'(0,k) > F(0,k)$ both for *in-situ* images and after ToF: there are more minima of infinitesimal depth with photon shot-noise than in the presence of atoms. This is attributed to the spatial extension of the density minima: a depletion of the atomic density extends over several pixels, preventing the appearance of another local minimum in the vicinity. By contrast, the photon shot-noise is uncorrelated between different pixels, and each individual pixel has a probability equal to $1/9$ of being a local minimum of infinitesimal depth.

Furthermore, the typical depth of a minimum appears to be much larger in the presence of atoms than with only photonic shot noise. To further character-

ize this, we calculate the mean depth

$$\bar{\delta}(k) = \int \left(\mathcal{P}(\delta,k) - \mathcal{P}'(\delta,k)\right)\, \delta \,\mathrm{d}\delta = \frac{\int F(\delta,k)\mathrm{d}\delta}{F(0,k)} - \frac{\int F'(\delta,k)\mathrm{d}\delta}{F'(0,k)} \tag{5.8}$$

where

$$\mathcal{P}(\delta,k) = -\frac{\partial F(\delta,k)/\partial\delta}{F(0,k)} \tag{5.9}$$

is the normalized probability distribution that a minimum in annulus k has a depth δ (and similarly for $\mathcal{P}', F'$). Note that we removed the contribution from the shot-noise induced minima in Eq. 5.8, in order to properly quantify the density fluctuations.

Note as well that the depth δ directly quantifies the number of missing atoms. Thus, we cannot readily compare two minima occurring in regions of different average intensity. For this reason, we define the contrast of a minimum by

$$\mathcal{C}(k) = \frac{\bar{\delta}(k)}{\delta_M(k)}. \tag{5.10}$$

where $\delta_M(k)$ is the maximal depth of a minimum in annulus k (no atoms detected). It is given by

$$\begin{aligned}\delta_M(r_k) &= \left\langle \frac{P_{\mathrm{wo}}^{(m)}(r)}{\langle P_{\mathrm{wi}}\rangle_m} - \frac{P_{\mathrm{wo}}^{(m)}(r)}{\langle P_{\mathrm{wo}}\rangle_m} \right\rangle_{k,m} \\ &= \frac{\langle P_{\mathrm{wo}}\rangle_{k,m} - \langle P_{\mathrm{wi}}\rangle_{k,m}}{\langle P_{\mathrm{wi}}\rangle_{k,m}}\end{aligned} \tag{5.11}$$

where the average rests both on the different images, and over the pixels contained in the k-th annulus. With this definition, $\mathcal{C} = 1$ if all the detected minima correspond to a full depletion of the atomic density. We show in Fig. 5.4 the evolution of $\mathcal{C}(k)$, both *in-situ* and after a ToF against R_k.

5.2.3. Qualitative interpretation

From Fig. 5.4, it appears that the contrast of the density minima is approximately multiplied by two between the *in-situ* images and the ToF data. This supports the presence of phase fluctuations in the *in-situ* atomic distribution, which are converted to density fluctuations by our short ToF.

Moreover, for the ToF data, the contrast of the minima increases with the

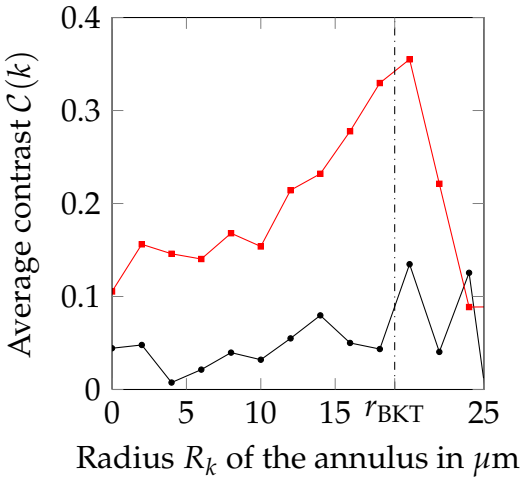

Figure 5.4.: Average contrast of the minima (see Eq. 5.10 for the definition), for an *in-situ* distribution (black circles), and for a 3 ms ToF (red squares).

radius, and is maximal around r_{BKT}, where the phase-space density is on the order of $\mathcal{D}_c$, and where the BKT transition is expected to take place.

However, these two observations are not sufficient to identify these minima with the microscopic vortices predicted by the BKT mechanism. Indeed, we can perform a similar analysis to the one presented above, but this time on the density maxima. We present in Fig. 5.5 the resulting distribution function, along with the previous results for the minima. The two distributions are identical, within the limits of the statistical error. Consequently, it is difficult to conclude with certainty that vortices are responsible for the observed density fluctuations. Indeed, at least in a simple picture, a vortex forms a sharp density hole in an otherwise flat density profile. In this limit, the symmetry between minima and maxima of the density distribution is explicitly broken, contrarily to what we observe.

Furthermore, a previous theoretical work by Giorgetti and colleagues [131] showed that the free vortices are completely absent in the strongly degenerate region (see Fig. 5.2): we only expect ~ 1 vortex for $\sim 10^5$ atoms. In a subsequent analysis, Foster and colleagues [132] calculated that the pairs of vortices are also strongly suppressed in this region: we expect at most ~ 1 pair for 10^4 atoms.

Consequently, it seems unlikely that all the fluctuations observed for $\mathcal{D} \geq 2\mathcal{D}_c$ are due to vortices, and it is more probable that they are dominated by phonons. Note that a recent experiment by Choi and colleagues [133] revealed the existence of loosely bound vortex pairs in the critical region, through similar techniques. In this experiment, the suppression of phononic excitations followed

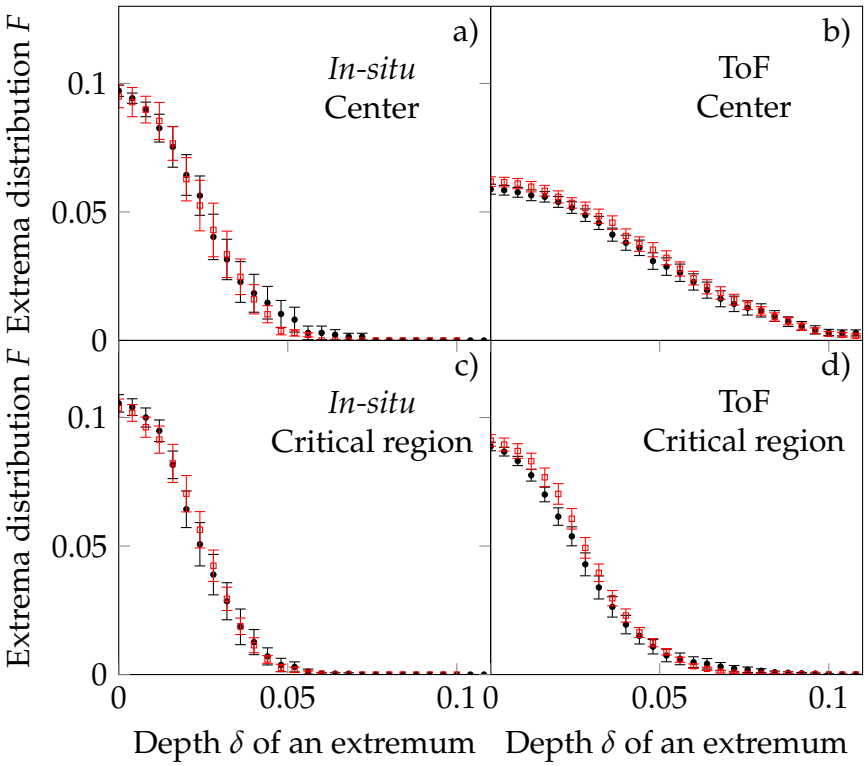

Figure 5.5.: Distribution function for the minima and maxima, for *in-situ* images (a) and (c) and after a 3 ms ToF (b) and (d). We show here two annuli: data for $0 \leq r \leq 10$ μm is shown in (a) and (b), and data for 17 μm $\leq r \leq 12$ μm is shown in (c) and (d). The minima are shown in black circles, and the maxima are shown in red squares.

by a ToF similar to ours revealed vortices in the critical region, while no vortices were observed in the degenerate part of the cloud. Thus, vortices also contribute to the minima shown in Fig. 5.3, but their contribution is probably hidden in the stronger phonon signal.

5.3. Density correlation function

In addition to the study of the distribution of local features such as the extrema of the density, one can also construct the *two-body* correlation function

$$g^{(2)}(\mathbf{r}, \mathbf{r}+\mathbf{r}', t) = \frac{\langle n(\mathbf{r}, t)\, n(\mathbf{r}+\mathbf{r}', t)\rangle}{\langle n(\mathbf{r}, t)\rangle \langle n(\mathbf{r}+\mathbf{r}', t)\rangle} \tag{5.12}$$

where $\langle \cdot \rangle$ denotes an ensemble average, which will be defined later.

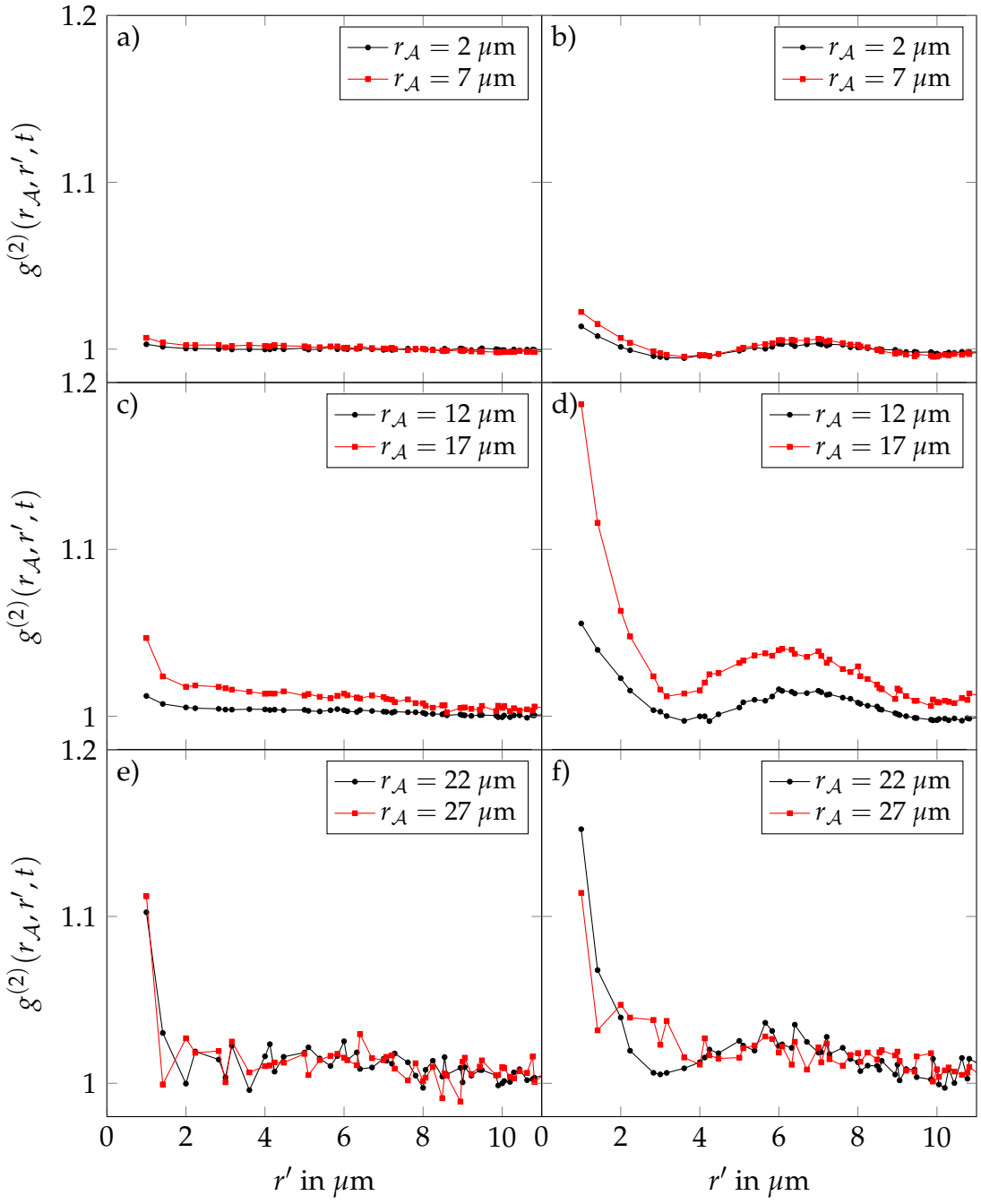

Figure 5.6.: Two-body correlation function $g^{(2)}(r_\mathcal{A}, r', t)$, for *in-situ* images (a,c,e) and a 3 ms ToF (b,d,f). The correlation function is calculated for varying $r_\mathcal{A}$.

5.3.1. Correlation in real space

Experimentally, we can only access the density of inhomogeneous systems. Note that this renders irrelevant the study of density correlations for distances r' comparable to the size of the cloud. In practice, we will limit ourselves to $r' < 10\ \mu$m. However, we can exploit the rotational symmetry of our samples to realize the averaging process. Thus, in our system, the *two-body* correlation function takes the form

$$g^{(2)}(r_{\mathcal{A}}, r', t) = \frac{\langle N(\mathbf{r}, t)\, N(\mathbf{r}+\mathbf{r}', t)\rangle_{\mathbf{r}\in\mathcal{A}}}{\langle N(\mathbf{r}, t)\rangle_{\mathbf{r}\in\mathcal{A}} \langle N(\mathbf{r}+\mathbf{r}', t)\rangle_{\mathbf{r}\in\mathcal{A}}} \tag{5.13}$$

where $\mathcal{A}$ denotes an annulus of typical radius $r_{\mathcal{A}}$. Note that the photonic shot-noise contributes to the value $g^{(2)}(r_{\mathcal{A}}, r' = 0, t)$, and should be accounted for. However, our signal-to-noise ratio was not sufficient to remove efficiently its contribution. For this reason, the value of $g^{(2)}(r_{\mathcal{A}}, r' = 0, t)$ will not be taken into account.

We show this correlation function in Fig. 5.6, both for *in-situ* and ToF images, for a few selected radii $r_{\mathcal{A}}$. The higher values taken by the $g^{(2)}$ function after ToF confirm the conversion of initial phase fluctuations into density fluctuations.

5.3.2. Correlations in reciprocal space

The oscillatory behavior of $g^{(2)}(r_{\mathcal{A}}, r', t)$ around 1 after ToF can be further studied by constructing its Fourier transform. We take advantage of the rotational symmetry of $g^{(2)}(r_{\mathcal{A}}, r', t)$, and subtract its asymptotic value to focus on the behavior of the Fourier transform at non-zero wavevectors. Thus, we define

$$\widetilde{g}^{(2)}(r_{\mathcal{A}}, q, t) = 2\pi \int \mathrm{d}r'\, r'\, J_0(r'\, q) \left(g^{(2)}(r_{\mathcal{A}}, r', t) - 1\right), \tag{5.14}$$

which is shown in Fig. 5.7, both for *in-situ* images, and after a ToF.

As expected, the *in-situ* correlation function $\widetilde{g}^{(2)}(r_{\mathcal{A}}, q, t = 0)$ does not show any marked structure. However, after a 3 ms ToF, a peak appears at $q \approx 1\ \mu\mathrm{m}^{-1}$ for all radii $r_{\mathcal{A}}$. Two additional peaks are also present at $q = 0.6\ \mu\mathrm{m}^{-1}$ and $q = 1.5\ \mu\mathrm{m}^{-1}$, for radii larger than 17 μm. The origin of these peaks can be qualitatively explained by the following argument, which is fully detailed in Annex B.

Let us consider a uniform system with average density n_0, subject to small

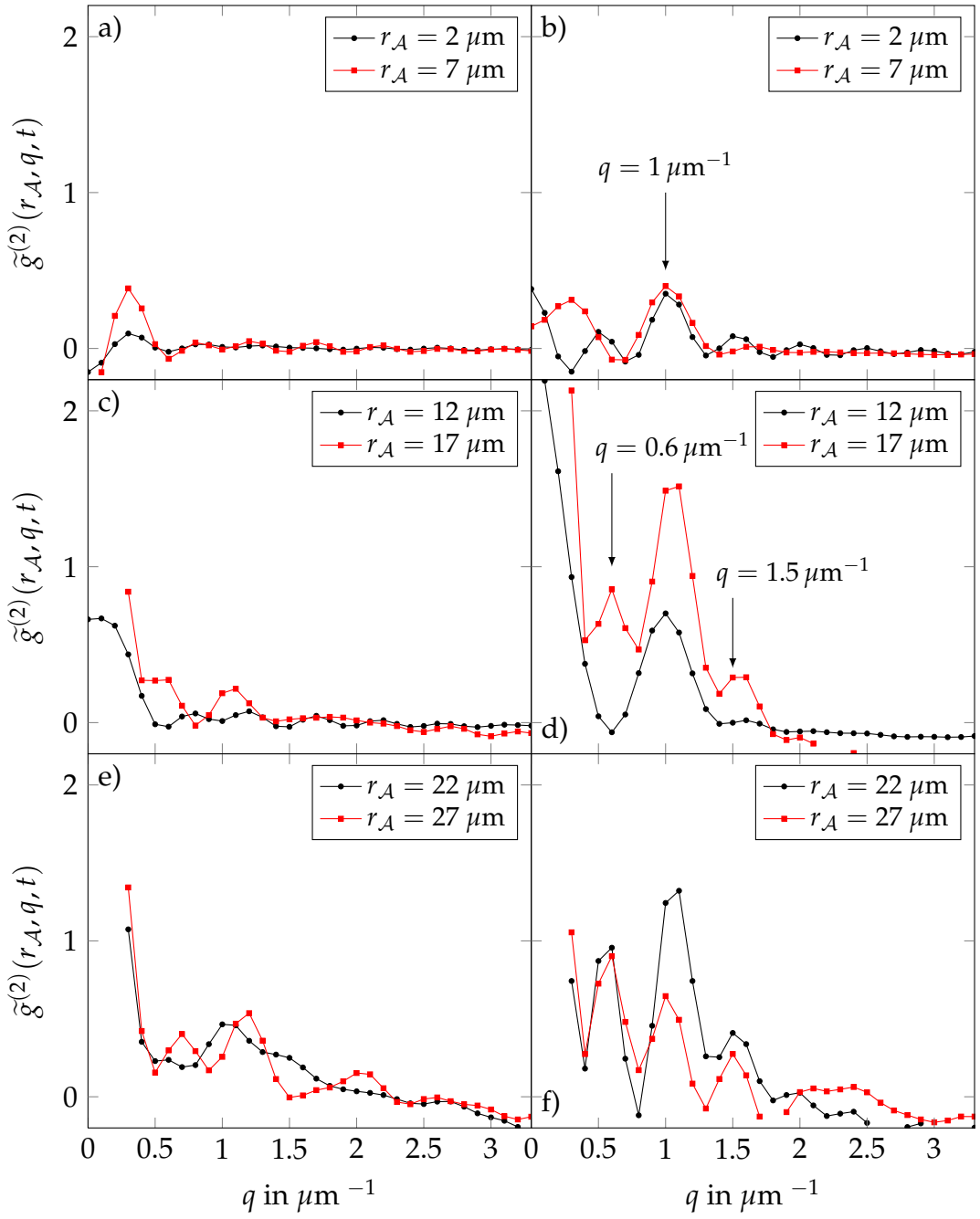

Figure 5.7.: Fourier transform of the correlation function presented in Fig. 5.6, calculated following Eq. 5.14, both for *in-situ* images (a), and for a 3 ms ToF (b).

density and phase fluctuations. The wavefuntion is therefore given by

$$\psi(\mathbf{r}, t=0) = \sqrt{n_0\,(1+\epsilon(\mathbf{r}))}e^{i\varphi(\mathbf{r})} \approx \sqrt{n_0}\left(1+\frac{\epsilon(\mathbf{r})}{2}+i\varphi(\mathbf{r})\right) \tag{5.15}$$

where ϵ (resp. φ) characterizes the density (resp. phase) fluctuations. We let this distribution evolve freely during a time t, as in our experiment. The Fourier transform $\widetilde{\rho}(\mathbf{q}, t)$ of the spatial density after this evolution is then given by

$$\widetilde{\rho}(\mathbf{q}, t) = \int \mathrm{d}^2 r e^{i\mathbf{q}\cdot\mathbf{r}}\,\psi^*(\mathbf{r}+\frac{\hbar t\mathbf{q}}{2m}, 0)\,\psi(\mathbf{r}-\frac{\hbar t\mathbf{q}}{2m}, 0). \tag{5.16}$$

In particular, the expectation value of $\widetilde{\rho}(\mathbf{q}, t)$ is directly related to the Fourier transform of the $g^{(1)}$ function. By injecting 5.15 into the expression for $\widetilde{\rho}(\mathbf{q}, t)$, we arrive at

$$\frac{\widetilde{\rho}(\mathbf{q}, t)}{n_0} \approx (2\pi)^2\,\delta(\mathbf{q}) + \cos\left(\frac{\hbar t q^2}{2m}\right)\,\widetilde{\epsilon}(q) + 2\sin\left(\frac{\hbar t q^2}{2m}\right)\,\widetilde{\varphi}(q). \tag{5.17}$$

where $\widetilde{\epsilon}$ and $\widetilde{\varphi}$ are the Fourier transforms of ϵ and φ. Finally, the Fourier transform of the $g^{(2)}$ function can simply be expressed as

$$\begin{aligned}\widetilde{g}^{(2)}(q, t) &= \int \mathrm{d}^2 r\, e^{i\mathbf{q}\cdot\mathbf{r}}\, g^{(2)}(r, t) \\ &= |\widetilde{\rho}(q, t)|^2 \\ &\approx \cos^2\left(\frac{\hbar t q^2}{2m}\right)\,(\widetilde{\epsilon}(q))^2 + 4\sin^2\left(\frac{\hbar t q^2}{2m}\right)\,(\widetilde{\varphi}(q))^2 + 2\,\widetilde{\epsilon}(q)\,\widetilde{\varphi}(q)\sin\left(2\frac{\hbar t q^2}{2m}\right)\end{aligned} \tag{5.18}$$

where the δ function was omitted. Thus, we expect the following behavior:

1. For a system dominated by phase fluctuations, the only contribution comes from the term in φ^2, and we expect a peak at $\hbar t q^2/(2m) = \pi/2$, which corresponds to $q = 1.2\ \mu\mathrm{m}^{-1}$. This constitutes the exact analog of the Talbot effect, where light passing through a phase grating exhibits an intensity modulation after some propagation length (see Appendix B for a more detailed discussion).

2. For a system which also contains density fluctuations, the terms in $\epsilon\cdot\varphi$ and ϵ^2 contribute as well, and we expect additional peaks at $\hbar t q^2/m = \pi/2$ and $\hbar t q^2/(2m) = \pi$, which respectively correspond to $q = 0.85\,\mu\mathrm{m}^{-1}$ and $q = 1.7\ \mu\mathrm{m}^{-1}$.

Thus, we qualitatively identify the peak at $q \approx 1\ \mu\text{m}^{-1}$ as resulting purely from phase fluctuations. Indeed, it appears for each radius, and begins to decay in the thermal region (see Fig. 5.2). By contrast, the peaks at $q = 0.6\ \mu\text{m}^{-1}$ and $q = 1.5\ \mu\text{m}^{-1}$ only appear in the critical and thermal regions, and they result from the contribution of the density fluctuations. The absence of these peaks for $\mathcal{D} \geq 16$ is in good agreement with the expected behavior of the two-dimensional Bose gas: the density fluctuations are strongly suppressed for $\mathcal{D} \gg 1$.

A more refined analysis of the strongly degenerate region was provided by Imambekov and colleagues [71], which accounted for the algebraic decay of the one-body correlation function. In particular, the first maximum of $\tilde{g}^{(2)}(r_{\mathcal{A}}, q, t)$ is predicted at $\hbar q^2 t/m \approx 2$, which is in good agreement with our observation $q = 1\ \mu\text{m}^{-1} \Rightarrow \hbar q^2 t/m = 2.2$. Thus, we confirm that the observed maximum is a direct manifestation of the phononic excitations in the two-dimensional Bose gas.

Furthermore, the same analysis showed that the height of this peak was directly related to η, where η is the exponent characterizing the decay of the one-

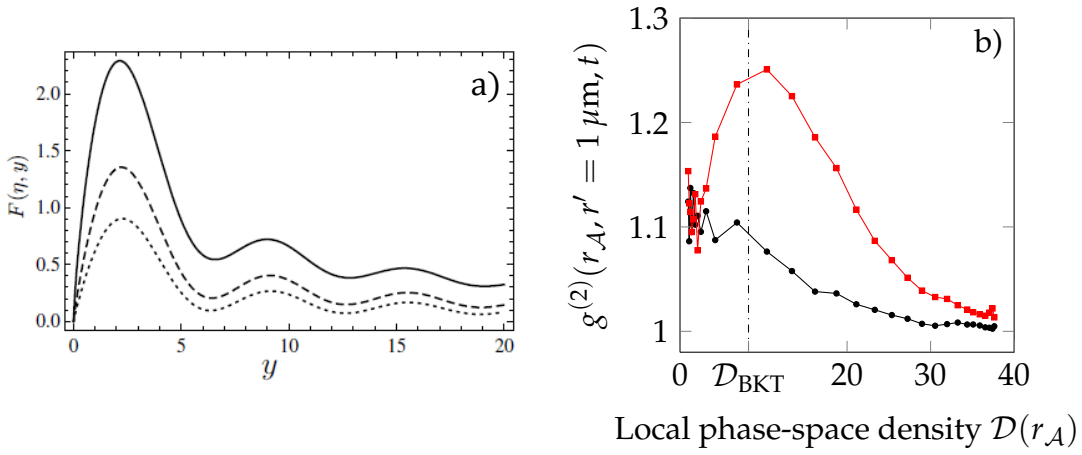

Figure 5.8.: (a) Figure taken from [71]. The function F is directly proportional to $\tilde{g}^{(2)}q, t)$, for an argument $y = \hbar q^2 t/m$. Curves from top to bottom correspond to $\eta = 0.25$ (solid, the Berezinskii-Kosterlitz-Thouless point), $\eta = 0.15$ (dashed), and $\eta = 0.10$ (dotted). (b) Two-body correlation function $g^{(2)}(r_{\mathcal{A}}, r' = 1\,\mu\text{m}, t = 3\,\text{ms})$, plotted against the local phase-space density, for *in-situ* images (black circles) and for a 3 ms ToF (red squares).

body correlation function in the strongly degenerate regime:

$$g^{(1)}(r) \propto \left(\frac{\xi}{r}\right)^{\eta} \qquad \text{for} \quad r \gg \xi \tag{5.19}$$

where ξ is the healing length. For a phase-space density $\mathcal{D} \gg \mathcal{D}_c$, we have $\eta = 1/\mathcal{D}$. We show in Fig. 5.8a the prediction from [71], for varying values of η. Though our signal-to-noise was not sufficient for a quantitative study, we feel that a similar information can be obtained from the value of $g^{(2)}(r_{\mathcal{A}}, r' = 0, t = 3\,\mathrm{ms})$. Indeed, this quantity is directly the integral of $\widetilde{g}^{(2)}(q,t)$ over all wavevectors, and it should therefore increase with increasing η, or equivalently with decreasing $\mathcal{D}$.

As we pointed out earlier, the photonic shot-noise introduces an uncertainty on the value of $g^{(2)}$ at the origin: consequently, we choose instead to look at $g^{(2)}(r_{\mathcal{A}}, r = 1\,\mu\mathrm{m}, t = 3\,\mathrm{ms})$. We show this quantity in Fig. 5.8b, plotted against the local phase space density $\mathcal{D}(r_{\mathcal{A}})$. As expected, this quantity increases for decreasing phase-space density, and reaches its maximum for $\mathcal{D} \approx \mathcal{D}_c$.

5.4. Concluding remarks

While this analysis remains a work in progress, we can make a few comments about our observations.

- The study of the extrema of density, both *in-situ* and after a ToF indicate that the dynamics of the degenerate two-dimensional Bose gas is dominated by phase fluctuations, while density fluctuations are essentially frozen. Furthermore, our analysis suggests that phonons are the primary fluctuation mechanism, at least in the degenerate region.
- This observation is consistent with the measurement of the Fourier transform of the two-body correlation function. Indeed, after a ToF, a peak appears in this distribution at a wavevector $q = 1\ \mu\mathrm{m}^{-1}$. This is in quantitative agreement with the analysis of [71], which was performed for a two-dimensional system dominated by phonons. Furthermore, the appearance of additional peaks for less degenerate regions at $q = 0.6\ \mu\mathrm{m}^{-1}$ and $q = 1.5\ \mu\mathrm{m}^{-1}$ is in qualitative agreement with an increase of density fluctuations in the thermal and critical regions.

6. The uniform two-dimensional Bose gas

In the introduction of the two-dimensional Bose gas in Ch. 1, we presented two phase transitions leading to a superfluid state. The BKT transition is *interaction–driven*, and the transition temperature is always non-zero. By contrast, the BEC transition is *statistics–driven*, and owing to the Mermin–Wagner theorem, it can only take place at zero temperature in the thermodynamic limit. However, in two dimensions, this limit is reached for exponentially large systems, which can never be achieved for realistic experimental parameters. For this reason, a *statistics–driven* transition to a BEC can exist at non-zero temperatures in a trapped system.

In an interacting system of finite size, these two mechanisms coexist, leading in principle to two separate phase transitions. Moreover, the comparison between the two transitions is further complicated in a spatially varying trapping potential. Indeed, the criterion for the existence of a BEC is global, and rests on the total atom number: it is associated with the saturation of the excited sates. In contrast, the presence of the BKT transition is dictated by a local condition: the phase–space density at the potential minima must be higher than the critical phase–space density (see Eq. 1.27).

The two transitions can be more readily compared by studying a system in a box-like potential. Let us consider such a system at a fixed temperature. As the particle number is increased, one of the two transitions will happen first: either the phase-space density reaches the critical value for the BKT transition, or the excited states become saturated, leading to the formation of a BEC. The order in which these transition take place depends on the size of the box and on the temperature: in an infinite system, the BKT transition will occur first (since BEC does not occur at a finite temperature), while in a sufficiently small system, the excited levels will saturate first. Thus, for a suitable box size, one can hope to observe separately the effect of both transitions, depending on the temperature of the system.

While a true box-like potential is experimentally difficult to create, one can generate similar geometries. By holographic techniques, it is feasible to create potentials which follow a power law $V(r) = Ar^{\alpha}$. For α sufficiently large, such a potential resembles the desired box-like potential. Alternately, one can project

the shadow of a mask on the atoms, and create a suitable intensity distribution. In the following, we will refer to such a potential as a *stadium* potential, irrespective of the method used to create it.

In the first section of this chapter, we present a theoretical study of both the box-like potential, and of the stadium potential. In the second section, we compare different experimental methods used to produce this stadium potential.

6.1. A brief theoretical analysis

In the absence of interactions, the transition occurs when the population of the excited states saturates, as was presented in 1.1.2. The critical atom number can either be calculated numerically if the energy spectrum is known, or it can be calculated analytically with a semi-classical approach. In 1.1.2, we presented a numerical calculation of the critical atom number inside a box of surface $\mathcal{S}$, either square or circular. We found that the critical atom number was well described by

$$N_{\mathrm{BEC}} = \frac{\mathcal{S}}{\lambda_{\mathrm{T}}^2} \ln\left(\eta \frac{\mathcal{S}}{\lambda_{\mathrm{T}}^2}\right) \tag{6.1}$$

where $\eta \approx 0.38$, with the precise value depending on the shape of the box. This equation can be rewritten in terms of the phase–space density

$$\mathcal{D}_{\mathrm{BEC}} = \ln\left(\eta \frac{\mathcal{S}}{\lambda_{\mathrm{T}}^2}\right). \tag{6.2}$$

This value can readily be compared to the critical phase–space density for the BKT transition $\mathcal{D}_{\mathrm{BKT}}$. We recall that $\mathcal{D}_{\mathrm{BKT}} = \ln(380/\tilde{g})$, where $\tilde{g}$ is the interaction parameter in two dimensions (see 1.2.4). Note that the critical phase–space density $\mathcal{D}_{\mathrm{BEC}}$ has been derived for the ideal gas: it is not sufficient to determine the location of the BEC transition in an interacting system. Though we cannot directly compare the two transitions in an interacting system with such an argument, this still leads to an interesting observation. For a given temperature, the system undergoes a phase transition at a lower atom number in the presence of interactions than in an ideal gas. In that sense, the interactions can facilitate the transition to a superfluid state in two dimensions.

However, since a true box-like potential cannot be created experimentally, we instead turn to the study of a realistic trap.

6.1.1. Ideal gas in a stadium potential

In this section, we take the trapping potential to be $V(r) = A\,r^\alpha$, with α a positive integer. This trapping potential allows us to define a characteristic length scale l_0 and a characteristic energy scale E_0 by

$$E_0 = A\,l_0^\alpha = \frac{\hbar^2}{2\,m\,l_0^2} \qquad \Rightarrow \qquad l_0 = \left(\frac{\hbar^2}{2m\,A}\right)^{\frac{1}{\alpha+2}} \text{ and } E_0 = \left(\frac{\hbar^2}{2m}\right)^{\frac{\alpha}{\alpha+2}} A^{\frac{2}{\alpha+2}} \tag{6.3}$$

This length scale (resp. energy scale) corresponds within a numerical factor of order unity to the typical size (resp. energy) of the ground state.

In the case of a harmonic potential, $A = m\,\omega^2/2$, $l_0 = \sqrt{\hbar/m\omega}$ and $E_0 = \hbar\omega/2$. For $\omega = 2\pi \times 20$ Hz, $l_0 = 2.39\ \mu$m and $E_0 = 470$ pK. Experimentally, we are able to create a trap with $\alpha = 12$ and $A = 100\,\text{nK}/(10\,\mu\text{m})^{12}$. In this case, we have $l_0 = 5.56\ \mu$m and $E_0 = 87$ pK.

Semi–classical approach We begin by calculating the density of states $\rho(E)$ in such a potential. In two dimensions, it is given by

$$\begin{aligned}\rho(E) &= \int \frac{r\mathrm{d}r\,p\mathrm{d}p}{\hbar^2}\delta\left(E - \frac{p^2}{2\,m} - E_0\left(\frac{r}{l_0}\right)^\alpha\right) \\ &= \frac{1}{4\,E_0}\left(\frac{E}{E_0}\right)^{\frac{2}{\alpha}}.\end{aligned} \tag{6.4}$$

This result is in agreement with two known cases: for a harmonic trap, the density of states varies linearly with the energy, and for a box-like potential ($\alpha \to \infty$), the density of states becomes constant. In the following, we will use the reduced temperature $\widetilde{T} = k_\mathrm{B}T/E_0$, and we calculate the critical atom number

$$\begin{aligned}N_{\mathrm{BEC,sc}} &= \frac{1}{4}\int_{\mathcal{C}}^{\infty} \frac{\mathrm{d}E/E_0\,\left(\frac{E}{E_0}\right)^{\frac{2}{\alpha}}}{\exp(E/k_\mathrm{B}T) - 1} \\ &= \frac{1}{4}\int_{\mathcal{C}}^{\infty} \frac{\mathrm{d}\epsilon\,\epsilon^{\frac{2}{\alpha}}}{\exp(\epsilon/\widetilde{T}) - 1} \\ &\approx \frac{1}{4}\zeta\left(\frac{\alpha+2}{\alpha}\right)\Gamma\left(\frac{\alpha+2}{\alpha}\right)\widetilde{T}^{\frac{\alpha+2}{\alpha}} - \frac{\alpha\,\widetilde{T}}{8}\mathcal{C}^{\frac{2}{\alpha}}\end{aligned} \tag{6.5}$$

where ζ is the Riemann zeta function, Γ is the gamma function, and $\mathcal{C}$ is a constant on the order of unity. For the harmonic trap and $\mathcal{C} = 0$, we recover the well known result $N_{\mathrm{BEC,sc}} = (\pi^2/6)\,(k_\mathrm{B}T/\hbar\omega)^2$. Note that the non-zero lower bound $\mathcal{C}$ in the integral is necessary for $\alpha > 2$. Indeed, though the integral always converges, its argument diverges in 0, and can lead to non-physical results.

Furthermore, reaching the thermodynamic limit in two dimensions typically require large system sizes. For this reason, we complement the semi–classical approach with a numerical determination of the energy spectrum.

Numerical resolution The energy spectrum is given by the solutions of the Schrödinger equation

$$-\frac{\hbar^2}{2\,m}\Delta\psi + A\,r^{12}\,\psi = E\psi \tag{6.6}$$

which we rewrite in dimensionless variables

$$-\Delta f + \rho^{12}\,f = \epsilon f \tag{6.7}$$

where $\rho = l/l_0$, $f(\rho,\theta) = l_0\,\psi(r,\theta)$, and $\epsilon = E/E_0$. A numerical resolution of Eq. 6.7 yields the eigenvalues ϵ_i, which in turn can be used to compute the maximal occupation of the excited states. In Fig. 6.1a, we show the density of states obtained by the numerical resolution, and compare it to the semi–classical result. In Fig. 6.1b, we show the critical atom number derived from the semi–classical approximation for $\mathcal{C} = 0$ and $\mathcal{C} = 1.97$ and from the numerical resolution.

In particular, it is clearly necessary to set $\mathcal{C} \neq 0$ in Eq. 6.5 to reach a quantitative agreement between the numerical and the semi–classical determinations. Consequently, the semi–classical limit in the true sense ($\mathcal{C} = 0$) only provides an imperfect description of the r^{12} potential in two dimensions.

6.1.2. Interacting gas in a stadium potential

Once the critical number of atoms needed to reach BEC in an ideal gas is known, we turn to the system in the presence of interactions. There, we can use the EoS of the 2D Bose gas to calculate the number of atoms needed to reach the BKT transition in the center of the trap. In [78, 79], the authors provide a numerical value for the critical phase–space density $\mathcal{D}_c = \ln(380/\tilde{g})$ and for the critical chemical potential $\mu_c = k_\mathrm{B}T\,\tilde{g}/\pi\ln(13.2/\tilde{g})$ at the BKT transition. We can then use the Local Density Approximation (LDA) and the scale invariance

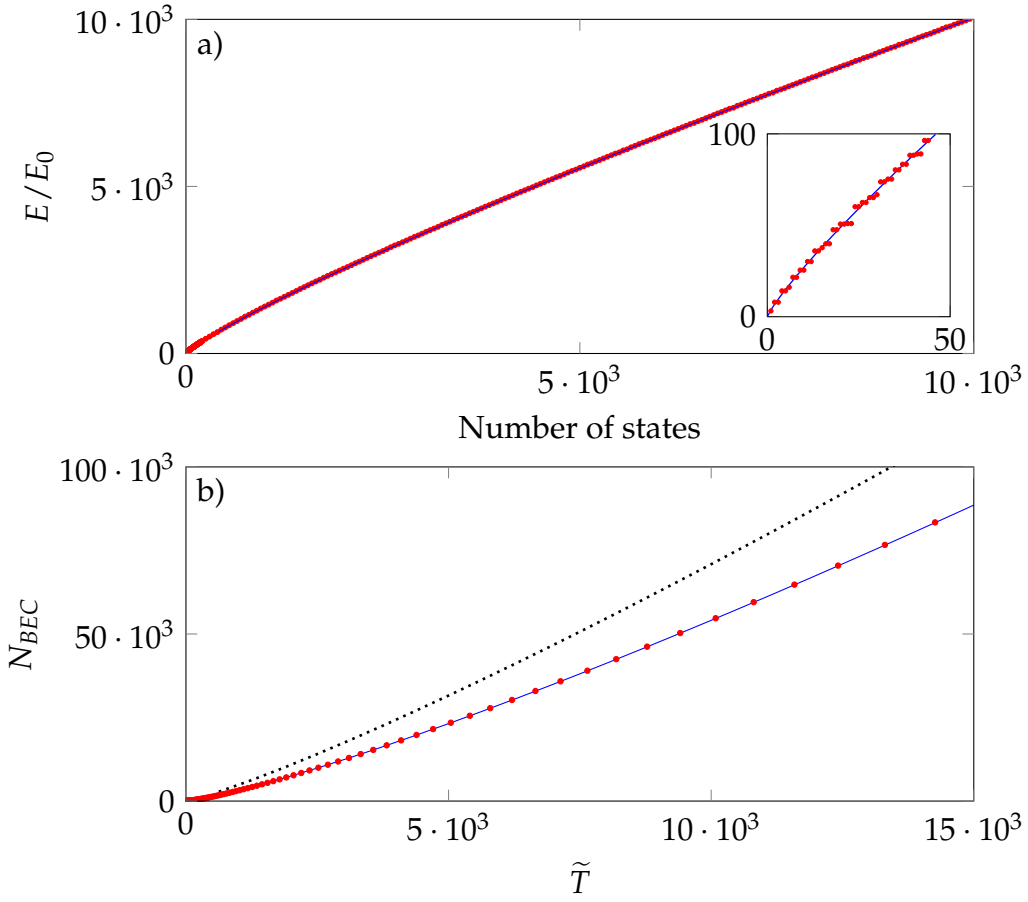

Figure 6.1.: (a) Energy spectrum of the r^{12} potential. The semi–classical approach is shown in blue line, and the numerical resolution of the Schrödinger equation is shown in dashed red line. The inset of Fig. (a) specifically shows the first levels of the numerical resolution. (b) Atom number needed to reach the BEC transition, determined semi–classically (see Eq. 6.5) with $\mathcal{C} = 0$ (black dotted line) and $\mathcal{C} = 1.97$ (blue line). The numerical determination is indicated in red points.

of the two-dimensional Bose gas to calculate required the number of atoms for a temperature T and a central chemical potential μ_c

$$\begin{aligned} N_{\mathrm{BKT}} &= \int \mathcal{D}\left(\frac{\mu_c - A\, r^\alpha}{k_{\mathrm{B}} T}\right) \frac{m\, k_{\mathrm{B}} T}{2\pi\hbar^2} 2\pi\, r\, \mathrm{d}r \\ &= \frac{1}{4} \widetilde{T}^{\frac{\alpha+2}{\alpha}} \int \mathcal{D}\left(\frac{\mu_c}{k_{\mathrm{B}} T} - u^{\frac{\alpha}{2}}\right) \mathrm{d}u \end{aligned}$$

$$= \frac{N_{\mathrm{BEC,sc}}(\widetilde{T})}{\zeta\left(\frac{\alpha+2}{\alpha}\right)\Gamma\left(\frac{\alpha+2}{\alpha}\right)} \int \mathcal{D}\left(\frac{\mu_c}{k_B T} - u^{\frac{\alpha}{2}}\right) \mathrm{d}u. \tag{6.8}$$

Here, we use the prediction from [79] for $\mathcal{D}$ to compute the integral. We find this atom number to be proportional to the critical atom number needed to reach the BEC transition. The proportionality coefficient does not depend on the tem-

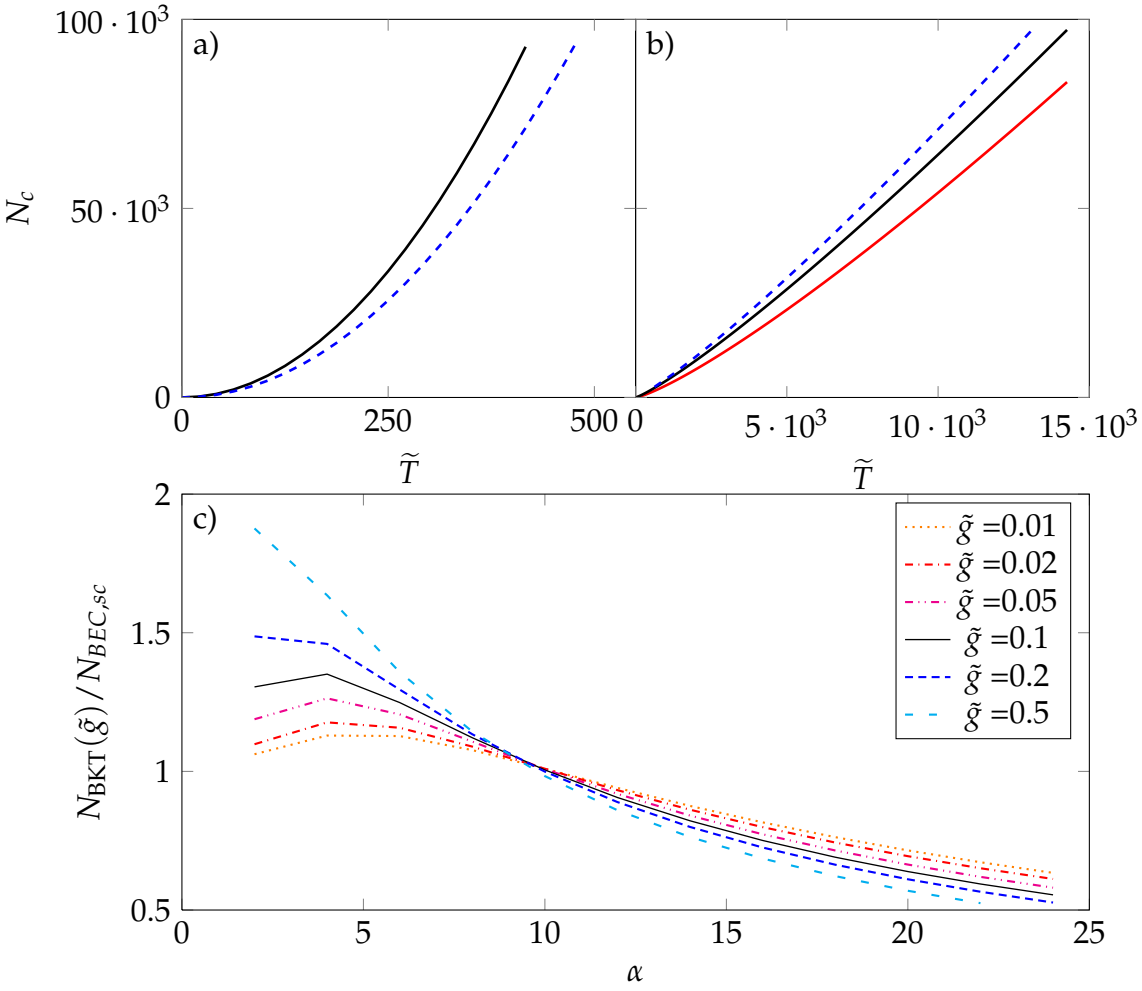

Figure 6.2.: Comparison of the atom number needed to reach either the BKT transition for $\tilde{g} = 0.1$ (black line) or the BEC transition in a harmonic trap (a), or in a power trap with $\alpha = 12$ (b). For the BEC transition, the semi–classical approach is shown in dashed blue line, while the numerical resolution of the Schrödinger equation for $\alpha = 12$ is shown in full red line. (c) Evolution of the ratio $N_{\mathrm{BKT}}(\tilde{g})/N_{BEC,sc}$ as a function of α for different interaction strengths.

perature, but only on the geometry (through the exponent α) and the interaction strength $\tilde{g}$. For the harmonic trap (see Fig. 6.2a), this number is always higher than the critical atom number needed to reach a BEC in an ideal gas. In the case of $\alpha = 12$, (see Fig. 6.2b), this number lies between the semi-classical result and the numerical estimation. Note that the EoS used to calculate this result already contains a semi-classical approximation: it is therefore probably more consistent to compare N_{BKT} to $N_{\mathrm{BEC,sc}}$. In this case, for a fixed temperature, the BKT transition is reached first when increasing the atom number.

We can also use Eq. 6.8 to find the minimal value of α for which $N_{\mathrm{BKT}} < N_{BEC,sc}$. In Fig. 6.2c, we plot the ratio $N_{\mathrm{BKT}}/N_{\mathrm{BEC,sc}}$ for different interaction strengths and different confinement. Oddly enough, the behaviour almost does not depend on the interaction strength: for $\alpha < 10$, the BEC transition occurs with less atoms than the BKT transition, while this property is reversed $\alpha > 10$. In particular, as was demonstrated in [74], the BEC transition always occurs first in a harmonic trap, irrespective of the interaction strength.

6.1.3. Experimental perspectives

One must be careful when interpreting the previous results. Indeed, these arguments are not sufficient to determine when the BEC transition takes place in an interacting system in general. Note though that the BKT transition is always accompanied by the appearance of a significant condensed fraction in a finite system of realistic size (see [74]). Indeed, the algebraic decay of the $g^{(1)}$ function in the superfluid phase leads is sufficiently slow for this function to retain a significant value over the whole system. With this in mind, let us propose an experiment to reveal the nature of the phase transition.

Let us suppose that we are able to consistently prepare a two-dimensional Bose gas with interaction strength $\tilde{g}$, either in a harmonic trapping potential, or in a stadium potential. The system is prepared such that its temperature is fixed, and that it contains just N_{BKT} atoms. As we pointed out earlier, the BKT transition necessarily implies the presence of a finite condensed fraction, which can be revealed by measuring the momentum distribution of the system. Let us now suppose that we are able to remove the interactions, or at least significantly reduce them. [1] In the harmonic trap, N_{BKT} is always larger than $N_{\mathrm{BEC,sc}}$. Consequently, even without interactions, the system should still contain a significant condensed fraction. By contrast, N_{BKT} is always smaller than $N_{\mathrm{BEC,sc}}$ in a sta-

1. The interaction strength in two dimensions can either be reduced by the use of a Feshbach resonance, or by reducing the confinement strength along the tightly confined direction (see Eq. 1.19).

dium trap. Thus, in the absence of interactions, the condensed fraction should vanish. In this gedanken experiment, the condensed fraction in the harmonic trap is *statistics*-induced, at least for weak interactions or in the ideal case, while the condensed fraction in the stadium trap is *interactions*-induced.

6.2. Experimental realization: preliminary studies

Our aim is to create a *stadium* potential, which must fulfill two conditions: the potential must be flat in a large region of space, and the "walls" of the potential must be steep enough. We already saw in section 2.1.3 that steep potentials can be created through the use of phase plates. Alternately, we can consider a simpler solution: we directly form the image of a mask on the atoms, to create a region with a flat potential. We will present both methods in the following, along with preliminary observations.

6.2.1. Creating a box-like potential: a holographic method

Principle A suitable trapping potential can be created similarly to the Hermite–Gauss beam, by a holographic method (see 2.1.3). To this end, we shine a collimated beam on a phase plate, then focus it on the atoms with a lens (see Fig. 6.3b). The phase plate imprints a six-fold vortex: a phase winding from 0 to 12π when completing a revolution around the plate (see Fig. 6.3a). Thus, in the

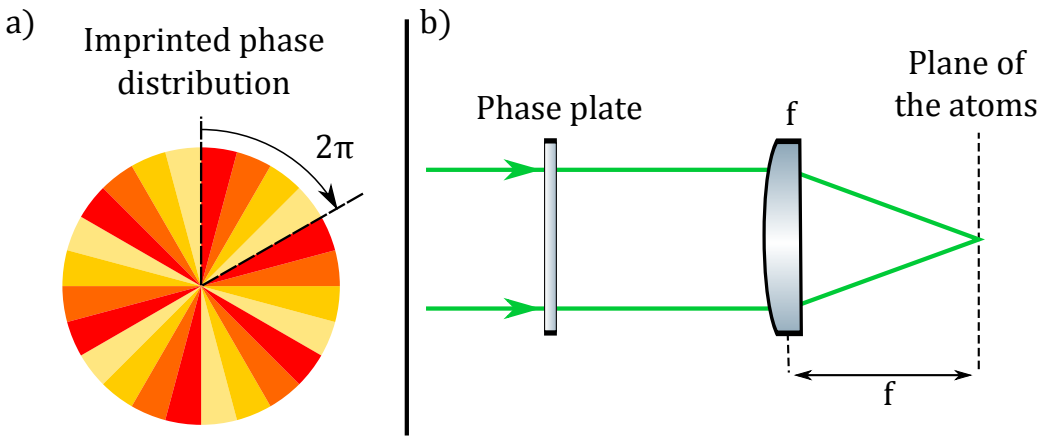

Figure 6.3.: (a) Six-fold phase vortex imprinted by the phase plate. Though only four phase sectors per 2π step are represented, our phase plates have 16 sectors per 2π step. (b) Experimental setup required to create a stadium with a phase plate.

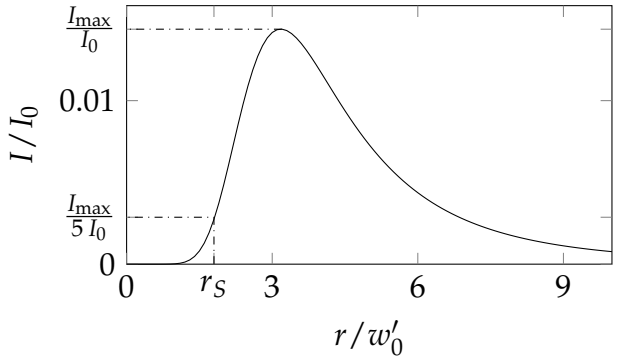

Figure 6.4.: Intensity distribution for a phase plate with a 12π phase winding. Here, I_0 is the intensity in the center of the beam without the phase plate.

paraxial approximation, the electric field at the location of the atoms is given by

$$E(\rho,\phi) = \int r\mathrm{d}r\mathrm{d}\theta E_0(r,\theta)\, e^{i\,6\theta} e^{i\,\frac{k}{f} r\,\rho\,\cos(\theta-\phi)} \tag{6.9}$$

where E_0 is the electric field distribution at the location of the phase plate, $k = 2\pi/\lambda$ with λ the wavelength the laser beam, f is the focal length of the lens, and ρ the polar coordinate at the location of the atoms. For a gaussian beam, this integral can be fully evaluated. Around the origin, and at the lowest order, it can be approximated by

$$E(\rho\to 0,\phi) = \frac{-1}{120}\sqrt{\frac{2\,P}{\pi w_0'^2}} e^{i\,6\phi} \left(\frac{\rho}{w_0'^2}\right)^6 \tag{6.10}$$

where P is the total power, and w_0' is the waist at the focus of the lens. It is related to the waist on the phase plate by the usual relation $\pi\, w_0\, w_0' = \lambda\, f$. We show in Fig. 6.4 the intensity profile generated with such a phase plate. The intensity maximum is approximately $I_{\max} \approx 0.01 \times 2P/(\pi w_0'^2)$. We define the radius of the stadium r_S as

$$I(r_S) = I_{\max}/5 \qquad \Rightarrow \qquad r_S = 1.8\, w_0'. \tag{6.11}$$

When such an intensity distribution is created by a blue-detuned laser, the trapping potential inside the beam then scales as r^{12}, which is well suited to study the connection between BEC and BKT transition presented above.

Our experiments will be performed on atomic samples at $T \sim 200$ nK: the barrier height must therefore be at least 1 μK to prevent evaporation. The trap

size is chosen to optimize the transfer from the hybrid trap (see 2.1.2) to this stadium potential. At the end of the evaporation sequence, the radius of the cloud is $\sim$ 10 μm, which must match the stadium size r_S. Consequently, the waist of the beam at the location of the atoms must be $w_0' = 5.5\,\mu$m (see Fig. 6.4). The trapping potential is given by $U(r) = \alpha\, I(r)$ where $\alpha = 6.5 \cdot 10^{-8}\,\mu K\,\mathrm{m}^2/\mathrm{W}$ for the dipole trap wavelength ($\lambda = 532$ nm). For a stadium of radius r_S, the barrier height is

$$U_{max} \approx \frac{1}{100}\frac{\alpha 2 P_S}{\pi (r_S/2)^2}. \tag{6.12}$$

Therefore, the laser power must be at least 60 mW to obtain $U_{max} \geq 1\ \mu$K. For a trap depth of 1 μK, the characteristic length and energy defined in Eq. 6.3 are respectively $l_0 = 3.8\ \mu$m and $E_0 = 180$ pK.

First results The preliminary tests were carried out by imaging the intensity distribution in the focus of the beams, at the location of the atoms. The measured intensity distribution is presented in Fig. 6.5a, along with its radial average in Fig. 6.5b. The observations are in qualitative agreement with the predicted profile: the potential is quite flat in the center of the beam, and is surrounded by steep edges. We can determine the steepness of the barrier by fitting the center of the profile ($r < r_S$) by

$$f_{\text{fit}} = I_0 + B\, r^{\beta} \tag{6.13}$$

and we find $\beta = 8$, instead of 12 as expected. Even though the potential is not as steep as expected, this high exponent should still be sufficient to show clear deviations in the behaviour of the two-dimensional Bose gas, with respect to a harmonic trap.

However, a closer inspection of the intensity distribution in the center of the trap reveals some irregularities. Indeed, as presented in Fig. 6.6a, the intensity in the center of the beam is not strictly zero. Instead, we reveal the presence of six intensity minima. This can be understood if we consider the phase plate as imprinting six individual phase vortices, instead of a single six-fold vortex. For an ideal phase plate, the center of each of the vortices coincide, and are equivalent to the expected six-fold vortex. However, if the center of the vortices are offset from one another, the total phase distribution is only equivalent to a six-fold vortex in the wings of the intensity distribution. Close to the center, the irregularities in the intensity distribution are directly linked to this imperfection in the phase plate.

These irregularities constitute a serious obstacle in the realization of a sta-

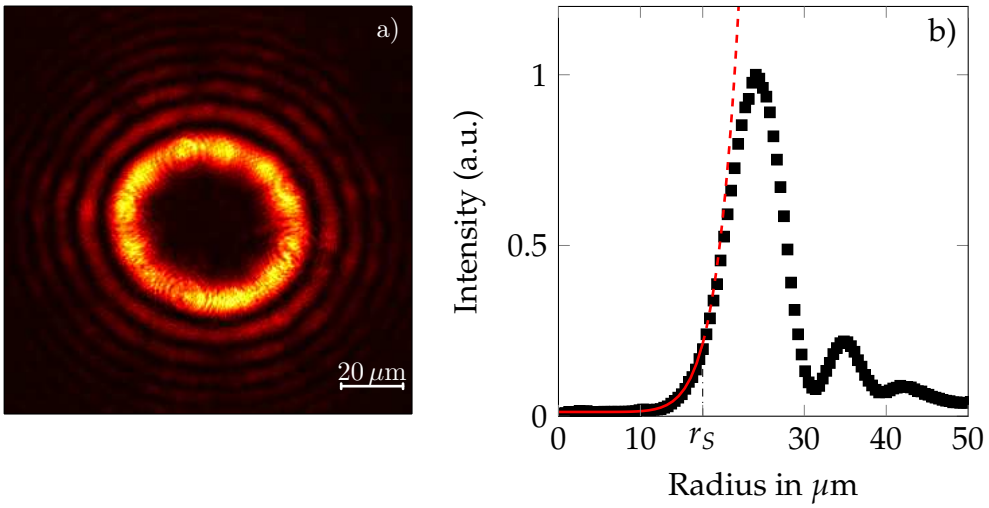

Figure 6.5.: (a) Intensity distribution created by a phase plate with a 12π winding. (b) Radial average of the intensity distribution (black line), along with a fit of the central region with the fitting function from Eq. 6.13 (red line). The fit is performed for $r \leq r_S$ (see Eq. 6.11), and the fitted power is 7.3, instead of 12 as expected from Eq. 6.10.

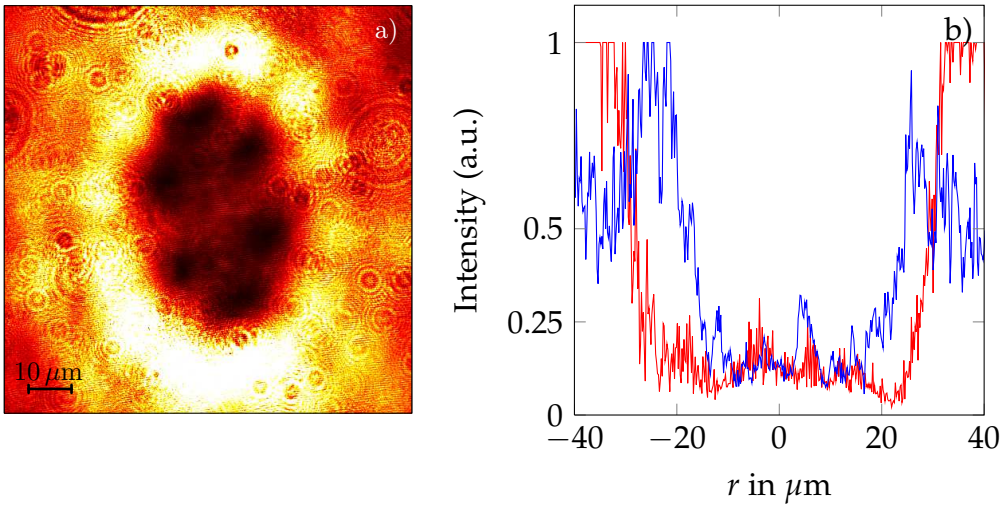

Figure 6.6.: (a) Intensity distribution created by a phase plate. The intensity has been rescaled to reveal the features in the center of the beam. (b) Two cuts of the intensity distribution shown in (a).

dium potential. Indeed, if we want to realize a uniform gas, the variations of the confining potential in the center of the trap must be small compared to the

chemical potential of the gas.

In the degenerate regime of interest to us, the chemical potential is itself smaller than the temperature. Indeed, at the BKT transition, we have $\mu_C = 0.15\, k_B T$ for $\tilde{g} = 0.1$. Due to the evaporation in this trap, the temperature itself must be small compared to the barrier height: usually, $U_{max} = 10\, k_B T$. By combining all these constraints, we find that the potential fluctuations must satisfy

$$\delta U \leq 0.015\, U_{max} \tag{6.14}$$

where δU characterizes the amplitude of the fluctuations.

For the potential shown in Fig. 6.6b, the barrier height is $U_{max} \approx 0.7$, while the standard deviation of the intensity in the center is $\delta U = 0.05$, which does not satisfy Eq. 6.14. For this reason, we present in the following section an alternative method to produce a uniform confinement.

6.2.2. Creating a box-like potential: by forming the image of a mask

Principle One can place a circular mask in the center of a blue-detuned laser beam, and form its image on the atoms, much in the way we generated the cleaning beam (see section 2.1.3). In this case, both the steepness of the barrier and the flatness of the bottom of the potential will be determined by the numerical aperture of the imaging system. Let us consider the following imaging setup (see Fig. 6.7): a single lens, of finite radius $\mathcal{R}$ creates the image of the

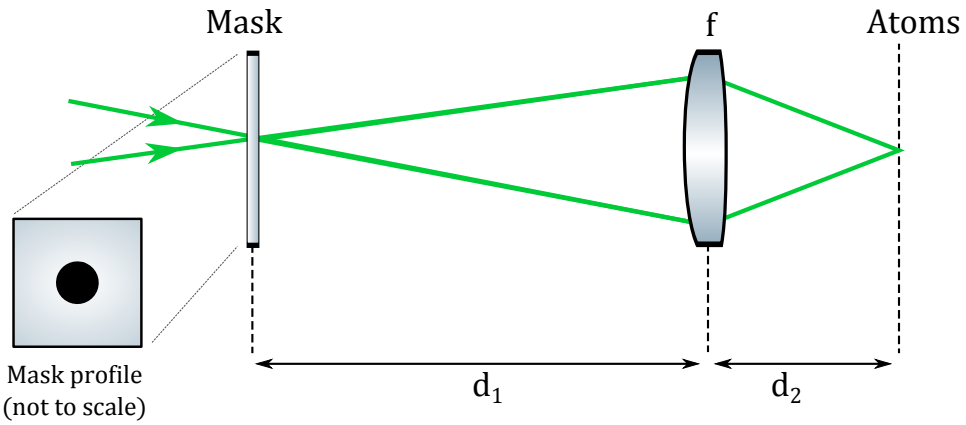

Figure 6.7.: Optical setup for the creation of a stadium potential, by projecting the image of a mask on the atoms. The distances are such that the plane of the mask and the plane of the atoms are conjugate.

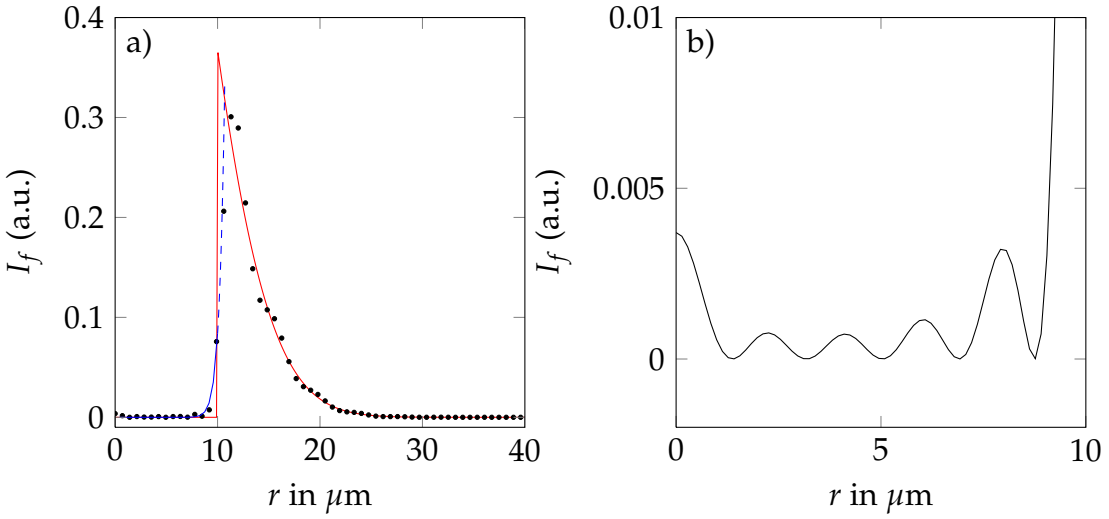

Figure 6.8.: (a) Intensity profile in the object plane (red line) and in the image plane (black points) calculated in the paraxial approximation. The fit of a power law, following Eq. 6.13 is shown in blue line, and the fitted exponent is 20. (b) Detailed view of the bottom of the stadium potential. The intensity fluctuations are due to the finite size of the imaging lens.

intensity distribution

$$I_i(r) = \frac{2P}{\pi w^2} e^{-2r^2/w^2}, \text{if } r > r_S \qquad \text{or} \qquad I_i(r) = 0, \text{if } r \leq r_s \tag{6.15}$$

where w is the waist of the laser at the position of the mask, P is the available laser power, and r_S is the radius of the mask. For a fixed laser power P, the intensity at the edge of the mask is maximal for $w = \sqrt{2}\, r_S$. Therefore, for a stadium of radius r_S, the trap depth is

$$U_{\max} = \frac{1}{e} \frac{\alpha\, 2\, P}{\pi\, (\sqrt{2} r_S)^2} \tag{6.16}$$

where P is the laser power, and $\alpha = 6.5 \cdot 10^{-8}\, \mu K \text{m}^2/\text{W}$. In particular, a stadium with $r_S = 10\ \mu$m and a trap depth of 1 μK requires 13 mW of laser power.

We aim to create a stadium of radius $r_S = 10\ \mu$m. Thus, the waist of the laser beam on the atoms must be $w = 14\ \mu$m. It is created by focusing a gaussian beam with an achromatic doublet of focal length $f = 150$ mm and radius $\mathcal{R} = 15$ mm. We show in Fig. 6.8 the intensity distribution in the image plane calculated in the paraxial approximation with such an imaging setup.

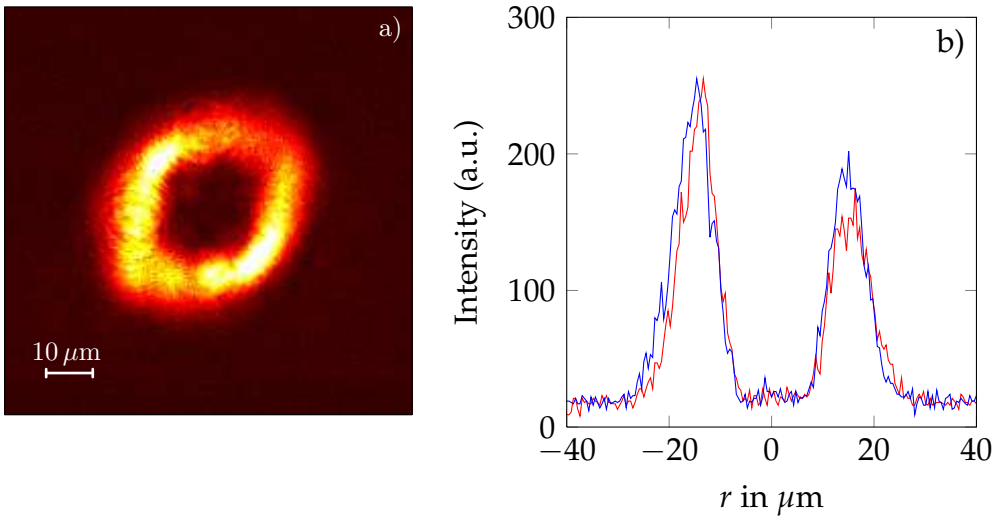

Figure 6.9.: (a) Intensity distribution realized by projecting the image of a mask of radius $r_M = 50$ μm, with a magnification $\mathcal{M} = 1/5$. (b) Two cuts of the image shown in (a).

From this calculation, it appears that this method is a valid way of creating a stadium potential. We summarize here its main features.

- In the center ($r < r_S$, with r_S), the intensity profile is well described by Eq. 6.13, and the intensity varies as r^{20} (see Fig. 6.8a).
- The intensity fluctuations caused by the finite resolution of the imaging system are as low as 1 % of the potential depth (see Fig. 6.8b).
- Achieving a trap depth of 1 μK requires comparatively less power than when using a phase plate (see Eqs. 6.12 and 6.16).

Preliminary results We present in Fig. 6.9a the first observations of the intensity distribution, following the optical setup detailed in Fig. 6.7. The mask is a circular spot, of radius $r_M = 50$ μm, created by optical lithography. Its image is projected on the atoms with a magnification $\mathcal{M} = 1/5$.

The observations are in qualitative agreement with the predicted profile: the potential is flat in the center of the beam, and is surrounded by steep edges. In particular, the standard deviation of the intensity in the center of the trap is $\delta U \approx 4.3$, which is comparable to the background noise of the measuring device, while the barrier height is $U_{\max} = 160$. Consequently, a stadium potential created in this manner should allow us to perform the experiment outlined in 6.1.3.

7. Single atom imaging scheme

As stated in the introduction, ultracold systems provide a versatile tool for the simulation of condensed matter phenomena, and the realization of many-body strongly correlated states. Of particular interest are the integer and the fractional quantum Hall effects (FQHE), which appear in two-dimensional systems exposed to a large transverse magnetic field, i.e. perpendicular to the plane in which the atoms move. Reaching such states rests on the formation of Landau levels, in which the interactions between atoms constitute the dominant energy scale. The FQH states arise when the atom number in the system is comparable to the number of magnetic flux quanta. For neutral atoms, such as ^{87}Rb , this requires the creation of an effective magnetic field. This can be achieved either by rotating the cloud (using the equivalence of the Lorentz and the Coriolis force) [134] or by generating artificial gauge fields with optical potentials [53, 54]. Both approaches have been demonstrated for a bulk fluid of bosonic atoms [16, 53], though the number of flux quanta generated in this manner remained small compared to the total atom number.

Consequently, an alternative path can be pursued: the number of atoms in the system can be instead tailored to match the number of flux quanta. In our experiment, we aim to prepare systems containing as few as three atoms, and at least three quanta of angular momentum. Even if the preparation of strongly correlated phases in this manner seems achievable, the detection of such phases requires a high performance imaging setup. In the case of such few-atoms systems, the most accessible and relevant observables are the two- and three-body correlation functions. Therefore, we need to be able to detect the positions of single atoms in order to form these correlations.

To this end, we chose to combine a deep optical lattice with an optical molasses: the lattice pins the atoms at fixed positions in space, while the molasses cools down the atoms. The fluorescence from the molasses is subsequently detected, and provides an image of the atomic distribution. This method was successfully used in the groups of D. Weiss [135] and D. Meschede [136] and more recently in the groups of M. Greiner [72, 137] and I. Bloch [73, 138] for lattices in the Bose–Hubbard regime.

In the first section, we present a model of this scheme, focusing first on the

molasses and then on the optical lattice. In particular, we discuss the choice of the operating parameters. In our case, the optical lattice will be used solely for the imaging system: our main concern will therefore be its depth, rather than the heating it induces. In the second section, we present the experimental realization, and the preliminary results obtained with this system.

7.1. Working principles

The single-atom detection scheme consists of a deep three-dimensional lattice, combined with a molasses operating on $|F = 2\rangle \rightarrow |F' = 3\rangle$. Since the molasses also weakly couples to the transition $|F = 2\rangle \rightarrow |F' = 2\rangle$, atoms can be depumped to the other hyperfine state $|F = 1\rangle$, and then remain undetected. For this reason, the atomic cloud is illuminated by a resonant repumping beam saturating the $|F = 1\rangle \rightarrow |F' = 2\rangle$ transition. In the rest of this section, we will assume that this beam is always present, and that it does not affect the problem in any other way.

7.1.1. Optical molasses

We chose to implement a $lin \perp lin$ molasses: this polarization configuration leads both to the lowest diffusion coefficient [139], and to the lowest temperature for a given laser power [140]. It was also found to be less sensitive to magnetic fields than a σ^+–σ^- configuration. The molasses consists of three orthogonal pairs of counter–propagating laser beams, with orthogonal linear polarizations within each pair. These beams are red-detuned with respect to the $|F = 2\rangle \rightarrow |F' = 3\rangle$ transition, with δ_M the detuning. The interaction between the electric field and the atoms is characterized by Ω, the Rabi frequency per running wave, and the natural linewidth of the transition is Γ.

In this section, we will briefly recall some characteristics of optical molasses, in order to provide a basis for the experimental implementation. The following theoretical results were derived for a simpler 1D molasses acting on a $|J = 1/2\rangle \rightarrow |J' = 3/2\rangle$ transition, and can be found in [141]. We will as well present a few experimental results for a 3D molasses.

Equilibrium temperature In the limit of large detunings $|\delta_M| \gg \Gamma$, the equilibrium temperature is given by

$$k_B T = \mathcal{C} \frac{\hbar \Omega^2}{\delta_M} \tag{7.1}$$

where $\mathcal{C}$ is a dimensionless constant. For a 1D molasses, the calculation from [141] yields $\mathcal{C} = 0.125$. In [140], Salomon and colleagues measured C $= 0.35$ in a 3D $lin \perp lin$ molasses.

Optical pumping time In a $lin \perp lin$ molasses, the existence of multiple ground-state sub-levels and of a long optical pumping time among the sub-levels is crucial to achieve sub-Doppler cooling. The pumping time is inversely proportional to the scattering rate

$$\tau_P = \frac{\mathcal{N}}{\gamma_M} \approx \mathcal{N} \frac{\delta_M^2}{\Omega^2} \frac{1}{\Gamma} \tag{7.2}$$

where $\mathcal{N}$ is a numerical constant characterizing the efficiency of the optical pumping process. Note that the precise value of this constant depends on the dimensionality, and on the choice of polarization. In a properly adjusted molasses, the pumping time is typically $\tau_P \sim 10\,\mu s$. In particular, the pumping time sets a lower bound for the other time scales of the problem. In the following, we give two examples of such limitations.

Capture velocity The velocity of the atoms in the molasses must be such that the distance covered during a pumping cycle is lower than the spatial period of the modulation of the light shift

$$v\,\tau_P \leq \lambda/4 \qquad \Rightarrow \qquad v \leq v_c = \frac{\lambda}{4\,\tau_P}. \tag{7.3}$$

where λ is the wavelength the atomic transition. Though Eq. 7.1 suggests lowering the laser power leads to arbitrarily low temperatures, this also lowers the capture velocity. Note that the term "capture velocity" is slightly misleading: it corresponds to the temperature range over which the friction force is linear in velocity, and the sub-Doppler mechanisms operate. In particular, atoms going faster than v_c will still be slowed down, though less efficiently.

Effect of magnetic fields In the previous discussion, we implicitly assumed the absence of magnetic fields. Let us relax this restriction, and consider an external magnetic field B. Even if it is not large enough to shift the energy levels of the atoms significantly compared to the AC Stark shift induced by the molasses, it will still couple its internal states together, and lead to Larmor precession. For large enough fields, the Larmor precession will compete with the optical pump-

ing phenomena, and interfere with the sub-Doppler cooling. For ^{87}Rb, the precession frequency is on the order of 1.4 MHz/G. Consequently, stray magnetic fields larger than 70 mG lead to Larmor precession rates comparable with the optical pumping rate, and degrade the efficiency of the sub-Doppler cooling [142]. In general, an external perturbation coupling the internal states of the atom can be neglected, provided that

$$\Delta_{\text{ext}} \ll \hbar\gamma_M \tag{7.4}$$

where Δ_{ext} is the coupling amplitude of the perturbation. In particular, we will evaluate in this manner the influence of the effective field generated by the optical lattice in the next section.

7.1.2. The pinning lattice

The purpose of the lattice is to pin the atoms at fixed positions in space. In order to efficiently suppress tunneling between sites, the depth of the lattice V_0 must be large compared to the temperature of the atoms. In our case, the temperature is fixed by the parameters of the molasses.

In general, choosing the best wavelength for an optical trap requires a trade off between the depth of the potential and the heating induced by spontaneous emission of photons from the beam. Here, this lattice is combined with an optical molasses, which cools down the atoms. Therefore, we can tolerate a moderate amount of heating by spontaneous emission. For a given amount of laser power, the depth of the lattice can be increased by choosing the frequency of the laser beams to be close to resonance.

In order to be able to control the lattice beams independently of the molasses beams, we choose to operate the lattice around the D_1 line ($\lambda = 795$ nm), and the molasses on the cycling transition in the D_2 line ($\lambda = 780$ nm). The different beams can therefore be combined or separated through dichroic optic elements.

7.1.2.1. Influence of the hyperfine structure of the excited states

One must be careful when choosing the parameters of the lattice beams: when the lattice detuning is comparable to the hyperfine splitting of the excited states, the hyperfine structure of the atomic transition cannot be neglected. In general, the dipole potential generated in this manner depends on the internal state of the atom, and couples the different the Zeeman sub-levels. If the precession rate resulting from this coupling is comparable to the optical pumping rate induced by the molasses beam, the Sisyphus mechanism will not operate anymore. To

estimate the magnitude of this effect, we consider in the following the interaction of a ^{87}Rb atom in the $|F = 2\rangle$ internal state with a linearly polarized laser beams of intensity I_0, and of angular frequency ω. We take the polarization to be along the quantization axis, which we call z. Since the laser is operated close to the D_1 line, the ground state can couple to the two hyperfine excited states $|F' = 1\rangle$ and $|F' = 2\rangle$. We write $\omega_{2\to 1'}$ (resp. $\omega_{2\to 2'}$) the angular frequency associated with the transition $|F = 2\,\rangle \to |F' = 1\,\rangle$ (resp. $|F = 2\,\rangle \to |F' = 2\,\rangle$) excited hyperfine state, and $\overline{\omega_2} = (\omega_{2\to 1'} + \omega_{2\to 2'})/2$ their mean. Using the appropriate Clebsch–Gordan coefficients, we find the resulting dipole potential

$$\widehat{V} = \frac{3\pi c^2 \Gamma}{2\overline{\omega_2}^3} I_0 \left(\frac{1}{\omega - \omega_{2\to 2'}} \frac{\widehat{F}_z^2}{12} + \frac{1}{\omega - \omega_{2\to 1'}} \frac{4 - \widehat{F}_z^2}{12} \right) \tag{7.5}$$

where c is the speed of light, Γ is the decay rate from the excited levels and $\widehat{F}_z$ is the projection of the angular momentum operator along the quantization axis. This equation can be linearized in the limit of large laser detuning:

$$\widehat{V} = V_s \left(1 + \frac{\delta_{hf}^{(e)}}{\delta_L} \frac{\widehat{F}_z^2 - 2}{4} \right) \qquad \text{with} \qquad V_s = \frac{\pi c^2 \Gamma}{2\overline{\omega_2}^3 \, \delta_L} I_0 \tag{7.6}$$

where $\delta_L = \omega - \overline{\omega_2}$ is the detuning of the lattice for the considered line, and $\delta_{hf}^{(e)} = \omega_{2\to 2'} - \omega_{2\to 1'}$ is the hyperfine splitting of the excited levels. As indicated by Eq. 7.6, the light shift operator lifts the degeneracy between the Zeeman sub-levels. During the operation of the molasses, this will in turn couple the different sub-levels necessary for the Sisyphus mechanism, and can inhibit the sub-Doppler cooling.

Let us now consider the combination of three linearly polarized laser beams, of equal intensities and arbitrary polarizations. We take each beam to be slightly detuned with respect to each other, and therefore neglect the interferences between them. The total dipole potential is then

$$\widehat{V}_T = V_s \left(3 + \frac{\delta_{hf}^{(e)}}{\delta_L} \frac{\sum_i \widehat{F}_i^2 - 6}{4} \right) \tag{7.7}$$

where $\widehat{F}_i$ is the projection of the angular momentum operator along the polarization direction of the beam i. If we choose the polarizations such that they are all orthogonal, the sum over the operators simplifies to $\widehat{F}^2$, and the potential becomes scalar again. Consequently, the ground state remains degenerate, and

the Sisyphus mechanism can operate effectively.

Spatial modulation of the intensity As we saw above, the combination of three beams with equal intensities and orthogonal polarization allows us to cancel the vector part of the potential. However, in the optical lattice, the intensity is modulated:

$$\widehat{V}_T(x,y,z) = V_0 \left((\sin^2(kx) + \sin^2(ky) + \sin^2(kz)) \left(1 - \frac{\delta_{hf}^{(e)}}{2\delta_L}\right) + \frac{\delta_{hf}^{(e)}}{4\delta_L} \left(\sin^2(kx)\widehat{F}_y^2 + \sin^2(ky)\widehat{F}_z^2 + \sin^2(kz)\widehat{F}_x^2\right) \right) \tag{7.8}$$

where $V_0 = 4\,V_s$, $k = 2\pi/\lambda_L$ and λ_L is the wavelength of the lattice beams. Without loss of generality, we assume the beam propagating along the x direction (respectively y and z) to be polarized along the y axis (respectively z and x). In general, this operator lifts the degeneracy between the Zeeman sublevels, except in locations where the intensity is equal for each beam. From Eq. 7.8, it appears that the maximal splitting between these levels is on the order of $V_0\delta_{hf}^{(e)}/\delta_L$. This configuration is reached for example when $x = y = 0$ and $z = \lambda_L/4$. At first glance, it appears that we need in general to satisfy $V_0\delta_{hf}^{(e)}/\delta_L \ll \hbar\,\gamma_M$ (see Eq. 7.4). Note though that this constitutes a pessimistic estimation, which assumes the atoms to be free to explore the whole potential landscape.

In this pinning lattice, we instead expect the atoms to remain on a single site, and only probe the trapping potential around its minima. To estimate the splitting between energy levels in this limit, we approximate the spatial variation of the laser intensity by a parabola

$$\widehat{V}_T(x,y,z) = V_0\,k^2 \left((x^2+y^2+z^2) \left(1 - \frac{\delta_{hf}^{(e)}}{2\delta_L}\right) + \frac{\delta_{hf}^{(e)}}{4\delta_L} \left(x^2\widehat{F}_y^2 + y^2\widehat{F}_z^2 + z^2\widehat{F}_x^2\right) \right). \tag{7.9}$$

The scalar part of this operator will not affect the efficiency of the molasses. To evaluate the effect of the vectorial part, we use a Born–Oppenheimer approximation, and diagonalize it at a fixed position x, y, z. The detailed calculation is presented in Appendix C. We then obtain five spatially varying sublevels

$E_i(x,y,z)$, with their average energy is given by

$$\langle E_i \rangle = \frac{\int E_i(\boldsymbol{r}) n(\boldsymbol{r})\, \mathrm{d}^3 r}{\int n(\boldsymbol{r})\, \mathrm{d}^3 r} \tag{7.10}$$

where $n(\boldsymbol{r})$ is the density distribution of the atoms in the lattice site. Here, we approximate this density by the Boltzmann distribution

$$n(r) = \mathcal{N} \exp\left(-\frac{V_0 k^2 r^2}{k_\mathrm{B} T}\right). \tag{7.11}$$

With this density distribution, a numerical integration of Eq. 7.10 leads to

$$\langle E_0 \rangle = \frac{3}{2} k_\mathrm{B} T \qquad \text{and} \qquad \langle E_\pm \rangle = \frac{3}{2} k_\mathrm{B} T \pm 1.78 \frac{\delta_{hf}^{(e)}}{4\delta_L} k_\mathrm{B} T \tag{7.12}$$

where the first value is obtained for three of the energy levels. The maximal splitting between the mean energy in the different sublevels is therefore given by

$$\Delta E_Z \equiv \hbar\, \omega_Z = 1.78 \frac{\delta_{hf}^{(e)}}{2\delta_L} k_\mathrm{B} T \tag{7.13}$$

The molasses will therefore operate properly provided that $\omega_Z \ll \gamma_M$, which constitutes a much more favorable case than our initial estimate.

7.1.2.2. Influence of the hyperfine structure of the ground state

When choosing the parameters of the lattice, one must also take into account the potential in the other hyperfine ground state $|F = 1\rangle$. During the operation of the molasses, an atom can be depumped to the $|F = 1\rangle$ state. For this atom, the light shift is approximately given by

$$V_{F=1} = \frac{3\pi c^2 \Gamma}{2\overline{\omega_1}^3} I_0 \frac{1}{3(\delta_L - \delta_{hf}^{(g)})} \tag{7.14}$$

where $\overline{\omega_1} = (\omega_{1\to 1'} + \omega_{1\to 2'})/2$, $\delta_{hf}^{(g)} = \overline{\omega_1} - \overline{\omega_2}$ is the hyperfine splitting of the ground state, and the vector contribution to the potential is neglected. We can divide our study into two configurations:

– the lattice frequency is chosen such that $\delta_L > 0$ and $\delta_L < \delta_{hf}^{(g)}$. In that case,

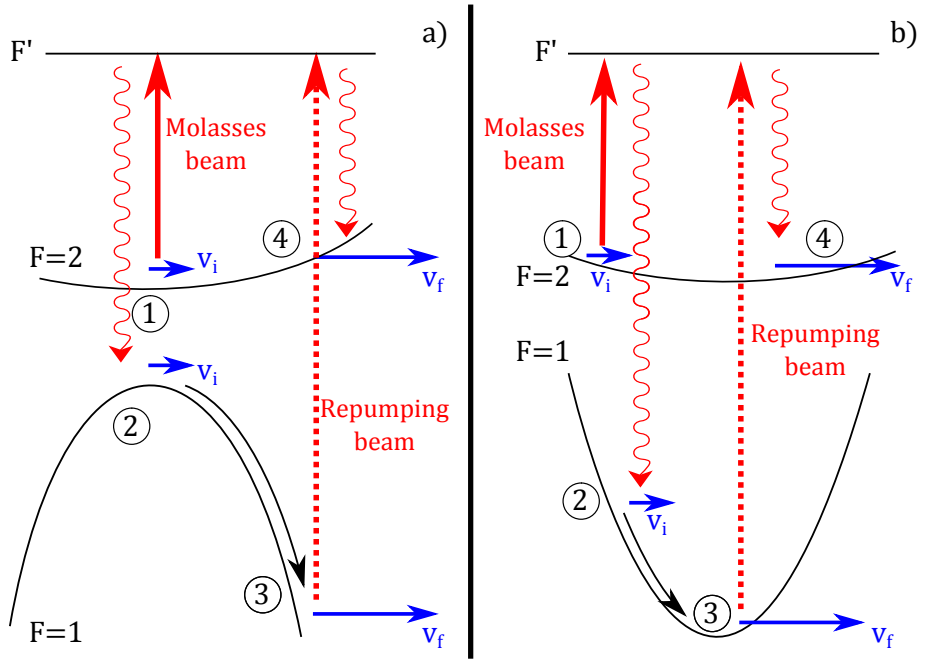

Figure 7.1.: Decomposition of the internal process during a depumping/repumping cycle, for $\delta_L > 0$ and $\delta_L < \delta_{hf}^{(g)}$ (a) and $\delta_L > 0$ and $\delta_L > \delta_{hf}^{(g)}$ (b). The atom starts on a lattice site in (1) with an initial velocity v_i. It is coupled to the excited states by the molasses, and it eventually decays to $|F = 1\rangle$, with the same velocity in (2). It is subsequently accelerated, and reaches the velocity v_f when it is repumped in (3). Finally, the atom returns to $|F = 2\rangle$, but keeps its velocity v_f in (4).

the nodes in the optical lattice are local minima of the potential for $|F = 2\rangle$, while they are local maxima for $|F = 1\rangle$ (see Fig. 7.1a).

– the lattice frequency is chosen such that $\delta_L > 0$ and $\delta_L > \delta_{hf}^{(g)}$. In that case, the nodes in the optical lattice are local minima of the potential for both hyperfine states. However, the curvature of the potential depends on the hyperfine state (see Fig. 7.1b).

First case: $\delta_L < \delta_{hf}^{(g)}$ Let us consider an atomic cloud in $|F = 2\rangle$, with a temperature T, coupled both to the lattice beams and to the molasses, with $0 \leq \delta_L \leq \delta_{hf}^{(g)}$. The lattice potential pins the atoms around a minimum of intensity. Whenever an atom is depumped to the $|F = 1\rangle$ hyperfine ground state, it sits at a potential maximum. It will therefore be accelerated to the final velocity v_f, before being repumped back into the $F = 2$ state (see Fig. 7.1). Close to the

maximum, the potential for $|F = 1\rangle$ can be linerarized:

$$V_{F=1} \approx -\frac{m\,\xi^2\,r^2}{2} \qquad \text{where} \qquad \xi = \sqrt{\frac{2V_0k^2}{m}\frac{\delta_L}{\delta_{hf}^{(g)} - \delta_L}}. \tag{7.15}$$

The repumping beam saturates the transition, so the atom will spend on average $\tau_R = 2/\Gamma$ in the $|F = 1\rangle$ state before being repumped. During that time, it is accelerated, and its final velocity is

$$v_f = v_i \cosh(\tau_R \xi) + r_i\,\xi \sinh(\tau_R \xi) \tag{7.16}$$

where v_i is the initial velocity of the atom and r_i its initial position. Both are given by the thermal distribution in the $|F = 2\rangle$ state. This in turn leads to a mean final kinetic energy

$$E_{k,f} = \frac{m\langle v_f^2\rangle}{2} = \frac{k_\mathrm{B}T}{2}\left(\cosh^2(\tau_R\xi) + \frac{\delta_L}{\delta_{hf}^{(g)} - \delta_L}\sinh^2(\tau_R\xi)\right). \tag{7.17}$$

A necessary condition for the atom to be recaptured by the molasses is that the final velocity v_f must be lower than the capture velocity v_c (see Eq. 7.3). However, if the final velocity is on the same order as the capture velocity, this represents an increase in energy much larger than the initial kinetic energy. Thus, such events must be rare enough in order for the excess energy to be dissipated. We therefore impose a stricter condition, which is sufficient to keep the atom on the same site: the kinetic energy gain should be at most $k_\mathrm{B}T$

$$E_{k,f} - \frac{k_\mathrm{B}T}{2} \leq k_\mathrm{B}T \qquad \Rightarrow \qquad \frac{\delta_{hf}^{(g)}}{\delta_{hf}^{(g)} - \delta_L}\sinh^2(\tau_R\,\xi) \leq 2. \tag{7.18}$$

Second case: $\delta_L > \delta_{hf}^{(g)}$ Alternately, let us consider the case where the lattice potential is blue detuned for both hyperfine ground states. In this configuration, if an atom in $|F = 2\rangle$ sits exactly at the center of the trap, it will not gain any energy if it is depumped to the $|F = 1\rangle$ hyperfine ground state. However, if the atom is located away from the center and is depumped to $|F = 1\rangle$, it will convert its potential energy into kinetic energy, until it is repumped. Since the potential in $|F = 1\rangle$ is much steeper, the atom can gain a substantial energy before being repumped. Close to the minimum, the potential for $|F = 1\rangle$ can be

linearized:

$$V_{F=1} \approx \frac{m\,\sigma^2\,r^2}{2} \qquad \text{where} \qquad \sigma = \sqrt{\frac{2V_0k^2}{m}\frac{\delta_L}{\delta_L - \delta_{hf}^{(g)}}}. \tag{7.19}$$

A calculation similar to the one performed in the previous case allows us to determine the mean kinetic energy after such a process. In this case as well, the energy gain must be at most $k_B T$

$$E_{k,f} - \frac{k_B T}{2} \leq k_B T \qquad \Rightarrow \qquad \frac{\delta_{hf}^{(g)}}{\delta_L - \delta_{hf}^{(g)}} \sin^2(\tau_R\,\sigma) \leq 2. \tag{7.20}$$

7.1.2.3. Heating by spontaneous emission of photons

Since the lattice is operated so close to resonance, it will necessarily heat the atoms by spontaneous emission of photons. As a first estimate, this heating can be neglected as long as scattering from the lattice is much less frequent than the photon scattering from the molasses. The scattering rate due to the lattice is

$$\hbar\gamma_L = \frac{\Gamma}{|\delta_L|}V_0 \tag{7.21}$$

and it can be neglected provided that

$$\gamma_L \ll \gamma_M. \tag{7.22}$$

7.1.2.4. "Gray molasses" effect from the lattice

Before choosing the lattice detuning, a final effect must be considered. When a laser is operated so close to the D_1 line, it can act as a gray molasses. This effect was initially proposed by Grynberg and Courtois [143], and successfully implemented in [144], and more recently in [145]. Contrarily to the usual case of a bright molasses, gray molasses act as a cooling source for blue-detuned beams, and heat the atoms for red-detuned beams. Since this phenomenon depends on the shelving of atoms in quasi-dark states, its magnitude is harder to link to the number of scattered photons than in the usual case of a bright molasses. For this reason, even when the lattice beams scatter less photons than the molasses beams, this effect may play a significant role. We will therefore choose a blue-detuned lattice, in order to minimize any spurious effect stemming from this

phenomenon.

7.1.3. Choosing the parameters

For the lattice For the pinning lattice to prevent the atoms from hopping from one site to the next, we require at least $V_0 = 10\,k_B T$ [135]. In optical molasses in free space, temperatures as low as 2.5 μK have been measured with Cs atoms

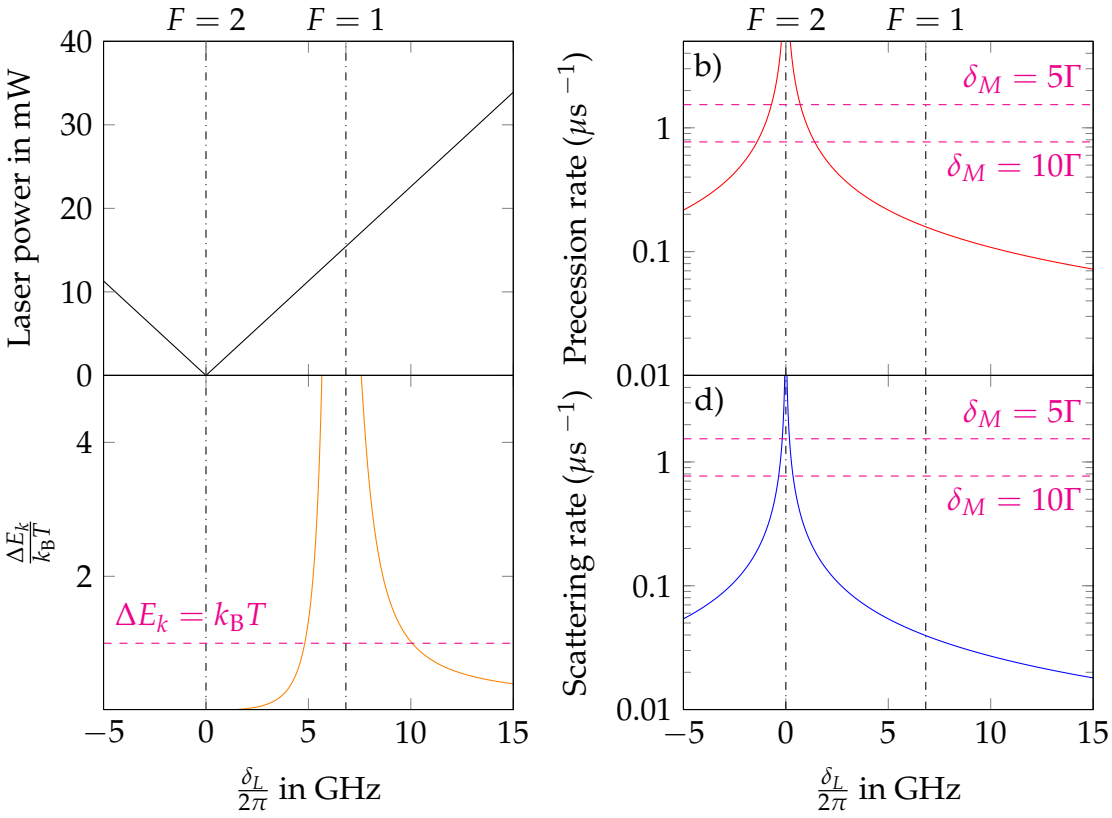

Figure 7.2.: (a) Required laser power in each lattice beam to obtain $V_0 = 2000 E_R$. The calculation is performed for gaussian beams with a waist $w_0 = 280\,\mu$m. (b) Precession rate stemming from the vector contribution to the light shift, following Eq. 7.13. (c) Kinetic energy gained after a depumping/repumping cycle, in units of $k_B T$, following Eqs. 7.18 and 7.20. The limit $\Delta E_k = 1$ is indicated in magenta dashed line. (d) Lattice scattering rate, following Eq. 7.22. In Figs. (b) and (d), we indicate the optical pumping rate in the molasses, for $\delta_M = 5\,\Gamma$ and $\delta_M = 10\,\Gamma$ in magenta dashed line. The transitions from $F = 1$ and $F = 2$ to the excited states are indicated in black dash-dotted line. All the calculations assume $V_0 = 2000\,E_R$ and $T = 20\,\mu$K, as was found in [73]

[140]. However, in previous single-atom imaging experiments (see [72, 73]), the equilibrium temperature was closer to 20 μK, and the lattice depth was chosen at $V_0 = 300\,\mu K$. In the following, we will set $V_0 = 2000 E_R = k_B \times 340\,\mu K = \hbar \times 2\pi \times 7.2$ MHz as our requirement, though it might be possible to relax this constraint.

In Fig. 7.2a, we present the required laser power generate such a deep lattice. The numerical calculations are performed assuming the lattice beams are gaussian, with a waist $w_0 = 280\,\mu$m. The hyperfine splittings are $\delta_{hf}^{(g)} = 2\pi \times 6.83$ GHz for the ground state, and $\delta_{hf}^{(e)} = 2\pi \times 814$ MHz for the excited state [146]. From this calculation, it appears that large potential depths are achievable with comparatively little laser power. We also present in Fig. 7.2b, c and d the limits determined in the previous section, for a lattice depth $2000 E_R$ and a temperature $T = 20\,\mu$K.

We finally present in Fig. 7.3 a qualitative summary of the different limits on the lattice detuning. In particular, the choice of δ_L is influenced by the molasses detuning δ_M. For $\delta_M = 10\,\Gamma$, the lattice detuning must be at least $2\pi \times 14$ Ghz, while $\delta_L \geq 2\pi \times 7$ GHz is sufficient for $\delta_M = 5\,\Gamma$. Indeed, a smaller molasses detuning allows for a higher scattering rate at a given molasses temperature, and is therefore more robust. In order to satisfy all these constraints, we will choose $\delta_L = 2\pi \times 10$ GHz, and each lattice beam must therefore contain at least 20 mW of laser power.

It has come to our attention that the vectorial contribution to the light shift

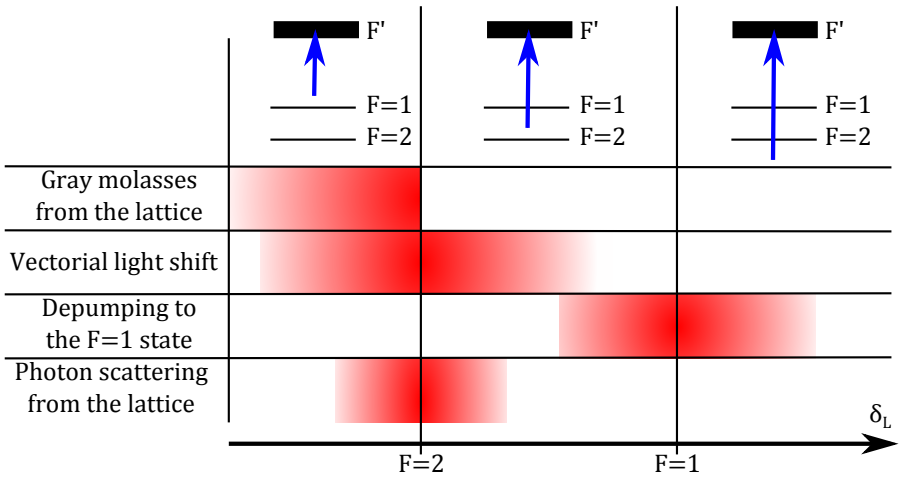

Figure 7.3.: Qualitative summary of the different limits which must be satisfied by the lattice beam detuning. The red areas indicate a range where the corresponding perturbation dominates the sub-Doppler cooling mechanisms.

was initially a limiting factor in I. Bloch's group [147]. There, the lattice was far detuned, with $\lambda_L = 1064$ nm. However, the polarization of one of their lattice beam initially had a circular component. In this case, the vectorial contribution to the light shift comes from the fine structure of ^{87}Rb , rather than from the hyperfine structure of the excited state. By replacing the hyperfine splitting by the fine splitting in Eq. 7.13, we find a precession frequency $\omega_Z \approx 100$ kHz, while the molasses scattering rate was measured at $\gamma_M = 150$ ms^{-1}. Indeed, such a configuration was not satisfactory to image single atoms. By contrast, when all the beams were linearly polarized, the vectorial contribution to the light shift vanished, and single atoms could be imaged.

Note that in the experiment performed in M. Greiner's group, a near-resonant pinning lattice was used, with $\delta_L/(2\pi) = 30 - 50$ GHz [72, 137]. Our detailed analysis shows this detuning was clearly sufficient to avoid the discussed problems.

For the molasses The molasses must fulfill two roles: cool down the atoms and scatter a large number of photons. For molasses detunings larger than the natural linewidth, the minimal temperature in the molasses is nearly independent of its detuning. However, this temperature will be reached at different scattering rates.

Note that the light shift caused by the lattice must be taken into account when choosing the molasses detuning. Since the lattice is blue-detuned, atoms strictly located at a potential minimum will not experience any light-shift. However, if an atom is momentarily located at an intensity maximum, its resonance will be red-shifted. Consequently, the molasses detuning must be chosen such that it is always red-detuned, even in the limiting case of an atom sitting at a potential maximum. For our choice of the lattice parameters, the main effect comes from the light shift of the ground state: the lattice is too far detuned from the D_2 line to have a significant effect on the excited states. For $V_0 = 2000E_R$, the resonance is at most shifted by $2\pi \times 7.2$ MHz.

However, the molasses detuning cannot be chosen too large either. For increasing molasses detuning, the depumping rate to $|F = 1\rangle$ increases as well. Indeed, the molasses beam also couple to the hyperfine $|F' = 2\rangle$ state, which can decay into the $|F = 1\rangle$ state. As we presented above, this can in turn lead to additional heating of the cloud.

Note that increasing the molasses detuning also reduces its scattering rate, thus reducing the fluorescence signal of the atoms on the CCD camera. However, as we present in Appendix D, an atom can be unambiguously detected in

only 200 μs, for $\delta_M = 5\,\Gamma$ and $T = 20\ \mu$K. Thus, even if the detuning was much larger than $\delta_M = 5\,\Gamma$, the required exposure time would remain well within the capabilities of our system. Consequently, the choice of the molasses detuning does not affect our ability to detect single atoms.

While none of these criteria impose a strict limit on the molasses detuning, we clearly benefit from small values. Closer to the resonance, the scattering rate increases, which suppresses the effect from the vector contribution to the light shift. At the same time, the depumping rate to $|F = 1\rangle$ decreases. In previous realizations of this setup ([72, 73]), the molasses was detuned by $2\pi \times$ 80 MHz, though it was found smaller molasses detunings did not compromise the efficiency of the scheme [147].

7.2. Characterizing our implementation

7.2.1. Experimental setup

The pinning lattice The light for the pinning lattice is produced by a laser diode emitting at 795 nm, amplified with a tapered amplifier (TA Pro, Toptica). The lattice is then generated in the conventional manner: in each direction, a laser beam is retro-reflected on a mirror, thus creating a standing wave. Each beam is slightly detuned ($\sim$ 10 MHz) with respect to each other, in order to avoid interference between the different lattice directions. The geometry of the laser beam is chosen such that its minimal waist lies on the retro-reflection mirror, in order to maximize the contrast of the interference at the location of the atoms. The retro-reflecting mirrors are located 125 mm away from the atoms, and the waist of the lattice beams on the mirrors is 250 μm, leading to a waist of 280 μm at the location of the atoms.

The spatial arrangement of the two lattice beams is shown in Fig. 7.4. Owing to geometrical constraints, it is not possible to send three orthogonal beams on the atoms. For this reason, the angle between two of the beams is 72°, and they are both orthogonal to the third one. The third lattice beam propagates along the same axis as the horizontal imaging beam and the dipole traps. It is superposed with the path of the imaging beam by a polarizing beam splitter, and is retro-reflected on an interferometric filter, which is reflective at 795 nm and transparent at 780 nm (see Fig. 7.5). As we showed in 7.1.2, each lattice beam should be linearly polarized, and the polarizations should be orthogonal. A possible choice is depicted in Fig. 7.4.

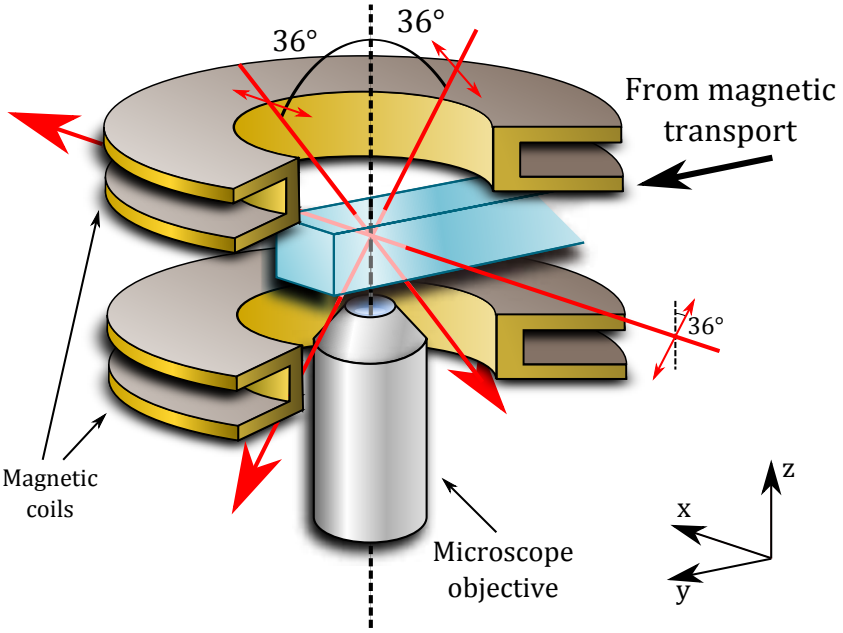

Figure 7.4.: Spatial arrangement of the three lattice beams, along with their polarization, respective to the glass cell. The atoms are located at the intersection of the three beams.

The molasses beam The molasses beams propagate along the same directions as the lattice beams. Each direction contains a pair of counter-propagating beams, with orthogonal linear polarizations. For this reason, the lattice beams are retro-reflected on interferometric filters, which are transparent at the molasses wavelength (780 nm). The beam balance is controlled within each pair by a retardation wave-plate, as well as between separate pairs. Since the molasses beams propagate in the same fiber, the beam waist on the atoms is also 280 μm.

Note that for a 3D molasses, the intensity is necessarily spatially modulated, which can in turn lead to inhomogeneities in the cooling efficiency and the scattering rate. To circumvent this problem, we introduce a temporal modulation of the phase of the molasses. This modulation must be slow compared to the cooling and scattering processes in the molasses, but fast compared to the imaging time. Experimentally, we chose to modulate at 1 kHz. For each of the directions, the position of a mirror is modulated by a piezo-electric crystal, thus modulating the phase of the interference pattern (see Fig. 7.5).

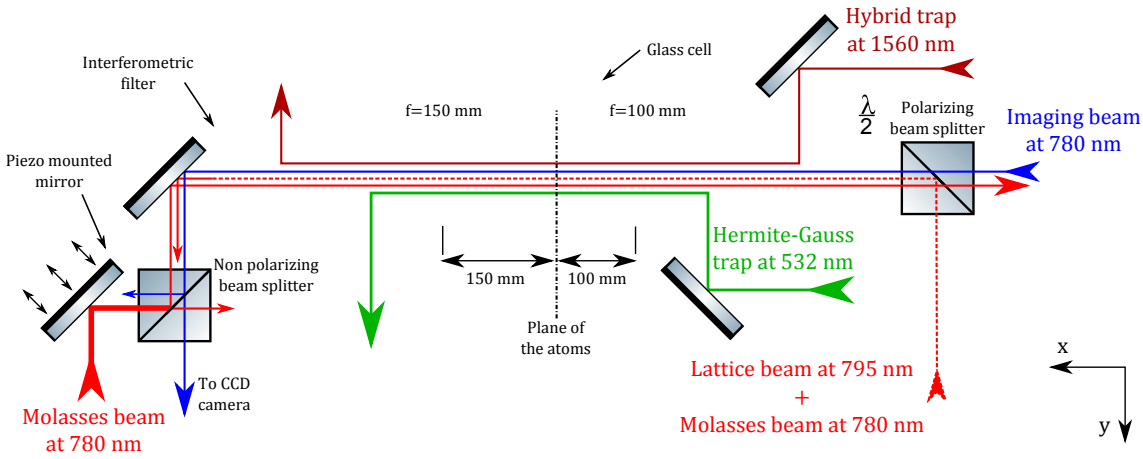

Figure 7.5.: Optical scheme in the xy plane. The hybrid trap and the Hermite-Gauss trap are indicated in dark red and green respectively (see Ch. 2.1). The imaging beam is indicated in blue. The molasses beams and the lattice are indicated in bright red. The two dipole traps are superposed and separated from the the other beams with dichroic mirrors, while the lattice beam is retro-reflected on an interferometric filter. A non-polarizing beam splitter must be used to add the second molasses beam orthogonally polarized to the first one.

7.2.2. Preliminary results

At the time of the writing, this experiment constitutes a work in progress. Consequently, we can only present preliminary results. When assembling this setup, we were able to test separately the lattice and the molasses.

Testing the molasses In our system, testing the molasses requires a specific preparation. Indeed, due to the re-scattering of photons, the atomic density in a molasses cannot exceed $n_{max} = 10^{12}$ atoms/cm^3 (see [148] for example [1]). Consequently, should one attempt to operate a molasses on a denser cloud, the excess density will lead to a fast expansion of the cloud, until it becomes sufficiently dilute. This is not an issue in most cold atoms experiments, where sub-Doppler cooling mechanisms only intervene in a Magneto-Optical Trap. However, this can constitute a limitation for these tests, and must be accounted for. Furthermore, the region where the molasses beams intersect is quite small: each beam has a waist $w_M = 280\ \mu$m, and the atoms must therefore be contained in a

1. This value was the highest density observed in a Magneto-Optical Trap, and overestimates the maximal density at which the sub-Doppler mechanisms can operate efficiently. However, this provides an indicative upper bound on the atomic density for our tests.

volume $V_M = 2 \cdot 10^{-5}$ cm^3. The finite size of the beams puts another limitation on our experiments: during the operation of the molasses, the expansion of the atomic cloud must remain contained within V_M. Consequently, if we require an order of magnitude between the size of the cloud and the waist of the beams, this means the cloud can contain at most $n_{\max} (w_M/10)^3 = 2 \cdot 10^4$ atoms.

The efficiency of the molasses can be characterized in two ways: by measuring the equilibrium temperature, or the spatial diffusion coefficient, which should be optimal for the same molasses parameters. The former requires to perform a time of flight experiment, in which the size of the cloud is doubled. However, the latter can be performed *in situ*, and yields a larger signal. Consequently, we monitor the size of the cloud, as a function of the time spent in the molasses beams. In an optical molasses, the motion of the atoms is well described by a diffusion equation

$$\frac{\mathrm{d}\left\langle x^2 \right\rangle}{\mathrm{d}t} = 2\,D \tag{7.23}$$

where x is the position of an atom and D is the spatial diffusion coefficient. Therefore, we choose the following fitting function to describe our data:

$$\sigma^2(t) = \sigma^2(0) + 2\,D\,t \tag{7.24}$$

where $\sigma(t)$ is the size of the cloud as a function of time in the molasses, and $\sigma(0)$ and D are the adjustable parameters.

Note that the hybrid trap (see 2.1.2) is not suited to this measurement: the magnetic field at the location of the atoms is much too large to allow for a proper operation of the molasses ($B \approx 200$ mG). The atoms are therefore transferred in an all-optical trap, and the magnetic fields extinguished. At the time $t = 0$, we switch off the optical confinement, and switch on the molasses beams. We then measure the size of the cloud as a function of time.

The density limitation discussed above can be circumvented in two manners. One can prepare a sufficiently dilute cloud by carefully decompressing the trap. Alternately, one can prepare a dense cloud, and let it expand until its density is sufficiently low. When the molasses is switched on, the first phase of the expansion is driven by the rescattered photons. After some time, the density becomes low enough for the molasses to operate properly, and the expansion slows down significantly. Therefore, the initial fast expansion can be discarded, and the second phase can be used to measure a diffusion coefficient. In practice, there will always be a fast initial expansion. We show such a measurement in Fig. 7.6, along with a fit by Eq. 7.24, and we measure $D = 75(4)\,\mu\mathrm{m}^2/\mathrm{ms}$.

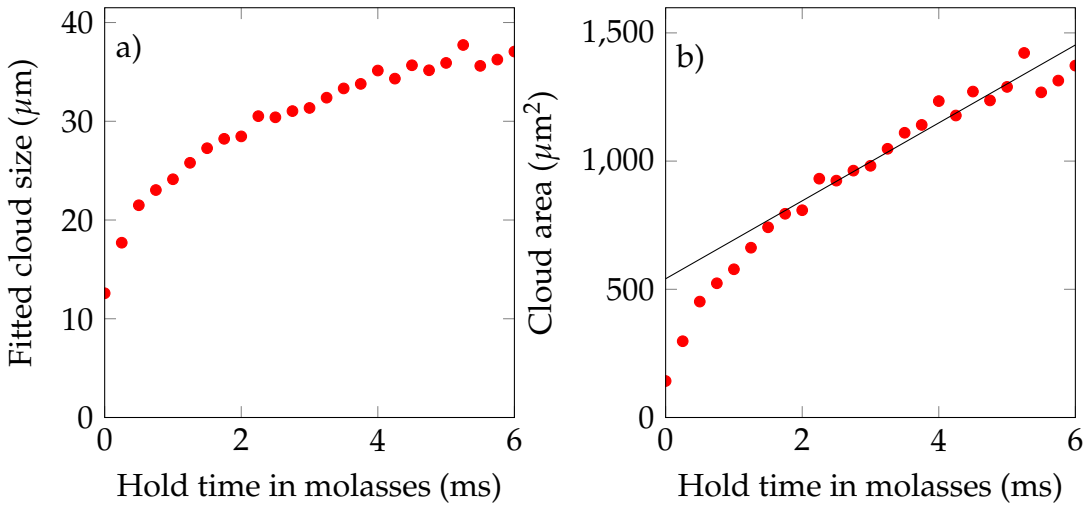

Figure 7.6.: Typical expansion of a dilute cloud in the molasses. The average cloud size is shown in (a), and presents the expected diffusive behaviour. The square of the size is shown in (b), along with a fit by Eq. 7.24 for hold times larger than 1.5 ms, and we find $D = 75(4)\,\mu\text{m}^2/\text{ms}$. The initial fast expansion is most likely due to a high initial density.

By comparison, the authors measured $D = 60\,\mu\text{m}^2/\text{ms}$ in a three-dimensional $lin \perp lin$ molasses in [139].

The experiment presented in Fig. 7.6 was performed on atomic samples containing typically 10^4 atoms. The size of the cloud was determined by fitting a gaussian to the density distribution. In particular, it appears the diffusive expansion sets in for sizes superior to 30 μm, which corresponds to densities lower than 10^{11} atoms/cm^3.

Loading the optical lattice Each lattice beam is separately aligned, and the depth of the resulting standing wave is measured by Raman-Nath diffraction at low lattice powers [149, 150]. To this end, we prepare a three dimensional BEC. The lattice beam is successively switched on, and extinguished after a interaction time τ_{int}. When the lattice beam is turned off, we simultaneously release the BEC from the trap, and let it expand for 4 ms. We then image the different momentum states resulting from the interaction with the lattice (see Fig. 7.7a). For shallow potentials ($V_0 \leq 4\,E_R$), we only populate the zeroth and first orders

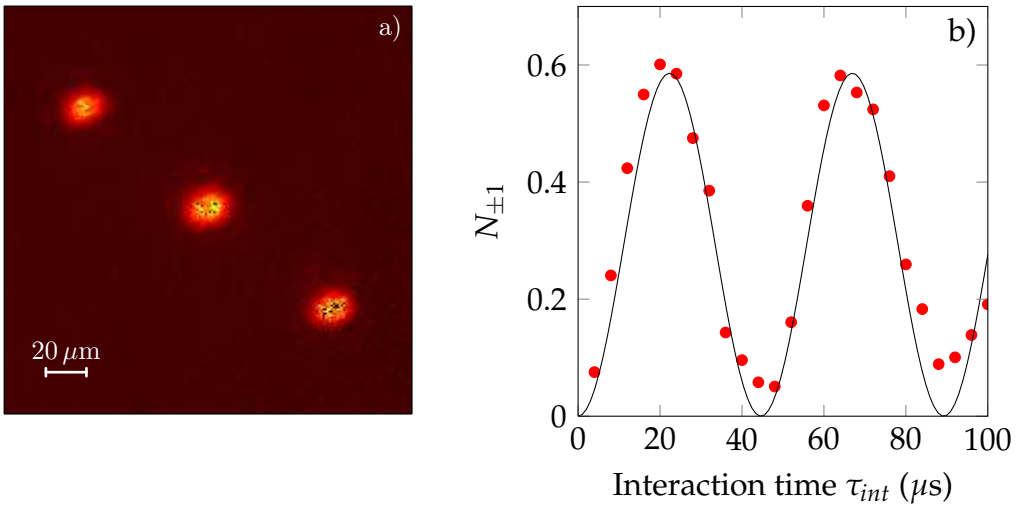

Figure 7.7.: (a) Zero-th and first orders, after diffraction of a BEC on the optical lattice, and subsequent time-of-flight. (b) Typical Rabi oscillations in the fraction of diffracted atoms. The fit from Eq. 7.25 is indicated in black line, and yields $V_0 = 6.71\, E_R$.

of the diffraction pattern, and the fraction of atoms in the first order is given by

$$N_{\pm 1}(t) = \frac{V_0^2}{2V_0^2 + 64E_R^2} \sin^2\left(\frac{\tau_{int}\, E_R}{2\hbar}\sqrt{16 + \frac{V_0^2}{2E_R^2}}\right). \tag{7.25}$$

For $V_0 = 6\, E_R$, the period of these Rabi oscillations is 45 μs, well within the temporal resolution of our experimental sequence (see Fig. 7.7b). We then use these results to extrapolate the depth of the lattice at full power.

For a blue detuned lattice, with $\delta_L = 2\pi \times 7$ GHz, we are able to achieve lattice depths of $\sim 800\, E_R$ in each arm, with a total power of 80 mW at the output of the fibers. However, the situation is quite different between the two vertical beams and the horizontal beam. In the two vertical beams, the depth is $\approx 45\, E_r/\text{mW}$, while it is only $15\, E_R/\text{mW}$ in the horizontal beam. By comparison, we ideally expect a lattice depth of $110\, E_R/\text{mW}$ at this lattice detuning (see Fig. 7.2a).

Note that this theoretical value assumes perfect transmission of all optical elements used to create the lattice. However, we measure non-negligible losses along the lattice path, thus decreasing the contrast of the interference pattern. For example, the vacuum windows do not have an anti-reflection coating. Consequently, the retro-reflected beam will attenuated, and the contrast of the inter-

ference pattern will decrease. For approximate losses of 4 % per interface,[2] this can reduce the lattice depth by 15 %, explaining a large part of the difference between the experiment and the prediction. Furthermore, the horizontal lattice beam is transmitted by several dichroic elements (see Fig. 7.5), which each further attenuate the beam, thus explaining the difference between this direction and the two vertical beams.

From these preliminary results, it is clear we are limited by the amount of available laser power. At the moment, the depth of the lattice is only $800\,E_R = 136\,\mu K$, which is probably not sufficient to prevent thermal hopping between sites: in I. Bloch's group, it was found that a lattice depth of 200 μK was necessary to fully suppress thermal hopping. To remedy this problem, we have planned to replace the source laser, which will multiply the available laser power by 4. In this configuration, we will be able to generate a sufficiently deep lattice, while maintaining a large enough detuning to suppress all the effects discussed in 7.1.2.

2. Note that this is the reflectivity of glass at normal incidence, while the two vertical beams form an angle of 54° with the surface. Thus, the actual reflectivity can be higher than 4 %.

Concluding remarks

Summary

In this thesis, we studied experimentally the two dimensional Bose gas. We measured the equation of state around the critical point, characterized the fluctuations, and measured the superfluid behavior of the system.

In chapter 3, we measured experimentally the equation of state (EoS) of the two-dimensional Bose gas, with two different methods. For a single atomic sample, we determined its temperature and central chemical potential by fitting the wings of the cloud by a mean–field equation of state. We could then deduce the EoS of the infinite 2D Bose gas by making use of the local density approximation (LDA). We also developed an alternative measurement of the EoS, inspired by a method developped at MIT [36]. We started by calculating the derivative and the integral of the density with respect to the local potential. From these quantities, we were able to measure the EoS of the 2D Bose gas with a single adjustable parameter: the detectivity of our imaging system. The EoS produced with these methods are both in very good agreement with the numerical prediction by Prokof'ev and Svistunov presented in [79].

We pursued our studies of the 2D Bose gas in chapter 4 by locally probing its superfluid behavior. Indeed, the measurements presented in the previous chapter only provided an indirect characterization of the BKT transition. By contrast, we were able to show evidence for both normal and superfluid regions in the phase diagram by looking at the response of the system to a moving defect. Furthermore, these results are in good agreement with the existence of a normal to superfluid transition.

In chapter 5, we presented a quantitative analysis of the fluctuations, both *in-situ* and after a short ToF. We observed a significant enhancement of the density fluctuations after ToF, indicating that the dynamics of the degenerate 2D Bose gas is dominated by phase fluctuations, and that density fluctuations are essentially frozen. Through analysis of the extrema of the atomic density, we identified phonons as being the primary fluctuation mechanism, rather than vortices, at least in the degenerate region. This picture was confirmed by a study of the two-body correlation function, which was in good agreement with

the prediction presented in [71].

Perspectives

From the work which has been presented here, we can define two broad research directions. We can further study the two-dimensional Bose gas, by realizing a uniform Bose gas as was described in Ch. 6. Alternately, once our single atom detection scheme is operational, we can take advantage of it to probe strongly correlated states with few particles. In the following, we will detail both of these perspectives.

On the uniform two dimensional Bose gas

A first extension of our work would be of course to complete the ongoing study of the interplay between BEC and BKT transition. Once a suitable box-like potential has been realized and characterized, we propose the following measurement.

For a given atom number, we measure the momentum distribution, either by time-of-flight experiments, or by performing state tomography (see [64] for such a measurement). As the sample temperature is lowered, the appearance of a sharp peak in the momentum distribution characterizes the onset of Bose-Einstein condensation. By performing this measurement for different atom numbers, we can obtain a determination of the critical temperature as a function of the atom number. This experiment can be performed both in a harmonic trap and in a box like potential. The effect of the different density of states would then be revealed by comparing the two measurements.

Furthermore, the realization of a uniform 2D Bose gas would allow for a more refined study of its fluctuations, similar to the one presented in chapter 5. In this case, we would not be limited by the inhomogeneity of the trapping potential, and we could probe the correlation properties of the gas on a larger scale. Moreover, a larger signal-to-noise ratio in the determination of the two-body correlation function after time of flight should allow us to demonstrate the algebraic decay of the *in-situ* one-body correlation function, and to measure its exponent.

One can as well take advantage of the uniform density to perform experiments with the stirring beam described in chapter 4. In this case, we would observe the wake left by the stirring beam, which should depend on the superfluid character of the fluid, and the velocity of the defect. In particular, above the critical velocity, one should observe a Cerenkov-like wave pattern. Such

an experiment was performed with polaritons in a semi-conductor microcavity [115], albeit in a non-equilibrium system.

On strongly correlated states

As we discussed in the introduction, ultracold atoms are particularly well suited to the simulation of condensed matter phenomena. In this context, we want to realize large effective magnetic fields, to reach the strongly-correlated states typical of fractional quantum Hall effect (FQHE), such as the Bosonic Laughlin state. Several possibilities to create such an effective magnetic field have been mentioned in chapter 7, such as the rotation of the trap [134], or the use of artificial gauge fields [54]. Both methods have been successfully realized [16, 53], though the magnetic field generated in this manner was too small to enter the strongly correlated regime. The maximal magnetic field is limited by the residual static anisotropy of the trap in the case of the rotation, while the spontaneous emission from the dressing beams limited the field in the case of artificial gauge fields.

To reach the strongly correlated regime, we therefore consider two options. First, instead of trying to increase the magnetic field, one can instead decrease the atom number. We therefore aim to prepare very small samples, containing between 3 and 10 atoms. The artificial magnetic field will be realized by injecting angular momentum in the system via optical dressing of the internal states, rather than by directly rotating the trap. Once the strongly correlated state has been reached, the wavefunction can be subsequently magnified by letting the cloud expand in two dimensions [151]. The density distribution will then by imaged by the single atom detection described in chapter 7.

A second way to produce a strongly correlated state lies in the realization of optical flux lattices [55, 152]. In such an optical lattice, the lower energy band is topologically equivalent to the lowest Landau level, which is crucial to the formation of many-body states. Note that such a scheme is not conceptually limited to small atom numbers. Indeed, the optical flux lattices generate a large magnetic flux per unit cell of the lattice, allowing for realization with large atom numbers.

A. Contribution of the excited states to the EoS, supplemental material of Phys. Rev. Lett. 107, 130401 (2011)

The following section was initially published in [69], and is reproduced without modifications

For a given T and μ, we self-consistently determine the population of the excited states using the method described in [64, 101], assuming the atoms in the excited states $j \geq 1$ of the z motion to be in the HFMF regime. In practice we restrict the analysis to the first ten levels. In order to give an estimation of the contribution of the various levels $j \geq 1$ to the total density, we show in Fig. A.1a numerical results obtained by applying this procedure to a numerically generated profile, produced using the prediction [79] with $T = 100\,\mathrm{nK}$ and

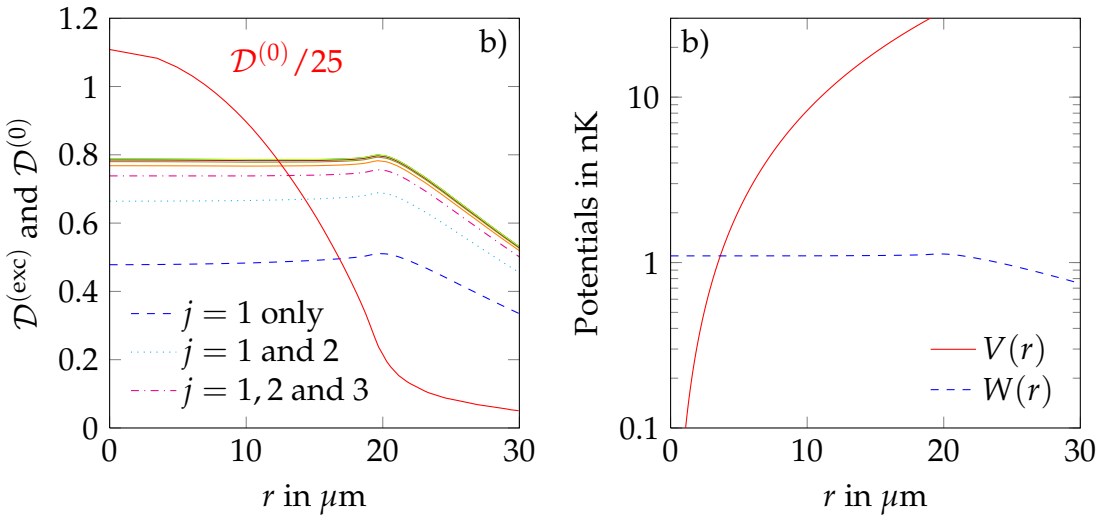

Figure A.1.: (a) Phase space density of the ground (solid red line) and excited state(s) of the z-motion, for $k_B T = \hbar\omega_z$. The n-th line from the bottom corresponds to the contributions of excited levels 1 to n. (b) Comparison of the trapping potential (red solid line) and the repulsive potential created by the excited atoms on the population in the ground state (blue dashed line).

$\mu/k_B T = 0.45$. This temperature is on the high side of our experimental range, where the influence of the atoms in the excited states along z is expected to be the most important. We plot in Fig. A.1a the phase space density of the excited states $\mathcal{D}^{(\mathrm{exc})}$, distinguishing the contribution of the state(s) $j = 1$, $j = (1,2)$, $j = (1,2,3)$, etc. For comparison we also plot the profile $\mathcal{D}^{(0)}$ obtained from [79], associated to the atoms in the ground state. Note that the contribution of the states $j > 4$ is already negligible. The phase space density associated to each excited state is lower than 0.5, which justifies to treat the atoms in these states within the HFMF approximation. The flattened shape of the density distributions in the central region is due to the repulsive interaction with the atoms in the ground state of the z motion.

This procedure also allows us to calculate the effective potential felt by the atoms in $j = 0$, when the repulsive potential $W(\boldsymbol{r})$ created by the atoms in $j \geq 1$ is taken into account. Plotting together $W(\boldsymbol{r})$ and the trapping potential $V(\boldsymbol{r})$ (Fig. A.1b) we see that $W(\boldsymbol{r})$ is essentially negligible ($\lesssim 1\,\mathrm{nK}$) and one can thus consider the density $n_0(\boldsymbol{r})$ to be insensitive to the presence of the atoms in $j \geq 1$.

B. Conversion of phase fluctuations into density fluctuations

B.1. Density distribution, in real and reciprocal space

The aim of this appendic is to link the spatial fluctuations of the two-body correlation function $g^{(2)}(r,t)$ to the initial dynamics of the system. We assume a free expansion: the wavefunction at time t is therefore directly deduced from the initial wavefunction by the Schrödinger propagator

$$\psi(\mathbf{r},t) = \left(\frac{m}{2\pi i\hbar t}\right) \int \exp\left(i\frac{m(\mathbf{r}-\mathbf{r}_1)^2}{2\hbar t}\right) \psi(\mathbf{r}_1,0)\, \mathrm{d}^2 r_1 \tag{B.1}$$

and the spatial density is given by

$$\begin{aligned}\rho(\mathbf{r},t) &= |\psi(\mathbf{r},t)|^2 \\ &= \left(\frac{m}{2\pi i\hbar t}\right)^2 \int \mathrm{d}^2 r_1\, \mathrm{d}^2 r_2 \exp\left(i\frac{m(r_2^2-r_1^2)}{2\hbar t}\right) \exp\left(i\frac{m(\mathbf{r}_1-\mathbf{r}_2)\cdot\mathbf{r}}{\hbar t}\right) \psi^*(\mathbf{r}_1,0)\,\psi(\mathbf{r}_2,0).\end{aligned} \tag{B.2}$$

In the following, we choose to express rather the Fourier transform of the density

$$\begin{aligned}\widetilde{\rho}(\mathbf{q}) &= \int \mathrm{d}^2 r\, e^{-i\mathbf{q}\cdot\mathbf{r}}\rho(\mathbf{r}) \\ &= \left(\frac{m}{i\hbar t}\right)^2 \int \mathrm{d}^2 r_1\, \mathrm{d}^2 r_2 \exp\left(i\frac{m(r_2^2-r_1^2)}{2\hbar t}\right) \delta\left(\mathbf{q} - \frac{m(\mathbf{r}_1-\mathbf{r}_2}{\hbar t}\right) \psi^*(\mathbf{r}_1,0)\,\psi(\mathbf{r}_2,0)\end{aligned} \tag{B.3}$$

We introduce the center of mass and relative motion variables $\mathbf{R} = (\mathbf{r}_1 + \mathbf{r}_2)/2$ and $\mathbf{r} = \mathbf{r}_1 - \mathbf{r}_2$. With these definitions, we obtain

$$\begin{aligned}\widetilde{\rho}(\mathbf{q}, t) &= -\int \mathrm{d}^2R\, \mathrm{d}^2r\, \exp\left(i\frac{m\mathbf{r}\cdot\mathbf{R}}{\hbar t}\right)\, \delta\left(\mathbf{r} - \frac{\hbar\mathbf{q}t}{m}\right)\, \psi^*\left(\mathbf{R} + \frac{\mathbf{r}}{2}, 0\right)\, \psi\left(\mathbf{R} - \frac{\mathbf{r}}{2}, 0\right) \\ &= -\int \mathrm{d}^2R\, e^{i\mathbf{q}\cdot\mathbf{R}}\psi^*\left(\mathbf{R} + \frac{\hbar t\mathbf{q}}{2m}, 0\right)\, \psi\left(\mathbf{R} - \frac{\hbar t\mathbf{q}}{2m}, 0\right) \end{aligned} \tag{B.4}$$

Similarly, we can derive a similar expression for the $g^{(2)}$ correlation function. In a homogeneous system of average density ρ_0, it is given by

$$g^{(2)}(r_1, t) = \frac{\langle \rho(\mathbf{r}, t)\, \rho(\mathbf{r} + \mathbf{r}_1, t)\rangle_{\mathbf{r}}}{\rho_0^2}. \tag{B.5}$$

Thus, its Fourier transform is given by

$$\begin{aligned}\widetilde{g}^{(2)}(\mathbf{q}, t) &= \int \mathrm{d}^2r\, e^{-i\mathbf{q}\cdot\mathbf{r}} g^{(2)}(r, t) \\ &= \frac{1}{(2\pi)^2}\left\langle |\widetilde{\rho}(\mathbf{q}, t)|^2 \right\rangle. \end{aligned} \tag{B.6}$$

Consequently, it is equivalent to know the power spectrum of the Fourier transform of the density, or the two-body correlation function.

B.2. Case of a small perturbation

Since ψ is a fluctuating quantity, we cannot assign a deterministic value to $\widetilde{\rho}$. However, we can perform the calculation for a given realization of ψ, and see which Fourier components emerge. We start with a weakly perturbed distribution

$$\psi(\mathbf{r}, t = 0) = \sqrt{n_0(1 + \epsilon(\mathbf{r})}e^{i\varphi(\mathbf{r})} \approx \sqrt{n_0}\left(1 + \frac{\epsilon(\mathbf{r})}{2} + i\varphi(\mathbf{r})\right) \tag{B.7}$$

where ϵ and φ are small perturbations of the density and phase respectively. From Eq. B.3, we find

$$\frac{\widetilde{\rho}(\mathbf{q}, t)}{n_0} \approx (2\pi)^2\, \delta(\mathbf{q}) + \cos\left(\frac{\hbar t q^2}{2m}\right)\, \widetilde{\epsilon}(q) + 2\sin\left(\frac{\hbar t q^2}{2m}\right)\, \widetilde{\varphi}(q). \tag{B.8}$$

As we pointed out above, the quantity of interest is the Fourier transform of $g^{(2)}$, given by

$$\widetilde{g}^{(2)}(q,t) \approx \cos^2\left(\frac{\hbar t q^2}{2m}\right)\,(\widetilde{\epsilon}(q))^2 + 4\sin^2\left(\frac{\hbar t q^2}{2m}\right)\,(\widetilde{\varphi}(q))^2 + 2\,\widetilde{\epsilon}(q)\,\widetilde{\varphi}(q)\,\sin\left(2\frac{\hbar t q^2}{2m}\right). \tag{B.9}$$

Thus, Fourier components at $\hbar t q^2/m = \pi/2, \pi, 2\pi...$ can contribute to the power spectrum, depending on the value of $\widetilde{\epsilon}(\mathbf{q})$ and $\widetilde{\varphi}(\mathbf{q})$ at these wavectors.

B.3. Interpretation in terms of Talbot effect

This calculation was also presented in [71], where the authors interpret it in terms of Talbot effect. Indeed, let us consider a 1D problem for simplicity, in the configuration described in Eq. B.7. Furthermore, we suppose that only small phase fluctuations are present, with a spatial modulation

$$\begin{aligned} \epsilon(x) &= 0 \\ \varphi(x) &= \alpha\cos(q_0\,x) \qquad \text{with} \qquad \alpha \ll 1. \end{aligned} \tag{B.10}$$

Thus, it is easy to calculate $\psi(x,t)$, which is given by

$$\psi(x,t) \approx \sqrt{\rho_0}\left(1 + i\alpha\cos(q_0 x)e^{-i\frac{\hbar q_0^2}{2m}t}\right) \tag{B.11}$$

and the density is finally given by

$$\rho(x,t) = n_0\left(1 + 2\alpha\cos(q_0 x)\,\sin\left(\frac{\hbar t q_0^2}{2m}\right)\right). \tag{B.12}$$

Thus, an initial phase modulation leads to a density modulation after propagation. This is the exact analog in the time domain of the Talbot effect, where light passing through a phase grating exhibits an intensity modulation after some propagation length.

C. Diagonalization of the vectorial light shift in a lattice

This appendix details the calculation of the average energy levels explored by an atomic ensemble pinned on a lattice site.

We start by obtaining the exact eigenenergies in the potential created by the lattice

$$\widehat{V}_T(x,y,z) = V_0\,k^2\left((x^2+y^2+z^2)\left(1-\frac{\delta_{hf}^{(e)}}{2\delta_L}\right)+\frac{\delta_{hf}^{(e)}}{4\delta_L}\left(x^2\widehat{F}_y^2+y^2\widehat{F}_z^2+z^2\widehat{F}_x^2\right)\right) \tag{C.1}$$

which was introduced in Eq. 7.9. Here, we apply a Born–Oppenheimer approximation to decouple the center of mass motion, and the internal degrees of freedom. The motion of the center of mass is treated classically, while we diagonalize the vector part of this operator for a fixed position (x,y,z). The vector part of this operator is

$$\begin{pmatrix} x^2+4y^2+z^2 & 0 & \sqrt{\frac{3}{2}}(z^2-x^2) & 0 & 0 \\ 0 & \frac{5x^2+y^2+5z^2}{2} & 0 & -\frac{3}{2}x^2+\frac{3}{2}z^2 & 0 \\ \sqrt{\frac{3}{2}}(z^2-x^2) & 0 & 3x^2+3z^2 & 0 & \sqrt{\frac{3}{2}}(z^2-x^2) \\ 0 & -\frac{3}{2}x^2+\frac{3}{2}z^2 & 0 & \frac{5x^2+y^2+5z^2}{2} & 0 \\ 0 & 0 & \sqrt{\frac{3}{2}}(z^2-x^2)2 & 0 & x^2+4y^2+z^2 \end{pmatrix} \tag{C.2}$$

which can then be diagonalized to yield the eigenenergies

$$E_{0,x} = V_0\,k^2\left((x^2+y^2+z^2)\left(1-\frac{\delta_{hf}^{(e)}}{2\delta_L}\right)+\frac{\delta_{hf}^{(e)}}{4\delta_L}(4x^2+y^2+z^2)\right) \tag{C.3}$$

$$E_{0,y} = V_0\,k^2\left((x^2+y^2+z^2)\left(1-\frac{\delta_{hf}^{(e)}}{2\delta_L}\right)+\frac{\delta_{hf}^{(e)}}{4\delta_L}(x^2+4y^2+z^2)\right) \tag{C.4}$$

$$E_{0,z} = V_0\, k^2 \left((x^2+y^2+z^2) \left(1 - \frac{\delta_{hf}^{(e)}}{2\delta_L} \right) + \frac{\delta_{hf}^{(e)}}{4\delta_L} (x^2+y^2+4z^2) \right) \tag{C.5}$$

$$E_{+} = V_0\, k^2 \left((x^2+y^2+z^2) + \frac{\delta_{hf}^{(e)}}{2\delta_L} \sqrt{x^4+y^4+z^4-x^2y^2-y^2z^2-z^2x^2} \right) \tag{C.6}$$

$$E_{-} = V_0\, k^2 \left((x^2+y^2+z^2) - \frac{\delta_{hf}^{(e)}}{2\delta_L} \sqrt{x^4+y^4+z^4-x^2y^2-y^2z^2-z^2x^2} \right). \tag{C.7}$$

Finally, we calculate the mean energy of an atomic ensemble in each of these sub-levels. We approximate the density by the Boltzmann distribution

$$n(r) = \mathcal{N} \exp\left(-\frac{V_0 k^2\, r^2}{k_\mathrm{B} T} \right). \tag{C.8}$$

The mean values are then evaluated numerically, and we find

$$\langle E_{0,x} \rangle = \langle E_{0,y} \rangle = \langle E_{0,z} \rangle = \frac{3}{2} k_\mathrm{B} T \tag{C.9}$$

$$\langle E_{\pm} \rangle = \frac{3}{2} k_\mathrm{B} T \pm 1.78 \frac{\delta_{hf}^{(e)}}{4\delta_L} k_\mathrm{B} T \tag{C.10}$$

D. Collection efficiency of the imaging system

This appendix details the estimation of photon detection rate during the single-atom imaging sequence. In this scheme, the atoms are pinned at fixed positions by the optical lattice, and simultaneously cooled down by the molasses. Furthermore, the molasses also plays a crucial role in the imaging process: it is responsible for the scattering of photons, which are then collected on the CCD camera.

However, only a small fraction of these scattered photons will reach the detector, owing the the finite collection efficiency of the imaging system, which is limited by the following factors.

- The numerical aperture of the imaging system is limited by the microscope objective (see 2.2.2), and is $NA = 0.45$. The solid angle of the objective is therefore $0.053 \times 4\pi$, and only 5.3 % of the scattered photons can reach the CCD camera.
- The vacuum window does not have an anti-reflection coating: it reflects 4 % of the incoming light at both interfaces, and its transmission is 92 %.
- The quantum efficiency of the CCD camera is 95 %.
- All the optics placed between the vacuum chamber and the CCD camera may contribute as well. However, all the surfaces are anti-reflection coated, so this effect should be negligible.

Overall, we expect a collection efficiency of 4.6 % of scattered photons at most.

In order to detect an atom without ambiguity, we require the number of detected photons to be larger than the read–out noise, which is specified at 3 counts per pixel. Note that we assume here that no stray light reaches the CCD camera. To fulfill this condition, it is sufficient to scatter 200 photons on average. In this case, 9 photons are detected on the CCD camera. Furthermore, the probability to detect less than 9 photons is inferior to 1 %. Thus, an atom has a probability inferior to 1% to remain undetected.

Finally, for a molasses with $\delta_M = 5\,\Gamma$ and $T = 20\ \mu$K, an atom scatters $\gamma_M \approx 1$ photons/μs (see Eqs. 7.1 and 7.2). Thus, an atom can be detected with as little as 200 μs exposure time.

Bibliography

[1] M. H. Anderson, J. R. Ensher, M. R. Matthews, C. E. Wieman, and E. A. Cornell. *Observation of Bose-Einstein condensation in a dilute atomic vapor*. Science **269**, 198 (1995).

[2] K. B. Davis, M.-O. Mewes, M. R. Andrews, N. J. van Druten, D. S. Durfee, D. M. Kurn, and W. Ketterle. *Bose–Einstein condensation in a gas of sodium atoms*. Phys. Rev. Lett. **75**, 3969 (1995).

[3] C. C. Bradley, C. A. Sackett, J. J. Tollett, and R. G. Hulet. *Evidence of Bose–Einstein condensation in an atomic gas with attractive interactions*. Phys. Rev. Lett. **75**, 1687 (1995).

[4] A. Einstein. *Quantentheorie des einatomigen idealen Gases*. Sitzungsberichte/Physikalische Klasse, Preussische Akademie der Wissenschaften **22**, 261 (1924).

[5] S. N. Bose. *Plancks Gesetz und Lichtquantenhypothese*. Z. Phys. **26**, 178 (1924).

[6] P. Kapitza. *Viscosity of liquid helium below the λ-point*. Nature **141**, 74 (1938).

[7] V. F. Sears and E. C. Svensson. *Pair correlations and the condensate fraction in superfluid* ^{4}He. Phys. Rev. Lett. **43**, 2009–2012 (1979).

[8] E. P. Gross. *Structure of Quantized Vortex*. Il Nuovo Cimento **20**, 454 (1961).

[9] L. P. Pitaevskii. *Vortex lines in an imperfect Bose gas*. Sov. Phys. JETP **13**, 451 (1961).

[10] M. R. Andrews, C. G. Townsend, H. J. Miesner, D. S. Durfee, D. M. Kurn, and W. Ketterle. *Observation of interference between two Bose condensates*. Science **275**, 637 (1997).

[11] I. Bloch, T. W. Hänsch, and T. Esslinger. *Measurement of the spatial coherence of a trapped Bose gas at the phase transition*. Nature **403**, 166 (2000).

[12] B. P. Anderson and M. A. Kasevich. *Macroscopic quantum interference from atomic tunnel arrays*. Science **282**, 1686 (1998).

[13] E. W. Hagley, L. Deng, M. Kozuma, J. Wen, K. Helmerson, S. L. Rolston, and W. D. Phillips. *A well-collimated quasi-continuous atom laser*. Science **283**, 1706 (1999).

[14] I. Bloch, T. W. Hänsch, and T. Esslinger. *An atom laser with a cw output coupler*. Phys. Rev. Lett. **82**, 3008 (1999).

[15] M. R. Matthews, B. P. Anderson, P. C. Haljan, D. S. Hall, C. E. Wieman, and E. A. Cornell. *Vortices in a Bose–Einstein condensate*. Phys. Rev. Lett. **83**, 2498 (1999).

[16] K. W. Madison, F. Chevy, W. Wohlleben, and J. Dalibard. *Vortex formation in a stirred Bose–Einstein condensate*. Phys. Rev. Lett. **84**, 806 (2000).

[17] J. R. Abo-Shaeer, C. Raman, J. M. Vogels, and W. Ketterle. *Observation of vortex lattices in Bose–Einstein condensates*. Science **292**, 476–479 (2001).

[18] B. DeMarco and D. D. Jin. *Onset of Fermi degeneracy in a trapped atomic gas*. Science **285**, 1703 (1999).

[19] A. Truscott, K. Strecker, W. McAlexander, G. Partridge, and R. G. Hulet. *Observation of Fermi pressure in a gas of trapped atoms*. Science **291**, 2570 (2001).

[20] F. Schreck, L. Khaykovich, K. L. Corwin, G. Ferrari, T. Bourdel, J. Cubizolles, and C. Salomom. *Quasipure Bose-Einstein condensate immersed in a Fermi sea*. Phys. Rev. Lett. **87**, 080403 (2001).

[21] I. Bloch, J. Dalibard, and W. Zwerger. *Many-body physics with ultracold gases*. Rev. Mod. Phys **80**, 885 (2008).

[22] P. Courteille, R. Freeland, D. Heinzen, F. van Abeelen, and B. Verhaar. *Observation of a Feshbach resonance in cold atom scattering*. Phys. Rev. Lett **81**, 69 (1998).

[23] S. Inouye, M. Andrews, J. Stenger, H. J. Miesner, D. M. Stamper-Kurn, and W. Ketterle. *Observation of Feshbach resonances in a Bose Einstein condensate*. Nature **392**, 151 (1998).

[24] J. Cubizolles, T. Bourdel, S. J. J. M. F. Kokkelmans, G. V. Shlyapnikov, and C. Salomon. *Production of Long-Lived Ultracold Li_2 Molecules from a Fermi Gas*. Phys. Rev. Lett. **91**, 240401 (2003).

[25] S. Jochim, M. Bartenstein, A. Altmeyer, G. Hendl, S. Riedl, C. Chin, J. Hecker-Denschlag, and R. Grimm. *Bose–Einstein Condensation of molecules*. Science **302**, 2101 (2003).

[26] M. Greiner, C. A. Regal, and D. S. Jin. *Emergence of a molecular Bose–Einstein condensate from a Fermi gas*. Nature **426**, 537 (2003).

[27] M. W. Zwierlein, C. A. Stan, C. H. Schunk, S. M. F. Raupach, S. Gupta, Z. Hadzibabic, and W. Ketterle. *Observation of Bose–Einstein condensation of molecules*. Phys. Rev. Lett. **91**, 250401 (2003).

[28] T. Bourdel, L. Khaykovich, J. Cubizolles, J. Zhang, F. Chevy, M. Teichmann, L. Tarruell, S. Kokkelmans, and C. Salomon. *Experimental study of the BEC-BCS crossover region in Lithium 6*. Phys. Rev. Lett. **93**, 050401 (2004).

[29] M. Bartenstein, A. Altmeyer, S. Riedl, S. Joachim, C. Chin, J. Hecker-Denschlag, and R. Grimm. *Crossover from a molecular Bose–Einstein condensate to a degenerate Fermi Gas*. Phys. Rev. Lett. **92**, 120401 (2004).

[30] C. A. Regal, M. Greiner, and D. S. Jin. *Observation of resonance condensation of fermionic atom pairs*. Phys. Rev. Lett. **92**, 040403 (2004).

[31] M. W. Zwierlein, C. A. Stan, C. H. Schunck, S. M. F. Raupach, A. J. Kerman, and W. Ketterle. *Condensation of pairs of fermionic atoms near a Feshbach resonance*. Phys. Rev. Lett. **92**, 120403 (2004).

[32] S. L. Cornish, N. R. Claussen, J. L. Roberts, E. A. Cornell, and C. E. Wieman. *Stable ^{85}Rb Bose–Einstein condensates with widely tunable interactions*. Phys. Rev. Lett. **85**, 1795 (2000).

[33] K. M. O'Hara, S. L. Hemmer, M. E. Gehm, S. R. Granade, and J. E. Thomas. *Observation of a strongly interacting degenerate Fermi gas of atoms*. Science **298**, 2179 (2002).

[34] T. Bourdel, J. Cubizolles, L. Khaykovich, K. Magalhaes, S. Kokkelmans, G. Shlyapnikov, and C. Salomon. *Measurement of the interaction energy near a Feshbach resonance in a ^6Li Fermi gas*. Phys. Rev. Lett. **91**, 020402 (2003).

[35] S. Nascimbène, N. Navon, K. J. Jiang, F. Chevy, and C. Salomon. *Exploring the thermodynamics of a universal Fermi gas*. Nature **463**, 1057 (2010).

[36] M. J. H. Ku, A. T. Sommer, L. W. Cheuk, and M. W. Zwierlein. *Revealing the Superfluid Lambda Transition in the Universal Thermodynamics of a Unitary Fermi Gas*. Science **335**, 563–567 (2012).

[37] B. Paredes, A. Widera, V. Murg, O. Mandel, S. Fölling, J. I. Cirac, G. V. Shlyapnikov, T. W. Hänsch, and I. Bloch. *Tonks-Girardeau gas of ultracold atoms in an optical lattice*. Nature **429**, 277 – 281 (2004).

[38] T. Kinoshita, T. Wenger, and D. S. Weiss. *Observation of a one-dimensional Tonks-Girardeau gas*. Science **305**, 1125–1128 (2004).

[39] Z. Hadzibabic, P. Krüger, M. Cheneau, B. Battelier, and J. Dalibard. *Berezinskii-Kosterlitz-Thouless crossover in a trapped atomic gas*. Nature **441**, 1118–1121 (2006).

[40] D. Jaksch, C. Bruder, J. I. Cirac, C. W. Gardiner, and P. Zoller. *Cold bosonic atoms in optical lattices*. Phys. Rev. Lett **81**, 3108 (1998).

[41] M. Greiner, M. O. Mandel, T. Esslinger, T. Hänsch, and I. Bloch. *Quantum phase transition from a superfluid to a Mott insulator in a gas of ultracold atoms*. Nature **415**, 39 (2002).

[42] T. Stöferle, H. Moritz, C. Schori, M. Köhl, and T. Esslinger. *Transition from a strongly interacting 1D superfluid to a Mott insulator*. Phys. Phys. Lett. **92**, 130403 (2004).

[43] I. B. Spielman, W. D. Phillips, and J. V. Porto. *The Mott insulator transition in two dimensions*. Phys. Rev. Lett. **98**, 080404 (2007).

[44] M. Köhl, H. Moritz, T. Stöferle, C. Schori, and T. Esslinger. *Superfluid to Mott insulator transition in one, two, and three dimensions*. Journal of Low Temperature Physics **138**, 635 (2005).

[45] R. Jördens, N. Strohmaier, K. Günter, H. Moritz, and T. Esslinger. *A Mott insulator of fermionic atoms in an optical lattice*. Nature **455**, 204–207 (2008).

[46] R. P. Feynman. *Simulating physics with computers*. International Journal of Theoretical Physics **21**, 467–488 (1982).

[47] N. R. Cooper. *Rapidly rotating atomic gases*. Advances in Physics **57**, 539–616 (2008).

[48] V. Bretin, S. Stock, Y. Seurin, and J. Dalibard. *Fast rotation of a Bose–Einstein condensate*. Phys. Rev. Lett. **92**, 050403 (2004).

[49] V. Schweikhard, I. Coddington, P. Engels, V. P. Mogendorff, and E. A. Cornell. *Rapidly rotating Bose–Einstein condensates in and near the lowest Landau level*. Phys. Rev. Lett. **92**, 040404 (2004).

[50] M. V. Berry. *Quantal phase factors accompanying adiabatic changes*. Proc. Roy. Soc. London A **392**, 45–57 (1984).

[51] G. Juzeliūnas, J. Ruseckas, P. Öhberg, and M. Fleischhauer. *Light-induced effective magnetic fields for ultracold atoms in planar geometries*. Phys. Rev. A **73**, 025602 (2006).

[52] K. J. Günter, M. Cheneau, T. Yefsah, S. P. Rath, and J. Dalibard. *Practical scheme for a light-induced gauge field in an atomic Bose gas*. Phys. Rev. A **79**, 011604 (2009).

[53] Y. Lin, R. L. Compton, K. Jiménez-García, J. V. Porto, and I. B. Spielman. *Synthetic magnetic fields for ultracold neutral atoms*. Nature **462**, 628–632 (2009).

[54] J. Dalibard, F. Gerbier, G. Juzeliūnas, and P. Öhberg. *Colloquium : Artificial gauge potentials for neutral atoms*. Rev. Mod. Phys. **83**, 1523–1543 (2011).

[55] N. R. Cooper. *Optical Flux Lattices for Ultracold Atomic Gases*. Phys. Rev. Lett. **106**, 175301 (2011).

[56] R. E. Peierls. *Quelques propriétés typiques des corps solides*. Ann. Inst. Henri Poincaré **5**, 177 (1935).

[57] N. D. Mermin and H. Wagner. *Absence of ferromagnetism or antiferromagnetism in one- or two-dimensional isotropic Heisenberg models*. Phys. Rev. Lett. **17**, 1133 (1966).

[58] P. C. Hohenberg. *Existence of long-range order in one and two dimensions*. Phys. Rev. **158**, 383 (1967).

[59] S. T. Bramwell and P. C. W. Holdsworth. *Magnetization: A characteristic of the Kosterlitz-Thouless-Berezinskii transition*. Phys. Rev. B **49**, 8811–8814 (1994).

[60] V. L. Berezinskii. *Destruction of long-range order in one-dimensional and two-dimensional system possessing a continuous symmetry group - II. quantum systems*. Soviet Physics JETP **34**, 610 (1971).

[61] J. M. Kosterlitz and D. J. Thouless. *Ordering, metastability and phase transitions in two dimensional systems*. J. Phys. C: Solid State Physics **6**, 1181 (1973).

[62] D. J. Bishop and J. D. Reppy. *Study of the superfluid transition in two-dimensional ^{4}He films*. Phys. Rev. B **22**, 5171–5185 (1980).

[63] P. Cladé, C. Ryu, A. Ramanathan, K. Helmerson, and W. D. Phillips. *Observation of a 2D Bose gas: from thermal to quasicondensate to superfluid*. Phys. Rev. Lett. **102**, 170401 (2009).

[64] S. Tung, G. Lamporesi, D. Lobser, L. Xia, and E. A. Cornell. *Observation of the presuperfluid regime in a two-dimensional Bose gas*. Phys. Rev. Lett. **105**, 230408 (2010).

[65] C.-L. Hung, X. Zhang, N. Gemelke, and C. Chin. *Observation of scale invariance and universality in two-dimensional Bose gases*. Nature **470**, 236 (2011).

[66] M. Cheneau. *Transition superfluide et potentiels géométriques dans le gaz de Bose bidimensionnel*. PhD thesis, Université Pierre et Marie Curie (2009).

[67] S. P. Rath. *Production and investigation of quasi-two-dimensional Bose gases*. PhD thesis, Université Pierre et Marie Curie (2010).

[68] T. Yefsah. *Thermodynamique du gaz de Bose à deux dimensions*. PhD thesis, Université Pierre et Marie Curie (2011).

[69] T. Yefsah, R. Desbuquois, L. Chomaz, K. J. Günter, and J. Dalibard. *Exploring the thermodynamics of a two-dimensional Bose gas*. Phys. Rev. Lett. **107**, 130401 (2011).

[70] R. Desbuquois, L. Chomaz, T. Yefsah, J. Léonard, J. Beugnon, C. Weitenberg, and J. Dalibard. *Superfluid behaviour of a two-dimensional Bose gas*. Nature Physics **8**, 645–648 (2012).

[71] A. Imambekov, I. E. Mazets, D. S. Petrov, V. Gritsev, S. Manz, S. Hofferberth, T. Schumm, E. Demler, and J. Schmiedmayer. *Density ripples in expanding low-dimensional gases as a probe of correlations*. Phys. Rev. A **80**, 033604 (2009).

[72] W. S. Bakr, J. Gillen, A. Peng, S. Fölling, and M. Greiner. *A quantum gas microscope for detecting single atoms in a Hubbard-regime optical lattice*. Nature **462**, 74–77 (2009).

[73] J. Sherson, C. Weitenberg, M. Endres, M. Cheneau, I. Bloch, and S. Kuhr. *Single-atom-resolved fluorescence imaging of an atomic Mott insulator*. Nature **467**, 68–72 (2010).

[74] Z. Hadzibabic and J. Dalibard. *Two-dimensional Bose fluids: An atomic physics perspective*. In R. Kaiser and D. Wiersma, editors, *Nano optics and atomics: transport of light and matter waves*, volume CLXXIII of *Proceedings of the International School of Physics Enrico Fermi, 2009*. IOS Press (2010). arXiv:0912.1490.

[75] S. K. Adhikari. *Quantum scattering in two dimensions*. American Journal of Physics **54**, 362–367 (1986).

[76] D. S. Petrov, M. Holzmann, and G. V. Shlyapnikov. *Bose–Einstein condensation in quasi-2D trapped gases*. Phys. Rev. Lett. **84**, 2551 (2000).

[77] D. S. Petrov and G. V. Shlyapnikov. *Interatomic collisions in a tightly confined Bose gas*. Phys. Rev. A **64**, 012706 (2001).

[78] N. V. Prokof'ev, O. Ruebenacker, and B. V. Svistunov. *Critical point of a weakly interacting two-dimensional Bose gas*. Phys. Rev. Lett. **87**, 270402 (2001).

[79] N. V. Prokof'ev and B. V. Svistunov. *Two-dimensional weakly interacting Bose gas in the fluctuation region*. Phys. Rev. A **66**, 043608 (2002).

[80] O. Penrose and L. Onsager. *Bose–Einstein condensation and liquid helium*. Phys. Rev. **104**, 576 (1956).

[81] A. Messiah. *Quantum Mechanics*, volume II. North-Holland Publishing Company, Amsterdam (1961).

[82] C. Chin, R. Grimm, P. Julienne, and E. Tiesinga. *Feshbach resonances in ultracold gases*. Rev. Mod. Phys. **82**, 1225–1286 (2010).

[83] J. Choi, S. W. Seo, W. J. Kwon, and Y. Shin. *Probing phase fluctuations in a 2D degenerate Bose gas by free expansion*. Phys. Rev. Lett. **109**, 125301 (2012).

[84] S. P. Rath, T. Yefsah, K. J. Günter, M. Cheneau, R. Desbuquois, M. Holzmann, W. Krauth, and J. Dalibard. *Equilibrium state of a trapped two-dimensional Bose gas*. Phys. Rev. A **82**, 013609 (2010).

[85] L.-C. Ha, C.-L. Hung, X. Zhang, U. Eismann, S.-K. Tung, and C. Chin. *Strongly interacting two-dimensional Bose gases*. arXiv:cond-mat/1211.34569 (2012).

[86] D. J. Bishop and J. D. Reppy. *Study of the superfluid transition in two-dimensional ^{4}He films*. Phys. Rev. Lett. **40**, 1727–1730 (1978).

[87] L. Pitaevskii and S. Stringari. *Bose–Einstein condensation*. Oxford University Press, Oxford (2003).

[88] C. Pethick and H. Smith. *Bose–Einstein condensation in dilute gases*. Cambridge University Press (2002).

[89] M. Holzmann, M. Chevallier, and W. Krauth. *Semiclassical theory of the quasi two-dimensional trapped gas*. Europhys. Lett. **82**, 30001 (2008).

[90] M. Holzmann, M. Chevallier, and W. Krauth. *Universal correlations and coherence in quasi-two-dimensional trapped Bose gases*. Phys. Rev. A **81**, 043622 (2010).

[91] A. Keshet and W. Ketterle. *A distributed, graphical user interface based, computer control system for atomic physics experiments*. Rev. Sci. Instrum. **84**, 015105 (2013).

[92] C. G. Townsend, N. H. Edwards, C. J. Cooper, K. P. Zetie, C. J. Foot, A. M. Steane, P. Szriftgiser, H. Perrin, and J. Dalibard. *Phase-space density in the magneto-optical trap*. Phys. Rev. A **52**, 1423 (1995).

[93] W. Petrich, M. H. Anderson, J. R. Ensher, and E. A. Cornell. *A stable, tightly confining magnetic trap for evaporative cooling of neutral atoms*. Phys. Rev. Lett. **74**, 3352 (1995).

[94] Y.-J. Lin, A. R. Perry, R. L. Compton, I. B. Spielman, and J. V. Porto. *Rapid production of ^{87}Rb Bose-Einstein condensates in a combined magnetic and optical potential*. Phys. Rev. A **79**, 063631 (2009).

[95] R. Dubessy, K. Merloti, L. Longchambon, P.-E. Pottie, T. Liennard, A. Perrin, V. Lorent, and H. Perrin. *^{87}Rb Bose-Einstein condensate in an optically plugged quadrupole trap*. Phys. Rev. A **85**, 013643 (2012).

[96] E. Akkermans and G. Montambaux. *Mesoscopic physics of eletrons and photons*. Cambridge University Press, Cambridge, England (2007).

[97] L. Chomaz, L. Corman, T. Yefsah, R. Desbuquois, and J. Dalibard. *Absorption imaging of a quasi-two-dimensional gas: a multiple scattering analysis*. New Journal of Physics **14**, 055001 (2012).

[98] G. Reinaudi, T. Lahaye, Z. Wang, and D. Guéry-Odelin. *Strong saturation absorption imaging of dense clouds of ultracold atoms*. Optics Letters **32**, 3143 (2007).

[99] S. R. Segal, Q. Diot, E. A. Cornell, A. A. Zozulya, and D. Z. Anderson. *Revealing buried information: Statistical processing techniques for ultracold-gas image analysis*. Phys. Rev. A **81**, 053601 (2010).

[100] T.-L. Ho and Q. Zhou. *Obtaining the phase diagram and thermodynamic quantities of bulk systems from the densities of trapped gases*. Nature Physics **6**, 131 (2009).

[101] Z. Hadzibabic, P. Krüger, M. Cheneau, S. P. Rath, and J. Dalibard. *The trapped two-dimensional Bose gas: from Bose–Einstein condensation to Berezinskii–Kosterlitz–Thouless physics*. New Journal of Physics **10**, 045006 (2008).

[102] R. N. Bisset, D. Baillie, and P. B. Blakie. *Analysis of the Holzmann-Chevallier-Krauth theory for the trapped quasi-two-dimensional Bose gas*. Phys. Rev. A **79**, 013602 (2009).

[103] M. Holzmann and W. Krauth. *Kosterlitz-Thouless transition of the quasi two-dimensional trapped Bose gas*. Phys. Rev. Lett. **100**, 190402 (2008).

[104] D. R. Nelson and J. M. Kosterlitz. *Universal jump in the superfluid density of two-dimensional superfluids*. Phys. Rev. Lett. **39**, 1201 (1977).

[105] I. Shvarchuck, C. Buggle, D. S. Petrov, K. Dieckmann, M. Zielonkowski, M. Kemmann, T. G. Tiecke, W. von Klitzing, G. V. Shlyapnikov, and J. T. M. Walraven. *Bose–Einstein condensation into nonequilibrium states studied by condensate focusing*. Phys. Rev. Lett. **89**, 270404 (2002).

[106] W. Ketterle and H.-J. Miesner. *Coherence properties of Bose–Einstein condensates and atom lasers*. Phys. Rev. A **56**, 3291 (1996).

[107] B. Fröhlich, M. Feld, E. Vogt, M. Koschorreck, W. Zwerger, and M. Köhl. *Radio-Frequency Spectroscopy of a Strongly Interacting Two-Dimensional Fermi Gas*. Phys. Rev. Lett. **106**, 105301 (2011).

[108] C. Raman, M. Köhl, R. Onofrio, D. S. Durfee, C. E. Kuklewicz, Z. Hadzibabic, and W. Ketterle. *Evidence for a critical velocity in a Bose–Einstein condensed gas*. Phys. Rev. Lett. **83**, 2502 (1999).

[109] D. E. Miller, J. K. Chin, C. A. Stan, Y. Liu, W. Setiawan, C. Sanner, and W. Ketterle. *Critical Velocity for Superfluid Flow across the BEC-BCS Crossover*. Phys. Rev. Lett. **99**, 070402 (2007).

[110] J. S. Langer and M. E. Fisher. *Intrinsic Critical Velocity of a Superfluid*. Phys. Rev. Lett. **19**, 560–563 (1967).

[111] M. Cross. *Statistical physics, third term*. Lecture at the California Institute of Technology (2005).

[112] C. Ryu, M. F. Andersen, P. Cladé, V. Natarajan, K. Helmerson, and W. D. Phillips. *Observation of Persistent Flow of a Bose-Einstein Condensate in a Toroidal Trap*. Phys. Rev. Lett. **99**, 260401 (2007).

[113] A. Ramanathan, K. C. Wright, S. R. Muniz, M. Zelan, W. T. Hill, C. J. Lobb, K. Helmerson, W. D. Phillips, and G. K. Campbell. *Superflow in a Toroidal Bose-Einstein Condensate: An Atom Circuit with a Tunable Weak Link*. Phys. Rev. Lett. **106**, 130401 (2011).

[114] S. Moulder, S. Beattie, R. P. Smith, N. Tammuz, and Z. Hadzibabic. *Quantised superflow glitches in an annular Bose–Einstein condensate*. arXiv:cond-mat/1112.0334 (2012).

[115] A. Amo, J. Lefrere, S. Pigeon, C. Adrados, C. Ciuti, I. Carusotto, R. Houdre, E. Giacobino, and A. Bramati. *Observation of Superfluidity of Polaritons in Semiconductor Microcavities*. Nature Physics **5**, 805 (2009).

[116] A. J. Leggett. *Quantum Liquids*. Oxford University Press (2006).

[117] R. Onofrio, C. Raman, J. M. Vogels, J. R. Abo-Shaeer, A. P. Chikkatur, and W. Ketterle. *Observation of Superfluid Flow in a Bose-Einstein Condensed Gas*. Phys. Rev. Lett. **85**, 2228–2231 (2000).

[118] C. Raman, R. Onofrio, J. Vogels, J. Abo-Shaeer, and W. Ketterle. *Dissipationless Flow and Superfluidity in Gaseous Bose-Einstein Condensates*. Journal of Low Temperature Physics **122**, 99–116 (2001). ISSN 0022-2291.

[119] P. Engels and C. Atherton. *Stationary and Nonstationary Fluid Flow of a Bose-Einstein Condensate Through a Penetrable Barrier*. Phys. Rev. Lett. **99**, 160405 (2007).

[120] T. W. Neely, E. C. Samson, A. S. Bradley, M. J. Davis, and B. P. Anderson. *Observation of Vortex Dipoles in an Oblate Bose-Einstein Condensate*. Phys. Rev. Lett. **104**, 160401 (2010).

[121] G. E. Astrakharchik and L. P. Pitaevskii. *Motion of a heavy impurity through a Bose-Einstein condensate*. Phys. Rev. A **70**, 013608 (2004).

[122] A. D. Chepelianskii, F. Chevy, and E. Raphaël. *Capillary-Gravity Waves Generated by a Slow Moving Object*. Phys. Rev. Lett. **100**, 074504 (2008).

[123] T. Frisch, Y. Pomeau, and S. Rica. *Transition to Dissipation in a Model of Superflow*. Phys. Rev. Lett. **69**, 1644 (1992).

[124] T. Winiecki, J. F. McCann, and C. S. Adams. *Pressure Drag in Linear and Nonlinear Quantum Fluids*. Phys. Rev. Lett. **82**, 5186 (1999).

[125] J. S. Stiessberger and W. Zwerger. *Critical Velocity of Superfluid Flow past Large Obstacles in Bose-Condensates*. Phys. Rev. A **62**, 061601(R) (2000).

[126] M. Crescimanno, C. G. Koay, R. Peterson, and R. Walsworth. *Analytical Estimate of the Critical Velocity for Vortex Pair Creation in Trapped Bose Condensates*. Phys. Rev. A **62**, 063612 (2000).

[127] F. Dalfovo, S. Giorgini, M. Guilleumas, L. Pitaevskii, and S. Stringari. *Collective and single-particle excitations of a trapped Bose gas*. Phys. Rev. A **56**, 3840–3845 (1997).

[128] P. O. Fedichev and G. V. Shlyapnikov. *Critical velocity in cylindrical Bose-Einstein condensates*. Phys. Rev. A **63**, 045601 (2001).

[129] V. Schweikhard, S. Tung, and E. A. Cornell. *Vortex proliferation in the Berezinskii-Kosterlitz-Thouless regime on a two-dimensional lattice of Bose–Einstein condensates*. Phys. Rev. Lett. **99**, 030401 (2007).

[130] S. Dettmer, D. Hellweg, P. Ryyty, J. J. Arlt, W. Ertmer, K. Sengstock, D. S. Petrov, G. V. Shlyapnikov, H. Kreutzmann, L. Santos, and M. Lewenstein. *Observation of phase fluctuations in elongated Bose–Einstein condensates*. Phys. Rev. Lett **87**, 160406 (2001).

[131] L. Giorgetti, I. Carusotto, and Y. Castin. *Semiclassical field method for the equilibrium Bose gas and application to thermal vortices in two dimensions*. Phys. Rev. A **76**, 013613 (2007).

[132] C. J. Foster, P. B. Blakie, and M. J. Davis. *Vortex pairing in two-dimensional Bose gases*. Phys. Rev. A **81**, 023623 (2010).

[133] J.-Y. Choi, S. W. Seo, and Y.-I. Shin. *Observation of thermally activated vortex pairs in a quasi-2D Bose gas*. arXiv:cond-mat/1211.5649v2 (2012).

[134] A. L. Fetter. *Rotating trapped Bose-Einstein condensates*. Rev. Mod. Phys. **81**, 647–691 (2009).

[135] K. D. Nelson, X. Li, and D. S. Weiss. *Imaging single atoms in a three-dimensional array*. Nature Physics **3**, 556–560 (2007).

[136] M. Karski, L. Förster, J. M. Choi, W. Alt, A. Widera, and D. Meschede. *Nearest-neighbor detection of atoms in a 1D optical lattice by fluorescence imaging*. Phys. Rev. Lett. **102**, 053001 (2009).

[137] W. S. Bakr, A. Peng, M. E. Tai, R. Ma, J. Simon, J. I. Gillen, S. Fölling, L. Pollet, and M. Greiner. *Probing the superfluid-to-Mott insulator transition at the single-atom level*. Science **329**, 547–550 (2010).

[138] C. Weitenberg, M. Endres, J. F. Sherson, M. Cheneau, P. Schauß, T. Fukuhara, I. Bloch, and S. Kuhr. *Single-spin addressing in an atomic Mott insulator*. Nature **471**, 319–324 (2011).

[139] T. W. Hodapp, C. Genl, C. Furtlehner, C. Westbrook, W. Phillips, and J. Dalibard. *Three-dimensional spatial diffusion in optical molasses*. Appl. Phys. B **60**, 135–143 (1995).

[140] C. Salomon, J. Dalibard, W. D. Phillips, A. Clairon, and S. Guellati. *Laser cooling of Cesium atoms below 3 μK*. Europhysics Letters **12**, 683–688 (1990).

[141] J. Dalibard and C. Cohen-Tannoudji. *Laser cooling below the Doppler limit by polarization gradients: simple theoretical models*. J. Opt. Soc. Am. B **6**, 2023 (1989).

[142] P. D. Lett, W. D. Phillips, S. L. Rolston, C. E. Tanner, R. N. Watts, and C. I. Westbrook. *Optical molasses*. J. Opt. Soc. Am. B **6**, 2084 (1989).

[143] G. Grynberg and J.-Y. Courtois. *Proposal for a magneto-optical lattice for trapping atoms in nearly-dark states*. Europhysics Letters **27**, 41 (1994).

[144] D. Boiron, C. Triché, D. R. Meacher, P. Verkerk, and G. Grynberg. *Three-dimensional cooling of cesium atoms in four-beam gray optical molasses*. Phys. Rev. A **52**, R3425–R3428 (1995).

[145] D. R. Fernandes, F. Sievers, N. Kretzschmar, S. Wu, C. Salomon, and F. Chevy. *Sub-Doppler laser cooling of fermionic 40 K atoms in three-dimensional gray optical molasses*. Europhysics Letters **100**, 63001 (2012).

[146] D. A. Steck. *Rubidium 87 D Line Data*. available online at http://steck.us/alkalidata page (revision 2.1.4) (2010).

[147] C. Weitenberg. *Single-atom resolved imaging and manipulyion in an atomic Mott insulator*. PhD thesis, Ludwig-Maximilians-Universität, München (2011).

[148] W. Petrich, M. H. Anderson, J. R. Ensher, and E. A. Cornell. *Behavior of atoms in a compressed magneto-optical trap*. J. Opt. Soc. Am. B **11**, 1332 (1994).

[149] Y. B. Ovchinnikov, J. H. Müller, M. R. Doery, E. J. D. Vredenbregt, K. Helmerson, S. L. Rolston, and W. D. Phillips. *Diffraction of a released Bose–Einstein condensate by a pulsed standing light wave*. Phys. Rev. Lett. **83**, 284 (1999).

[150] B. Gadway, D. Pertot, R. Reimann, M. G. Cohen, and D. Schneble. *Analysis of Kapitza-Dirac diffraction patterns beyond the Raman-Nath regime*. Opt. Express **17**, 19173–19180 (2009).

[151] N. Read and N. R. Cooper. *Free expansion of lowest-Landau-level states of trapped atoms: A wave-function microscope*. Phys. Rev. A **68**, 035601 (2003).

[152] N. Cooper and J. Dalibard. *Reaching fractional quantum Hall states with optical flux lattices*. arXiv:cond-mat/1212.3552v1 (2012).

Résumé

Les propriétés physiques d'un système homogène à l'équilibre thermodynamique sont fortement contraintes par sa dimensionnalité. Le gaz de Bose à deux dimensions est un système particulier de ce point de vue : bien que l'établissement d'un ordre à longue portée soit impossible à température non-nulle, il existe néanmoins une transition de phase vers un état superfluide à basse température. De plus, la dimensionalité réduite du système rend son équation d'état invariante par changement d'échalle pour de faibles interactions atomiques répulsives.

Dans ce manuscrit de thèse, nous présentons une étude expérimentale du gaz de Bose à deux dimensions. Nous mesurons son équation d'état de deux methodes différentes, et trouvons un résultat en bon accord avec les prédictions analytiques et numériques. Ces résultats ont également permis de confirmer l'invariance d'échelle du système. De plus, l'une des méthodes ne nécessite qu'un seul paramètre ajustable pour la mesure de l'équation d'état. Nous présentons ensuite une mesure locale du caractère superfluide du gaz. À cet effet, nous avons mis en évidence l'absence de dissipation lors de la perturbation du système par un obstacle en mouvement. Enfin, nous effectuons une analyse des fluctuations du gaz de Bose 2D, qui a permis de confirmer la suppression des fluctuations de densité dans la phase superfluide, ainsi que le rôle dominant joué par les phonons dans les fluctuations de phase.

Mots-clés : Condensation de Bose–Einstein, basse dimension, équation d'état, invariance d'échelle, superfluidité, transition de phase

Abstract

The physical properties of a homogeneous system at the thermodynamic equilibrium are strongly constrained by its dimensionality. In this respect, the two dimensional Bose gas constitutes a particularly interesting system: while it is impossible to observe a long range order at non-zero temperatures, there exists nevertheless a phase transition to a superfluid state at low temperatures. Furthermore, owing to the reduced dimensionality, the equation of state of the weakly interacting two-dimensional Bose gas is scale invariant.

In this thesis, we present an experimental study of the two-dimensional Bose gas. We measure its equation of state with two different methods, and find a good agreement with analytic and numerical predictions. These results confirm as well the scale invariance of the system. Furthermore, one of the methods allows for a determination of the equation of state with a single adjustable parameter. We then characterize the superfluid response of the system., by showing evidence for a dissipationless response of the system to a moving perturbation. Finally, we analyze the fluctuations dynamics of the 2D Bose gas, which confirms both the suppression of density fluctuations in the superfluid phase, and the dominating contribution of phonons to the phase fluctuations.

Key words: Bose–Eisntein condensation, low dimension, equation of state, scale invariance, superfluidity, phase transition